Polymorphism of Biomembranes at the Nanoscale

D I S S E R T A T I O N

zur Erlangung des akademischen Grades

doctor rerum naturalium
(Dr. rer. nat.)
im Fach Physik

eingereicht an der
Mathematisch-Naturwissenschaftlichen Fakultät
der Humboldt-Universität zu Berlin

von
MSc Vahid Satarifard

Präsidentin der Humboldt-Universität zu Berlin:
Prof. Dr.-Ing. Dr. Sabine Kunst

Dekan der Mathematisch-Naturwissenschaftlichen Fakultät:
Prof. Dr. Elmar Kulke

Gutachter:
1. Prof. Dr. Reinhard Lipowsky, Humboldt-Universität zu Berlin
2. Prof. Dr. Sabine Klapp, Technische Universität Berlin
3. Prof. Dr. Gerhard Gompper, University of Cologne

Tag der mündlichen Prüfung: 23.06.2020

Abstract

Liquid-liquid phase separation has been studied for a long time in the context of chemical physics. More recently, it has been discovered that this process also occurs in living cells. Homogeneous fluid demixing of macromolecules, such as nucleic acids and proteins into liquid phases, leads to the formation of biomolecular condensates, also known as membraneless organelles. Such biomolecular condensates can also nucleate at the membrane, thereby generating mechanical forces. In the context of chemical physics and biophysics, the response of biomembranes to liquid-liquid phase separation of aqueous polymer solutions and the resulting water-in-water droplets have been studied at the micrometer scale, using optical microscopy and membrane elasticity theory. These systems involve membrane wetting phenomena, which are caused by the attractive interactions of the condensate droplets with the elastic membranes. In this thesis, we use computational methods to study the polymorphism of biomembranes at the nanoscale.

In chapter three, we use molecular simulations based on dissipative particle dynamics to investigate nanodroplets with high interfacial tensions of the order of mN/m. When a droplet adheres to the membrane, it forms a contact area which is bounded by a contact line. For a micrometer-sized droplet, the line tension associated with this contact line can usually be ignored compared to the surface tension. However, for a small nanoscopic droplet, this line tension is expected to affect the membrane-droplet morphology. The effects of line tension on the droplet-membrane morphology are shown to depend strongly on another key parameter, the mechanical tension of the membrane. For a large membrane tension, a droplet adhering to the membrane can only be partially engulfed by the membrane, and the membrane-droplet system exhibits an axisymmetric morphology. A reduction of the membrane tension leads to an increase in the droplet-membrane contact area and a decrease in the interfacial area of the droplet. During this process, the system initially retains its axisymmetric shape, which implies a circular contact line and a circular membrane neck. However, when the tension falls below a certain threshold value, the system undergoes a morphological transition towards a non-axisymmetric morphology with a non-circular membrane neck. This morphology persists until the nanodroplet is completely engulfed by the membrane and the membrane neck has closed into a tight-lipped shape. It is found that this breaking of axisymmetry is caused by a negative line tension, which is shown to be a robust feature of membrane-droplet systems. A closed membrane neck with a tight-lipped shape would suppress both thermally-activated and protein-induced scission of the neck, implying a reduction in the cellular uptake of nanodroplets by pinocytosis and fluid-phase endocytosis.

In chapter four, we study nanodroplets with low interfacial tensions of the order of μN/m. For such low tension as found for biomolecular condensates, molecular simulations become unfeasible. As we decrease the interfacial tension, the width of the interface increases, and we would need to simulate larger and larger droplets to obtain reliable results. Therefore, to explore the low interfacial tension regime,

we used an alternative approach based on energy minimization, which is computationally less expensive. This approach allows us to explore a wide range of parameters and to systematically determine the dependence of membrane wetting phenomena on interfacial tension, bending rigidity, line tension, and spontaneous curvature. We observe a new morphological transformation that involves both vesicles and droplets, including another regime with broken rotational symmetry. Finally, we determine the boundary between symmetric and asymmetric contact line geometries within the three-dimensional parameter space corresponding to vanishing spontaneous curvature.

In chapter five, we use molecular simulations to monitor the morphological transformations of individual nanovesicles with different degrees of asymmetry between the two leaflets of the bilayer membranes. We start with the assembly of spherical vesicles that enclose a certain volume of water and contain a certain total number of lipids. When we reduce their volume, the spherical vesicles transform into a multitude of nonspherical shapes such as oblates and stomatocytes as well as prolates and dumbbells. This polymorphism can be controlled by redistributing a small fraction of lipids between the inner and outer leaflets of the bilayer membranes. As a consequence, the inner and the outer leaflets experience different mechanical tensions. Small changes in the vesicle volume reduce the overall bilayer tension by two orders of magnitude, thereby producing tensionless bilayers. We show how to determine, for a certain total number of lipids, the unique spherical vesicle for which both leaflet tensions vanish individually. We also compute the local spontaneous curvature of the spherical membranes by identifying the first moment of the spherically symmetric stress profiles across the lipid bilayers with the nanoscopic torque as derived from curvature elasticity. This systematic study makes it possible to distinguish the induced spontaneous curvature due to lipid density mismatch from the one induced by absorbed particles. Another rather interesting question is the nucleation of liquid droplets at membranes. For multi-site nucleation, the different droplets will compete for membrane area and may then lead to coexistence of partially and completely engulfed droplets.

Zusammenfassung

Die Phasentrennung in Flüssigkeitsmischungen in der chemischen Physik seit langem untersucht. In jüngster Zeit konnten solche Prozesse auch in lebenden Zellen beobachtet werden. Die homogene Entmischung von Makromolekülen, wie Nukleinsäuren und Proteinen, im Cytosol der Zellen, führt zur Bildung von biomolekularen Kondensaten, auch bekannt als membranlose Organellen. Solche biomolekularen Kondensate können sich auch an der Membran bilden und so mechanische Kräfte auf diese ausüben. Die Reaktion von Biomembranen auf die Phasentrennung von wässrigen Polymermischungen und die dabei entstehenden Wasser-in-Wasser-Tröpfchen im Mikrometerberreich, wurden mit Hilfe von optischer Mikroskopie und der Theorie der Membranelastizität untersucht. Bei diesen Systemen spielen Membranbenetzungsphänomene, die durch die attraktiven Wechselwirkungen der Kondensattröpfchen mit den elastischen Membranen verursacht werden, eine wichtige Rolle. In dieser Arbeit untersuchen wir den Polymorphismus von Biomembranen im Nanometerbereich anhand von molekularer Modellierung und Computersimulationen.

Im dritten Kapitel werden molekulare Simulationen basierend auf Dissipative Particle Dynamics genutzt, um Nanotröpfchen mit relativ großen Oberflächenspannungen in der Größenordnung von mN/m zu untersuchen. Wenn ein Tröpfchen an der Membran haftet, bildet es eine Kontaktfläche, welche durch eine Kontaktlinie begrenzt wird. Bei einem mikrometergroßen Tropfen kann die mit dieser Kontaktlinie verbundene Linienspannung im Vergleich zur Oberflächenspannung normalerweise ignoriert werden. Bei einem nanoskopisch kleinen Tröpfchen ist jedoch zu erwarten, dass diese Linienspannung die Membran-Tropfen-Morphologie beeinflusst. Es kann gezeigt werden, dass die Auswirkungen der Linienspannung auf die Tropfen-Membran-Morphologie zusätzlich stark von einem weiteren Schlüsselparameter abhängen, der mechanischen Spannung der Membran. Bei einer großen Membranspannung kann ein an der Membran haftender Tropfen nur teilweise von der Membran umschlossen werden, und das Membran-Tropfen-System weist eine achsensymmetrische Morphologie auf. Eine Reduzierung der Membranspannung führt zu einer Vergrößerung der Kontaktfläche zwischen Tropfen und Membran und einer Verringerung der Grenzfläche des Tropfens. Dabei behält das System zunächst seine achsensymmetrische Form, was bedeutet, dass sowohl die Kontaktlinie als auch der Membranhals kreisförmig sind. Fällt die Spannung jedoch unter einen bestimmten Schwellenwert reduziert wird, vollzieht sich im System ein morphologischer Übergang zu einer nicht-achsensymmetrischen Morphologie mit einem länglichen Membranhals. Diese Morphologie bleibt bestehen, bis das Nanotropfen vollständig von der Membran umschlossen ist und sich der Membranhals zu einer engen Lippenform geschlossen hat. Dieser Bruch der Achsensymmetrie wird durch eine negative Linienspannung verursacht, die sich als robuste Eigenschaft von Membran-Tropfensystemen erweist. Solch ein geschlossener Membranhals mit einer eng anliegenden Form würde sowohl die thermisch aktivierte als auch die proteininduzierte Fission des Halses unterdrücken, was eine Verringerung der zellulä-

ren Aufnahme von Nanotropfen durch Pinozytose und Flüssigphasen-Endocytose bedeuten würde.

Im vierten Kapitel untersuchen wir Nanotropfen die eine relativ kleine Oberflächenspannungen in der Größenordnung von μN/m haben. Für solche Spannungen, wie sie etwa bei biomolekularen Kondensaten auftreten, sind molekulare Simulationen nicht mehr mit vertretbarem Rechenaufwand möglich. Wenn die Grenzflächenspannung abnimmt, wächst die Unschärfe der Grenzfläche, man muss größere und größere Tropfen simulieren, um zuverlässige Ergebnisse zu erhalten. Daher haben wir für die Untersuchung des Regimes der niedrigen Grenzflächenspannungen einen alternativen Ansatz gewählt, der auf der Energieminimierung basiert, die rechnerisch kostengünstiger ist. Dieser Ansatz ermöglicht es uns, eine Vielzahl von Parametern zu variieren und die Abhängigkeit der Membranbenetzungsphänomene von Grenzflächenspannung, Biegesteifigkeit, Linienspannung und spontaner Krümmung der Membran systematisch zu untersuchen. Wir beobachten einen neuen morphologischen Übergang, der sowohl Vesikel als auch Tröpfchen betrifft, und zu einer weiteren Systemgeometrie mit gebrochener Rotationssymmetrie führt. Schließlich bestimmen wir die Grenze zwischen symmetrischen und asymmetrischen Geometrien der Kontaktlinie innerhalb des dreidimensionalen Parameterraums der sich für verschwindende spontane Krümmung ergibt.

In Kapitel fünf verwenden wir erneut molekulare Simulationen, um die morphologischen Transformationen einzelner Nanovesikel, die sich der Dichte-Asymmetrie zwischen den beiden Einzelschichten der Lipid-Doppelschicht unterscheiden. Wir beginnen mit kugelförmigen Vesikeln, die ein bestimmtes Wasservolumen umschließen deren Membranen eine bestimmte Gesamtzahl von Lipiden enthalten. Wenn das umschlossene Volumen reduziert wird, transformieren sich die kugelförmigen Vesikel in eine Vielzahl von nicht-kugelförmigen Formen wie Oblaten und Stomatozyten sowie Prolaten und Hantelformen. Dieser Polymorphismus kann durch Umverteilung weniger Lipide zwischen der inneren und der äußeren Schicht der Doppelmembranen gesteuert werden. Infolgedessen erfahren die innere und äußere Lipidschicht unterschiedliche mechanische Spannungen. Kleine Änderungen des Vesikelvolumens verringern die gesamte mechanische Spannung der Doppelmembran um zwei Größenordnungen, so dass spannungsfreie Doppelschichten entstehen.

Für eine bestimmte Gesamtzahl von Lipiden kann so die spezielle kugelförmige Vesikel eindeutig bestimmt werden, bei der die Spannung in beiden Monoschichten einzeln verschwindt. Wir berechnen auch die lokale spontane Krümmung der kugelförmigen Membranen, indem wir das erste Moment des kugelsymmetrischen Spannungsprofiles der Lipiddoppelschichten mit dem nanoskopischen Drehmoment, das sich aus der Krümmungselastizität ergibt, gleichsetzten. Eine solche systematische Analyse ermöglicht es, die spontane Krümmung, die durch unterschiedliche Lipiddichten in den beiden Monoschichten induziert wird von der zu unterscheiden, die durch absorbierte Partikel erzeugt wird. Eine weitere offene und sehr interessante Fragestellung betrifft die Nukleation der Tröpfchen an der Membran. Falls die Nukleation zur Bildung von mehreren Tröpfchen führt, dann könnte der Wettbewerb um Membranfläche zur Koexistenz von partiell und vollständig eingeschlossenen Tröpchen führen.

Contents

1 Introduction

1.1 Biomembranes

Cellular plasma membranes are biological entities that primarily act as a guarding wall against extracellular invasion. Plasma membranes, also known as biomembranes, are an indispensable part of life by keeping cells under non-equilibrium conditions and making cellular communication via cell signaling possible. The cellular plasma membranes are mainly composed of three classes of amphipathic lipids, namely, phospholipids, glycolipids, and sterols as well as other biomolecules such as transmembrane proteins and glycosylphosphatidylinositol (GPI)-anchored proteins. Biomembranes are elastic-fluid sheets with a finite thickness, which is primarily constructed from the self-assembly of amphipathic lipids in the form of bilayers. Phospholipid molecules are the most abundant lipid component in the cell membranes. Phospholipids consist of two hydrophobic fatty acid tails and a hydrophilic head of phosphate functional groups. Examples of phospholipid molecules include PC, PS, PE, PG, and many other [1].

The hydrophobic and hydrophilic interactions in aqueous conditions lead to self-assembly of lipid molecules above critical micelle concentration (CMC), in distinct structures, such as micelles, planar bilayers, spherical vesicles (liposome) and micellar structure. This is known as lipid polymorphism, where different phases emerge as a result of self-assembly in distinct physicochemical conditions.

Phospholipid bilayers are highly dynamic thanks to their fluid-elastic nature. The latter leads to the mechanical response of phospholipid bilayers to external stimuli. The most well know stimulus is the change of physicochemical properties of the membrane by exposing bilayers to an asymmetric condition. The bilayer asymmetry can arise both from lipid density/compositional differences during self-assembly or from being exposed to asymmetric aqueous environments. Such asymmetry can give rise to membrane remodeling by formation of structures like membrane buds or nanotubes [2]. Such membrane nanotubes act as lipid area reservoirs and increase the stability of the membrane against mechanical perturbations [3].

The complex and heterogeneous composition of the plasma membrane makes it hard to understand the underlying physics of biomembranes. However, such complexity can be reduced to much simpler components using model membranes that contain only lipids. The research on model membranes was started around two decades ago by the study of the most fundamental aspects of bilayer vesicles consisting of pure

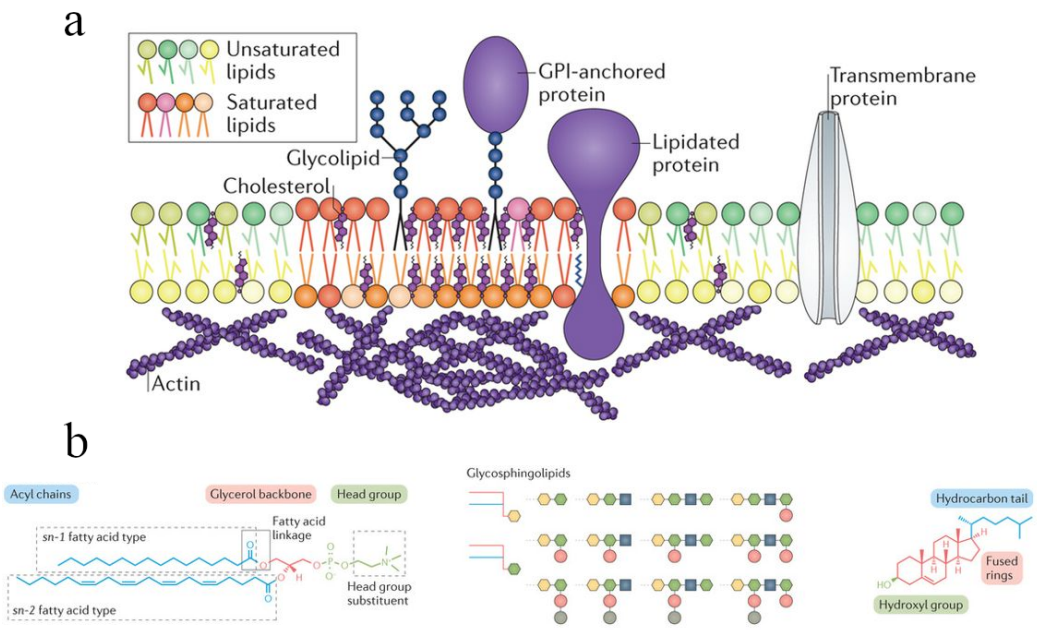

Figure 1.1. (a) The schematic view of molecular heterogeneity in plasma membrane, adapted from Ref. [4]. (b) The example of amphipathic lipids, Glycerophospholipids (GPLs), complex glycosphingolipids (GSLs) and cholesterol (left to right), adapted from Ref [1].

phospholipids. Vesicles are structures that enclose aqueous phases by lipid bilayers. The model membranes categorized in three classes based on their size: giant unilamellar vesicles (GUVs) with a size in range of 1-200 μm, large unilamellar vesicles (LUVs) with a size of 0.1-1 μm and small unilamellar vesicles (SUVs) with a size within the range of 20-100 nm. The most commonly studied form of model membranes are GUVs, which have a comparable size to cells [5].

The level of complexity of model membranes has increased extensively by incorporating different essential components. The current state of the art studies embraces the ambitious goal of creating a minimal form of life by synthesizing the minimal artificial cells via a bottom-up approach. One of the instances of such activities is the ongoing research project MaxSynBio launched by Max Planck's research network in synthetic biology [6].

1.2 Theoretical Description of Membranes

Fluid bilayer membranes can be described theoretically via continuum models as thin fluid-elastic sheets. There are different energetic contributions associated with this description of fluid bilayers. These contributions correspond to the bending energy,

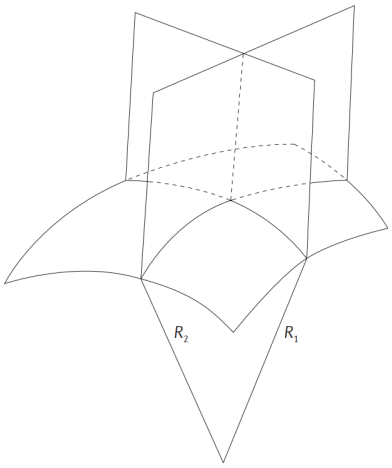

Figure 1.2. Two principle radii are shown for a locus on the membrane surface by R_1 and R_2. The principal curvatures are defined by the inverse of principle radii as $C_1 = 1/R_1$ and $C_2 = 1/R_2$, respectively. The figure is adapted from Ref. [10]

stretching energy, and elasticity arising from leaflets area difference. Here we briefly explain these models that have been used during the last decades for the description of lipid membranes [7, 8].

1.2.1 Bending energy

The local shape of a surface (such as lipid bilayers) can be characterized by its two principal curvatures, i.e., C_1 and C_2, see Figure 1.2. Principal curvatures are directly related to the first and second fundamental forms and can be calculated from the eigenvalues and the eigenvectors of the Hessian matrix [9]. The absolute values of the curvatures are given by eigenvalues of the Hessian matrix, where the eigenvectors point in the direction of the minimal and maximal curvatures. The arithmetic average of the principal curvatures defines the mean curvature by:

$$M = \frac{C_1 + C_2}{2} \tag{1.1}$$

and the product of principal curvatures is called the Gaussian curvature:

$$K = C_1 * C_2 \tag{1.2}$$

The mean and Gaussian curvatures are two invariants of the curvature tensor, and the bending energy of a membrane is defined based on them. The Helfrich-Canham equation accounts for the bending energy of small elastic deformations of a membrane

up to second order in the principal curvatures by [11, 7]

$$E_{be} = \int dA[2\kappa(M-m)^2 + \kappa_G K] \tag{1.3}$$

where κ and κ_G are the bending rigidity and Gaussian curvature modulus, respectively. The preferred curvature of the membrane is called the local spontaneous curvature m, which can arise due to asymmetry in the bilayer. The spontaneous curvature, bending rigidity, and Gaussian bending rigidity are three material parameters. This means that the latter parameters are only affected by the physicochemical make-up and do not depend on the shape of the membrane. The sign of the spontaneous curvature and the mean curvature are defined via a convention. Based on the Gauss-Bonnet theorem, the Gaussian curvature term does not contribute to the bending energy as long as the topology in conserved [9].

Bending rigidity. The bending rigidity is the measure of the membrane's ability to respond to deformations. For membrane with low bending rigidity, one expects large deformations in response to environmental stimuli, whereas small deformations for rigid membranes with high κ. The bending rigidity sets the energy scale in the system.
For experiments, there are several techniques for measurement of bending rigidity [12]. These techniques can be categorized in three general methods: i) analyzing the thermal fluctuation of giant unilamellar vesicles (GUVs), ii) analyzing the force required to deform the membrane under external fields such as electro-deformation, micropipette aspiration or optical tweezers and iii) scattering methods. The most common method is a fluctuation analysis of the thermally excited membrane. This experimental approach links the vesicle shape deviation around equilibrium spherical shape by analyzing the trajectory of optical microscopy images. Typically, the bending rigidity of phospholipid bilayer found from such analysis is of the order of $\kappa \sim 10^{-19}$ J. More details on experimental techniques for measurement of bending rigidity can be found in the comprehensive review by Rumiana Dimova [12].
In addition, the bending rigidity can be calculated from the molecular dynamic (MD) simulations. Two commonly used procedures include analysis of the membrane undulation spectrum and calculation of the bending rigidity based on the relation between area compressibility modulus and the bending rigidity [13]. In the first method, the undulation spectrum $S(q) =< |\tilde{h}(q)|^2 >$ can be generated by Fourier transform of the height variable $\tilde{h}(q)$ from MD trajectories, where q is dimensionless wave number in Fourier space. The undulation spectrum can be decomposed to two regimes of bending and protrusions modes by [13]:

$$S(q) \sim \frac{k_B T}{\kappa q^4} + \frac{k_B T}{\sigma_{pr} q^2} \tag{1.4}$$

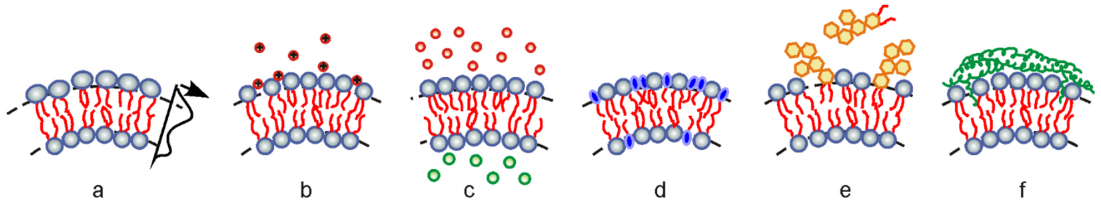

Figure 1.3. Spontaneous curvature can arise as a response to a) difference in the head group size, b) asymmetry of the ionic concentrations, c) exposing to different aqueous solutions of small molecules, such as sugars, d) asymmetric distribution of amphiphilic molecules in different leaflets, e) asymmetric adsorption/desorption of water-soluble molecules, like glycolipid molecules and f) adsorption of proteins with specific shape. The figure is adapted from Ref. [2]

where κ and σ_{pr} are the bending rigidity and the protrusion tension, respectively. The bending mode is dominant at large scales where the wavelength is larger than the bilayer thickness ℓ_{me}. The protrusion tension, which is a measure of the roughens of the bilayer interfaces from the relative displacements of individual amphiphilic molecules at small scales, is dominant at wavelength smaller than bilayer thickness ℓ_{me}. The crossover between bending and protrusion modes is characterized by q_c, called characteristic wave number. The latter method of bending energy calculation is computationally demanding, the less expensive procedure for calculation of bending rigidity is offered by the relation [13]

$$\kappa = \frac{K_A \ell_{me}^2}{48} \tag{1.5}$$

where K_A and ℓ_{me} are area compressibility modulus and bilayer thickness, respectively. It has been shown that these methods lead to essentially the same prediction of the bending rigidity for identical systems [14]. Direct measurement of the Gaussian curvature modulus is challenging; however, is has been shown that κ_G and κ are of the same order of magnitude [15].

Spontaneous curvature. The second and the most important material parameter governing the shape of biomembranes is the spontaneous curvature, denoted by m in Eq. 1.3. Spontaneous curvature is the measure of asymmetry across the lipid bilayer. Such asymmetry can arise either from an asymmetric physicochemical environment of the two leaflets or from a compositional asymmetry of lipids. A schematic representation of different possibilities for inducing spontaneous curvature of the lipid bilayers are illustrated in Figure 1.3. The commonality among all examples shown in Figure 1.3 is that the membrane mean curvature deviates in comparison to the state with a symmetric environment. The latter occurs to minimize bending energy by adopting the mean curvature to the local spontaneous curvature, see Eq. 1.3.

There are different methods to determine spontaneous curvature from experiment and from MD simulations. Here, we briefly discuss some of the commonly used methods. In experiments with GUVs, the spontaneous formation of inward or outward nanotubes can be attributed to the presence of a significant spontaneous curvature. Visual inspections of spontaneous tubulation are usually done by optical microscopy observation. The spontaneous curvature can be quantified in experiments with different methods [2]. Here, we provide an example of the tube-pulling experiment for quantifying spontaneous curvature. The force required for pulling a tube from a GUV which is aspirated with a micropipette has a simple force balance equation [16]:

$$f = 2\pi\sqrt{2\kappa\Sigma_{asp}} - 4\pi\kappa m \tag{1.6}$$

where Σ_{asp} is the aspiration pressure exerted by the micropipette. The latter equation has been recently used in combination with optical tweezers to measure the spontaneous curvature (and simultaneously the bending rigidity) for an asymmetric distribution of the glycolipid GM1 in bilayer leaflets [17] and in asymmetric ionic conditions [18].

For computation of spontaneous curvature in MD simulation, the notion of torque density has been employed [14]. For a tensionless membrane with $\Sigma_{mec} = 0$, it can be shown that nanoscopic torque density is a result of pure bending energy $\mathcal{T}_{nan} = -2\kappa m$. Hence, one can identify the nanoscopic and microscopic torque densities and obtain [14]:

$$-2\kappa m = \int_{-\infty}^{+\infty} dz\ s(z)\ z \tag{1.7}$$

where $s(z) = -[P_T - P_N]$ is the stress profile across the membrane arising from anisotropy in the tangential P_T and normal P_N components of the pressure tensor. Here, z coordinates are set to be the normal to membrane, then $P_T = P_{xx} = P_{yy}$ and $P_N = P_{zz}$. The right-hand side of the Eq. 1.7 is referred to the first moment of the stress profile or alternatively microscopic torque density $\mathcal{T}_{mic}$. Eq. 1.7 is frequently used to calculate the spontaneous curvature from MD trajectories [14, 19, 20].

1.2.2 Stretching energy

In the absence of any external constraints, the molecular area of lipid molecules attains an optimal value of A_0, which corresponds to the optimal packing of molecules. At optimal packing, the membrane is tensionless $\Sigma_{mec} = 0$; however, when the area of the membrane deviates from the optimal area A_0, then the membrane experiences a mechanical tension. This mechanical tension can be expressed as a linear function of

such area deviations [8, 21]:

$$\Sigma_{mec}(A) = K_A \frac{A - A_0}{A_0} \tag{1.8}$$

where K_A is the area compressibility modulus and is related to the bending energy by Eq. 1.5. The membrane area can deviate both ways, either to larger areas $A > A_0$, where membrane experiences stretching $\Sigma_{mec} > 0$ or to smaller area $A < A_0$ where membrane experiences compression $\Sigma_{mec} < 0$. The mechanical tension is the stretching (or compression) energy density. The stretching energy E_{st} is defined as the work associated with stretching (or compression) from the optimal packing area by[21]:

$$E_{st}(A) = \int_{A_0}^{A} dx\ \Sigma_{mec}(x) = (1/2) K_A \frac{(A - A_0)^2}{A_0} \tag{1.9}$$

The mechanical tension of the membrane can be obtained by integrating the stress profile, similar to the surface tension of liquids [22]:

$$\Sigma_{mec} = \int_{-\infty}^{+\infty} dz\ s(z) \tag{1.10}$$

where the stress profile is defined previously $s(z) = -[P_T - P_N]$ as the anisotropy of tangential P_T and normal P_N components of the pressure tensor. The stress profile is not an experimental observable, yet it is a theoretical notion that can be obtained from the trajectory of the MD simulations and can be related to mesoscopic elastic properties of the membranes (such as the mechanical tension). The most popular method to calculate the stress tensor includes the Goetz-Lipowsky force decomposition [23] and central force decomposition [24]. None of these force decompositions are unique, and they lead to different stress profiles. But, the results of each method are plausible as long as the fundamental physical laws (such as energy and momentum conservation) are not violated by these force decomposition procedures [24].

The combination of bending rigidity and spontaneous curvature leads to an intrinsic tension scale called spontaneous tension $\sigma \equiv 2\kappa m^2$ [16], which represents the bending energy density of a weakly curved membrane segment. The latter quantity is particularly interesting when the spontaneous curvature is relatively high, and the mean curvature cannot adapt itself to this spontaneous curvature. Then it is useful to decompose the total membrane tension $\hat{\Sigma}$ into two contributions:

$$\hat{\Sigma} = \Sigma_{mec} + \sigma = \Sigma_{mec} + 2\kappa m^2 \tag{1.11}$$

where Σ_{mec} represents the mechanical tension of the membrane. Generally, the mechanical tension depends on the external constraints; whereas, the spontaneous tension depends on the curvature-elastic material parameters of the membrane.

1.2.3 Area difference elasticity

In the spontaneous curvature model, as discussed in the bending energy subsection, it is implicitly assumed that area difference can automatically adapt itself by flip-flops of molecular components between the two leaflets of the bilayer. Thus the bending energy provides a local constraint and can be obtained by the area integral over a local energy density. If the membrane molecular components cannot undergo flip-flops between the two leaflets, then the number of molecules in each leaflet is constant. The latter leads to the optimal area difference ΔA_0 between the leaflets [8]. Thus, the area difference of the bilayer leaflets imposes an extra non-local constraint on the bending of the membrane. The energy E_{ADE} associated with such a non-local area difference elasticity is expressed [25, 8]:

$$E_{ADE} = \frac{\kappa_\Delta \pi}{2A\ell_{me}^2}(\Delta A - \Delta A_0)^2 \tag{1.12}$$

where κ_Δ is the non-local bending rigidity, ℓ_{me} is the membrane thickness, A is the total area of the membrane, and ΔA is the area difference of two leaflets under non-local elastic deformation. The area difference ΔA up to the first order in membrane thickness is given by [8]:

$$\Delta A \approx 2\ell_{me} \int dAM = 2\ell_{me} I_M \tag{1.13}$$

where M is the mean curvature of the membrane, and the integral runs over the membrane surface to give the integrated mean curvature I_M. Measurement of the non-local bending rigidity is hard; however, the fraction of local and non-local bending rigidities is theoretically estimated to be close to unity $\kappa_\Delta/\kappa = 3/\pi$ [26].

Unlike to local spontaneous curvature m due to asymmetric condition, the area difference elasticity introduces a non-local spontaneous curvature m_{nlo}. The sum of these contributions gives an effective spontaneous curvature [26]:

$$m_{eff} \equiv m + m_{nlo} \tag{1.14}$$

It can be shown that the non-local spontaneous curvature is given by [26]:

$$m_{nlo} \equiv \pi \frac{\kappa_\Delta}{\kappa} \frac{I_{M,0} - \mathcal{I}_M\{S^j\}}{A} \tag{1.15}$$

where $\{S^j\}$ denotes the stationary shape. It has been shown that stationary shapes of the area difference elasticity and the spontaneous curvature model are identical.

1.2.4 Total energy

The total energy of a bilayer membranes is the sum of all energetic contributions, namely bending, stretching and area difference elasticity energies along with volume energy:

$$E_{tot} = E_{be} + E_{st} + E_{ADE} + E_{vol} \tag{1.16}$$

The volume energy is the work associated to change of the enclosed volume of the vesicle. The latter change can occur as a response to imbalance of osmotically active and impermeable molecules in the exterior and interior aqueous solutions [27]. The associated volume energy can be expressed in terms of a small deviation from the optimal volume V_0 of the vesicle [27]:

$$E_{vol} \approx \frac{1}{2} k_B T \rho_{ext} \frac{(V - V_0)^2}{V_0} \tag{1.17}$$

where ρ_{ext} is the density of osmotically active molecules in the bulk solution outside the vesicle. In general, we deal with six material parameters namely: the bending rigidity κ, the Gaussian bending rigidity κ_G, the non-local bending rigidity κ_Δ, the local spontaneous curvature m, the area compressibility modulus K_A, and the membrane thickness ℓ_{me}.

Many of the energetic contributions in Eq. 1.16 can be ignored or simplified in most of the instances. The energy scale of bending and stretching energies are set by κ and $K_A A_0$, respectively. The area compressibility modulus for most of the amphiphilic membranes is in the order of $K_A \sim 0.2\ J/m^2$ and the bending energy in the order of $\kappa \sim 10^{-19}\ J$. Thus, the fraction of two quantity leads to the length scale of $\sqrt{\kappa/K_A} \sim 0.7\ nm$. The latter length scale suggests that the stretching energy is much larger than the bending energy as long as $\sqrt{A_0} \gg 0.7\ nm$, which is the case for vesicles ranging from SUV to GUV. Due to the separation of energy scales between bending and stretching energy, one can ignore the effect of stretching energy by conserving the area around the optimal area of the membrane $A = A_0$. A similar line of argument goes for the work of volume. As long as the density of osmotically active molecule is much larger than $\kappa/k_B T V_0 \ll \rho_{ext}$, this term can be ignored by conserving the volume of vesicle at the optimal volume $V = V_0$. As a consequence of such simplifications, for a membrane where lipid molecules can undergo flip-flops, we are left with the bending energy.

1.2.5 Multiscale modeling of membranes

In principle, the modeling of a biomembrane is performed in a multiscale manner. Depending on the time and length scale of the phenomena of interest, different methods can be used. The multiscale modeling of the membrane can be broadly classified into three main categories: i) numerical minimization of membrane bending energy, ii) fi-

nite element modeling of triangulated membranes based on a discretized version of the bending energy and iii) molecular simulations of the membranes with different levels of resolution of the lipid molecules. All three approaches have been widely used to address a different aspect of membrane biophysics. The choice of the method depends on the type of problem and the relevant time and length scales. Examples include membrane remodeling, the interaction of nanoparticles and proteins with the membrane and membrane fission and fusion, and many other interesting problems. In the following, we briefly discuss all three procedures and provide some examples of the application of each method.

Numerical minimization of membrane energy

At the continuum level, the membrane energy can be described by bending energy, as discussed in the previous subsection. For a flat membrane patch, the bending energy in the minimum state is trivial, because the mean curvature is zero $M = 0$, and therefore the bending energy should also vanish $E_{be} = 0$ for vanishing spontaneous curvature. The bending energy of a vesicle is less trivial. The energy of a vesicle with shapes $\mathcal{S}$ and preserved area and volume can be represented in the form of an energy functional [28]

$$\mathcal{E}_{ves}\{\mathcal{S}\} = \mathcal{E}_{be}\{\mathcal{S}\} - \Delta P \mathcal{V}_{ves}\{\mathcal{S}\} \ + \Sigma \mathcal{A}_{ves}\{\mathcal{S}\} \tag{1.18}$$

where ΔP and Σ are two Lagrange multipliers introduced to conserve the vesicle volume V_{ves} and vesicle area A_{ves}, respectively. The curly brackets refer to being a functional of membrane shape $\mathcal{S}$. The energy minimization of the functional $\mathcal{E}_{ves}\{\mathcal{S}\}$ leads to the Euler-Lagrange equation [28]

$$\Delta P - 2\Sigma M + 2\kappa \nabla_{LB}^2 M + 4\kappa(M - m)\Big[M(M + m) - K\Big] = 0 \tag{1.19}$$

where ∇_{LB} denotes the Laplace-Beltrami operator. The Euler-Lagrange equation 1.19 (also called shape equation) is a fourth-order non-linear partial differential equation (PDE), and a general analytical solution does not exist. A more practical way is to assume that the minimum shape will be axially symmetric and thus parametrize the shape in axisymmetric geometry and exploit variational calculus for functional energy minimization of Eq. 1.18. The latter leads to a set of second-order non-linear ordinary differential equations (ODE) which can be solved numerically [7]. A set of shape equation for axially symmetric vesicle shape which is parametrized based on arc

length is given by [7]:

$$\begin{aligned}
\ddot{\psi} &= \frac{cos\psi sin\psi}{r^2} - \frac{\dot{\psi}}{r}cos\psi + \frac{\Delta P}{2\kappa}rcos\psi + \frac{\Upsilon}{\kappa r}sin\psi \\
\dot{\Upsilon} &= \frac{k}{2}\dot{\psi}^2 - \frac{ksin^2\psi}{2r^2} + \Sigma + \Delta Prsin\psi \\
\dot{r} &= cos\psi
\end{aligned} \tag{1.20}$$

where the parametrization is done in cylindrical coordinates $(z(t), r(t))$ based on three parameters: distance from symmetry axis $r(t)$, local tilt angle $\psi(t)$ and the arc length $s(t)$, where t is the general contour parameter, see Figure 8.1 in *Appendix* 2 as an example. The overdots denote the derivative with respect to the arc length s. For more details, see Ref. [7]. Various methods such as shooting algorithm [7] or Runge-Kutta method [29] can be used for numerical solution of Eqs. 1.20.

A morphology diagram of vesicles. The numerical solution of shape equations Eqs. 1.20 provides the stationary shapes of the vesicles under defined constraints. The bending energy κ sets the characteristic energy scale, and the vesicle area can be used to define the characteristic length scale $R_{ves} = \sqrt{A_{ves}/4\pi}$. Two control parameters are typically used to study the morphology diagram, namely the reduced spontaneous curvature $\bar{m} = mR_{ves}$ and the reduced volume of the vesicle $v = V/(4/3)\pi R_{ves}^3$. Morphological transformation of a vesicle can occur both by osmotic deflation of the vesicle, *i.e.,* by reducing the volume of the enclosed aqueous solution $v < 1$, or by introducing a spontaneous curvature. During a morphological transformation, the spherical vesicles transform into different classes of shapes, including prolates, oblates, stomatocytes, and pears, see Figure 1.4a,c. The reduced bending energy $E_{be}/8\pi\kappa$ of the vesicle as a function of the reduced volume v is shown in Figure 1.4b. Three different branches of prolates, oblates, and stomatocytes exist for zero spontaneous curvature $m = 0$. The morphology diagram of the vesicle with spontaneous curvature as a function of the reduced volume v is depicted in Figure 1.4d. For a given reduced spontaneous curvature $\bar{m}$ and reduced volume v, the morphology diagram shows the stationary shape with the lowest bending energy. The morphology diagram of vesicles demonstrates that, unlike free droplets and bubbles, which always attain a spherical geometry in equilibrium, vesicles have a very rich morphology diagram in equilibrium.

The same procedure has been used to study many interesting problems such as domain induced budding [30, 31], nanoparticle engulfment by vesicles [32], and droplet induced budding of membranes [33, 29].

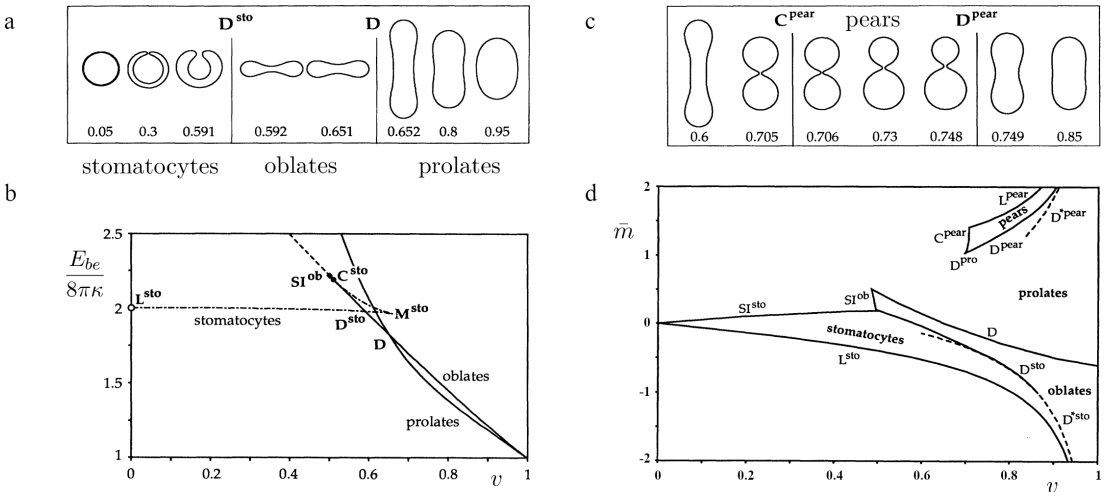

Figure 1.4. a) The vesicle shapes at zero spontaneous curvature $\bar{m} = 0$ for different reduced volume v, b) the reduced bending energy $E_{be}/8\pi\kappa$ of vesicle as a function of the reduced volume v, c) the vesicle shapes at spontaneous curvature $\bar{m} = 1.2$ for different reduced volume v and d) the morphology diagram of spontaneous curvature model. The figure is adapted from Ref. [7]

Finite element modelling

There are a couple of shortcomings associated with numerical minimization. First of all, the method is only applicable for axially symmetric shapes; moreover, it only considers the minimum energy state at zero temperature. Indeed, the latter deficiencies of the method would restrict us from exploring more interesting problems such as spontaneous symmetry breaking and thermally induced patter formation. To overcome these problems, finite element modeling based on membrane triangulation offers a very versatile tool.

In finite element modeling, the membrane energy is described via a discretized form of the continuum energy on a triangulated mesh. The bending energy is assigned to the mesh vertices or facets along with volume and area constraints. Then, the total energy of the system is minimized by numerical methods such as gradient descent or the conjugate gradient method. The finite element modeling leads to essentially the same solutions as obtained from solving the shape equation unless the symmetry constraint is lifted during the minimization. Furthermore, finite element modeling makes it possible to incorporate the thermal fluctuations and also mimic the fluidity of the membrane. To do so, the links of the triangulated mesh can undergo a flip-flop using a Boltzmann energy distribution criteria such as the one used in the Metropolis algorithm [34, 35].

This finite element method has been extensively used in membrane remodeling studies, for example to model nanoparticle-membrane interactions [35], membrane multi-

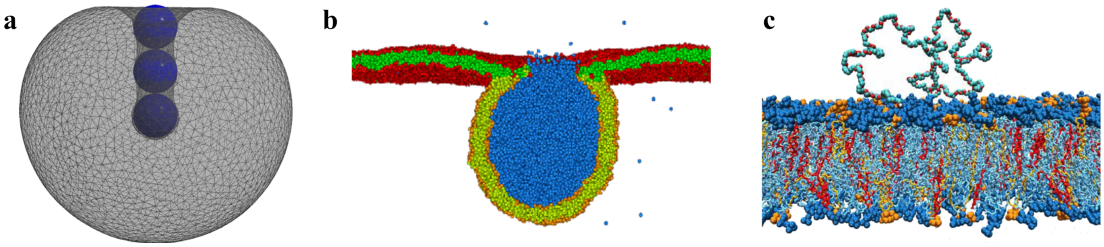

Figure 1.5. Examples of multiscale modeling of membranes, a) interaction of nanoparticles with vesicle using triangulated mesh, b) coarse-grained DPD simulation snapshot of the vesicle-membrane fusion process and c) lipid membrane interacting with poly(ethylene glycol) (PEG) molecule in atomistic resolution. The panel a of the figure is adapted from Ref. [35], b from Ref. [40] and c from Ref. [41]

domain polymorphism [36, 37] and membrane remodeling with adhesive objects [38]. An open-source package called "surface evolver" is a well-established software for such studies that provides various implementations of the bending energy calculation. The relevant length and time scales in finite element modeling are similar to those in numerical minimization of the membrane energy. Figure 1.5a shows an example of fluid membrane interactions with nanoparticles described by triangulated mesh [35].

Molecular simulations

Both methods described above are only applicable to mesoscale and exclude all molecular details. However, at smaller size, the molecular structure matters. To include molecular details, the model requires a particle-based description of the system. The molecular details can be incorporated into the model at different resolutions using the force fields [39]. The force fields describe sub-molecular interactions using a set of potential forms and interaction parameters. High resolution models describe all-atoms (AA) interactions in the force field [39]. The AA force fields are very versatile models that include atomic details of the molecules but ignore electronic structure. The typical length and time scales that can be described by AA force fields are in the range of a few tens of nanometers and hundreds of nanoseconds. To reach lover resolutions, one can sweep out the atomic details of AA models by treating the group of atoms as a single coarse-grained (CG) beads. The CG force fields allow the phenomenological study of much larger systems of the order of μm and in μs time scales. In principle, it is also possible to model the system in multiscale resolution by treating specific sites of the membrane in AA resolution and the rest in CG resolutions; however, this poses the challenge of how to treat interactions between the two scales [42].

Molecular models are often simulated using molecular dynamics (MD). This simulation method solves newton's equations of the motions numerically to obtain a molecular

trajectory. Initially, molecules are located in a simulation box with periodic boundary conditions, and each atom is assigned a velocity picked from a Boltzmann distribution. Then, from the force field, one calculates the force acting on each atom and then using methods likes velocity-Verlet integrator, the new position, and velocity is obtained. Repeating the latter procedure for a specified number of steps leads to a dynamical trajectory. The molecular dynamics simulations exploit thermostat and barostat to remain in the canonical (NVT) and isothermal-isobaric (NPT) ensembles, respectively [39]. A special example of a thermostat based on the fluctuation-dissipation theorem (FDT) is part of the method called dissipative particle dynamics (DPD). The DPD method was developed to preserve hydrodynamic behavior and has been extensively applied to model membrane systems at the mesoscale [43, 44, 45]. Two examples of molecular simulations of lipid bilayers are shown in Figure 1.5. A snapshot of DPD simulations of fusion of the vesicle with flat membrane [40] is shown in Figure 1.5b, and a conformation of the MD simulation of poly(ethylene glycol) (PEG) adsorption on a lipid membrane in atomistic resolutions [41] is illustrated in Figure 1.5c. There are many other methods that have been used in the last decades for membrane simulations, and an interested reader is recommended to look at the review in the Ref. [34].

1.3 Membrane Wetting Phenomena

Wetting typically refers to the interaction of liquid droplets with solid substrates, where the droplet maintains a contact angle with the surface. The force balance of macroscopic droplet on an ideal flat surface, *i.e*, smooth and chemically homogeneous surface, can be described by Young's equation [22]:

$$\cos\theta_Y = \frac{\Sigma_{sv} - \Sigma_{sl}}{\Sigma_{lv}} \tag{1.21}$$

which relates droplet contact angle θ_Y to three surface tensions Σ_{sv}, Σ_{sl} and Σ_{lv}, where solid, liquid and vapor phases are denoted by s, l and v. Young's equation 1.21 is valid for rigid substrates. However, for non-rigid surfaces, the elasticity of flexible substrates like lipid membrane can be coupled to the capillary forces arising from liquid interfaces, which is referred to membrane wetting.

Phase separation of aqueous solutions of PEG and dextran enclosed within GUVs provides the first example of membrane wetting [46]. The phase separation of PEG-dextran solutions inside vesicles can be induced by temperature change or osmotic deflation, which both lead to the change in weight fraction of polymeric solutions. After phase separation, two phases, a PEG-rich phase α and a dextran-rich phase β, are formed inside vesicles, which are separated from the exterior γ phase by the vesicle membrane. In principle, for a system of a vesicle enclosing phase-separated α and β phases, there

exist three different wetting morphologies: (i) complete wetting (CW) of the vesicle by the phase α, (ii) CW of the vesicle by the phase β and (iii) partial wetting (PW) of the vesicle by both aqueous phases. The phase diagram of PEG-dextran solutions and the corresponding membrane wetting morphologies [41] are illustrated in Figure 1.6. The two-phase co-existence region in the phase diagram is shown in pink and turquoise, see Figure 1.6. The latter colors refer to two subregions of CW of the membrane with α phase (pink) and PW of the membrane with both phases (turquois). The red dashed line illustrates the tie line where the system undergoes a wetting transition from a CW to a PW state. Due to the limitation of the experimental resolution, it is still unknown whether the wetting transition is continuous or discontinuous [41]. The solid red line is a segment of the binodal line which system undergoes from one phase region (white) to the CW region (pink). Similarly, the blue line is binodal, which separates one phase region (white) from the PW region (turquoise) of the phase diagram. The dotted red line indicates the capillary condensation of PEG-rich phase α on the membrane when approaching to CW segment of binodal (red line) from the one-phase region (white). The wetting layer transforms to a mesocopically thick layer as one reaches to the binodal line of the CW segment. No such wetting layer has observed once approaching to PW segment of the binodal line from one phase region. The critical demixing point is shown by the orange dot. The precise location of the tie-line separating CW from PW is influenced by the composition of the lipid mixture.

1.3.1 Apparent contact angles

For the partial wetting regime, both aqueous α and β phases are in contact with the membrane, see Figure 1.7a, and partition the vesicle into an $\alpha\gamma$ segment (blue) and a $\beta\gamma$ segment (red). The $\alpha\beta$ interface between two aqueous phases is shown with broken orange, see Figure 1.7a. The membrane wetting is typically studied using optical microscopy. In the resolution of optical microscopy, the two membrane segments and the $\alpha\beta$ liquid interface form three spherical caps. These spherical caps intersect along the three-phase contact line $\alpha\beta\gamma$ with sharp angles called apparent contact angles θ_α,θ_β and θ_γ with $\theta_\alpha + \theta_\beta + \theta_\gamma = 2\pi$, see Figure 1.7a. By combining the shape equations of the two membrane segments and the Laplace equation for the interface $\alpha\beta$, one obtains a relationship between the geometry, curvature, and the tension [47, 5]

$$M_{\alpha\gamma}\left(\frac{\Sigma^{eff}_{\alpha\gamma}}{\Sigma_{\alpha\beta}} - \frac{\sin\theta_\beta}{\sin\theta_\gamma}\right) = M_{\beta\gamma}\left(\frac{\Sigma^{eff}_{\beta\gamma}}{\Sigma_{\alpha\beta}} - \frac{\sin\theta_\alpha}{\sin\theta_\gamma}\right) \tag{1.22}$$

where $M_{i\gamma}$ and $\Sigma^{eff}_{i\gamma}$ are curvature of the spherical cap and the effective tension of the membrane $i\gamma$ segment with $i = \alpha$ or β. The interfacial tension is denoted by $\Sigma_{\alpha\beta}$. The

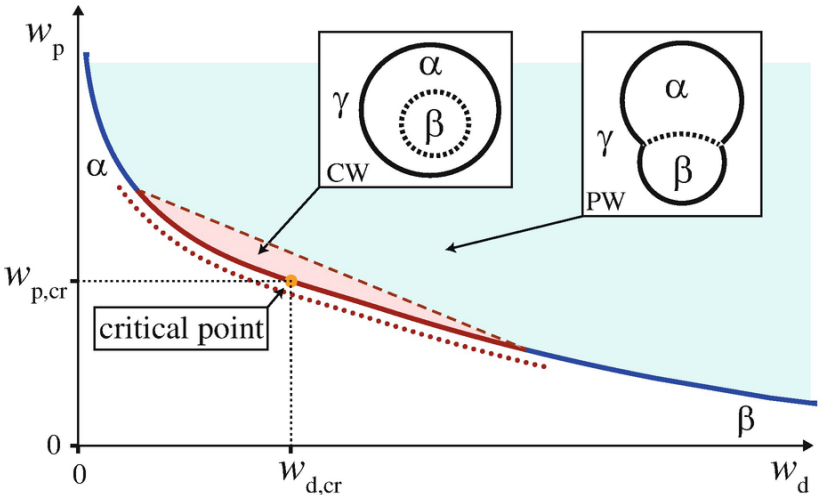

Figure 1.6. The phase diagram of aqueous PEG-dextran solutions and corresponding wetting morphology as a function of weight fraction of PEG w_p and dextran w_d. The phase diagram consists of three subregions, one phase region (white), the two-phase region where the membrane is completely wetted (CW) by PEG-rich α phase (pink), and two-phase region where the membrane is partially wetted (PW) by both aqueous phases. The CW and PW segment of the binodal line are indicated by solid red and blue lines, respectively. The dashed red line indicates the wetting transition from CW to PW subregions. The dotted red line is where a wetting layer of phase α starts to form on the membrane when we approach the CW segment of binodal from the one-phase region. The critical demixing point is located as $(w_{d,cr}, w_{p,cr}) = (0.0451, 0.0361)$ and indicated by orange dot. The figure is adapted from Ref. [5]

effective segment tension can be decomposed into two contributions [47]:

$$\Sigma_{i\gamma}^{eff} = \hat{\Sigma}_{i\gamma} - 2\kappa_{i\gamma} m_{i\gamma} M_{i\gamma} \tag{1.23}$$

where the first term is the membrane segment tension $\hat{\Sigma}_{i\gamma}$ and the second term is a curvature dependent term $2\kappa_{i\gamma} m_{i\gamma} M_{i\gamma}$. The membrane segment tension (as defined previously in Eq. 1.11) can be decomposed into two more contributions [47]:

$$\hat{\Sigma}_{i\gamma} = \Sigma_{i\gamma} + \sigma_{i\gamma} \tag{1.24}$$

where the first term is the mechanical segment tensions $\Sigma_{i\gamma}$ (defined in the same way as Σ_{mec} in the Eq. 1.8) and the second term is the spontaneous tension $\sigma_{i\gamma} \equiv 2\kappa_{i\gamma} m_{i\gamma}^2$. The mechanical segment tension can be furthur decomposed into $\Sigma_{i\gamma} = \Sigma + W_{i\gamma}$, with Σ being lateral membrane stress (Lagrange multiplier conjugate to the total membrane area) and $W_{i\gamma}$ is the adhesion free energy densities (or alternatively called adhesive strength) of the membrane segments. The lateral membrane stress Σ depends on the

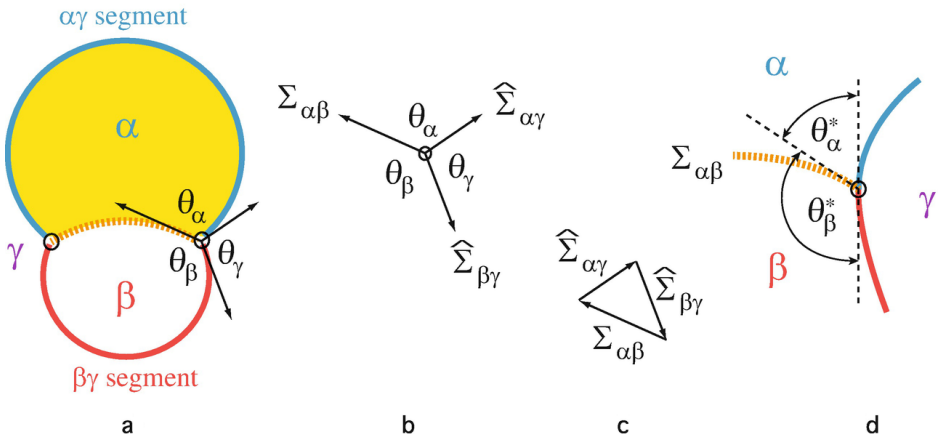

Figure 1.7. Schematic of vesicle which enclose two aqueous phases α and β in PW regime. The membrane segment are coloured red and blue for $\beta\gamma$ and $\alpha\gamma$ segments, the $\alpha\beta$ interface is shown with broken orange line. b) the force balance of total membrane tensions $\hat{\Sigma_{\alpha\gamma}}$ and $\hat{\Sigma_{\beta\gamma}}$ with interfacial tension $\Sigma_{\alpha\beta}$, for certain parameter space. c) Force balance shown in Neumann triangle representation. d) The smoothly curved membrane along the three phase contact line, two intrinsic contact angles θ^*_α and θ^*_β are defined from the angles between common tangent line of membrane segments and tangent to $\alpha\beta$ interface. The figure is adapted from Ref. [5]

vesicle size and shape, thus Σ can be different for vesicles even with the same lipid composition. However, the adhesive strength of the membrane segments $W_{i\gamma}$ is a material parameter which is determined by the molecular interaction of the lipids with the aqueous phase in the hydrophilic interfaces of the bilayer. Consequently, the difference of the mechanical segment tensions of the two membrane segments can be written as the difference of adhesive strength [47]:

$$\Sigma_{\beta\gamma} - \Sigma_{\alpha\gamma} = W_{\beta\gamma} - W_{\alpha\gamma} = W_{\beta\alpha} \tag{1.25}$$

which is independent of the shape and size of the vesicles.

In order to describe the force balance along the apparent contact line, we consider two regimes of parameters: small and large spontaneous curvatures of membrane segments [47]. If the spontaneous curvature is small or comparable to the mean curvature of the membrane segment $m_{i\gamma} \leq M_{i\gamma}$ and the interfacial area is large compared to $(18\pi\kappa_{i\gamma}/\Sigma_{\alpha\beta}) \ll A_{\alpha\beta}$, then $i\gamma$ belong to small spontaneous curvature regime. On the other hand, if the spontaneous curvature is large enough in comparison to the mean curvature of membrane segment $M_{i\gamma} \ll m_{i\gamma}$, then $i\gamma$ belong to large spontaneous curvature regime. It can be shown that, if the membrane segments belong to one of these

parameter spaces then the force balance conditions read [47]:

$$\frac{\Sigma_{\alpha\beta}}{\sin\theta_\gamma} = \frac{\hat{\Sigma}_{\alpha\gamma}}{\sin\theta_\beta} = \frac{\hat{\Sigma}_{\beta\gamma}}{\sin\theta_\alpha} \tag{1.26}$$

this force balance relates the membrane segment tension to the apparent contact angles and can be alternatively expressed in the form of tension ratios:

$$\frac{\hat{\Sigma}_{\alpha\gamma}}{\Sigma_{\alpha\beta}} = \frac{\sin\theta_\beta}{\sin\theta_\gamma} \quad \text{and} \quad \frac{\hat{\Sigma}_{\beta\gamma}}{\Sigma_{\alpha\beta}} = \frac{\sin\theta_\alpha}{\sin\theta_\gamma} \tag{1.27}$$

these equations describes the force balance condition along the apparent contact line and can be visually expressed in the form of Neumann's triangle, see Figure 1.7c.

For the PW regime of membrane wetting with PEG-dextran solutions, it has been observed that the membrane form nanotubes which are protruding toward the PEG-rich phase α. This implies a negative and large spontaneous curvature in the $\alpha\gamma$ segment of the membrane, where the mechanical segment tension is much smaller than the spontaneous segment tension $\Sigma_{\alpha\gamma} \ll \sigma_{\alpha\gamma}$, thus the $\hat{\Sigma}_{\alpha\gamma} \approx \sigma_{\alpha\gamma} = 2\kappa_{\alpha\gamma} m_{\alpha\gamma}^2$. The asymptotic behaviour of the first equation in Eq. 1.27 for large spontaneous curvature regime leads to:

$$m_{\alpha\gamma} = -\left(\frac{\Sigma_{\alpha\beta}}{2\kappa_{\alpha\gamma}} \frac{\sin\theta_\beta}{\sin\theta_\gamma}\right)^{1/2} \tag{1.28}$$

the negative sign accounts for the experimental observation of internal nanotube formation which reflects the negative spontaneous curvature. The relationship in Eq. 1.28 is very handy when it comes to interpreting experimental measurements, since the apparent contact angles θ_β and θ_γ can be measured using optical microscopy and the other two material parameters, being $\Sigma_{\alpha\beta}$ and $\kappa_{\alpha\gamma}$ can be measured separately. It has been shown that the value obtained for spontaneous curvature with Eq. 1.28 is in agreement with two independent methods of measurements [41].

The spherical cap approximation leading to the above force-balance conditions Eq. 1.27, is only valid at the micro-meter scale where the interfacial energy $\Sigma_{\alpha\beta} A_{\alpha\beta}$ is much larger than the bending rigidity κ. This implies a characteristic length scale $R^* \equiv \sqrt{\kappa/\Sigma_{\alpha\beta}} \ll \sqrt{A_{\alpha\beta}/\pi} \equiv R_{\alpha\beta}$. As discussed before, the bending rigidity is of the order of $\kappa \sim 10^{-19}$ and the interfacial tension of macromolecular condensate is of the order of $\Sigma_{\alpha\beta} \sim 10\ \mu N/m$. The latter orders implies the characteristic length scale $R^* \sim 100\ nm$ which spherical cap approximation is valid.

1.3.2 Intrinsic contact angle

At sub-nanometer length scales, $R^* \leq 100\ nm$, unlike optical microscopy observation suggests, the membrane should be smoothly curved, as it is visualized in Figure 1.7d, rather than persisting the kink along the three-phase contact line. Otherwise, the bending energy of the membrane with kink would be infinite. By taking the common tangent plane of two membrane segments along the contact line, one can define two new geometric measures called intrinsic contact angles θ^*_α and θ^*_β with $\theta^*_\alpha + \theta^*_\beta = \pi$.

The energy minimization of droplet-membrane system with an axisymmetric morphology, with three main energetic contributions of bending energy, interfacial energy and three phase contact line energy, leads to a tangential force balance condition along the three phase contact line [47]:

$$\Sigma_{\beta\gamma} - \Sigma_{\alpha\gamma} = \Sigma_{\alpha\beta} \cos\theta^*_\alpha + \lambda_{\alpha\beta\gamma} \frac{\cos\psi_{\rm co}}{R_{\rm co}} + \Delta_{\Sigma,\rm co} \tag{1.29}$$

where the mechanical segment tension are denoted by $\Sigma_{\beta\gamma}$ and $\Sigma_{\alpha\gamma}$, the interfacial tension by $\Sigma_{\alpha\beta}$ and the line tension by $\lambda_{\alpha\beta\gamma}$, as will be discussed in the following. The angle ψ_{co} is the tilt angle between the common tangent plane of the membrane segments at contact line and the symmetry axis. The radius of the contact line is denoted by R_{co}, see Figure 8.1. The last term $\Delta_{\Sigma,\rm co}$ is a curvature dependent contribution and arises due to a possible discrepancy of the curvature-elastic properties of the two membrane segments. The explicit form of this term is given by:

$$\Delta_{\Sigma,\rm co} = \frac{1}{2}\Big(\kappa_{\beta\gamma} Q_{\beta\gamma}(s_1+\epsilon) - \kappa_{\alpha\gamma} Q_{\alpha\gamma}(s_1+\epsilon)\Big) \tag{1.30}$$

where the curvature dependent terms are $Q_{i\gamma} = C_1^2(s) - [C_2(s) - 2m_{i\gamma}]^2$ with $i = \alpha$ and β. If the membrane segments have the same curvature-elastic properties (i.e., $\kappa_{\beta\gamma} = \kappa_{\alpha\gamma}$ and $m_{\beta\gamma} = m_{\alpha\gamma}$) then the term $\Delta_{\Sigma,\rm co}$ will vanish from the force balance Eq. 1.29. In the latter case and from Eqs. 1.25 and 1.29, the force balance takes a simplified form:

$$\Sigma_{\beta\gamma} - \Sigma_{\alpha\gamma} = W_{\beta\gamma} - W_{\alpha\gamma} = \Sigma_{\alpha\beta} \cos\theta^*_\alpha + \lambda_{\alpha\beta\gamma} \frac{\cos\psi_{\rm co}}{R_{\rm co}} \tag{1.31}$$

where the force balance depends on the adhesive strength of membrane segments $W_{\beta\gamma}$ and $W_{\alpha\gamma}$, the interfacial tension $\Sigma_{\alpha\beta}$ between the aqueous phases and the three phase contact line tension $\lambda_{\alpha\beta\gamma}$. For detailed derivation of Eq. 1.31 see *Appendix* 2. By combining the force balance Eq. 1.31 with the tension ratio equations 1.27 one obtains

[47, 5]

$$\cos\theta_{\alpha}^{*} = \frac{\sin\theta_{\alpha} - \sin\theta_{\beta}}{\sin\theta_{\gamma}} - \frac{\lambda_{\alpha\beta\gamma}}{\Sigma_{\alpha\beta}}\frac{\cos\psi_{\mathrm{co}}}{R_{\mathrm{co}}} \tag{1.32}$$

which connects the intrinsic contact angle θ_{α}^{*}, which is not accessible to optical microscopy, to the apparent contact angles obtained from optical microscopy observation. However, it should be noted that the latter equality in Eq. 1.32, is only valid if the membrane segments belong to small spontaneous curvature or very large spontaneous curvature regimes.

The last term in Eqs. 1.31 and 1.32 is the effect of line tension in the force balance. This contribution can be safely ignored for GUVs as the radius of contact line R_{co} is of the order of micrometers, where the interfacial energy is the dominant energetic contribution. However, the effect of line tension can not be neglected at the nanometer scale. In the following part, we will discuss the notion as well as the effect of line tension.

1.3.3 The effect of line tension

The concept of line tension was first introduced by Gibbs in analogy to surface tension [48]. By definition, the surface tension $\Sigma_{\alpha\beta}$ is the excess free energy per unit area of an interface between α and β phases. Similarly, the line tension $\lambda_{\alpha\beta\gamma}$ is defined as the excess free energy per unit length of the contact line of three co-existing α, β and γ phases. The linear excess $\Omega^{\alpha\beta\gamma}$ to the grand canonical free energy Ω of three co-existing α, β and γ can be written as [22]

$$\Omega^{\alpha\beta\gamma} = \lambda_{\alpha\beta\gamma}L_{\alpha\beta\gamma} = \Omega + PV - (\Omega^{\alpha\beta} + \Omega^{\alpha\gamma} + \Omega^{\beta\gamma}) \tag{1.33}$$

where $V = V^{\alpha} + V^{\beta} + V^{\gamma}$ is the total volume and $\Omega^{\alpha\beta} = \Sigma_{\alpha\beta}A_{\alpha\beta}$ is the surface excess of $\alpha\beta$ interface to the grand canonical free energy Ω, and similarly for the $\beta\gamma$ and $\alpha\gamma$ interfaces. Using the mechanical definition, one can find the interfacial tension from the work expended to increase the area of planar $\alpha\beta$ interface [22]

$$\Sigma_{\alpha\beta} = \int_{-\infty}^{\infty}[P_N(z) - P_T(z)]dz \tag{1.34}$$

where P_N and P_T are normal and tangential components of the stress tensor, here the z direction is chosen to be the normal to the interface. A similar mechanical definition for increase of the contact line of cylindrical droplet leads to the definition of the line tension [49, 50]

$$\lambda_{\alpha\beta\gamma} = \lim_{r\to\infty}\int\int_{B(r)}[P_N - P_T - P_B]dxdy \tag{1.35}$$

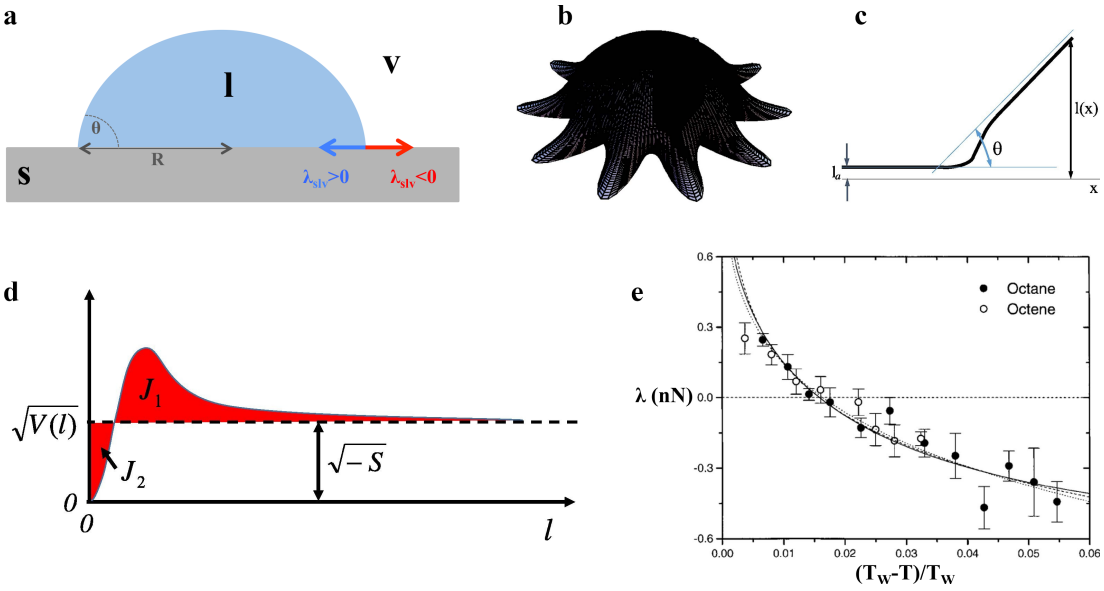

Figure 1.8. a) Schematic of liquid droplet partially wetting a solid substrate with radius R and contact angle θ. b) A spherical cap liquid with perturbed contact line. c) A close vicinity of three phase contact line with liquid wedge. d) The interface potential as a function of liquid thickness, the J_1 and J_2 refers to the same areas that appeared in Eq. 1.40. e) The line tension of n-octane and 1-octene on silicon wafer coated with hexadecyltrichlorosilane near first-order phase transition. The panel b is adapted from Ref. [51] and panels c-e are adapted from Ref. [52]

where $B(r)$ is circular region with radius of r, P_B is the bulk pressure far away from the three phase co-existing zone, here the three phase contact line is chosen to be along z-axis. The Eq. 1.34 and 1.35 indicate that interfacial tensions and line tensions arise due to anisotropy of stress tensor near the interface or three phase contact line zone.

In order to elaborate on the effect of line tension we will consider the example of a sessile droplet on a solid substrate, see Figure 1.8a. By minimizing the free energy with respect to the contact angle θ at the constant droplet volume, one gets the modified Young's equation:

$$\cos\theta = \frac{\Sigma_{sv} - \Sigma_{sl}}{\Sigma_{lv}} - \frac{\lambda_{slv}}{\Sigma_{lv} R} = \cos\theta_Y - \frac{\lambda_{slv}}{\Sigma_{lv} R} \tag{1.36}$$

where s, l and v denoted the three solid, liquid and vapour phases, respectively. The radius of the contact line is R and θ_Y denotes the macroscopic Young's contact angle. The last term in Eq. 1.36 accounts for the effect of line tension as a deviation from macroscopic contact angle $\theta \neq \theta_Y$ of spherical cap-shaped droplet. For a cylindrical droplet, however, the contact angle will be unaffected from line tension $\theta = \theta_Y$ since the contact line curvature is zero $1/R = 0$.

The mechanical stability of deformable interfaces requires a positive interfacial tension. However, there is no such restriction for the sign of the line tension, as first suggested by Gibbs [53, 22]. In general, if the line tension is positive, it is expected that the contact line decreases the length to reduce the free energy of the system. However, for negative values of the line tension, the contact line tends to elongate the three-phase contact line, see blue and red arrows in Figure 1.8a. The contact line can also be perturbed in different ways, as well. An example of a perturbed contact line with periodic structure is shown in Figure 1.8b [51]. For positive line tension $\lambda_{\alpha\beta\gamma} > 0$, it has been shown that droplets are stable for a large class of perturbations. However, for the contact line with negative tension, $\lambda_{\alpha\beta\gamma} < 0$ a restricted class of perturbations is proven to govern the stability under thermodynamic equilibrium [51].

The total energy of a droplet on a solid surface is mainly affected by the surface tension and line tension. Thus the ratio of these two quantities defines a characteristic length scale

$$\xi = \Big|\frac{\lambda_{slv}}{\Sigma_{lv}}\Big| \tag{1.37}$$

known as line tension length. Below line tension length, the effect of line tension is dominant, and above, the surface tension plays a prominent role. The estimated values of the line tension from mean-field theory span two orders of magnitude $|\lambda_{theory}| \sim 10^{-12} - 10^{-10}\ N$. The surface tension of most of the organic liquids is on the order of $\Sigma \sim 20\ mN/m$, which would lead to a maximum line tension length $\xi_{theory} \sim 5\ nm$. The latter arguments suggest that the effect of line tension is only relevant at the nanometer scale and can be safely ignored in macroscopic interfacial phenomena [54]. However, near the wetting transition, the line tension length is not a valid measure to assess the effect of line tension. An alternative length scale, called the spreading pressure line tension length ξ_S, is a more relevant measure near wetting transitions, where the solid-vapor surface energy Σ_{sv} is comparable to solid-liquid Σ_{sl} and liquid-vapor Σ_{lv} energies. The spreading pressure line tension length is given by [54]

$$\xi_S = \Big|\frac{\lambda_{slv}}{S}\Big| = \Big|\frac{\lambda_{slv}}{\Sigma_{sv} - (\Sigma_{sl} + \Sigma_{lv})}\Big| = \Big|\frac{\lambda_{slv}}{\Sigma_{lv}(\cos\theta_Y - 1)}\Big| \tag{1.38}$$

where $S = \Sigma_{sv} - (\Sigma_{sl} + \Sigma_{lv})$ is the spreading coefficient. Near the wetting transition the contact angle is very small which leads to the increase of the spreading pressure line tension length. For instance, the contact angle of $\theta_Y = 1\ ^\circ$ leads to $\xi_S \sim 50\ \mu m$, which suggest a very dominant role of the line tension near a wetting transition, even for macroscopically large liquid droplets.

In order to calculate the line tension and its behaviour near wetting transition, Indekeu employed the interface displacement model [55]. In this model line tension is

expressed as a functional of interfacial thickness $l(x)$

$$\lambda_{slv}[l(x)] = \int_{-\infty}^{\infty} dx \left[\frac{1}{2} \Sigma_{lv} \Big(\frac{dl}{dx} \Big)^2 + V(l(x)) \right] + const \tag{1.39}$$

where the first term accounts for the energetic contribution of the surface tension and the second term includes the interfacial potential close to the surface. The interfacial potential takes the microscopic surface structure into account in the close vicinity of three phase contact zone. To do so, the adsorbtion of liquid film of thickness l_a on solid surface and an existence of liquid wedge at three phase contact line are assumed, see Figure 1.8c. The interfacial potential includes van der Waals $V_{vdW}(l)$, screened Coulombic $V_C(l)$ and off-coexistence $V_{cx}(l)$ potentials in the model which are dominant energetic terms close to liquid wedge where three phases meet. The functional minimization of Eq. 1.39 with respect to interfacial thickness $l(x)$ gives line tension for partially wetting regime of liquid droplet

$$\lambda_{slv} = \sqrt{2} \Sigma_{lv} \xi \int_0^{\infty} dL \left[\sqrt{\frac{V(L)}{\Sigma_{lv}}} - \sqrt{\frac{-S}{\Sigma_{lv}}} \right] = \sqrt{2\Sigma_{lv}} \xi [J_1 - J_2] \tag{1.40}$$

where ξ is the charactristic length scale along the surface and L is dimensionless film thickness. Two areas J_1 and J_2 are shown in Figure 1.8d which provide a simple interpretation for line tension sign near wetting transition. For relatively large spreading coefficient S one gets $J_1 \ll J_2$ which leads to negative line tension $\lambda_{slv} < 0$. However, for a critical values of the spreading coefficient S^* where $J_1 = J_2$ one obtains a zero line tension $\lambda_{slv} = 0$, and finally for relatively small spreading coefficient $S < S^*$ or at the first order wetting transition temperature T_w, one expects the change of sign for the line tension from negative to positive $\lambda_{slv} > 0$.

Experimental approach for measurement of the line tension. Experimental measurements of the line tension rely on the modified Young's equation, see Eq. 1.36. The central problem is to measure contact angle $\cos\theta$ as a function of inverse droplet radius $1/R$. The linear dependence between $\cos\theta$ and droplet curvature $1/R$ can be extrapolated to deduce macroscopic contact angle $\cos\theta_Y$ and the line tension λ_{slv}. The surface tension Σ_{lv} is measured independently and assumed to be curvature independent. However, the issue of curvature dependent surface tension can be incorporated in the model by including the Tolman length effect [56]. The measurement of contact angle θ and droplet radius R are usually done by either optical microscopy or atomic force microscopy (AFM) measurements [54]. In the optical microscopy method, the optical interference pattern is used to precisely measure the small contact angles. This makes the optical interference techniques a very useful tool to study droplets near the

first-order wetting transition. Such measurements are, for example, done for droplets of Octane and Octene residing on a silicon wafer with different temperatures [57], see Figure 1.8e. The change of line tension sign is observed near wetting transition temperature as expected from the results of Indekeu's interface displacement model, see Figure 1.8d and e, and the magnitude reside in the range of $\sim \ 1 - 3(\times 10^{-10})$ N. On the other hand, AFM provides high spatial resolution and is suitable for droplets far from the wetting transition. The early measurements are done for sessile fullerene nanodroplets on the surface of silica and found a negative line tension in the range of -10^{-11} to -10^{-10} N [58].

There are several experimental measurements of very large line tension $\lambda_{\alpha\beta\gamma} \sim 1\ \mu N$ for millimeter-sized droplets based on modified Young's equation, Eq. 1.36. The latter observation has lead to great controversy in the field [54]. The main critique of such observations states that Young's equation is only valid for droplets much smaller than the capillary length $l_{cap}^{-1} = \sqrt{\Sigma_{lv}/\rho g} \ \sim 1\ mm$ (where ρ and g are the liquid density and acceleration of the gravity, respectively). Thus, one needs to include gravitational energy in the total energy of the system to deduce the force balance from energy minimization [54]. However, there is no such generalization so far, which includes both effects of gravity and line tension.

Molecular simulations for calculation of the line tension. In molecular simulations, the line tension of spherical droplet can be calculated similarly as an experiment, based on modified Young's equation [59, 60]. The contact angle θ and the radius of the droplet R is typically measured from a spherical cap approximation from the density profiles. In addition, the surface tension components can be estimated from the integral of stress profile, see Eq. 1.34. The line tension is then deduced from the force balance Eq. 1.36. The calculation of the line tension for Lenard-Jones nanodroplets, as an example, revealed negative line tensions ranging from -10^{-12} to -10^{-11} N, depending on the nanodroplet wettability [59]. Very recent work shows that water nanodroplet can attain both negative and positive signs of line tension with magnitude in the range of $10^{-11} - 10^{-10}$ N, which depends on surface thermodynamic of the liquid-solid-gas system rather than the local intermolecular interactions in the three-phase contact zone [61]. Additionally, the line tension can also be calculated from stress tensor; see Eq. 1.35 for cylindrical droplets. Two MD simulation studies have reported negative line tensions for the liquid-liquid-gas contact zone for cylindrical droplets [49, 50]. A different aspect related to the line tension is elaborated in a comprehensive review by Bruce M. Law and *et.al.,* in Ref. [54]

1.4 Biomolecular Condensates

Liquid-liquid phase separation of biomacromolecules is found to be responsible for the formation of membranes-less organelles that behave like liquid droplets inside cells [62]. The membrane-less organelles have been named biomolecular condensates. The growing list of biomolecular condensates as functional sub-cellular compartments has started to challenge our textbook view of intracellular machinery based on vesicle-like organelles [62]. These condensates can form in different parts of the cells which include [62, 63]: (i) nuclear organelles, such as nucleoli, Cajal bodies and heterochromatin, (ii) cytoplasmic organelles, such as P granules, stress granules and processing bodies and (iii) membrane adhered organelles, like membrane receptor clusters and transport channel in the nuclear pore complex.

Such intracellular phase separation typically occurs in the presence of a multicomponent mixture of biomolecules, and the in-vivo realization still remains to be understood[62, 63]. Phase separating proteins typically contain the intrinsically disordered regions (IDRs). The IDRs are enriched with charged and polar amino acids, which prevent proteins from folding into highly ordered structures. The main driving force for liquid-liquid phase separation is the existence of IDRs and multivalent interaction domains between proteins and protein-RNA complexes. In addition, the biomolecular (protein and RNA) concentration, pH, and salt concentrations have been shown to play a prominent role in liquid-liquid phase separation of biomolecules [62, 63].

Biomolecular condensation has implications for understanding cell organization as well as protein aggregation diseases. There is a growing body of research on identifying and elucidating the functional importance of biomolecular condensates. The possible functional consequence includes [63]: (i) buffering the protein concentration, (ii) activation of reactions by increasing the local concentration, (iii) inactivation or suppression of a reaction by excluding the critical component from dilute phase, (iv) sensing and adaptive response to external stimuli such as heat and pH stress, (v) mediation of the localization of specific proteins in an existing condensate, (vi) formation of mechanical and physicochemical filter on nuclear pore or other membrane channels and (vii) generating the mechanical force on cell membrane as a consequence of wetting.

Biomolecular condensates are the most relevant examples of liquid droplets in the context of cell biology. As discussed above, these droplets can generate a mechanical force on the cell membrane, which can lead to cellular endocytosis [64]. The process is directly related to the wetting of the membrane, as discussed in the previous section. Despite massive experimental investigations, the theoretical and computational studies of such processes remain an unexplored area of the research.

In the following chapters of the thesis, we will use computational methods to study the polymorphism of biomembranes at the nanoscale, which is related to membrane wetting phenomena. In chapter two, we will review the methods that have been used

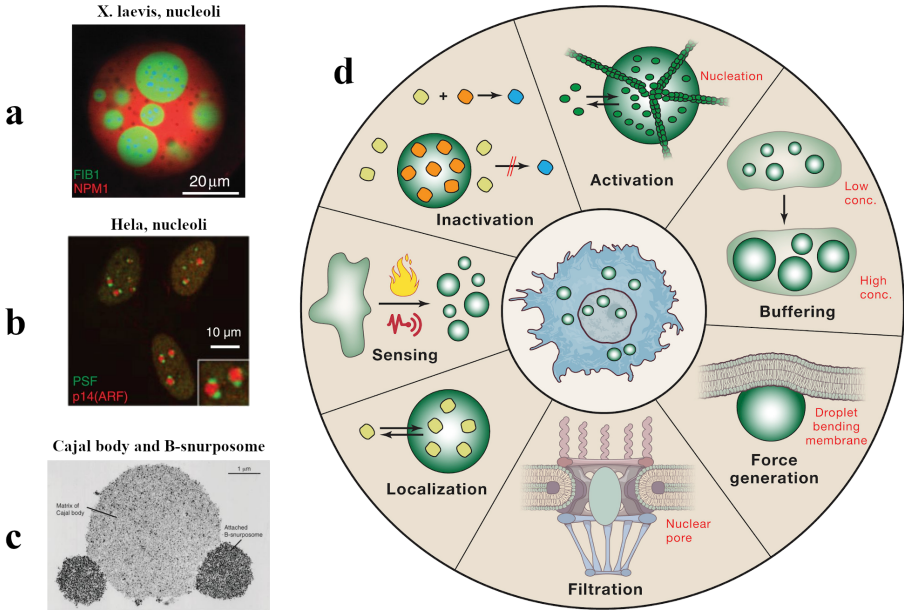

Figure 1.9. Multiphase droplet architecture for a) X. laevis, and b) HeLa,nucleoli and c) Cajal body with attached B-snurposome. (d) The functional consequence of biomolecular condensates. The panel a-c is adapted from Ref. [62] d is adapted from Ref. [63]

for these studies. In chapters three and four, we will study the membrane wetting by nanodroplet in different interfacial tension regimes. In chapter five, we will address the morphological transformations of individual nanovesicles with different degrees of asymmetry between the two leaflets of the bilayer membranes in aqueous solutions. Finally, we will conclude the main finding of the study and provide an outlook in chapter six. In addition, we will provide two detailed mathematical derivations and a numerical algorithm as three septate appendices.

2 Methods

In this chapter, we present technical details of computational methods that are used in our study. First, we present details on the dissipative particle dynamics method, which is used in chapters three and five. Then we discuss the curvature-elastic membrane model that is used in chapter four for modeling of the membrane wetting and in chapter five for the morphological transformation of vesicles. Each chapter includes a separate method section with further technical details. In addition, appendix 3 describes the numerical algorithm for the calculation of bending energy from the trajectory of particle-based simulations.

2.1 Dissipative Particle Dynamics.

Dissipative particle dynamics (DPD) technique is originally introduced for simulation of complex fluids by Hoogerbrugge and Koelman [43] and then further developed by Warren, Español and Groot [44, 45]. DPD has been previously used to elucidate the properties of bilayer membranes at molecular and nanoscopic scales [65, 66, 14, 67, 68, 69, 70, 71]. In DPD simulations three additive two body forces are considered: (*i*) conservative force $\vec{F}_{ij}^{C}$, (*ii*) dissipative force $\vec{F}_{ij}^{D}$, and (*iii*) random force $\vec{F}_{ij}^{R}$. Two beads of type i and j repel each other by short-ranged conservative forces of magnitude f_{ij}. The same beads also interact by a random and a dissipative force connected *via* the dissipation-fluctuation theorem that act as a thermostat. The total force $\vec{F}_i$ acting on bead i due to surrounding beads is the sum of all force contributions:

$$\vec{F}_i = \sum_{j \neq i} \left(\vec{F}_{ij}^{C} + \vec{F}_{ij}^{D} + \vec{F}_{ij}^{R} \right) \tag{2.1}$$

The force acts along beads lines of centres and conserves the linear and angular momentum of the system. The conservative force consists of soft short range repulsive force:

$$\vec{F}_{ij}^{C} = f_{ij}(1 - r_{ij}/d)\hat{r}_{ij} \tag{2.2}$$

where the unit vector $\hat{r}_{ij} = \vec{r}_{ij}/r_{ij}$ points in the direction of center of beads of type i and j. The force parameter f_{ij} depends on the bead type and provides the amplitude of the conservative forces between a bead of type i and a bead of type j.

The dissipative force is due to the friction between particles and represents the viscosity of aqueous media.The dissipative force reads:

$$\vec{F}_{ij}^{D} = -\gamma_{ij}(1 - r_{ij}/d)^2(\hat{r}_{ij}.\vec{v}_{ij})\hat{r}_{ij} \tag{2.3}$$

where friction coefficient is represented by γ_{ij} which depends on the bead type and modulate the amplitude of the dissipative forces. Besides, $\vec{v}_{ij} = \vec{v}_i - \vec{v}_j$ relates the dissipative force to relative velocity of beads.
The random force represent the thermal energy of the system. The latter force considers thermal fluctuation as a results of coupling of the system to a thermal bath in equilibrium. The random force reads:

$$\vec{F}_{ij}^{R} = \sqrt{2\gamma_{ij}k_BT}(1 - r_{ij}/d)\zeta_{ij}\hat{r}_{ij} \tag{2.4}$$

where ζ_{ij} correspond to the Gaussian white noise with zero mean value $< \zeta_{ij}(t) >= 0$ and correlation function of $\left\langle \zeta_{ij}(t)\zeta_{kl}(t') \right\rangle = (\delta_{ik}\delta_{jl} + \delta_{il}\delta_{jk})\delta(t - t')$. All three conservative, dissipative and random forces are truncated for $r_{ij} > d$ by setting $\vec{F}_{ij}^{C} = 0$, $\vec{F}_{ij}^{D} = 0$ and $\vec{F}_{ij}^{R} = 0$.
To represent the lipid molecules, the bonding and bending energies are also considered as other sources of conservative forces. The harmonic potential acts on adjacent beads to consider the bonding of lipid beads:

$$V_{bond}(r_{ij}) = \frac{1}{2}k_b(r_{ij} - r_{ij}^{eq})^2 \tag{2.5}$$

where $k_b = 128\ k_BT/d^2$ is the spring constant and $r_{ij}^{eq} = 0.5\ d$ is the equilibrium separation of adjacent beads of type i and j. The stiffness of lipid chains are governed by a bending potential over three consecutive beads along each chain:

$$V_{bend}(\theta_{ijk}) = k_\phi\Big[1 - cos(\theta_{ijk} - \theta_{ijk}^{eq})\Big] \tag{2.6}$$

here the bending constant $k_\phi = 15\ k_BT$ and equilibrium angle $\theta_{ijk}^{eq} = 180$ are used for three consecutive beads. The beads ij and jk are mutually connected with the harmonic bonding potential $V_{bond}(r_{ij})$ and form the angle θ_{ijk} among three beads.

Our simulations were based on the molecular model of Ref. 14, in which all lipid molecules consist of three hydrophilic H beads and two hydrophobic chains, each consisting of six hydrophobic C beads. In chapter three, two types of liquid beads, liquid-A and liquid-B beads, were used to model the coexisting liquid phases in contact with the membrane: the α phase is enriched in liquid-A beads while the β phase consists primarily of liquid-B beads. In chapter five, one types of liquid bead denoted by W is used. All beads have the same diameter d which provides the basic length scale of the system. The basic energy scale is taken to be the thermal energy $k_{\mathrm{B}}T$.

Time integration scheme. Newton's equations of motions are considered to govern the time evolution of the interacting beads:

$$m_b \frac{d\vec{r}_i}{dt} = m_i \vec{v}_i, \; m_b \frac{d\vec{v}_i}{dt} = \vec{F}_i \tag{2.7}$$

where the bead's mass is set to be constant $m_b = 1$ for all beads which leads to identical acceleration for mutual interactions. To solve the equations of motions we used the velocity-Verlet schemes for time integration:

$$\begin{aligned}
\vec{r}_i(t + \Delta t) &= \vec{r}_i(t) + \Delta t \vec{v}_i(t) + \frac{1}{2}(\Delta t)^2 \vec{F}_i(t)\,, \\
\tilde{v}_i(t + \Delta t) &= \vec{v}_i(t) + \frac{1}{2}\Delta t \vec{F}_i(t)\,, \\
\vec{f}_i(t + \Delta t) &= \vec{F}_i(\vec{r}(t + \Delta t), \tilde{v}(t + \Delta t))\,, \\
\vec{v}_i(t + \Delta t) &= \vec{v}_i(t) + \frac{1}{2}\Delta t(\vec{F}_i(t) + \vec{F}_i(t + \Delta t))\,.
\end{aligned} \tag{2.8}$$

where Δt is the time step of integration. Because the dissipative force depends on the relative velocity of beads, the bead velocity in the subsequent step $\tilde{v}_i$ is estimated based on the current velocity and the force. This estimated velocity $\tilde{v}_i$ is then used to calculate the force and finally correct the velocity for the next step. By solving the set of equations in eq. 2.8 in an iterative manner, we advance the set of positions and velocities from a random initial condition and obtain the trajectory of simulations for the desired time. For all simulations, we used LAMMPS (Large Scale Atomic/Molecular Massively Parallel Simulator), which is a highly efficient, parallelized classical molecular dynamics simulator [72].

2.2 Curvature Elastic Membrane Model.

The elastic membrane surface is modeled using a triangulated mesh. The deformation energy is calculated using the Helfrich Hamiltonian, the total energy, E, of the vesicle reads:

$$E = \int dA[2\kappa(M - m)^2] + \Sigma A_{ves} - PV_{ves} \tag{2.9}$$

Elastic properties of the membrane characterize the elastic energy of membrane via bending rigidity κ, the spontaneous curvature m and the local mean curvature of membrane M. The last two terms in Eq. 2.9, employ two different Lagrange multipliers, namely, Σ and P, to keep the vesicle's area A_{ves} and volume V_{ves} constant. For vesicle-nanodroplet system, the interfacial energy of the nanodroplet interface $\Sigma_{\alpha\beta}\ A_{\alpha\beta}$ and the line energy of the three-phase contact line $\lambda_{\alpha\beta\gamma} L_{\alpha\beta\gamma}$ should be included in the total

energy, as will be discussed in chapter four.

Energy minimization. Here, we used the Surface Evolver (SE) package version 2.70y for triangulation and energy minimization [73] of the vesicle-nanodroplet (chapter four) and vesicle (chapter five) systems. The calculation of the mean curvature and the corresponding bending energy is done based on the Surface Evolver method called "*star_perp_sq_mean_curvature*" [73]. In this method, the mean curvature at each vertex v is given by:

$$M_v = \frac{1}{2}\frac{\nabla A_v \cdot \nabla V_v}{(\nabla A_v \cdot \nabla A_v)/3} \tag{2.10}$$

where ∇A_v and ∇V_v are the area gradient and the volume gradient at vertex v. Then the bending energy is the sum over the vertices:

$$E_b = 2\kappa \sum_{v}^{n} \frac{A_v}{3}\Big[\frac{3}{2}\frac{\nabla A_v \cdot \nabla V_v}{\nabla A_v \cdot \nabla A_v} - m_v\Big]^2 \tag{2.11}$$

where A_v is the area of adjacent facets, m_v is the spontaneous curvature (*intrinsic curvature* in SE terminology), and κ is the bending rigidity of the membrane (*modulus* in SE terminology).

To keep the membrane area constant, the "$facet\_area$" method is used along with a prescribed Lagrange multiplier. Similarly, the "*edge_length*" method is used with line tension $\lambda_{\alpha\beta\gamma}$(*modulus* in SE terminology) to take the line energy into account. The tension value $\Sigma_{\alpha\beta}$ is only prescribed in liquid facets of $\alpha\beta$ interface where the area is not kept constant. The vertices along the contact line $\alpha\beta\gamma$ are subject to a specified contact line constraint. The combination of gradient descent and conjugate gradient methods are used for minimization of the total energy of the system by taking all constraint and boundary conditions into account.

3 Nanodroplets Interacting with Membranes Patches: High Interfacial Tension Regime

3.1 Introduction

Aqueous two-phase (or biphasic) systems [74], which are intimately related to water-in-water emulsions [75], have been frequently used in biochemical analysis and biotechnology [76, 77] to separate biomolecules, organelles, and cell membranes. The classic example is aqueous solutions of PEG and dextran which undergo phase separation when the weight fractions of the polymers exceed a few percent [78]. More recently, water-in-water droplets have also been observed in the form of biomolecular condensates [79, 80] in living cells. So far, the response of membranes and vesicles to such water-in-water droplets has been studied by optical microscopy and elasticity theory for fluid interfaces and membranes [81, 82, 41, 47]. In these studies, the droplets and vesicles as well as the membrane necks had linear dimensions in the micrometer range which implies that one could ignore the line tension associated with the droplets' contact lines on the membranes.

However, when the phase separation leads to individual, well-separated droplets, it proceeds *via* nucleation and growth, starting from droplets with a linear dimension in the nanometer range. When such a nanoscopic droplet is nucleated at a membrane surface, the line tension is expected to play an important role. Likewise, the engulfment of nanodroplets by cellular membranes represents an essential step of pinocytosis and fluid-phase endocytosis which has been recently used to deliver imaging agents [83, 84] or drugs [85, 86, 87] to biological cells. Such pinocytic processes are also involved in the uptake of hydrocarbons by microorganisms [88, 89].

Here, we study such nanodroplets in contact with membranes by coarse-grained molecular simulations using Dissipative Particle Dynamics [44, 45, 65]. We start with a nanodroplet that adheres to a bilayer membrane as displayed in Figure 3.2. The initial axisymmetric morphology is stabilized by the mechanical tension experienced by the membrane, a tension that we control by varying the lateral size of the simulation box for a certain, fixed number of lipid molecules. The droplet consists of the liquid phase α and is bounded by two surface segments: the $\alpha\beta$ interface between the droplet and the liquid bulk phase β as well as the droplet's contact area with the membrane corre-

sponding to the $\alpha\gamma$ membrane segment in Figure 3.2. When we reduce the mechanical tension, the droplet's contact area increases and the area of the $\alpha\beta$ interface decreases. Initially, the droplet-bilayer morphology remains axisymmetric and the contact line retains its circular shape. However, when the tension falls below a certain threshold value, the system undergoes an unexpected transition to a non-axisymmetric morphology. The latter morphology persists until the nanodroplet is completely engulfed by the membrane and the membrane neck has closed into a tight-lipped shape. A detailed analysis of the force balance along the contact line reveals that these non-axisymmetric morphologies arise from negative values of the line tension.

For liquid mixtures without membranes, the concept of line tension was introduced by Gibbs [53] who already pointed out that line tensions can be positive or negative, see, *e.g.*, Ref. 22. In contrast, interfacial tensions must always be positive to ensure thermodynamic stability. Negative values of the line tension have been observed for sessile liquid droplets on solid surfaces [90], for lens-shaped droplets between two bulk liquids [91], and in simulations of Lennard-Jones fluids [59]. Negative line tensions have also been found for Plateau borders in foams. [92] None of these previous studies provided evidence for a morphological transition as described here for membrane-engulfed nanodroplets.

The formation of a tight-lipped membrane neck provides an example for a liquid nanostructure that undergoes a morphological transition with a spontaneously broken symmetry. In addition, the elongated, tight-lipped neck has important consequences for the pinocytosis and cellular uptake of nanodroplets. Indeed, such a neck shape implies a large increase in the free energy barrier for thermally-activated scission of the neck. Likewise, a tight-lipped neck can hardly be cleaved by the known protein-based mechanisms for membrane scission. Indeed, our current models for membrane scission by proteins such as dynamin [93] and ESCRT [94, 95] are all based on the assumption that the membrane neck has a circular shape.

3.2 Methods

3.2.1 Dissipative Particle Dynamics.

In our molecular simulations, we used the Dissipative Particle Dynamics (DPD) method [44, 45, 65] which is based on discrete particles or beads that represent groups of liquid molecules as well as groups of atoms within the head groups and hydrophobic tails of the lipid molecules. The technical details about the DPD simulations can be found in chapter two.

Choice of DPD force parameters. In general, the DPD force parameters are chosen in such a way that they reproduce certain nanoscopic and mesoscopic properties of the system. Thus, the force parameter values $f_{\mathrm{AA}} = f_{\mathrm{BB}} = 25\, k_{\mathrm{B}}T/d$ ensure that the liquid density is equal to $3/d^3$ as appropriate for water.

The complete parameter set DPD-1 that we used to obtain the simulation results in Figures 3.3 - 3.9 is given in Table 3.1. The data in Figure 3.10 correspond to the extended parameter set DPD-2 given in Table 3.2. Both parameter sets DPD-1 and DPD-2 lead to symmetric bilayers with negligible spontaneous curvature and intrinsic contact angles close to 90°. We also studied asymmetric bilayers, using the parameter set DPD-3 with $f_{\mathrm{BH}} \neq f_{\mathrm{AH}}$, see Table 3.3.

3.2.2 Geometry of simulation box and boundary conditions.

The simulation box was taken to be a cuboid with its edges parallel to the Cartesian coordinates x, y, and z; the base of the cuboid with area $A_{\parallel} = L_{\parallel}^2$ was taken to be parallel to the xy-plane. Initially, a planar bilayer of lipid molecules was assembled parallel to the xy-plane, together with a hemispherical nanodroplet of liquid-A beads

Table 3.1. Parameter set DPD-1 for symmetric bilayers used to generate Figures 3.3 - 3.9. The parameter f_{ij} provides the amplitude of the conservative forces between a bead of type i and a bead of type j, in units of $k_{\mathrm{B}}T/d$. Lipid head beads are abbreviated by H, lipid chain beads by C, and the two types of liquid beads by A and B.

f_{ij}	H	C	A	B
H	30	50	25	25
C	50	10	75	75
A	25	75	25	50
B	25	75	50	25

Table 3.2. Parameter set DPD-2 for symmetric bilayers with variable force parameters f_{AB} and f_{AH}, which were chosen as indicated by the 16 red crosses in Figure 3.10a. The symbols have the same meaning as in Table 3.1, the f_{ij}-values are again in units of $k_{\mathrm{B}}T/d$.

f_{ij}	H	C	A	B
H	30	50	f_{AH}	f_{AH}
C	50	10	75	75
A	f_{AH}	75	25	f_{AB}
B	f_{AH}	75	f_{AB}	25

Table 3.3. Parameter set DPD-3 for asymmetric bilayers. Force parameters f_{ij} in units of $k_{\mathrm{B}}T/d$, used to study different affinity contrasts Δ_{aff} as defined in Eq. 3.11. All parameters have the same values as those in Table 3.1, except for the parameter f_{AH} which was taken to be 22.5, 25, and 27.5 $k_{\mathrm{B}}T/d$, corresponding to the affinity contrasts $\Delta_{\mathrm{aff}} = 0.1, 0$, and -0.1.

f_{ij}	H	C	A	B
H	30	50	f_{AH}	25
C	50	10	75	75
A	f_{AH}	75	25	50
B	25	75	50	25

that formed a circular contact area with the bilayer. The remaining volume of the box was filled with liquid-B beads. The bilayer consisted of 13225 lipids per leaflet. Two droplet volumes consisting of 21707 and 43414 A beads were simulated, both of which were much smaller than the combined number of about 3.445 million A and B beads. The corresponding droplet volumes $V_{\alpha,1} = 6837.6\ d^3$ and $V_{\alpha,2} = 2\,V_{\alpha,1} = 13675.3\ d^3$ can be estimated from the volume of a spherical α droplet immersed in the β phase. The density profiles were analyzed using the Matlab image processing toolbox [96] and VMD [97] was used for visualization.

During the simulations, the liquid-A beads were forced to stay on one side of the membrane using a planar and semipermeable wall that repelled the A beads by a purely repulsive Lennard-Jones potential with cut-off $r_c = 1.122\ d$. The semipermeable wall could adjust its z-coordinate to ensure mechanical equilibrium between the β and γ phase with $P_\beta = P_\gamma = 23.7\,k_{\mathrm{B}}T/d^3$. In this way, we obtained two distinct bulk phases β and γ on the two sides of the membranes: the β phase contained some liquid-A beads whereas the γ phase contained only liquid-B beads. Periodic boundary conditions were used in the all three Cartesian directions. In addition, the lateral

diffusion of the nanodroplet was compensated by lateral displacements of the system so that the center-of-mass of the droplet remained at $x = y = 0$. All beads were taken to have the same mass m_b. A time step of $0.01\,\tau$ was used, where the basic time scale $\tau = \sqrt{d^2 m_\mathrm{b}/(k_\mathrm{B}T)}$ corresponds to about 1 ns and the bead diameter d to about 1 nm as estimated in Refs. 66 and 14 from the lateral diffusion constant of the lipid molecules and from the thickness of the bilayer membrane, respectively.

3.2.3 Mechanical definition of surface tensions.

The tension of an interface between two liquid phases can be defined in two ways. First, it can be defined using the thermodynamic limit and an expansion of the system's free energy in powers of the system size L. The interfacial tension is then obtained from the term proportional to L^2 (for three-dimensional systems). Second, it can be defined mechanically by the work expended to increase the area of the interface. One then obtains the interfacial tension from the integral over the local stress profile $s(r, z)$ which is derived from the pressure tensor. Even though these two definitions look quite different, they are in fact equivalent, see, *e.g.*, Ref. 22. The situation for membranes is somewhat different. On the one hand, a sufficiently large membrane segment that is under mechanical tension can always lower its free energy by rupture or poration. Therefore, we cannot perform the thermodynamic limit of a membrane under tension. On the other hand, the membrane tension can still be defined by the local stress profile [23] and can then be calculated for relatively small membrane segments as considered here.

3.2.4 Control parameters.

For a given lateral size $L_y = L_x \equiv L_\parallel$ of the simulation box, we first used an NPT ensemble with the Berendsen barostat [98] and adjusted the perpendicular extension L_z of the box in such a way that the pressure P_{zz} attained the standard DPD value $P_{zz} = 23.7\ k_\mathrm{B}T/d^3$ corresponding to the bulk liquid density $3/d^3$. We then kept the perpendicular extension L_z at the adjusted value and continued our simulations in the corresponding NVT ensemble. For the simulations of tense membranes, the lateral box size $L_\parallel$ was increased in a stepwise manner, using $L_\parallel = 130$, 135, 140, 145, 150. For each $L_\parallel$-value, we collected data from two separate simulations with 3500 τ. The three dimensional pressure and density profiles were calculated on a cubic grid with mesh size equal to the bead diameter d using Irving-Kirkwood contours and the algorithm described in Refs. 99 and 100 for the local pressure.

The sequence of snapshots as shown in Figure 3.3 was based on a more elaborate simulation protocol with a time-dependent lateral box size $L_\parallel = L_\parallel(t)$. The system was first equilibrated for $L_\parallel = 130\,d$ as described in the previous paragraph. We then switched from the NVT to the NPT ensemble to keep the bulk pressure P_{zz} at its

standard DPD value $P_{zz} = 23.7\, k_{\mathrm{B}}T/d^3$ as we decreased the lateral size $L_{\parallel}$ and thus the overall lateral stress acting on the membrane, using a small and constant rate $\mathrm{d}L_{\parallel}/\mathrm{d}t$. The constant bulk pressure and the constant bead number imply a constant volume of the simulation box. Therefore, the perpendicular extension L_z of the simulation box increased with decreasing $L_{\parallel}$ as can be seen in Figure 3.3.

For the snapshots displayed in Figure 3.3, the box compression rate was taken to be $\mathrm{d}L_{\parallel}/\mathrm{d}t = -0.0025\, d/\mathrm{ns}$ which reduced the lateral size $L_{\parallel}$ from $130\, d$ to $120\, d$ within $4\, \mu\mathrm{s}$. Additional simulations with different values of the rate $\mathrm{d}L_{\parallel}/\mathrm{d}t$ confirmed that the sequence of observed morphologies does not depend on the precise value of $\mathrm{d}L_{\parallel}/\mathrm{d}t$ as long as $|\mathrm{d}L_{\parallel}/\mathrm{d}t| \lesssim 0.01\, d/\mathrm{ns}$.

3.2.5 Free energy of membrane-droplet system.

The two membrane segments $\alpha\gamma$ and $\beta\gamma$ with areas $A_{\alpha\gamma}$ and $A_{\beta\gamma}$ experience the mechanical tensions $\Sigma_{\alpha\gamma}$ and $\Sigma_{\beta\gamma}$, each of which includes both the overall lateral stress applied *via* the prescribed lateral area $A_{\parallel} \equiv L_{\parallel}^2$ and the adhesion free energy between the membrane and the adjacent liquid phase [47]. The $\alpha\beta$ interface with area $A_{\alpha\beta}$ contributes the interfacial free energy $\Sigma_{\alpha\beta}A_{\alpha\beta}$ and the volume term $P_{\alpha\beta}V_{\alpha}$ with the pressure difference $P_{\alpha\beta} \equiv P_{\alpha} - P_{\beta} > 0$ between the pressures P_{α} and P_{β} within the α droplet and the β phase. In addition, the contact line with length $L_{\alpha\beta\gamma}$ contributes the line free energy $\lambda_{\alpha\beta\gamma}L_{\alpha\beta\gamma}$ which is proportional to the line tension $\lambda_{\alpha\beta\gamma}$.

The local membrane shape is described by the mean curvature M which tries to adapt to the spontaneous curvatures $m_{\alpha\gamma}$ and $m_{\beta\gamma}$ of the two membrane segments. The total free energy E of the membrane-droplet system is then given by

$$E = \sum_{j=\alpha,\beta} \int dA_{j\gamma}[2\kappa_{j\gamma}\,(M - m_{j\gamma})^2 + \Sigma_{j\gamma}] + \Sigma_{\alpha\beta}A_{\alpha\beta} - P_{\alpha\beta}V_{\alpha} + \lambda_{\alpha\beta\gamma}L_{\alpha\beta\gamma} \qquad (3.1)$$

with the bending rigidities $\kappa_{\alpha\gamma}$ and $\kappa_{\beta\gamma}$ of the two membrane segments. Two Lagrange multipliers $\Sigma_{\alpha\gamma}$ and $\Sigma_{\beta\gamma}$ are set to ensure that the area of membrane segments are constant. However, it can be shown these Lagrange multipliers are equal to mechanical segment tensions $\Sigma_{\alpha\gamma} = \Sigma_{\alpha\gamma}^{mec}$ and $\Sigma_{\beta\gamma} = \Sigma_{\beta\gamma}^{mec}$ in equilibrium, see *Appendix* 1. The basic energy scale is taken to be the thermal energy $k_{\mathrm{B}}T$ which is equal to $4 \times 10^{-21}\,\mathrm{J}$ at room temperature. For negligible spontaneous curvatures $m_{\alpha\gamma}$ and $m_{\beta\gamma}$, the first variation of E with respect to the position of the contact line leads to the force balance Eq. 3.9. A detailed derivation of this force balance, using variational calculus, is given in *Appendix* 2.

3.2.6 Mechanical tensions from stress profiles.

For the axisymmetric membrane-droplet morphologies, we calculated the mechanical tension from the two-dimensional stress profiles $s(z, r)$, using trapezoidal numerical integration. The integration domains are chosen in such a way that the membrane segments and the $\alpha\beta$ interface are essentially flat, see yellow, red, and white boxes in Figure 3.6a. The mechanical segment tensions $\Sigma_{\alpha\gamma}$ and $\Sigma_{\beta\gamma}$ and the interfacial tension $\Sigma_{\alpha\beta}$ of the $\alpha\beta$ interface are then obtained by integrating the stress profile using a cubic lattice of discrete sites with a lattice constant d. The profile $s(z, r)$ was obtained by integrating the local stress $s(x, y, z)$ over the angular coordinate (or azimuth). This angular integration was performed by summing up all values of the local stress within an annulus with inner radius $r - d/2$ and outer radius $r + d/2$.

3.2.7 Calculation of the area per lipid

For the axisymmetric membrane-droplet morphologies, we employed the projected area A_p in the planar $\beta\gamma$ segment to calculate the area per lipid using:

$$a_{l,\beta\gamma} = \frac{2A_p}{(N_{il} + N_{ol})} \,. \tag{3.2}$$

where N_{il} and N_{ol} are the number of lipids in inner and outer leaflets, respectively. The leaflet in contact with the nanodroplet is considered to be the outer leaflet. The area in the curved segment of $\alpha\gamma$ is estimated by a spherical cap approximation. The spherical cap areas of the inner leaflet A_{il} and the outer leaflet A_{ol} are calculated separately by fitting the head group coordinates in the upper and lower leaflets to a sphere. Then, the mean area per lipid is obtained by averaging the area per lipid in the different leaflets:

$$a_{l,\alpha\gamma} = \frac{1}{2}\Big(\frac{A_{il}}{N_{il}} + \frac{A_{ol}}{N_{ol}}\Big) \,. \tag{3.3}$$

the membrane segment in close vicinity of the three-phase contact zone is excluded from the calculation to eliminate deviations from the spherical cap approximation.

3.2.8 Leaflet-water interfaces from density profiles.

The three-dimensional density profile $\rho(x, y, z)$ is first calculated as a function of the Cartesian coordinates x, y, and z using a cubic lattice. For axisymmetric morphologies, one can then calculate the density

$$\rho(r, z) = \frac{1}{N_r} \sum_{0 \le \varphi \le 2\pi} \rho(x, y, z) \tag{3.4}$$

which depends on the cylindrical coordinates $r = \sqrt{x^2 + y^2}$ and z but is independent of the azimuth φ. The sum runs over the number N_r of lattice points within an annulus of radius $r \pm d/2$. Two-dimensional density profiles are then generated by two-dimensional interpolation within the (r, z)-plane as illustrated in Figure 3.6b for $L_{||} = 130\ d$.

The location of the leaflet-water interfaces is based on iso-density stripes, which are defined by a certain range of H bead density ρ_{H} as given by $0.15/d^3 \leq \rho_{\mathrm{H}} \leq 0.3/d^3$. In order to extract the spatial location of these stripes, image files are generated from the two-dimensional density profiles $\rho(r, z)$ as obtained from Eq. 3.4 and the Matlab image processing toolbox [96] is used for image segmentation of these density profile images.

3.2.9 Bending energy of tight-lipped membrane necks.

For a uniform membrane with negligible spontaneous curvature and uniform bending rigidity κ, the contribution from the bending energy in Eq. 3.1 reduces to $2\kappa \int \mathrm{d}A\, M^2$, which represents the surface integral over the square of the local mean curvature M. We now apply this expression to closed membrane necks. If the neck closed in an axisymmetric manner, the diameter of the circular contact line would be comparable to the membrane thickness ℓ_{me} and its perimeter to $\pi\ell_{\mathrm{me}}$. When the neck closes into a tight-lipped shape as in Figure 3.3d, the contact line resembles two straight and parallel line segments which are connected by two highly curved line segments, each of which has the curvature radius $\pi\ell_{\mathrm{me}}/2$. Therefore, the two straight segments of the contact line have the combined length $\Delta L_{\alpha\beta\gamma} = L_{\alpha\beta\gamma} - \pi\ell_{\mathrm{me}}$. Along these straight segments, the membrane has a roughly hemicylindrical shape, see Figure 3.3d. The radius $R_\perp$ of these hemicylinders is comparable to the membrane thickness ℓ_{me} which implies that their mean curvature $M \simeq 1/(2\ell_{\mathrm{me}})$ and their area $A \simeq \pi\ell_{\mathrm{me}}\Delta L_{\alpha\beta\gamma}$. The bending energy of these hemicylinders is then given by

$$\frac{\Delta E_{\mathrm{be}}}{L_{\alpha\beta\gamma}} \simeq \pi\ell_{\mathrm{me}}\, 2\kappa \left(\frac{1}{2\ell_{\mathrm{me}}}\right)^2 \frac{\Delta L_{\alpha\beta\gamma}}{L_{\alpha\beta\gamma}} = \frac{\pi}{2}\frac{\kappa}{\ell_{\mathrm{me}}} \left(1 - \frac{\pi\ell_{\mathrm{me}}}{L_{\alpha\beta\gamma}}\right) \tag{3.5}$$

per unit length of the contact line.

3.2.10 Numerical computation of bending energies

To calculate the bending energies, we use the following numerical protocol. For a given bead configuration, as obtained from the DPD simulations, we first construct the midsurface of the bilayer membrane, from the positions of the lipid head beads in the two leaflets, and triangulate this surface using a Delaunay scheme. For each vertex i of the Delaunay triangulation, we consider the K_i triangles (or faces) adjacent to vertex i, i.e., those triangles for which vertex i represents one corner, and label these triangles by $k_i = 1, \ldots, K_i$. Each triangle k_i has the area $A(k_i)$. The effective vertex area is then

defined by

$$A_i \equiv \frac{1}{3} \sum_{k_i=1}^{K_i} A(k_i) \tag{3.6}$$

where the sum runs over all triangles adjacent to vertex i. The factor 1/3 takes into account that three vertices share one triangle and ensures that the total area of the midsurface is given by $\sum_i A_i$, i.e., by the sum over the effective vertex areas. The mean curvature M_i associated with vertex i is computed using the algorithm introduced in Ref. 101. For a symmetric bilayer with zero spontaneous curvature and bending rigidity κ, the discretized bending energy is then given by

$$E_{\rm be}^{\rm dis}\{A_i, M_i\} = 2\kappa \sum_i A_i M_i^2 \tag{3.7}$$

where the sum runs over all vertices of the triangulation. For the parameter set DPD-1, the bending rigidity κ has the value $\kappa \simeq 12.6\, k_{\rm B}T$, which was calculated from the area compressibility modulus as in Refs. 13 and 19.

When we insert the effective vertex areas $A_i^{(0)}$ and the mean curvatures $M_i^{(0)}$ of the original Delaunay triangulation into Eq. 3.7, we obtain the bending energy $E_{\rm be}^{(0)} \equiv E_{\rm be}^{\rm dis}\{A_i^{(0)}, M_i^{(0)}\}$. We then start to smoothen the small-scale roughness of the bilayer membrane by applying the mean face normal filter developed in Ref. 102 to the triangulated midsurface. For this smoothened surface, we again compute the effective vertex areas $A_i^{(1)}$ and the vertex-associated mean curvatures $M_i^{(1)}$ to obtain the bending energy $E_{\rm be}^{(1)} = E_{\rm be}^{\rm dis}\{A_i^{(1)}, M_i^{(1)}\}$. The smoothening and the associated computation are iterated several times, thereby generating a series of bending energy values $E_{\rm be}^{(n)}$. The iterative smoothening is stopped when the change in the bending energy falls below $1\, k_{\rm B}T$, i.e., it is stopped at $n = N$ with $|E_{\rm be}^{(N)} - E_{\rm be}^{(N-1)}| < k_{\rm B}T$. The detailed description of the numerical algorithm is explained in *Appendix* 3.

The numerical procedure just described was used to calculate the bending energies shown in Figure 3.9. When we apply the same procedure to the membrane in Figure 3.3d, which exhibits a tight-lipped membrane neck, we obtain the bending energy $E_{\rm be}^{(N)} = 438.5\, k_{\rm B}T$ after $N = 61$ smoothening iterations. To compute the excess bending energy of the neck, we substract the bending energy $8\pi\kappa$ of a spherical $\alpha\gamma$ membrane segment and take into account that the bending energy of a planar $\beta\gamma$ membrane segment vanishes. For the bending rigidity $\kappa = 12.6\, k_{\rm B}T$, we then obtain the bending energy

$$\Delta E_{\rm be} = E_{\rm be}^{(N)} - 8\pi\kappa = 438.5\, k_{\rm B}T - 316.7\, k_{\rm B}T = 121.8\, k_{\rm B}T\,. \tag{3.8}$$

Using the length $L_{\alpha\beta\gamma} \simeq 70\, d$ of the contact line in Figure 3.3d, we obtain the contribution $\Delta E_{\rm be}/L_{\alpha\beta\gamma} \simeq 1.74\, k_{\rm B}T/d$ to the effective line tension $\lambda_{\rm eff}$ from the highly curved

membrane segments along the contact line.

3.3 Results and Discussion

3.3.1 Phase separation in binary AB mixture

The binary mixture of liquid-A and liquid-B beads provides a relatively simple model system that undergoes phase separation into two aqueous phases, the A-rich phase α and the B-rich phase β. In Figure 3.1, we describe the simulation geometries used to determine the interfacial tension $\Sigma_{\alpha\beta}$ and the two-phase coexistence region.
The DPD force parameter f_{AB} determines the interfacial tension $\Sigma_{\alpha\beta}$ of the $\alpha\beta$ interface. We measured this tension for the slab geometry shown in Figure 3.1a. For

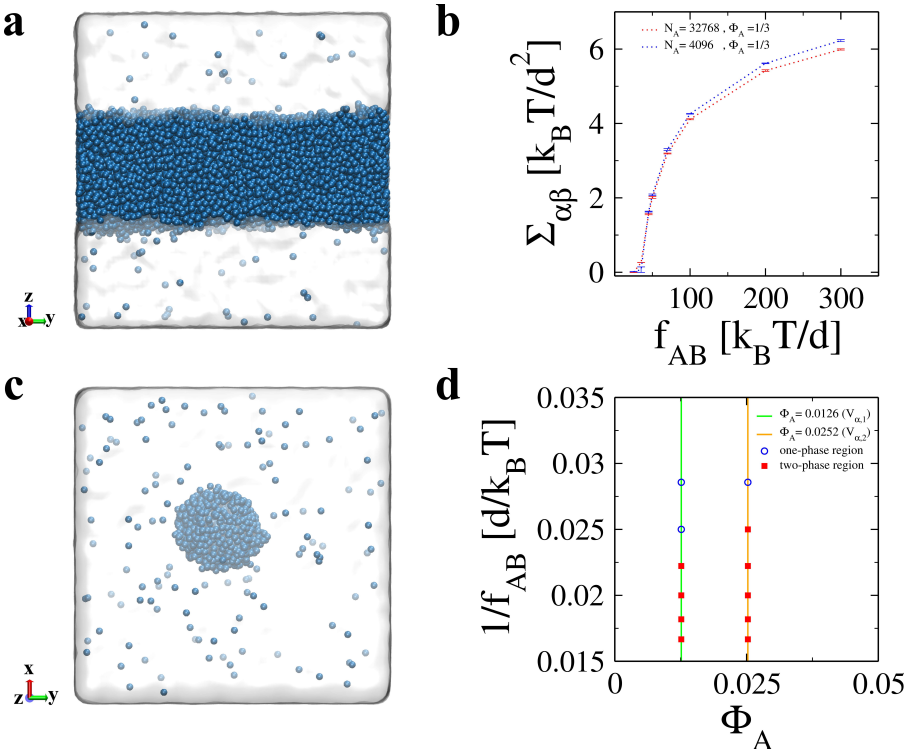

Figure 3.1. Two-phase coexistence and interfacial tension in a binary mixture of A and B water beads: (a) Two planar $\alpha\beta$ interfaces between the A-rich α phase (dark blue) and the B-rich β phase (white). This slab geometry is convenient to measure the interfacial tension $\Sigma_{\alpha\beta}$ via the stress profile; (b) The interfacial tension $\Sigma_{\alpha\beta}$ as a function of the force parameter f_{AB} for constant force parameters $f_{\mathrm{AA}} = f_{\mathrm{BB}} = 25$; (c) Small droplet of α phase immersed in the β phase. The stability of such an α droplet provides a simple criterion for the coexistence of α and β; and (d) Depending on the mole fraction Φ_{A} of the A beads and on the effective temperature $1/f_{\mathrm{AB}}$, small droplets of α phase remain stable (solid squares, red) or dissolve (open circles, blue). The left and right vertical line corresponds to the smaller volume $V_{\alpha,1}$ and to the larger volume $V_{\alpha,2} = 2V_{\alpha,1}$, respectively.

$40\,k_BT/d \leq f_{AB} \leq 60\,k_BT/d$, the interfacial tension lies within the interval $0.8\,k_BT/d^2 \leq \Sigma_{\alpha\beta} \leq 2.6\,k_BT/d^2$, see Figure 3.1b. The force parameters f_{HH}, f_{HC}, and f_{CC} were chosen as in Ref. 14 in order to obtain a linear relationship between the mechanical membrane tension and the molecular area per lipid, as observed experimentally, and to ensure that flip-flops of lipids between the two leaflets are suppressed over microsecond time scales.

The liquid phases are built up from a binary mixture of two types of beads, liquid-A and liquid-B beads. This mixture undergoes phase separation into the A-rich phase α and the B-rich phase β, see Figure 3.1, and provides a relatively simple model for aqueous two-phase systems with small solutes, such as PEG and salt [74], or for two different liquids such as water and oil that demix above a certain concentration of one molecular component. Oil-in-water nanoemulsions are stabilized by surfactants which reduce the interfacial tension of the oil-water interface and shield the droplets against hydrophobic interactions. In our coarse-grained model, the surfactants are taken into account by a reduced force parameter f_{AB} which implies a reduced interfacial tension, see Figure 3.1.

3.3.2 Bilayer membranes exposed to three liquid phases.

We studied bilayer membranes in contact with nanodroplets by molecular simulations, using Dissipative Particle Dynamics (DPD) with three different sets of force parameters f_{ij} as described in the *Methods* section. The bilayer membranes are assembled from coarse-grained lipids as described previously [14]. To obtain symmetric bilayers, the lipid head (H) beads and the lipid chain (C) beads were taken to experience the same interactions with the A and B liquid beads, corresponding to the equalities $f_{AH} = f_{BH}$ and $f_{AC} = f_{BC}$ between the force parameters f_{ij}, see Tables 3.1 and 3.2 in the *Methods* section. To study $\alpha\gamma$ membrane segments with bilayer asymmetry, the interactions of the lipid H beads with the A beads were chosen to be different from those with the B beads, corresponding to $f_{AH} \neq f_{BH}$, see Table 3.3 in the *Methods* section.

Each bilayer membrane was exposed to three liquid phases, denoted by α, β, and γ as depicted in Figure 3.2. The α phase formed the nanodroplet adhering to the membrane, the β phase coexisted with the α droplet, and the γ phase was an inert spectator phase, consisting only of B beads. As shown in Figure 3.2, the resulting membrane-droplet morphology involves three surface segments: the $\alpha\beta$ interface between the α droplet and the β phase as well as two membrane segments $\alpha\gamma$ and $\beta\gamma$ which are in contact with the α droplet and the β phase, respectively.

The bilayer membrane displayed in Figure 3.2 experiences a significant tension that prevents this membrane from increasing its contact area with the nanodroplet, thereby engulfing the droplet and decreasing the area of the $\alpha\beta$ interface. Such an engulfment process was observed as soon as we reduced the membrane tension by decreasing the

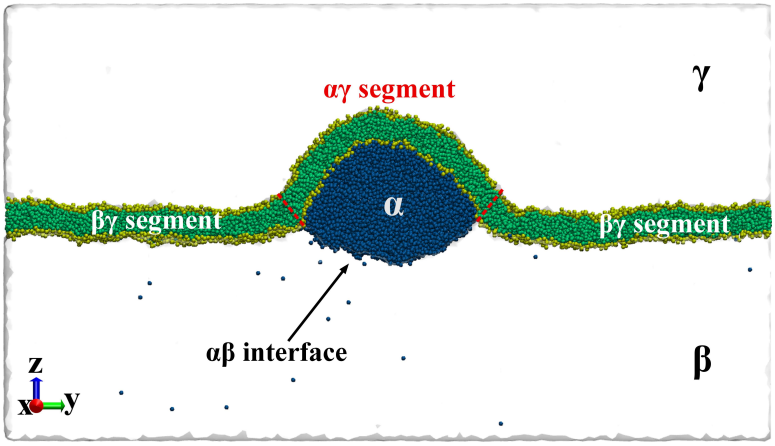

Figure 3.2. Nanodroplet of α phase (dark blue) adhering to a bilayer membrane (green). The nanodroplet coexists with the bulk phase β (white with blue dots). The liquid phase γ (white) above the membrane corresponds to an inert spectator phase. The membrane-droplet morphology involves three surface segments: the $\alpha\beta$ interface between the α droplet and the β phase as well as two membrane segments $\alpha\gamma$ and $\beta\gamma$ which are in contact with the α droplet and the β phase, respectively. The simulation box is a cuboid with lateral size $L_\parallel$. The image represents a cross-subsection parallel to the yz-plane as indicated by the right-handed orthonormal trihedron (red-green-blue) in the lower left corner.

lateral size $L_\parallel$ of the simulation box, see Figure 3.3. This reduction of $L_\parallel$ was performed in such a way that the number of lipid molecules within the bilayer, the numbers of liquid-A and liquid-B beads, the bulk pressure of the liquid phases, and the volume $L_\parallel^2 L_z$ of the simulation box remained constant. Because of the latter constraint, the reduction of $L_\parallel$ leads to an increase in the perpendicular box size L_z, see Figure 3.3.

Engulfment of nanodroplets by symmetric bilayers.

We first investigated the behavior of symmetric bilayers corresponding to the force parameter set DPD-1 as described by Table 3.1 in the *Methods* section. We started from a membrane-droplet morphology as in Figure 3.2 and then reduced the lateral box size $L_\parallel$ and the concomitant membrane tension over a time period of 4 μs. The resulting evolution of the membrane-droplet morphology is shown in Figure 3.3.

Inspection of Figure 3.3a shows that the initial, axisymmetric droplet was only partially engulfed by the membrane and formed an extended $\alpha\beta$ interface with the β phase. As we reduced the lateral box size $L_\parallel$, the area $A_{\alpha\beta}$ of the $\alpha\beta$ interface decreased and the contact area $A_{\alpha\gamma}$ between the membrane and the droplet increased, see also Figure 3.4. During the initial reduction of the membrane tension, the droplet-bilayer morphology remained axisymmetric and the contact line retained its circular shape. However, when

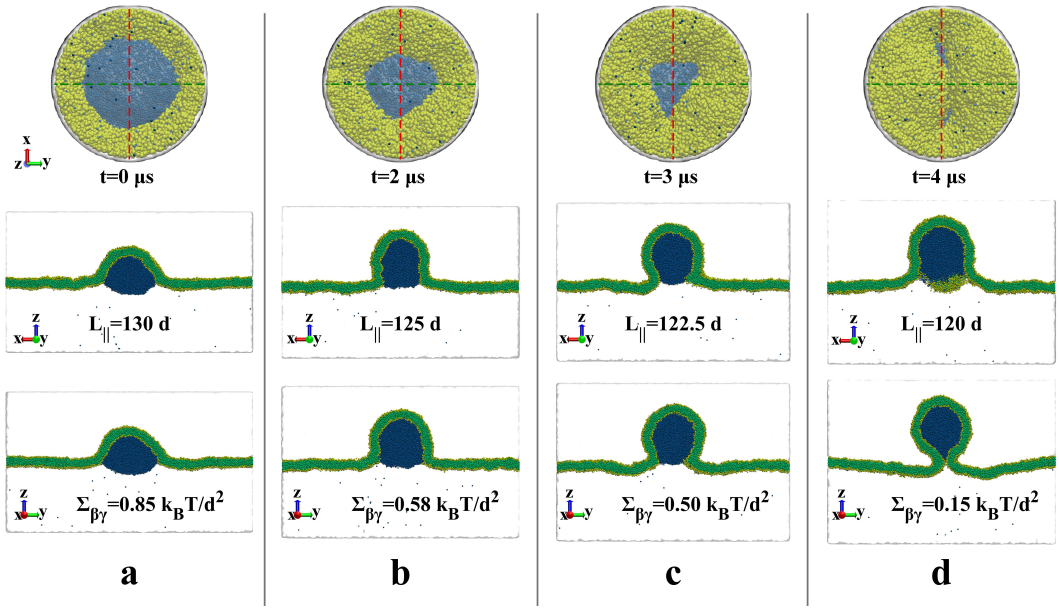

Figure 3.3. Time-dependent engulfment of a nanodroplet by a bilayer membrane from the initial time $t = 0$ in column (a) to the final time $t = 4\,\mu$s in column (d). The columns (b) and (c) correspond to the intermediate time points $t = 2\,\mu$s and $t = 3\,\mu$s. The engulfment process is driven by a reduction in the lateral box size $L_\parallel$, for fixed volume of the simulation box, from $L_\parallel = 130\,d$ at $t = 0$ to $L_\parallel = 120\,d$ at $t = 4\,\mu$s, where the bead diameter d is of the order of 1 nm. This decrease of $L_\parallel$ reduces the mechanical tension $\Sigma_{\beta\gamma}$ within the membrane segment $\beta\gamma$. The panels in the top row show bottom views of circular membrane segments (yellow-green) around the $\alpha\beta$ interface (blue), separated by the contact line which is circular at $t = 0$, strongly non-circular after $t = 3\,\mu$s, and has closed into a tight-lipped shape after $t = 4\,\mu$s. The cross sections in the middle and bottom row are taken along the red and green dashed lines in the top row.

we reached a certain threshold value of the mechanical tension, the system underwent an unexpected transition to a non-axisymmetric morphology. Close to this transition, the contact line underwent strong shape fluctuations, see Figure 3.3b,c. As we further reduced the membrane tension, the non-axisymmetric morphology persisted until the nanodroplet was completely engulfed by the membrane and the membrane neck had been closed into an unusual, tight-lipped shape, see Figure 3.3d. The sum of the contact area $A_{\alpha\gamma}$ and of the interfacial area $A_{\alpha\beta}$ is equal to the total surface area of the α droplet. As shown in Figure 3.4, the surface area $A_{\alpha\gamma} + A_{\alpha\beta}$ remained almost constant during the whole shape evolution in Figure 3.3, implying that the overall shape of the α droplet stayed close to a sphere even though the droplet created the tight-lipped membrane neck that breaks the rotational symmetry.

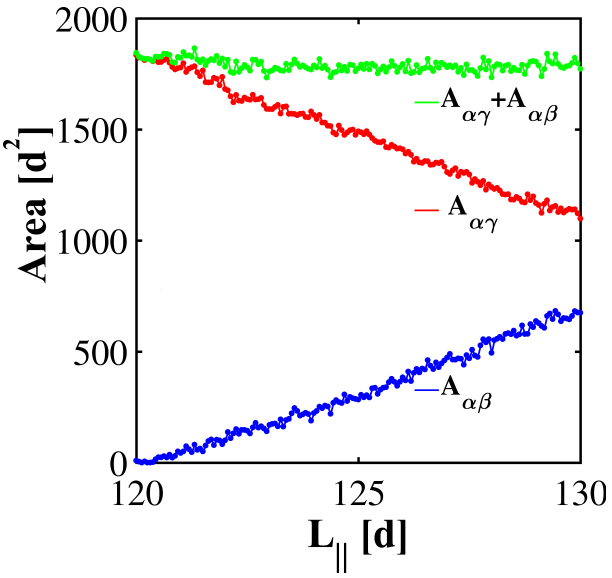

Figure 3.4. Dependence of the contact area $A_{\alpha\gamma}$ (red data) and interfacial area $A_{\alpha\beta}$ (blue data) of the nanodroplet on the lateral size $L_\parallel$ of the simulation box which is reduced from $L_\parallel = 130\,d$ at time $t = 0$ to $L_\parallel = 120\,d$ at time $t = 4\mu$s, where the bead diameter d is of the order of one nanometer and provides the basic length scale. During this reduction of $L_\parallel$, the interfacial area $A_{\alpha\beta}$ goes to zero because the membrane forms a closed neck that replaces the $\alpha\beta$ interface. For comparison, we also include the combined area $A_{\alpha\gamma} + A_{\alpha\beta}$ (green data) which represents the surface area of the droplet and stays essentially constant for all $L_\parallel$-values. Therefore, apart from the tight-lipped neck, the nanodroplet has an essentially spherical shape.

Fluid-elastic parameters of symmetric bilayers.

To understand the origin for the tight-lipped shape of the membrane neck as shown in Figure 3.3d, we now consider the different parameters that determine the free energy of the membrane-droplet system. The explicit form of this free energy is given by eq 3.1 in the *Methods* section. The two membrane segments $\alpha\gamma$ and $\beta\gamma$ experience the mechanical tensions $\Sigma_{\alpha\gamma}$ and $\Sigma_{\beta\gamma}$, each of which includes both the overall lateral stress applied *via* the prescribed lateral area $A_\parallel \equiv L_\parallel^2$ and the adhesive energy between the membrane and the adjacent liquid phases [47]. For symmetric bilayers, both membrane segments have negligible spontaneous curvatures and both segments have the same bending rigidity. The $\alpha\beta$ interface has the interfacial tension $\Sigma_{\alpha\beta}$ and the interfacial area $A_{\alpha\beta}$ which implies the interfacial free energy $\Sigma_{\alpha\beta}A_{\alpha\beta}$. In addition, the contact line with length $L_{\alpha\beta\gamma}$ contributes the line free energy $\lambda_{\alpha\beta\gamma}L_{\alpha\beta\gamma}$ which is proportional to the line tension $\lambda_{\alpha\beta\gamma}$. The latter tension has been ignored in previous studies of membrane wetting which focussed on giant vesicles [103, 47].

In contrast to the interfacial tension $\Sigma_{\alpha\beta}$, which is always positive as required by

thermodynamic stability, the sign of the line tension $\lambda_{\alpha\beta\gamma}$ can be positive or negative [22]. A negative line tension acts to elongate the contact line and provides the main driving mechanism for the formation of non-axisymmetric buds as illustrated in Figure 3.3c,d and explained further below. In principle, the closed neck of the membrane could be further stabilized by effectively attractive forces between the two membrane segments that are in close contact along the elongated contact line. In order to examine this possibility, we performed additional simulations of two planar membranes which were in close contact but found no evidence for such attractive interactions.

Axisymmetric membrane-droplet morphologies.

An axisymmetric shape of the membrane-droplet system is uniquely defined by its one-dimensional shape contour which can be obtained from any cross-subsection that contains the axis of rotational symmetry. Such a parametrization is not possible for non-axisymmetric shapes which are intrinsically two-dimensional, and it is then much more difficult to compute the different free energy contributions in Eq. 3.1. Therefore, we first studied axisymmetric shapes which we obtained by increasing the lateral box size $L_\parallel$ for fixed bead number and fixed volume of the simulation box, thereby increasing the mechanical tensions $\Sigma_{\beta\gamma}$ and $\Sigma_{\alpha\gamma}$ within the two membrane segments. For the symmetric bilayers studied here, axisymmetric shapes were obtained for $\Sigma_{\beta\gamma} \gtrsim 0.6\,\Sigma_{\alpha\beta}$. For these tensions, the nanodroplet was partially engulfed by the membrane with a circular contact line, at which the $\alpha\beta$ interface and the membrane form the intrinsic contact angle θ^*_α, see Figure 3.5 [103, 47]. In the latter figure, we also define two additional quantities that characterize the contact line of an axisymmetric shape: the radius $R_{\rm co}$ of the contact line and the angle $\psi_{\rm co}$ between the membrane contour and the projected contact line, which is perpendicular to the axis of rotational symmetry.

The first variation of the free energy with respect to the position of the contact line leads to several boundary conditions, see *Appendix* 2, one of which describes the balance of the tangential force components at the contact line. For symmetric bilayers with negligible spontaneous curvatures, this boundary condition has the form

$$\Sigma_{\beta\gamma} - \Sigma_{\alpha\gamma} = \Sigma_{\alpha\beta} \cos\theta^*_\alpha + \frac{\lambda_{\alpha\beta\gamma}}{R_{\rm co}} \cos\psi_{\rm co} \tag{3.9}$$

which involves, apart from the geometric quantities θ^*_α, $\psi_{\rm co}$, and $R_{\rm co}$ as defined in Figure 3.5, the mechanical tensions $\Sigma_{\alpha\gamma}$ and $\Sigma_{\beta\gamma}$ of the two membrane segments, the interfacial tension $\Sigma_{\alpha\beta}$ of the liquid-liquid interface, and the line tension $\lambda_{\alpha\beta\gamma}$ of the three-phase contact line.

To determine the three surface tensions $\Sigma_{\alpha\gamma}$, $\Sigma_{\beta\gamma}$, and $\Sigma_{\alpha\beta}$, we use the mechanical rather than the thermodynamic definition of these tensions, as discussed in more detail in the *Methods* section. Thus, all three tensions are calculated from the components

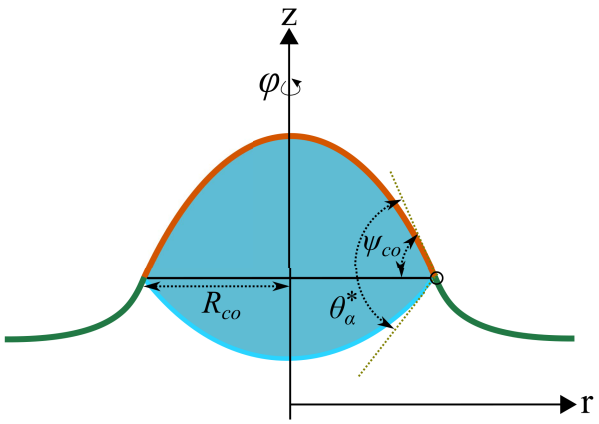

Figure 3.5. Cross section through an axisymmetric shape of a partially engulfed droplet, compare Figure 3.2, with the axis of rotational symmetry provided by the z-axis and the cylindrical coordinates r, z. and φ. The cross section contains the contour of the membrane shape, consisting of the $\alpha\gamma$ (red) and $\beta\gamma$ (green) segments, the circular contour of the $\alpha\beta$ interface between the α droplet (blue) and the β phase (white), and the projected contact line corresponding to the horizontal black line. Important geometric parameters that enter the force balance Eq. 3.9 are the intrinsic contact angle θ^*_α between the membrane contour and the interface contour, the angle ψ_{co} between the membrane contour and the projected contact line, and the contact line radius R_{co}.

P_{xx}, P_{yy}, and P_{zz} of the local pressure tensor which defines the stress profile [23, 99] $s(r,z) = P_{zz} - \frac{1}{2}(P_{xx} + P_{yy})$ as displayed in Figure 3.6a. All geometric quantities can be directly obtained from the simulation data, see Figure 3.6b-c. We are then left with only one unknown parameter in the force balance Eq. 3.9, the line tension $\lambda_{\alpha\beta\gamma}$, which can be computed by inserting the measured values of the other parameters into Eq. 3.9. Next, we will describe in some detail how we obtained the different mechanical tensions and the intrinsic contact angle from the simulations.

Mechanical tensions for axisymmetric shapes.

The different mechanical tensions are obtained by integrating the stress profile $s(r,z)$ in Figure 3.6a across the $\alpha\beta$ interface and across the two membrane segments. To obtain well defined normal and tangential stresses for the curved $\alpha\beta$ interface as well as for the curved $\alpha\gamma$ and $\beta\gamma$ membrane segments, we calculate the stress profile locally for those spatial regions in which the $\alpha\beta$ interface and the two membrane segments are almost planar and essentially normal to the z-axis. Those regions are indicated by the red, yellow, and white boxes in Figure 3.6a. The regions are discretized using a cubic lattice of mesh points with lattice constant d. We first calculate the stress profile $s(z,r)$

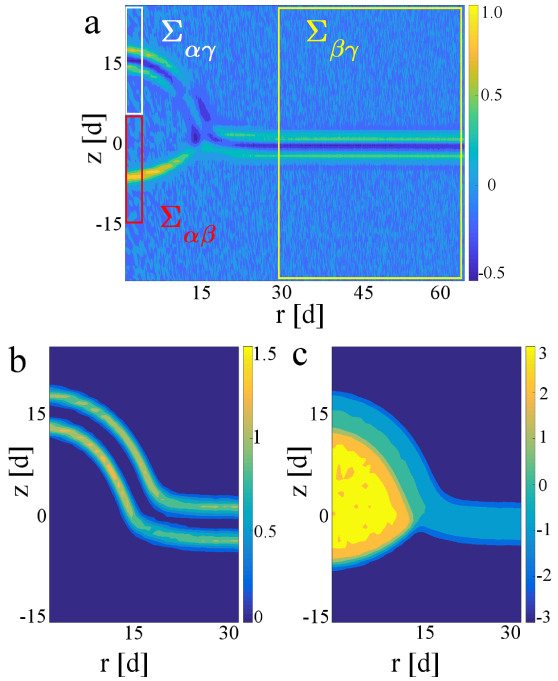

Figure 3.6. Axisymmetric stress and density profiles for the smaller α droplet with volume $V_{\alpha,1}$. The profiles are plotted as functions of the radial coordinate r and the coordinate z parallel to the symmetry axis; both coordinates are measured in units of the bead diameter d: (a) Stress profile $s(r,z) = P_{zz} - \frac{1}{2}(P_{xx} + P_{yy})$ in units of $k_{\mathrm{B}}T/d^3$. This profile varies from $s = -0.5$ (dark blue) to $s = +1$ (yellow). Away from the membrane, the three liquid phases are characterized by $s = 0$ (light blue). The tensions $\Sigma_{\alpha\beta}$, $\Sigma_{\alpha\gamma}$, and $\Sigma_{\beta\gamma}$ are computed from the stress profiles in the red, white, and yellow boxes, respectively; (b) Density profile $\rho_{\mathrm{H}}(r,z)$ of lipid head groups in units of $1/d^3$, which varies from $\rho_{\mathrm{H}} = 0$ (dark blue) away from the membrane to $\rho_{\mathrm{H}} = 1.5$ within the lower head group layer of the $\alpha\gamma$ membrane segment. Note that the head group density in the latter segment exceeds the one in the $\beta\gamma$ segment which implies that the $\alpha\gamma$ segment is compressed compared to the $\beta\gamma$ segment; and (c) Profile of the density difference $\rho_{\mathrm{A}}(r,z) - \rho_{\mathrm{B}}(r,z)$ which varies from the negative bulk density $-\rho_{\mathrm{B}} = -3/d^3$ of the liquid-B beads (dark blue) to the positive bulk density $\rho_{\mathrm{A}} = +3/d^3$ of the liquid-A beads (yellow).

by integrating over the angular coordinate (or azimuth). The different mechanical tensions are then obtained by integrating the latter stress profile, see *Methods* section, which leads to the tension values displayed in Figure 3.7a as a function of the base area $A_{\parallel} = L_{\parallel}^2$; for the precise numerical values of the different tensions, see Tables 3.4 and 3.5.

The interfacial tension $\Sigma_{\alpha\beta}$ measured for the membrane-droplet system is very close to the tension calculated for a planar $\alpha\beta$ interface, see broken horizontal line in Figure 3.7a as well as Figure 3.1b. Therefore, the measured values of $\Sigma_{\alpha\beta}$ were not affected

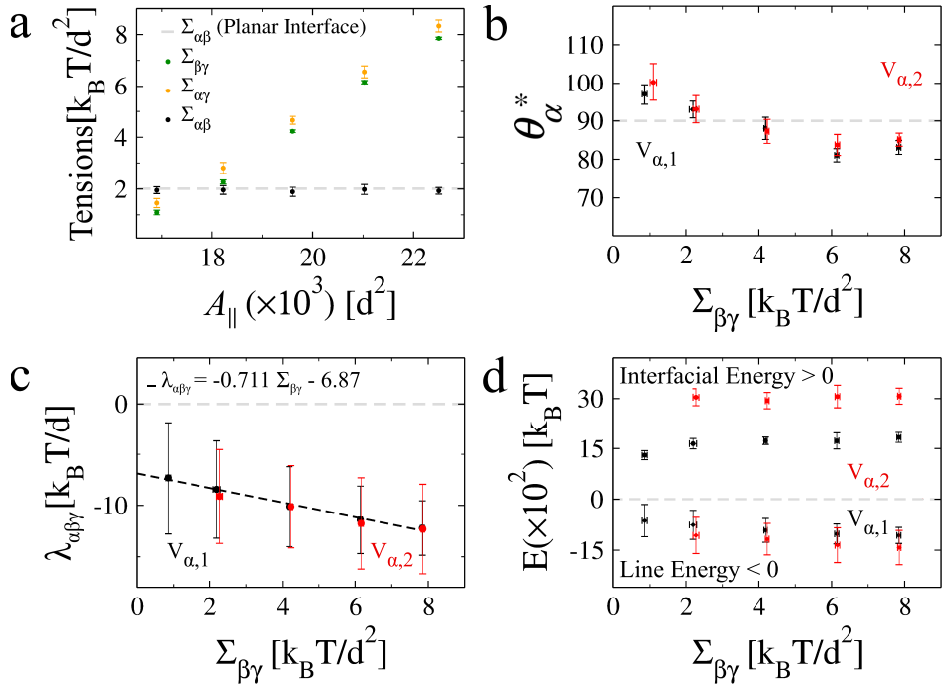

Figure 3.7. (a) Mechanical tensions $\Sigma_{\alpha\beta}$, $\Sigma_{\alpha\gamma}$, and $\Sigma_{\beta\gamma}$ as a function of the base area $A_\parallel = L_\parallel^2$ of the cuboid-shaped simulation box for droplet volume $V_{\alpha,2}$. The interfacial tension $\Sigma_{\alpha\beta}$ for a large planar $\alpha\beta$ interface is also displayed as the horizontal dashed line; (b) Intrinsic contact angle θ_α^*, (c) Line tension $\lambda_{\alpha\beta\gamma}$, as well as (d) Interfacial free energy $\Sigma_{\alpha\beta}A_{\alpha\beta} > 0$ and line free energy $\lambda_{\alpha\beta\gamma}L_{\alpha\beta\gamma} < 0$ as functions of the mechanical segment tension $\Sigma_{\beta\gamma}$. In all three panels b, c, and d, the black and red data points were obtained for small droplet volume $V_{\alpha,1}$ and large droplet volume $V_{\alpha,2} = 2\,V_{\alpha,1}$, respectively. The black dashed line in panel c corresponds to the functional dependence $\lambda_{\alpha\beta\gamma} = -0.711\,d\,\Sigma_{\beta\gamma} - 6.87\,k_\mathrm{B}T/d$ and represents a linear fit to the data for droplet volume $V_{\alpha,1}$. The error bars indicate the standard deviations around the average values.

by the curvature of the $\alpha\beta$ interface. Inspection of Figure 3.7a shows that the mechanical segment tensions $\Sigma_{\alpha\gamma}$ and $\Sigma_{\beta\gamma}$ increase linearly with the projected area $A_\parallel = L_\parallel^2$. The tension values obtained in this manner are essentially independent of the exact limits of integration for the z-integrals, as long as these limits are well separated from the membrane and the $\alpha\beta$ interface.

Intrinsic contact angles for axisymmetric shapes.

For axisymmetric membrane-droplet shapes, the intrinsic contact angle has a constant value along the contact line. In order to measure this angle, we determined the locations of the different surfaces from the density profiles depicted in Figure 3.6b,c. We used the density profile ρ_H of the head group beads as shown in Figure 3.6b and image

segmentation to define the locations of the interfaces separating the lower membrane leaflet from the α droplet and the β phase, respectively; see *Methods* section for more details. The location of the $\alpha\beta$ interface was obtained from the crossing criterion $\rho_{\mathrm{A}} = \rho_{\mathrm{B}}$ for the densities ρ_{A} and ρ_{B} of the A and B beads, see Figure 3.6c. To obtain the location of the contact line, the interfaces separating the lower membrane leaflet from the two liquid phases α and β were simultaneously fitted with basis-splines while the $\alpha\beta$ interface was fitted to a circular segment as in Figure 3.5. The intersection of these two fitting curves defined the contact line and thus the contact line radius R_{co} and the tilt angle ψ_{co} introduced in Figure 3.5. Finally, the intrinsic contact angle θ^*_α was obtained from the tangents of the two fitting curves at the contact line. The results for the intrinsic contact angle θ^*_α are displayed in Figure 3.7b as a function of the mechanical tension $\Sigma_{\beta\gamma}$ of the $\beta\gamma$ membrane segment, both for the droplet volume $V_{\alpha,1}$ and for $V_{\alpha,2} = 2\,V_{\alpha,1}$ as defined in the *Methods* section; for the precise numerical values of the contact angle θ^*_α, see Tables 3.6 and 3.7. The simulation data in Figure 3.7b show that, for a given mechanical tension $\Sigma_{\beta\gamma}$, the intrinsic contact angle has the same value for both volumes $V_{\alpha,1}$ and $V_{\alpha,2}$, within the accuracy of our simulations.

Area per lipid for axisymmetric shapes.

The areas per lipid of the membrane segments are shown as a function of the membrane projected area in Figure 3.8. We find that the area per lipid in the curved $\alpha\gamma$ segment $a_{l,\alpha\gamma}$, where the nanodroplet is in contact with the membrane, is larger than the area per lipid in the planar segment $a_{l,\beta\gamma}$ of the membrane. This implies that the membrane is more stretched in the curved $\alpha\gamma$ segment. The latter expectation is consistent with the measured mechanical tension. As shown in Figure 3.7a and by the data provided in Tables 3.4 and 3.5, the curved $\alpha\gamma$ segment has a higher mechanical tension than the planar $\beta\gamma$ segment. The larger errorbar in the curved $\alpha\gamma$ segment of the membrane suggests the larger fluctuations which are consistent with the higher tension fluctuations in the same segment, see Figure 3.7a. Furthermore, simulation in ultra-high lateral tension leads to the membrane rupture in the $\alpha\gamma$ segment where the nanodroplet is in contact with membrane (results are not shown). The latter provides further confirmation of the higher tension and larger area per-lipid in the $\alpha\gamma$ segment of the membrane.

3.3.3 Negative values of the line tension.

Using the different mechanical tensions and the geometric parameters of the axisymmetric membrane-droplet morphologies as obtained from the simulation data for mechanical tensions $\Sigma_{\beta\gamma} \gtrsim 0.6\,\Sigma_{\alpha\beta}$ of the $\beta\gamma$ membrane segment, we can now compute the line tension $\lambda_{\alpha\beta\gamma}$ of the contact line from the force balance Eq. 3.9. All line tension values obtained in this way are negative as shown in Figure 3.7c where the line tension

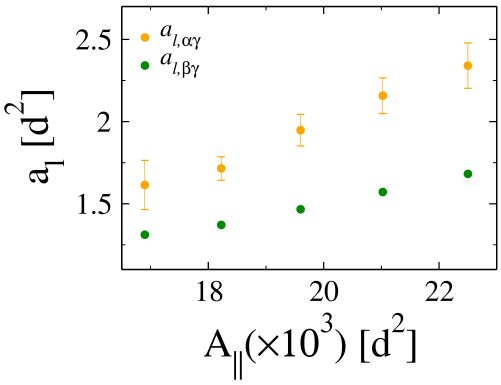

Figure 3.8. Area per lipid in the curved $a_{l,\alpha\gamma}$ and in the planar $a_{l,\beta\gamma}$ segment of the membrane as a function of membrane base area $A_{||} = L_{||}^2$ of the cuboid-shaped simulation box for droplet volume $V_{\alpha,2}$.

Table 3.4. Mechanical properties of the symmetric bilayers obtained for the parameter DPD-1 in Table 3.1 and volume $V_{\alpha,1} = 6837.6\ d^3$ of the α droplet. Lateral box size $L_{||}$, interfacial tension $\Sigma_{\alpha\beta}$, mechanical tensions $\Sigma_{\alpha\gamma}$ and $\Sigma_{\beta\gamma}$ of the two membrane segments, and line tension $\lambda_{\alpha\beta\gamma}$ of the contact line.

	$L_{\|}[d]$	$\Sigma_{\alpha\beta}[k_BT/d^2]$	$\Sigma_{\alpha\gamma}[k_BT/d^2]$	$\Sigma_{\beta\gamma}[k_BT/d^2]$	$\lambda_{\alpha\beta\gamma}[k_BT/d]$
$V_{\alpha,1}$	130	1.861 ± 0.19	1.404 ± 0.18	0.854 ± 0.07	-7.305 ± 5.46
	135	1.913 ± 0.19	2.793 ± 0.27	2.193 ± 0.10	-8.430 ± 4.75
	140	1.889 ± 0.13	4.771 ± 0.19	4.184 ± 0.05	-10.008 ± 3.89
	145	1.852 ± 0.25	6.634 ± 0.20	6.141 ± 0.06	-11.402 ± 3.29
	150	1.952 ± 0.16	8.430 ± 0.17	7.842 ± 0.05	-12.203 ± 2.65

Table 3.5. Mechanical properties of symmetric DPD-1 bilayers for larger α droplet with volume $V_{\alpha,2} = 2V_{\alpha,1} = 13675.3\ d^3$. Lateral box size $L_{||}$, interfacial tension $\Sigma_{\alpha\beta}$, mechanical tensions $\Sigma_{\alpha\gamma}$ and $\Sigma_{\beta\gamma}$ of the two membrane segments, and line tension $\lambda_{\alpha\beta\gamma}$.

	$L_{\|}[d]$	$\Sigma_{\alpha\beta}[k_BT/d^2]$	$\Sigma_{\alpha\gamma}[k_BT/d^2]$	$\Sigma_{\beta\gamma}[k_BT/d^2]$	$\lambda_{\alpha\beta\gamma}[k_BT/d]$
$V_{\alpha,2}$	135	1.959 ± 0.17	2.804 ± 0.21	2.272 ± 0.08	-9.110 ± 4.59
	140	1.891 ± 0.17	4.657 ± 0.15	4.229 ± 0.05	-10.122 ± 4.01
	145	1.982 ± 0.19	6.559 ± 0.23	6.160 ± 0.06	-11.748 ± 4.46
	150	1.928 ± 0.13	8.331 ± 0.23	7.854 ± 0.05	-12.302 ± 4.36

Table 3.6. Geometric properties of symmetric DPD-1 bilayers for smaller α droplet with volume $V_{\alpha,1} = 6837.6\ d^3$. Lateral box size $L_\parallel$, corresponding segment tension $\Sigma_{\beta\gamma}$ in units of $k_\mathrm{B}T/d^2$ as in Table 3.4, base area $A_\parallel = L_\parallel^2$, intrinsic contact angle θ_α^*, contact line radius R_{co}, and cosine of tilt angle, $\cos\psi_{co}$, at contact line.

	$L_\parallel[d]$	$\Sigma_{\beta\gamma}$	$A_\parallel[d^2]$	θ_α^*[degree]	$R_{co}[d]$	$\cos\psi_{co}$
$V_{\alpha,1}$	130	0.854	16900	96.984 ± 2.63	13.75 ± 0.09	0.6 ± 0.03
	135	2.193	18225	92.988 ± 2.19	14.24 ± 0.06	0.83 ± 0.03
	140	4.184	19600	88.184 ± 2.88	14.38 ± 0.19	0.92 ± 0.02
	145	6.141	21025	81.058 ± 1.74	14.22 ± 0.03	0.98 ± 0.01
	150	7.842	22500	83.100 ± 1.80	14.14 ± 0.06	0.95 ± 0.01

Table 3.7. Geometric properties of symmetric DPD-1 bilayers for larger α droplet with volume $V_{\alpha,2} = 2V_{\alpha,1} = 13675.3\ d^3$. Lateral box size $L_\parallel$, corresponding segment tension $\Sigma_{\beta\gamma}$ in units of $k_\mathrm{B}T/d^2$ as in Table 3.5, base area $A_\parallel = L_\parallel^2$, intrinsic contact angle θ_α^*, contact line radius R_{co}, and cosine of tilt angle, $\cos\psi_{co}$, at contact line.

	$L_\parallel[d]$	$\Sigma_{\beta\gamma}$	$A_\parallel[d^2]$	θ_α^*[degree]	$R_{co}[d]$	$\cos\psi_{co}$
$V_{\alpha,2}$	135	2.272	18225	93.059 ± 3.55	18.59 ± 0.06	0.87 ± 0.04
	140	4.229	19600	87.288 ± 3.13	18.48 ± 0.06	0.93 ± 0.02
	145	6.160	21025	83.744 ± 2.73	18.32 ± 0.05	0.96 ± 0.01
	150	7.854	22500	85.116 ± 1.72	18.43 ± 0.06	0.96 ± 0.01

$\lambda_{\alpha\beta\gamma}$ is plotted as a function of the mechanical segment tension $\Sigma_{\beta\gamma}$. The numerical values of $\lambda_{\alpha\beta\gamma}$ are given in Tables 3.4 and 3.5. Inspection of Figure 3.7c shows that a larger membrane tension $\Sigma_{\beta\gamma}$, imposed by a larger box size $L_\parallel$, leads to a more negative value of the line tension. Furthermore, a linear extrapolation of these data to vanishing segment tension $\Sigma_{\beta\gamma} = 0$ leads to the line tension $\lambda_{\alpha\beta\gamma} = -6.87\ k_\mathrm{B}T/d$, indicating that the line tension remains negative even for tensionless membranes.

For the range $0.85\,k_\mathrm{B}T/d^2 \leq \Sigma_{\beta\gamma} \leq 8\,k_\mathrm{B}T/d^2$ of segment tensions $\Sigma_{\beta\gamma}$ as displayed in Figure 3.7c, the line tension varies within the interval $-12.2\ k_\mathrm{B}T/d \lesssim \lambda_{\alpha\beta\gamma} \lesssim -7.30\ k_\mathrm{B}T/d$. Using the thermal energy $k_\mathrm{B}T = 4 \times 10^{-21}\,\mathrm{J}$ at room temperature and the bead diameter $d = 1\,\mathrm{nm}$, we obtain the interval $-4.9 \times 10^{-11}\,\mathrm{N} \lesssim \lambda_{\alpha\beta\gamma} \lesssim -2.9 \times 10^{-11}\,\mathrm{N}$, which is comparable to the three-phase contact line tensions that have been theoretically estimated in the absence of a membrane [104, 54]. For such membraneless droplets, the experimentally deduced values of $\lambda_{\alpha\beta\gamma}$ vary over a much wider range but several experimental studies have also found negative line tensions with a

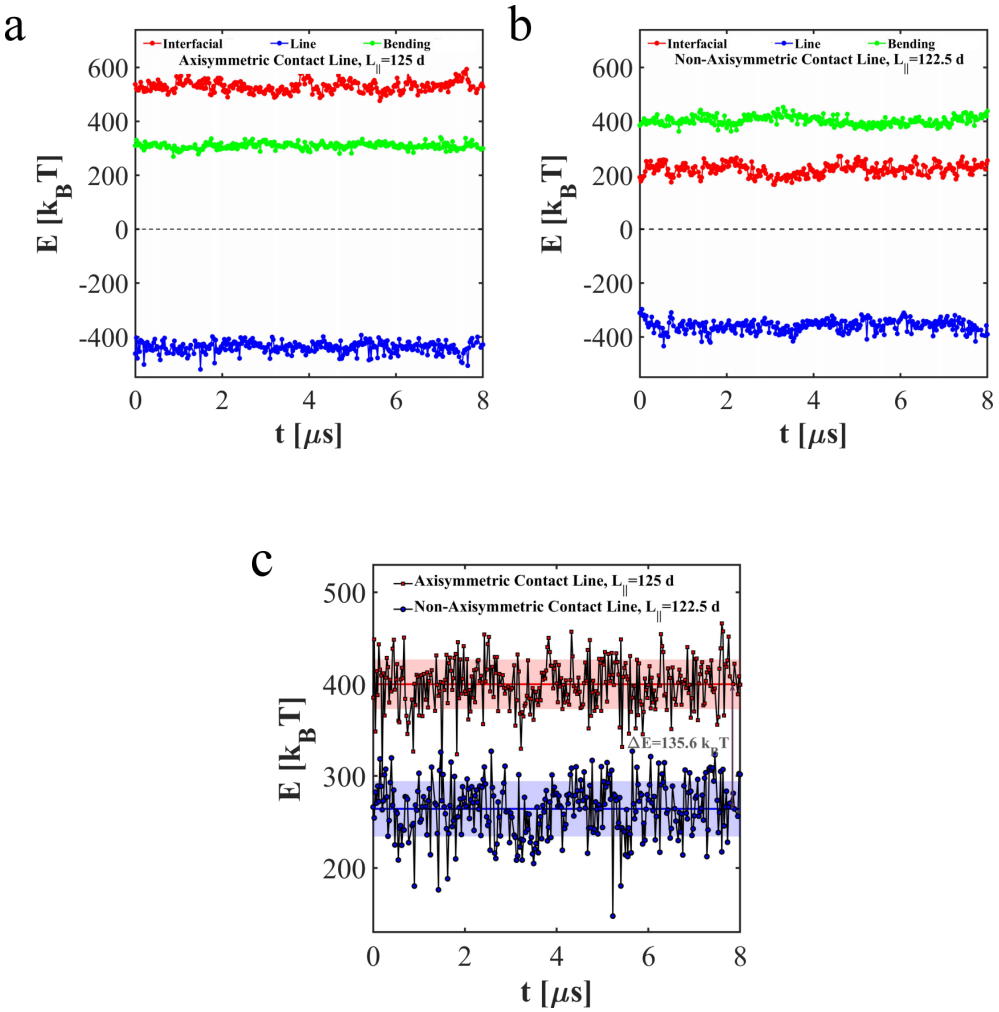

Figure 3.9. (a,b) Positive interfacial free energy (red), positive bending energy (green), and negative line free energy (blue) as a function of time t for two values of the lateral box size $L_{\parallel}$: (a) For $L_{\parallel} = 125\,d$, the membrane-droplet system is axisymmetric with a circular contact line; (b) For the slightly smaller value $L_{\parallel} = 122.5\,d$, the axisymmetry is broken and the contact line has an elongated, noncircular shape. During the transition from (a) to (b), the interfacial free energy is strongly reduced, the bending energy is slightly increased, and the line free energy remains almost constant; and (c) Total free energy E for the axisymmetric morphology with $L_{\parallel} = 125\,d$ (top) and for the non-axisymmetric morphology with $L_{\parallel} = 122.5\,d$ (bottom). Thus, during the morphological transition from the axisymmetric to the non-axisymmetric shape, the total free energy is reduced by $\Delta E = 135.6\,k_{\mathrm{B}}T$.

similar order of magnitude [90, 91].

Negative line tension creates tight-lipped membrane necks.

The negative value of the line tension explains the elongation of the contact line and the formation of the tight-lipped membrane neck as shown in Figure 3.3d. Indeed, the contact line with length $L_{\alpha\beta\gamma}$ reduces the free energy of the system by $L_{\alpha\beta\gamma}\lambda_{\alpha\beta\gamma} < 0$, a reduction that becomes more significant for larger $L_{\alpha\beta\gamma}$-values and thus favors the elongation of the contact line.

As explained in the *Methods* section, see Eq. 3.1, the total free energy of the membrane-droplet system can be decomposed into separate contributions, corresponding to the interfacial free energy $\Sigma_{\alpha\beta}A_{\alpha\beta}$ of the $\alpha\beta$ interface, the bending energy $E_{\rm be}$ of the membrane, and the line free energy $\lambda_{\alpha\beta\gamma}L_{\alpha\beta\gamma}$ of the contact line. These different free energy contributions are displayed in Figure 3.9 for two values of the lateral box size $L_\parallel$.

The symmetry breaking also increases the bending energy of the membrane but this increase is overcompensated by the negative line free energy, see Figure 3.9. The increase in bending energy arises primarily from the highly curved membrane segment along the contact line, because the overall shape of the completely engulfed droplet remains close to a sphere as follows from Figure 3.4. For the tight-lipped membrane neck in Figure 3.3d, these highly curved membrane segments resemble hemicylinders with curvature radius $R_\perp = \pi\ell_{\rm me}/2$ which is of the order of the membrane thickness $\ell_{\rm me}$. As shown in the *Methods* section, see Eq. 3.5, the associated bending energy increase $\Delta E_{\rm be}$ is proportional to the bending rigidity κ of the membrane and leads to the effective line tension

$$\lambda_{\rm eff} = \lambda_{\alpha\beta\gamma} + \frac{\Delta E_{\rm be}}{L_{\alpha\beta\gamma}} = \lambda_{\alpha\beta\gamma} + \frac{\pi}{2}\frac{\kappa}{\ell_{\rm me}}\left(1 - \frac{\pi\ell_{\rm me}}{L_{\alpha\beta\gamma}}\right) \tag{3.10}$$

corresponding to the superposition of the 'bare' line tension $\lambda_{\alpha\beta\gamma}$ and the bending energy contribution $\Delta E_{\rm be}/L_{\alpha\beta\gamma}$. The tight-lipped shape of the closed membrane neck will be energetically favorable compared to the closed axisymmetric shape as long as $\lambda_{\rm eff} < 0$.

For the symmetric bilayers studied here, the bending rigidity has the value $\kappa \simeq 12.6\,k_{\rm B}T$, which was calculated from the area compressibility modulus as in Ref. 13 and 19. This κ-value falls within the range of experimental values measured for a typical phospholipid such as POPC at room temperature [105]. Using the bending rigidity $\kappa \simeq 12.6\,k_{\rm B}T$ together with the bilayer thickness $\ell_{\rm me} \simeq 5\,d$ and the length $L_{\alpha\beta\gamma} \simeq 70\,d$ of the contact line in Figure 3.3d, we obtain the estimate $\Delta E_{\rm be}/L_{\alpha\beta\gamma} \simeq 3.1\,k_{\rm B}T/d$ for the positive line tension contribution from the highly curved membrane segments. This estimate is somewhat larger than the numerically calculated value $\Delta E_{\rm be}/L_{\alpha\beta\gamma} \simeq 1.74\,k_{\rm B}T/d$ obtained for the tight-lipped membrane neck in Figure 3.3d. On the other hand, the 'bare' line tension $\lambda_{\alpha\beta\gamma}$ as plotted in Figure 3.7c is always smaller than $-6.97\,k_{\rm B}T/d$. It then follows from Eq. 3.10 that the effective line tension

λ_{eff} is negative for all of these $\lambda_{\alpha\beta\gamma}$-values and leads to a tight-lipped membrane neck as observed in our simulations. Furthermore, because the bending energy increase ΔE_{be} is proportional to κ, we also conclude from Eq. 3.10 that the effective line tension remains negative for significantly larger κ-values up to about $28\,k_{\text{B}}T$.

Negative line tensions for enlarged parameter set.

The negative values of the line tension as depicted in Figure 3.7c apply to symmetric bilayers with vanishing spontaneous curvature as obtained for the parameter set DPD-1 in Table 3.1. To find out whether the negative sign of the line tension is a robust property of membrane-droplet systems, we next studied symmetric bilayers for the enlarged parameter set DPD-2 in Table 3.2. In the latter set, we varied the two force parameters f_{AB} and f_{AH} in a systematic manner, retaining the symmetry condition $f_{\text{BH}} = f_{\text{AH}}$. The two parameters f_{AB} and f_{AH} are likely to have the largest effect on the force balance Eq. 3.9 because they determine the properties of the three interfaces that meet at the contact line. We combined four different values of f_{AB} as given by $f_{\text{AB}} = 45, 50, 55$, and $60\,k_{\text{B}}T/d$ with four different values of f_{AH} as provided by $f_{\text{AH}} = 20, 25, 30$, and $35\,k_{\text{B}}T/d$, corresponding to the red crosses in Figure 3.10a. As shown in this figure, the line tension was found to be negative for all of these parameter combinations. For intermediate parameter values as indicated by the different colors in Figure 3.10a, the line tension was obtained by two-dimensional interpolation.

In Figure 3.10b, we replot the $\lambda_{\alpha\beta\gamma}$-values as a function of the interfacial tension $\Sigma_{\alpha\beta}$, which is determined by the force parameter f_{AB}, see Figure 3.1b. For each of the four values of f_{AH} used in Figure 3.10a, we obtain an essentially linear dependence of the line tension on the interfacial tension. Indeed, each set of data is well fitted by a linear expression of the form $c_1\Sigma_{\alpha\beta} + c_0$ with $c_0 < 0$ and $c_1 < 0$, see inset of Figure 3.10b. Thus, these linear expressions remain negative for all positive values of the interfacial tension $\Sigma_{\alpha\beta}$, *i.e.*, for the whole physically meaningful range of this tension. Therefore, the linear fits of our data predict that the line tension is negative for all possible values of the interfacial tension $\Sigma_{\alpha\beta}$.

Interfacial tensions in nanoemulsions and aqueous two-phase systems.

In Figure 3.10b, the interfacial tension $\Sigma_{\alpha\beta}$ is given in units of $k_{\text{B}}T/d^2$ which is about 4 mN/m at room temperature, comparable to the interfacial tensions of oil-in-water droplets stabilized by surfactants in nanoemulsions [106, 107]. Droplets in aqueous two-phase systems, on the other hand, exhibit interfacial tensions $\Sigma_{\alpha\beta}$ that can vary over a fairly wide range. The highest interfacial tensions measured in aqueous PEG-dextran solutions, for example, were of the order of 1 mN/m whereas the lowest tensions were only about 0.2×10^{-3} mN/m, reflecting the vicinity of a critical demixing point [78, 47]. The linear extrapolation of our data as displayed in Figure 3.10b should provide

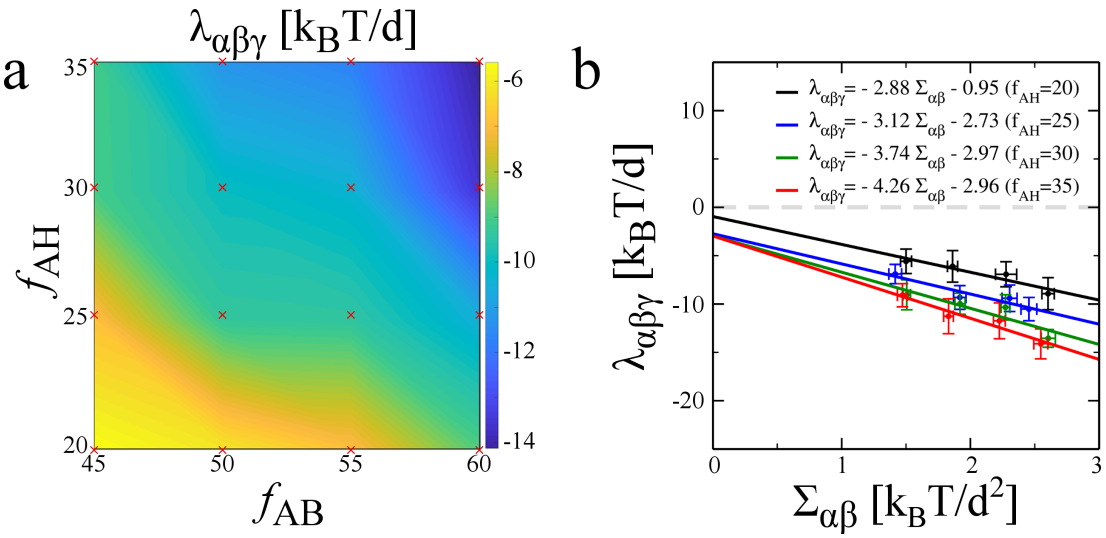

Figure 3.10. Line tension $\lambda_{\alpha\beta\gamma}$ as obtained for the enlarged parameter set DPD-2: (a) Contour plot for the line tension $\lambda_{\alpha\beta\gamma}$, in units of k_BT/d, as a function of the DPD force parameters f_{AB} and f_{AH}. The red crosses ($\times$) indicate the 16 parameter combinations that have been simulated. For the displayed range of parameters, the line tension $\lambda_{\alpha\beta\gamma}$ was always found to be negative and to have a value between $-5\,k_BT/d$ (yellow) and $-14\,k_BT/d$ (dark blue), see vertical bar with color code. All simulations were performed for the smaller droplet volume $V_{\alpha,1}$, lateral box size $L_\parallel = 140\,d$, and force parameter f_{BH} equal to f_{AH} as in Table 3.2; and (b) Line tension $\lambda_{\alpha\beta\gamma}$ as a function of interfacial tension $\Sigma_{\alpha\beta}$, which is directly determined by the force parameter f_{AB}, see Figure 3.1b, for different values of the force parameter f_{AH}. The four straight lines, corresponding to the linear expressions in the inset, provide good fits to the data for all four values of f_{AH}. Furthermore, linear extrapolation of the data to small values of $\Sigma_{\alpha\beta}$ suggests that the line tension remains negative even in the limit of small interfacial tensions. The basic tension scale k_BT/d^2 is about 4 mN/m.

reliable estimates for $\Sigma_{\alpha\beta} \simeq 1\,\mathrm{mN/m}$ but may become unreliable for $\Sigma_{\alpha\beta} \simeq 10^{-3}\,\mathrm{mN/m}$. Therefore, we predict that the line tension $\lambda_{\alpha\beta\gamma}$ is also negative for aqueous two-phase systems, provided one considers two-phase coexistence sufficiently far from the critical demixing point.

To obtain reliable predictions for interfacial tensions that are much smaller than $k_BT/d^2 \simeq 4\,\mathrm{mN/m}$, we would have to study much larger simulation boxes. Indeed, if we decreased the interfacial tension $\Sigma_{\alpha\beta}$ by decreasing the force parameter f_{AB}, the width of the $\alpha\beta$ interface would increase and the interface would become more and more fuzzy. More precisely, hyperscaling [108] implies that the interfacial width grows as $\sqrt{k_BT/\Sigma_{\alpha\beta}}$ as we approach a critical demixing point. Now, to determine the membrane-droplet geometry in a reliable manner, we need to consider droplet sizes that are large compared to this interfacial width. To study interfacial tensions $\Sigma_{\alpha\beta}$ that are

of the order of $0.1\,k_{\mathrm{B}}T/d^2$, for example, we would have to simulate droplets with linear dimensions that are increased by a factor $10^{1/2} \simeq 3.3$ or, equivalently, with volumes V_α that are increased by a factor $10^{3/2} \simeq 32$. In principle, such droplet sizes are accessible to our simulation approach but they would be computationally very expensive. An alternative approach based on energy minimization can be used to tackle this problem, which is computationally less expensive. We will use this approach in the next chapter to explore a wide range of parameters.

3.3.4 Engulfment of nanodroplets by asymmetric bilayers.

So far, we discussed the engulfment of nanodroplets by symmetric bilayers for which the lipid heads and chains experience the same interactions with the liquid-A and liquid-B beads. As a consequence, the α and the β phase have the same adhesion free energy per unit area. If the membrane were planar and the droplet sufficiently large so that we could ignore the line tension $\lambda_{\alpha\beta\gamma}$, the symmetry condition $f_{\mathrm{BH}} = f_{\mathrm{AH}}$ would lead to the intrinsic contact angle $\theta_\alpha^* = 90^\circ$. As shown in Figure 3.7b, the nanodroplets studied here exhibit contact angles in the range $80^\circ \lesssim \theta_\alpha^* \lesssim 100^\circ$, with deviations from 90° that arise from the line tension.

We will now describe the engulfment of nanodroplets by asymmetric bilayers that are obtained for force parameters $f_{\mathrm{BH}} \neq f_{\mathrm{AH}}$, corresponding to the parameter set DPD-3 in Table 3.3, and show that these systems lead to negative line tensions as well.

Affinity contrast and spontaneous curvature

The interactions of the lipid head (H) beads with the A and B water beads are described by the DPD force parameters f_{AH} and f_{BH}. If $f_{\mathrm{BH}} > f_{\mathrm{AH}}$, the H beads prefer to be in contact with the A beads; if $f_{\mathrm{AH}} > f_{\mathrm{BH}}$, the H beads prefer the B beads. The different interactions of the liquid-A and liquid-B beads to the lipid head beads H will be characterized by the affinity contrast

$$\Delta_{\mathrm{aff}} \equiv \frac{f_{\mathrm{BH}} - f_{\mathrm{AH}}}{f_{\mathrm{BH}}}\,. \tag{3.11}$$

For symmetric bilayers with $f_{\mathrm{BH}} = f_{\mathrm{AH}}$ as discussed above, the affinity contrast Δ_{aff} vanishes. Positive values of Δ_{aff} are obtained for $f_{\mathrm{BH}} > f_{\mathrm{AH}}$ which describe lipid head groups that prefer liquid-A beads over liquid-B beads. In contrast, negative values of Δ_{aff} correspond to $f_{\mathrm{AH}} > f_{\mathrm{BH}}$ and thus to a stronger affinity between the lipid head beads and the liquid-B beads. For planar membranes and sufficiently large droplets, affinity contrasts $\Delta_{\mathrm{aff}} > 0$ and $\Delta_{\mathrm{aff}} < 0$ would lead to contact angles $\theta_\alpha^* < 90^\circ$ and $\theta_\alpha^* > 90^\circ$, respectively.

To determine the spontaneous curvature m arising from a nonzero affinity contrast, we used the parameter set DPD-3 as given in Table 3.3. Apart from f_{AH}, all force

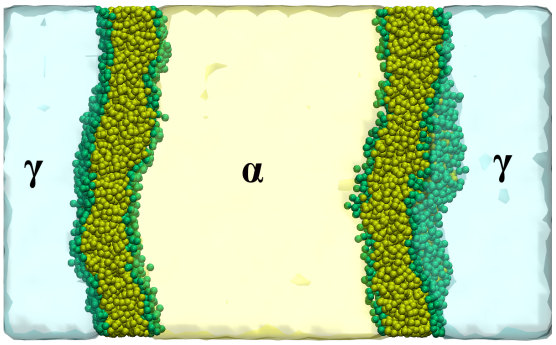

Figure 3.11. Simulation snapshot of the two planar bilayers used to measure the spontaneous curvature $m_{\alpha\gamma}$ of the $\alpha\gamma$ membrane segment. Both bilayers are in contact with the A-rich phase α (yellow) and the liquid phase γ which consists only of B beads (light blue) over the time scale of our simulations.

parameters have the same values as for the parameter set DPD-1. The force parameter f_{AH} between the A water beads and the lipid head beads was taken to be 22.5 and 27.5 $k_{\mathrm{B}}T/d$ in addition to the value $f_{\mathrm{AH}} = f_{\mathrm{BH}} = 25\,k_{\mathrm{B}}T/d$ for a symmetric bilayer. For fixed force parameter $f_{\mathrm{BH}} = 25\,k_{\mathrm{B}}T/d$, the three f_{AH}-values 22.5, 25, and 27.5 $k_{\mathrm{B}}T/d$ correspond to the affinity contrasts $\Delta_{\mathrm{aff}} = 0.1, 0$, and -0.1.

In order to determine the spontaneous curvature $m_{\alpha\gamma}$ associated with this bilayer asymmetry, we used the protocol developed in Ref. 14. We considered two planar bilayers spanning the simulation box, both exposed to the α and γ phases as in Figure 3.11, and calculated the stress profile $s_{\alpha\gamma}$ across both bilayers as shown in Figure 3.12a1-c1. We then divide the stress profile $s_{\alpha\gamma}$ up into two stress profiles, $s_{z<0}$ and $s_{z>0}$, across the two individual bilayers. The first moments of these individual stress profiles are related to the spontaneous curvature $m_{\alpha\gamma}$ via

$$\int_{-25d}^{0} \mathrm{d}z\, s_{z<0}(z)z = \int_{25d}^{0} \mathrm{d}z\, s_{z>0}(z)z = -2\kappa m_{\alpha\gamma} \tag{3.12}$$

from which we can deduce the spontaneous curvature $m_{\alpha\gamma}$ using the bending rigidity $\kappa = 12.6\ k_{\mathrm{B}}T$.

On the time scales of our simulations, the lipid bilayers are essentially impermeable to the liquid-A and liquid-B beads. This impermeability can be inferred from the density profiles of the liquid-A beads as shown in Figure 3.12a2-c2. This figure displays the bead densities of the α and γ phases which are now separated by two planar bilayers. The α phase consists primarily of liquid-A beads whereas the γ phase contains no such beads at the beginning of the simulations. If the bilayers were permeable to the A beads, these beads should eventually show up in the γ phase. However, we do not find

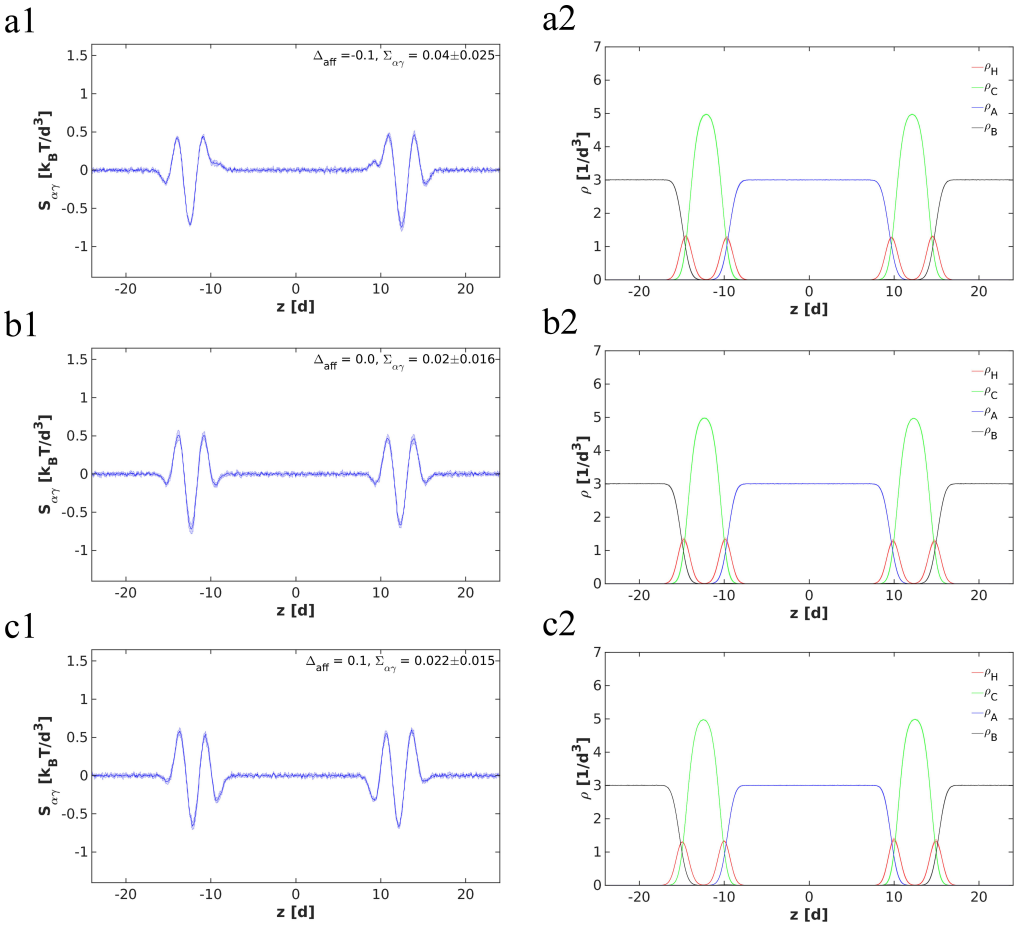

Figure 3.12. (a1 - c1) Stress profiles $S_{\alpha\gamma}$ and (a2 - c2) bead density profiles ρ as functions of the coordinate z perpendicular to the two bilayers in Figure 3.11. The profiles in (a1) and (a2) correspond to the affinity contrast $\Delta_{\mathrm{aff}} = -0.1$, the profiles in (b1) and (b2) to a symmetric membrane with $\Delta_{\mathrm{aff}} = 0$, and those in (c1) and (c2) to $\Delta_{\mathrm{aff}} = +0.1$. Using the relation in Eq. 3.12 with the bending rigidity $\kappa = 12.6\,k_{\mathrm{B}}T$, we obtain the spontaneous curvatures $m = 0.047/d, 0.003/d$, and $-0.044/d$ for $\Delta_{\mathrm{aff}} = 0.1, 0$, and -0.1, respectively.

any such beads even after 25 microseconds.

It is important to note that a nonzero affinity contrast $\Delta_{\mathrm{aff}} \neq 0$ has two important consequences. First, this contrast affects the overall adhesion energy of the membrane-droplet system. Indeed, for positive and negative affinity contrast Δ_{aff}, the system tries to maximize the contact area $A_{\alpha\gamma}$ and the non-contact area $A_{\beta\gamma}$, respectively, for fixed total number of lipid molecules and fixed droplet volume V_α. Second, a nonzero affinity contrast also implies that the $\alpha\gamma$ membrane segment acquires a spontaneous curvature

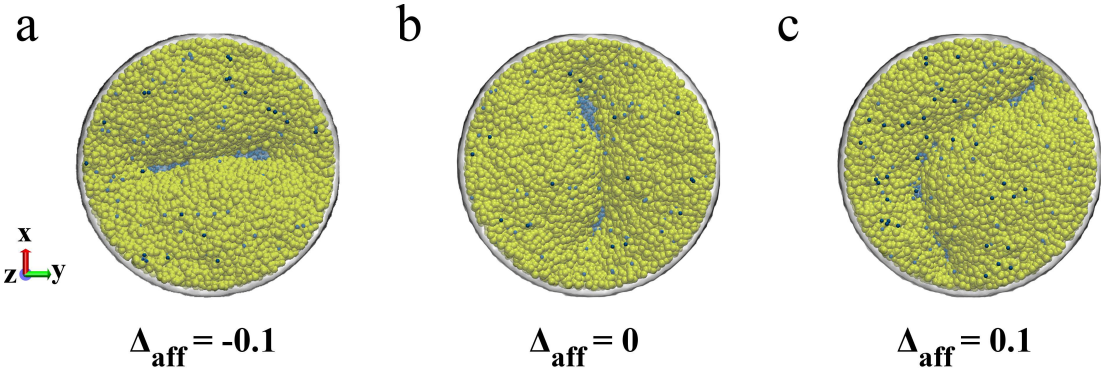

Figure 3.13. Contact lines and membrane necks of nanodroplets that adhere to the lower bilayer leaflets, which are now taken to be the outer leaflets: (a) Negative affinity contrast $\Delta_{\text{aff}} = -0.1$, corresponding to lipid heads that prefer the B liquid beads, see Eq. 3.11, and to an asymmetric bilayer with negative spontaneous curvature $m_{\alpha\gamma} = -1/(21.3\,d)$; (b) Vanishing affinity contrast $\Delta_{\text{aff}} = 0$, corresponding to a symmetric bilayer with $m_{\alpha\gamma} = 0$ as in Figure 3.3d; and (c) Positive affinity contrast $\Delta_{\text{aff}} = +0.1$, corresponding to lipid heads that prefer the A water beads and to an asymmetric bilayer with positive spontaneous curvature $m_{\alpha\gamma} = +1/(22.7\,\text{nm})$. In all cases, the membrane neck closes into a tight-lipped shape.

which can be positive or negative.

During pinocytosis and fluid-phase endocytosis of nanodroplets, the droplets originate from the exterior solution and adhere to the outer bilayer leaflets. To compare our results with pinocytic and endocytic processes, it will be convenient to use the convention that the spontaneous curvature $m_{\alpha\gamma}$ is *negative* if the $\alpha\gamma$ bilayer segment prefers to bulge towards the spectator phase γ, which then represents the interior solution. Likewise, the mean curvature of a membrane patch is also taken to be negative if this patch bulges towards the γ phase. This convention implies that the $\alpha\gamma$ membrane segment in Figure 3.2 has a negative mean curvature. As illustrated by Figures 3.11 and 3.12, the spontaneous curvature $m_{\alpha\gamma}$ of the $\alpha\gamma$ membrane segment can be determined by studying planar bilayers, with one leaflet exposed to the α phase and the other leaflet exposed to the γ phase. The latter method leads to positive and negative values of $m_{\alpha\gamma}$ for positive and negative affinity contrasts, respectively, because the membrane segment prefers to enlarge the area of the bilayer leaflet in contact with the A-rich phase α for $\Delta_{\text{aff}} > 0$ and the area of the other leaflet in contact with the A-poor phase γ for $\Delta_{\text{aff}} < 0$.

The affinity contrasts $\Delta_{\text{aff}} = +0.1$ and $\Delta_{\text{aff}} = -0.1$, for example, generate the spontaneous curvatures $m_{\alpha\gamma} = +0.047/d$ and $-0.044/d$ which are quite large. Indeed, for bead diameter $d \simeq 1\,\text{nm}$, we obtain $|m_{\alpha\gamma}| \simeq 1/(20\,\text{nm})$ in both cases. For such strongly

asymmetric bilayers, the force balance condition along the contact line, which is given by Eq. 3.9 for symmetric bilayers, becomes more complicated and involves additional terms that depend on the local membrane curvatures close to the contact line [47]. In fact, minimization of the total free energy as described by Eq. 3.1 leads to a discontinuity of the mean curvature across the contact line, which is, however, difficult to determine by simulations. Thus, instead of deducing the line tension $\lambda_{\alpha\beta\gamma}$ from the force balance equation for asymmetric bilayers, we directly studied the droplet engulfment by such bilayers. Using the same simulation protocol as in Figure 3.3, we observed elongated contact lines and tight-lipped membrane necks for all spontaneous curvatures within the range $-1/(20\,\mathrm{nm}) \leq m_{\alpha\gamma} \leq 1/(20\,\mathrm{nm})$ as illustrated in Figure 3.13. Therefore, we conclude that the line tension is negative for all of these $m_{\alpha\gamma}$-values.

3.3.5 Hysteresis of the nanodroplet engulfment process

Index of sphericity.

To study the hysteresis of the engulfment process, we used an order parameter called the index of sphericity. The index of sphericity is a measure of the variation of any two dimensional (2D) irregular shapes from a circle. The latter index is originally used to quantify the islet sphericity throughout the healthy human pancreas [109]. For a circle the ratio of circle perimeter $C_p = 2\pi R$ and it's diameter $C_d = 2R$ is a constant $\pi = C_p/C_d$. The same ratio can be found for any arbitrary irregular 2D shape as

$$I_\pi \equiv \frac{P_m}{d_m} \tag{3.13}$$

where P_m and d_m are the perimeter and the mean diameter of the irregular shape. The shape diameter can be calculated either form shape area $d_a = \sqrt{(4A_m/\pi)}$ or from shape perimeter $d_p = P_m/\pi$. The mean diameter is the arithmetic average of these two diameters $d_m = (d_a + d_p)/2$. The index of sphericity is given by:

$$I_s \equiv \frac{I_\pi}{\pi} \tag{3.14}$$

For a perfect circle, the index of sphericity remains constant $I_s = 1$; however, for shapes deviated from a circle, this index increases $I_s > 1$. The spontaneous symmetry breaking can be characterized using the index of sphericity.

Sphericity of the three phase contact line.

To characterize the breaking of symmetry of the three phase contact line, we first find the droplet beads which are located in the $\alpha\beta$ interface. Then, we define the perimeter of the contact line for the shape. This is done by Cartesian coordinates of droplet beads,

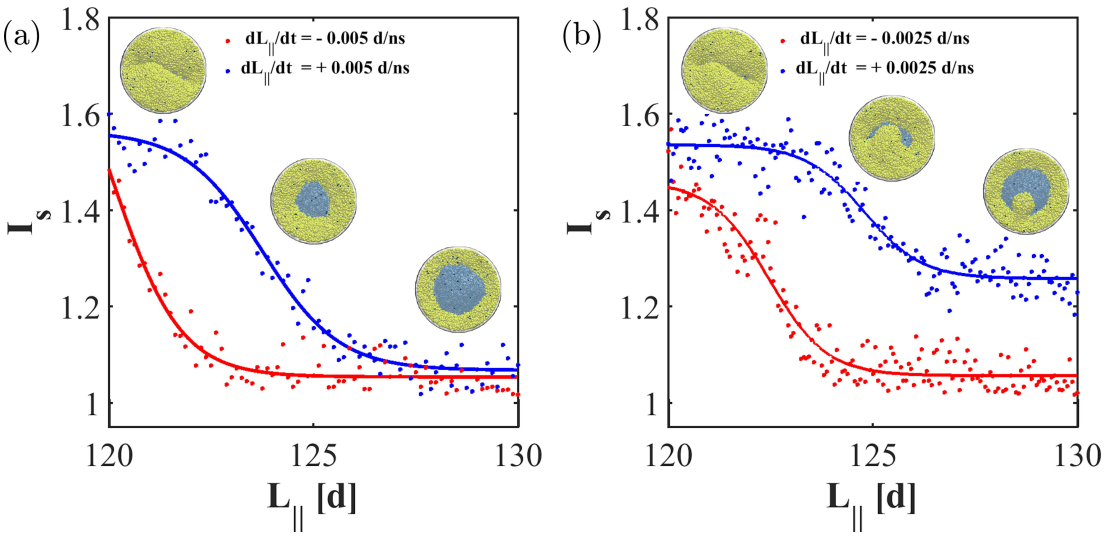

Figure 3.14. The index of sphericity I_s of the three-phase contact line in compression and expansion paths in a different rate. Symmetry breaking is characterized by increasing the I_s in: (a) high rate $|dL_{||}/dt|= 0.005$ ns/d and (b) low rate $|dL_{||}/dt|= 0.0025$ ns/d. The red and blue data points correspond to the compression path and expansion paths, respectively. The curves correspond to the fit of data over the logistic function. The snapshots in the inset are the bottom view in the expansion path for $L_{||} = 120$, $L_{||} = 125$ and $L_{||} = 130$, respectively. The shape change of the contact line in the compression path is similar to one shown in the first row of Figure 3.3.

where we find a closed boundary curve which envelopes all droplet beads. Finally, we calculate the perimeter and area of the boundary curve and subsequently, the I_s of the three-phase contact line.

Following this procedure, the index of sphericity is calculated for both compression and expansion paths in different rates. We studied two compression/expansion rates: (a) high rate $dL_{||}/dt = 0.005$ ns/d and (b) low rate $dL_{||}/dt = 0.0025$ ns/d. In Figure 3.14, the red and blue data points belong to compression and expansion paths, respectively. And the red and blue solid lines are the generalized logistic fit over the data points. As shown in Figure 3.14 for the high rate of compression/expansion $dL_{||}/dt = 0.005$ ns/d, a hysteresis loop exists. However, for the low rate $dL_{||}/dt = 0.0025$ ns/d, the hysteresis loop is not closed and the system does not have the same state at high tension. During the compression process, because of the reduction of lateral tension, the capillary force pushes the droplet inside the membrane to reduce the interfacial energy. For large box sizes, the index of sphericity remain close to circle (*i.e.*, $I_s \approx 1$) and around a critical box size $L_{||} \approx 122.5$ d, index of sphericity grows exponentially, which quantifies the symmetry breaking of three phase contact line. For the low compression rate, because the lipids have more time to diffuse and

remodel themselves in the three-phase zone, the index of sphericity is a sigmoid-like curve, see Figure 3.14b. On the other hand, during the expansion process, the lateral tension eventually compensates the capillary force and opens up the neck. At a high rate of expansion the index of sphericity decays to the initial circular geometry on a sigmoid-like curve and completes the hysteresis loop. But the same expansion process at a low rate leads to a different state, where a small nano-metric bud partially covers the $\alpha\beta$ interface, see inset in Figure 3.14b. Formation of such bud seems favorable because the reduced interfacial energy compensates for the increased bending energy caused by formation the nano-bud.

3.3.6 Increased stability of tight-lipped necks against membrane scission.

In order to cleave a membrane neck by membrane scission, one has to create two hydrophobic edges across the membrane segment that forms the neck. The corresponding free energy barrier is proportional to the combined length $L_{\rm ed}$ of the two edges. For a closed circular neck, the neck has a diameter that is comparable to the bilayer thickness $\ell_{\rm me} \simeq 5\,d$ which implies the neck perimeter $\pi\ell_{\rm me} \simeq 15.7\,d$ and the combined edge length $L_{\rm ed} = 2\pi\ell_{\rm me} \simeq 31\,d$. On the other hand, the tight-lipped neck displayed in Figure 3.3d has an increased perimeter of about $70\,d$ and cleavage of the latter neck leads to the combined edge length $L_{\rm ed} \simeq 140\,d$. Therefore, the free energy barrier for the tight-lipped neck is about $140/31 = 4.5$ times larger than the barrier for a circular neck.

In general, a neck can be cleaved by thermal fluctuations or by some active protein machinery. For thermally-activated scission, the scission rate depends exponentially on the free energy barrier. As a consequence, the increased barrier for cleavage of the tight-lipped neck leads to a strong reduction of thermally-activated scission. On the other hand, during protein-induced scission, proteins such as dynamin [93] form a constrictive ring around the neck whereas other proteins such as ESCRT [94, 110, 95] form an adhesive cone within the neck. In all models that have been used to describe these protein-mediated scission processes, the neck is taken to have a circular shape. In fact, according to these standard models for protein-induced scission, tight-lipped necks as observed in our simulations, see Figure 3.3d and Figure 3.13, can hardly be cleaved by any of these proteins. Therefore, a tight-lipped neck shape suppresses both thermally-activated and protein-induced scission which implies that such a neck may arrest the pinocytic process in the completely engulfed state.

Membrane necks arising from wetting by micrometer-sized droplets.

Finally, we discuss the implications of our results for the formation of closed membrane necks between micrometer-sized water-in-water droplets in contact with GUVs as observed in Ref. 111 and theoretically studied in Ref. 47. When the aqueous solution

within the vesicle undergoes phase separation, the coarsening of small droplets eventually leads to two coexisting droplets. The two droplets will be completely engulfed by the vesicle membrane provided the combined volume of these droplets is sufficiently small and/or the membrane area is sufficiently large [47]. Such a wetting morphology, corresponding to exocytic engulfment, implies a closed membrane neck that replaces the $\alpha\beta$ interface between the two droplets. Likewise, when the exterior aqueous solution undergoes phase separation, droplets of the minority phase can adhere to the outer leaflet of a vesicle membrane. Such an adhering droplet can also become completely engulfed by the membrane, provided the droplet volume is sufficiently small and/or the membrane area sufficiently large. The latter wetting morphology provides an example for endocytic engulfment and again involves a closed membrane neck that now replaces the $\alpha\beta$ interface between the droplet and the aqueous bulk phase.

If these closed membrane necks are assumed to be circular, they are governed by a stability condition that is completely analogous to the condition for two-domain vesicles, with the line tension of the domain boundary replaced by the contact line tension $\lambda_{\alpha\beta\gamma}$ [47]. However, in view of the simulation results presented here, the assumption of a circular neck does not apply in general. Indeed, it follows from Figure 3.10b that the line tension $\lambda_{\alpha\beta\gamma}$ is negative for interfacial tensions $\Sigma_{\alpha\beta}$ of the order of mN/m. The latter tension values apply, *e.g.*, to oil-in-water emulsions stabilized by surfactants [106, 107] as well as to aqueous two-phase systems sufficiently far from the critical demixing point [78]. Indeed, for the oil-in-water emulsion droplets studied in Ref. 106, the surfactant monolayers at the oil-water interface reduced the interfacial tension to about 2 mN/m. Therefore, when such an oil-in-water or a water-in-water droplet adheres to a lipid membrane, the corresponding contact line should have a negative line tension and should attain an elongated, tight-lipped shape when the membrane tension falls below a certain threshold value.

As we approach the critical demixing point of an aqueous two-phase system, the interfacial tension $\Sigma_{\alpha\beta}$ of water-in-water droplets becomes ultralow and eventually vanishes. [78] The linear extrapolation of our simulation data to small $\Sigma_{\alpha\beta}$-values is consistent with a negative line tension for the whole range of physically meaningful tensions $\Sigma_{\alpha\beta} > 0$, see the straight lines in Figure 3.10b, but we cannot exclude the possibility that the line tension depends on the interfacial tension in a nonlinear manner and becomes positive for sufficiently small $\Sigma_{\alpha\beta}$. For a positive line tension, the membrane neck will be axisymmetric and governed by the stability condition derived in Ref. 47.

4 Nanodroplets Interacting with Vesicles: Low Interfacial Tension Regime

4.1 Introduction

Wetting is a ubiquitous phenomenon in nature with implications ranging from daily-life examples to industrial applications [112]. Wetting is essential in understanding the physicochemical properties of interfaces. The classic example is the wetting of a rigid substrate, which can be described via Young's equation as a force balance along the contact line. The interaction of liquid droplets with flexible substrates such as lipid membranes as described in the previous chapter, is a generalized example of wetting, which represents a new and relatively unexplored research field. One example is provided by liquid-liquid phase separation of polymer solutions within lipid vesicles. Such aqueous two-phase systems enclosed in lipid vesicles lead to partial to complete wetting transitions, vesicle budding and membrane tubulation [113, 114].

Analogous wetting phenomena are also relevant in the context of cell biology. Liquid-liquid phase separation of proteins within the cytosol leads to biomolecular condensates (also known as membrane-less organelles), which behave like liquid droplets [115]. Such biomolecular condensates have a very low interfacial tensions in the range of $1 - 100$ μN/m [115, 116, 117], similar to interfacial tension of polymeric condensates [118]. Liquid-liquid phase separation leads to a wide range of functional consequences [63], which is not yet fully understood. biomolecular condensates can interact with distinct bimolecular entities inside cells. For instance, biomolecular condensates inside the cell nucleus have been shown to change the structure of the genome by forming a capillary bridge among chromatin fibers [119]. Furthermore, protein condensates are observed to generate mechanical forces on the membrane. The latter can take place either by invagination of the cell membrane [64] or engulfment of a liquid droplet in partial wetting regime [120]. Additionally, a very recent study suggests an active involvement of protein phase separation in the formation of cell-cell tight junctions [121]. On the other hand, likewise to the interaction of biomolecular condensates with membranes, a cluster of synaptic vesicles has been observed to form a liquid phase in aqueous solutions [122]. Such vesicle rich droplets, eventually interact with the cell membrane in synapses to deliver neurotransmitters. All these examples would be better understood in the context of membrane wetting phenomena.

A theory of membrane wetting has been developed based on the mechanical definition and using variational calculus [103, 29]. The obtained force balance is a generalized form of the Young's equation which couples the elasticity of the membrane to the capillary force arising from the liquid-liquid interface. The latter force balance links the mechanical segment tensions to the intrinsic contact angle of the droplet, the interfacial tension, the three-phase line tension as well as the spontaneous curvature of membrane [103, 29, 114]. In macrometer-scale the effect of line tension can be considered negligible [103, 114, 113, 29]. However, the DPD simulations described in the last chapter revealed that at the nanometer scale the line tension makes a considerable contribution to the total energy. The line tension is found to be negative in sign and leads to elongation of contact lines, which eventually forms a tight-lipped membrane necks. The system studied with DPD are characterized by hight interfacial tension, with magnitudes that correspond to those of oil-water interfaces (*i.e.,* $\propto mN/m$). These tension values are three orders of magnitude larger than those observed for macromolecular condensations. As explained above, the study of membrane wetting by nanodroplets with low interfacial tensions is computationally expensive. As we decrease this tension, the interface becomes fuzzier, and we would need to simulate larger droplets to obtain reliable results.

Therefore, to explore the low tension regime, we use an alternative approach, which is computationally less expensive. Here we study liquid nanodroplets with low interfacial tension interacting with elastic vesicle membranes with an energy minimization approach. We systematically explore the effect of a wide range of parameters, namely, interfacial tension, bending rigidity, line tension, and spontaneous curvature on membrane wetting phenomena. The effect of material parameters and the droplet-induced spontaneous curvature are studied on the morphological transformation of the vesicle and the wetting energy. Finally, we determine the boundary between symmetric and asymmetric contact line geometries within the three-dimensional parameter space obtained for vanishing spontaneous curvature.

4.2 Methods

4.2.1 Continuum model for membrane wetting.

The main energetic contributions of the vesicle-nanodroplet system include bending energy of the vesicle, interfacial energy of the nano-droplet and the line energy of the three phase contact line, as described before in the literature [114, 123]. Thus, the total energy of the wetted state, E_W, of the vesicle-nanodroplet reads

$$E_W = \sum_{i=\alpha,\beta} \int dA_{i\gamma}[2\kappa_{i\gamma}(M-m_{i\gamma})^2] + \Sigma_{\alpha\beta}\, A_{\alpha\beta} + \lambda_{\alpha\beta\gamma} L_{\alpha\beta\gamma} + \Sigma_{ves} A_{ves} - P_{\gamma\beta} V_{ves} - P_{\alpha\beta} V_{\alpha} \tag{4.1}$$

The subscripts α, β and γ refer to the three distinct liquid phases. The nanodroplet is named α phase, the enclosed liquid phase inside vesicle is defined by γ phase and the external liquid phase is specified by β phase. The first term on the right-hand side shows the total elastic energies of the two membrane segments with areas $A_{\alpha\gamma}$ and $A_{\beta\gamma}$, where the vesicle is in contact with the α and β phase, respectively.

These membrane segments are in principle characterized by the two bending rigidities $\kappa_{\alpha\gamma}$ and $\kappa_{\beta\gamma}$ and the two spontaneous curvatures $m_{\alpha\gamma}$ and $m_{\beta\gamma}$. M is the local mean curvature of the membrane. The second and third terms in Eq. 4.1 are the interfacial energy of the nanodroplet and the line energy of the vesicle-nanodroplet contact line, respectively. Here $\Sigma_{\alpha\beta}$ and $\lambda_{\alpha\beta\gamma}$ are the interfacial tension of $\alpha\beta$ interface and the three-phase $\alpha\beta\gamma$ contact line tension, respectively. Finally, the last three terms in Eq. 4.1, employ three different Lagrange multipliers: Σ_{ves}, $P_{\alpha\beta}$ and $P_{\gamma\beta}$, to keep the vesicle's area and volume as well as nanodroplet's volume constant. The area of the nanodroplet is not conserved. To reduce the number of parameters, the bending rigidity is taken to be the same in both segment $\kappa = \kappa_{\alpha\gamma} = \kappa_{\beta\gamma}$, and we assume that the spontaneous curvature in the membrane $\beta\gamma$ segment is negligible $m_{\beta\gamma} = 0$, unless it is specified. Furthermore, it should be mentioned that in this study, we exclude the effect of nanodroplet adhesion, by considering the special case of zero adhesion strength $|W| = 0$.

4.2.2 Energy minimization.

There are three different methodologies for studying the vesicle-nanodroplet system: (i) molecular simulations as described in chapter three, (ii) solving the shape equations derived from the first variation of the parametrized energy functional (based on parametrized form of Eq. 4.1, see *Appendix* two) or (iii) a finite element calculation of a discretized form of the continuum model (Eq. 4.1) using a triangulated mesh. The first approach is computationally expensive, as discussed before. The second approach, without employing axisymmetry, leads to second-order non-linear partial differential

equations (PDE), and there is no general solution even with numerical algorithms (results are not shown). However, the variational calculus for axisymmetric shapes lead to the solvable ordinary differential equation (ODE), that has been used to study membrane-nanoparticle interaction [32] and membrane-droplet system [103, 29]. The third approach, however, can be generally employed for minimizing the energy of an arbitrary shape interacting with elastic membranes [124, 125]. Here, we used the energy minimization scheme introduced in chapter two to investigate the wetting of vesicles by nanodroplets.

The contact line is parametrized on an elliptic curve $(x/R_a)^2 + (y/R_b)^2 = 1$, where the R_a and R_b are the major and minor axes. These two axes are treated as two independent optimization parameters in the energy minimization. Initially, the two axes are set to be equal $R_a = R_b$ to avoid any initial condition bias. The contact line can then either remain in a circular geometry or can deviate from it to attain an elliptic shape as a result of the energy minimization. Such contact line parametrization can be considered as the first perturbation mode. This can be extended to higher-order perturbations by different parametrization of the contact line.

4.2.3 Wetting energy.

The wetting energy is defined based on the energy difference between wetted state E_W from Eq. 4.1 and non-wetted state E_{NW} as:

$$\begin{aligned}\Delta E &= E_W - E_{NW} \\ &= E_W - \left(\int dA_{\beta\gamma}[2\kappa_{\beta\gamma}(M)^2] + \Sigma_{\alpha\beta}\ A_{\alpha\beta} + \Sigma_{ves}A_{ves} - P_{\gamma\beta}V_{ves} - P_{\alpha\beta}V_{\alpha} \right)\end{aligned} \tag{4.2}$$

here the interfacial area $A_{\alpha\beta}$ is the area of nanodroplet in spherical geometry $A_{\alpha\beta} = 4\pi\ \sqrt[2/3]{3V_\alpha/4\pi}$ where the droplet is not in contact with the vesicle. The bending energy of the non-wetted state is calculated for the vesicle that is not in contact with the α droplet and thus completely wetted by the β phase. The wetting energy is scaled by the bending energy of sphere $8\pi\kappa$ to $\overline{\Delta E} = \Delta E/8\pi\kappa$

4.2.4 Unit transformations.

The results of the energy minimization depend only on the relation of the morphology of the vesicle-nanodroplet system to the relative length and energy scale. Therefore, we will work in the reduced units that scale length by the nanodroplet radius R_α and the energy by the membrane bending rigidity κ. Thus, we define the reduced interfacial tension $\bar{\Sigma}_{\alpha\beta} = \Sigma_{\alpha\beta}(R_\alpha^2/\kappa)$, line tension $\bar{\lambda}_{\alpha\beta\gamma} = \lambda_{\alpha\beta\gamma}(R_\alpha/\kappa)$ and spontaneous curvature $\bar{m} = m_{\alpha\gamma}R_\alpha$. If we take the nanodroplet volume to be two orders of magnitude smaller than the vesicle volume, for a nanodroplet volume $V_\alpha = 0.1\ d^3$, this correspond to

$R_\alpha \approx 0.288\ d$ and $R_{ves} \approx 1.337\ d$. On the other hand, if the size scaled up based on the nanodroplet size of 100 nm as the characteristic length scale(*i.e.,* $1\ d \cong 347.293$ nm), then the vesicle size will be $R_{ves} \approx 464.16$ nm which is in the range of large unilamellar vesicles (LUV). To define the state of wetting, we define the fraction of contact area of the droplet as $A^* = A_{\alpha\gamma}/(A_{\alpha\gamma} + A_{\alpha\beta})$. The actual volume of the vesicle is $V_0 = 10\ d^3$, which can only attain spherical geometry with the prescribed area of $A_0 = 4\pi\ \sqrt[2/3]{3V_0/4\pi}$. The reduced volume of the vesicle is defined by $v = V/V_0$ as a control parameter. The membrane area A_0 and volume V is conserved during energy minimization.

4.2.5 Consideration of capillary waves.

In the presence of the thermally excited capillary waves [126], the liquid interface roughness ξ is proportional to $\propto \sqrt{k_BT/\Sigma_{\alpha\beta}}$. This proportionality indicates that for very small nanodroplets with ultra-low interfacial tension, the roughness of the interface becomes comparable to the nanodroplet size. Capillary waves hinder the formation of any arbitrary small droplet sizes. Thus, one can conclude that for fixed droplet size, we cannot observe nanodroplets with arbitrary low interfacial tension. Therefore, here we took $R_\alpha > 6\xi$, or equivalently $\Sigma_{\alpha\beta} > 36(k_BT/R_\alpha^2)$, as the lower threshold for the interfacial tension of a constant nanodroplet size. This implies that for a nanodroplet with radius $R_\alpha = 100\ nm$, the lower threshold of interfacial tension should be $\Sigma_{\alpha\beta} = 15\ \mu N/m$, which is in the order of macromolecular condensates interfacial tensions.

4.2.6 Physical scale of material parameters.

We limit the parameter space to the values corresponding to lipid-vesicles and biomolecular condensates. Lipid membranes have bending rigidities in the range of κ =5-100 k_BT. And, bimolecular condensates have interfacial tensions in the range $\Sigma_{\alpha\beta}$ =1-100 $\mu N/m$. Based on theoretical estimates and experimental observations, the magnitude of the line tension can vary over two orders of magnitude $\lambda_{\alpha\beta\gamma}$ =1-100 pN with both positive and negative signs [127, 54]. In addition, as discussed in the last chapter, the line tension interdependently linked to the interfacial tension. Here, we use the results of the DPD simulations to find the range of physically meaningful values of the line tension in the low tension regime. The special case of $\lambda_{\alpha\beta\gamma} = 0\ pN$ is considered as a control system. We study different combinations of material parameters with interfacial tensions ranging from $\Sigma_{\alpha\beta}$ =15 to 85 $\mu N/m$, bending rigidities of $\kappa = 12.6,\ 20,\ 30$ and $50\ k_BT$ and line tensions $\lambda_{\alpha\beta\gamma} = -5$ to $0\ pN$

Table 4.1. Nanoroplet size R_α and membrane bending rigidity κ used to calculate the reduced interfacial tension and line tension. Nanodroplet radius is estimated from the droplet volume of two spherical caps from density profile, the first number in parentheses. The bending rigidity is calculated from area compressibility modulus, the second number in parentheses. The length and energy units are d and k_BT, respectively.

f_{AB} \ f_{AH}	20	25	30	35
45	(9.87, 11)	(9.87, 12.6)	(9.94, 14)	(9.84, 15.3)
50	(10.07, 11)	(10.14, 12.6)	(10.39, 14)	(9.95, 15.3)
55	(10.08, 11)	(10.50, 12.6)	(10.59, 14)	(10.38, 15.3)
60	(10.16, 11)	(10.50, 12.6)	(10.38, 14)	(10.42, 15.3)

4.2.7 Dependence of line tension on the interfacial tension.

In order to find the dependence of line tension to interfacial tension in the reduced unit, we analyze the nanodroplet size R_α and the bending rigidity κ of the membrane for a range of DPD parameters, as listed in Table 4.1. The interaction parameters f_{AH} and f_{AB}, modulate the membrane bending rigidity and the nanodroplet interfacial tension, respectively (more details can be found in chapter three). The bending rigidity is calculated from the area compressibility modulus [13]. In addition, the nanodroplet radius is estimated from density profile results and using the spherical cap approximations. The results are tabulated in Table 4.1

4.3 Results and Discussion

4.3.1 Nanodroplet induces morphological transformations on vesicle.

We studied the wetting of a vesicle by nanodroplets. The size of nanodroplet is taken to be $R_\alpha = 100\ nm$ as a characteristic length scale for unit transformations, which implies the vesicle size in the range of LUVs. The enclosed liquid phase by vesicle is called γ, and the third exterior phase is named β phase. In all of the simulations, the nanodroplet is in contact with the membrane from the outside.

Initially, we minimized the energy of nanodroplet and the vesicle in the non-wetted state. As expected for liquid droplets in equilibrium, the nanodroplet attains spherical geometry. The vesicle morphology, however, transforms to prolate shape in the reduced volume of $v = 0.7 - 0.9$, Figure 4.1a. Such a shape transformation is known for vesicles with reduced volume at zero spontaneous curvature [8]. It has been shown that the prolate branch of solutions has lower energy compared to oblate branch [8], in this range of reduced volume (*i.e.,* $v = 0.7 - 0.9$). Next, we started our numerical minimization when the nanodroplet and vesicle initially have a small contact area. Once the vesicle is in contact with the nanodroplet, in response to the capillary force arising from $\alpha\beta$ interface, nanodroplet deforms the membrane and partially wets the vesicle surface. The Lagrange multiplier Σ_{ves} is coupled to vesicle's area A_{ves} and act as mechanical tension [21]. The bending energy counteracts the capillary force and prevents any arbitrary and strong vesicle deformation in presence of the vesicle's are and volume constraint. We observed that wetting of vesicles by nanodroplets induces a morphological shape transformation. We found three distinct classes of morphologies, namely, discocyte, stomatocytes I, and stomatocytes II, Figure 4.1a. The intermediate morphology of stomatocytes II is distinguished from stomatocytes I based on the negative curvature in the south pole of the vesicle surface and based on the fraction of contact area $A^* > 0.6$ from discocyte morphology, respectively.

Four different morphology diagrams are illustrated in Figure 4.1b-e for different combinations of material parameters. Two top panels correspond to control state of zero line tension and for bending rigidity of $\kappa = 20\ k_BT$ and $\kappa = 50\ k_BT$, where the wetting state is solely driven by interfacial and bending energies, Figure 4.1b,c. Two lower panels correspond to the states with constant negative line tension $\lambda_{\alpha\beta\gamma} = -2\ pN$ for bending rigidity of $\kappa = 20\ k_BT$ and $\kappa = 50\ k_BT$. In the latter cases, both interfacial energy and line energy together with vesicle bending energy contribute to the wetting of vesicle, Figure 4.1d,e. The color of enclosed square on shape morphology Figure 4.1a has a one-to-one correspondence to the color on morphology diagrams, Figure 4.1b-e. Our result demonstrates that all material parameters, bending rigidity κ, interfacial tension $\Sigma_{\alpha\beta}$ and line tension $\lambda_{\alpha\beta\gamma}$ can modulate the final morphology of the minimized shape. This suggests that a local perturbation of a vesicle by a nanodroplet can propagate over the whole membrane geometry and cause a global shape transformation.

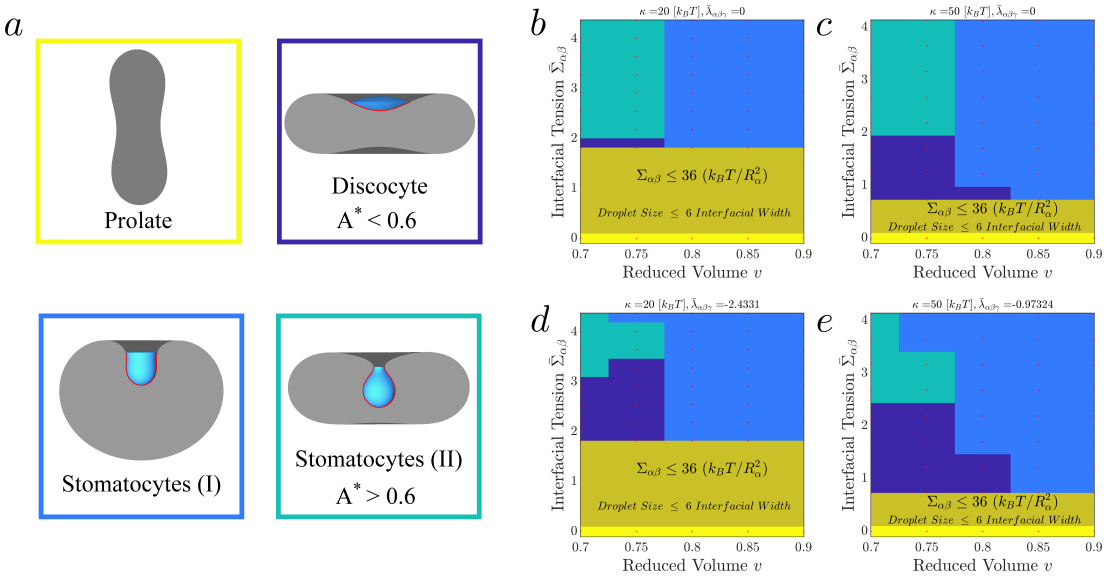

Figure 4.1. The nanodroplet-vesicle shape morphology and morphology diagram. (a) The shapes illustrate the morphology of vesicles interacting with nanodroplets. The vesicle surface is shown in gray and the nanodroplet in blue. All shapes are shown in half with a cutaway on the longitudinal plane. The $\alpha\gamma$ segment of the membrane is highlighted with a thick red curve. In the absence of nanodroplet, we observe a prolate shape, for the reduced volume of the vesicle in the range of $v = 0.7 - 0.9$. However, in the same reduced volume, nanodroplets induce shape transformation from prolate to discocyte and stomatocytes I. There is an intermediate shape between these known morphologies, that we call stomatocytes II. The fraction of the contact area $A^* > 0.6$ and the negative curvature of the membrane in the south pole of the vesicle are used to distinguish the shape of stomatocytes II from stomatocytes I. The morphology diagram for different parameter combinations are shown (b) $\kappa = 20\ k_BT$ and $\bar{\lambda}_{\alpha\beta\gamma} = 0$, (c) $\kappa = 50\ k_BT$ and $\bar{\lambda}_{\alpha\beta\gamma} = 0$, (d) $\kappa = 20\ k_BT$ and $\bar{\lambda}_{\alpha\beta\gamma} = -2.4331$ and finally (e) $\kappa = 50\ k_BT$ and $\bar{\lambda}_{\alpha\beta\gamma} = -0.97324$. The spontaneous curvature is taken to be zero $\bar{m} = 0$ for all cases. The color of enclosed square on shape morphology (a) corresponds to the color in the morphology diagrams (b)-(e). The olive-colored region highlights the interfacial tension regime, which is hindered due to thermally excited capillary waves. Red stars show the scanned data points. The triangulation-based nearest-neighbor interpolation is used to construct the non-scanned regions on the morphology diagram.

Similar shape transformations have been reported for the system of nanoparticles and vesicles [125]. The wetting induced shape transformation is the result of global energy minimization, where the cost of vesicle deformation is paid off by gaining both interfacial energy and line energy.

4.3.2 Wetting energy.

We define the wetting energy as the energy difference between the non-wetted state and the wetted state. When the vesicle is completely wetted by the exterior β phase, it is recognized as the non-wetted state. We use the nanodroplet fraction of contact area A^* as the order parameter to study the wetting. In non-wetted state $A^* = 0$, while $A^* = 1$ indicates the state where the nanodroplet phase α is completely engulfed by vesicle. The partially wetted state is defined when $0 < A^* < 1$. Both axisymmetric and non-axisymmetric solutions are found in the partially wetted sate. The example of non-axisymmetric solutions are shown in Figure 4.2a,b. Since we do not exactly know how the line tension varies as a function of interfacial tension and bending rigidity, we will consider two scenarios: i) first, we study the case where the line tension is constant and is not dependent on the interfacial tension and the bending rigidity; ii) second, we study the wetting for a vesicle with low bending rigidity $\kappa = 12.6\ k_BT$, where the line tension varies linearly based on the DPD simulation results, see chapter three.

(I) Constant line tension: First, we studied the case where the line tension is negative and constant $\lambda_{\alpha\beta\gamma} = -2\ pN$, and there is no dependence on interfacial tension and bending rigidity. We took the special case of zero line tension $\lambda_{\alpha\beta\gamma} = 0\ pN$ as a control case. The result shows that the bending energy of the vesicle always increases as a result of wetting, see Figure 4.2c (green data points). However, the system gains energy by reducing the interfacial energy (red data points) and gaining line energy (blue data points), see Figure 4.2c. In contrary to nanoparticles, the area of nanodroplet is not fixed and can vary freely. As a consequence, the interfacial energy gain as a function of A^* is not a simple quadratic decay. The negative line energy as a function of the fraction of contact area has a positive slope, which indicates that the engulfment of nanodroplet reduces the three-phase contact line. The same arguments holds for the bending energy and interfacial energy of the control case of zero line tension, except the line energy remains zero. Figure 4.2d compares the total wetting energy for different bending rigidities. The total negative energy suggests that the wetting of LUVs with nanodroplets should occur spontaneously. The low contact area fraction (*i.e.,* $\approx A^* < 0.4$) belongs to unphysical nanodroplets because of thermally excited capillary waves. Thus, the low contact areas region is hindered in nanodroplet-LUV scale. This region is colored by red in Figure. 4.2c-e. In an intermediate region of contact area (*i.e.,* $A^* \approx 0.4 - 0.5$) we observed elongated contact lines, where the nanodroplet spreads on the membrane and take the shape of doubly connected ellipsoidal caps. In this regime, only non-axisymmetric solutions exist, highlighted with dark gray in Figure 4.2c,d. The latter symmetry breaking is the effect of negative values of the line tension in elongation of the three-phase contact line. In higher contact areas, however, $A^* \approx 0.5 - 0.6$ both axisymmetric and non-axisymmetric solutions are observed, as highlighted with a light gray color, see Figure 4.2c,d. The data points on the white region are all found to be axisymmetric.

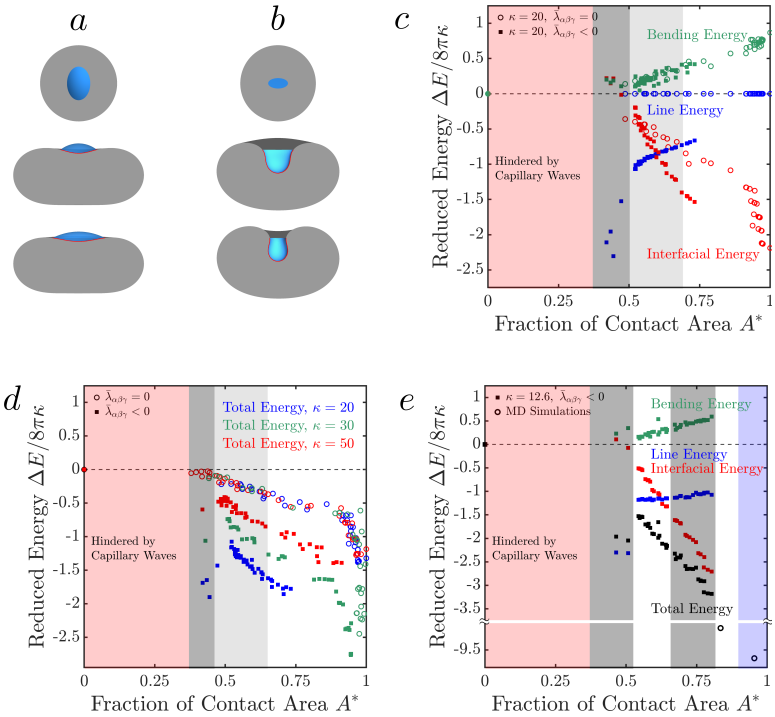

Figure 4.2. The morphology of vesicle-nanodroplet system with non-axisymmetric contact line geometry in (a) low contact area $A^* < 0.5$ and (b) high contact area $A^* > 0.7$. The panels in the top row of (a) and (b) show the top views of the elliptic contact line. The second and third rows show two vertical cutaway on longitudinal planes. The red region corresponds to the lower interfacial tensions ($\Sigma_{\alpha\beta} < 15\ \mu N/m$), which are hindered because of thermally excited capillary waves. The dark gray region highlights the regime where the symmetry of the surface and the three-phase contact line is broken. In the light gray, both axisymmetric and non-axisymmetric solutions coexist. The blue region is where the broken symmetry is observed for DPD simulations from chapter three. And finally, in the white region only the axisymmetric solutions are observed. (c) Three main energetic contributions, namely, line energy (blue), interfacial energy (red), and the bending energy (green), are shown for $\kappa = 20\ k_BT$ and $\lambda_{\alpha\beta\gamma} = -2\ pN$. (d) The wetting energy of the vesicle for three different bending rigidities $\kappa = 20\ k_BT$ (blue), $\kappa = 30\ k_BT$ (green) and $\kappa = 50\ k_BT$ (red) with constant line tension $\lambda_{\alpha\beta\gamma} = -2\ pN$. The solid squares and the open circles correspond to line tension of $\lambda_{\alpha\beta\gamma} = -2\ pN$ and $\lambda_{\alpha\beta\gamma} = 0\ pN$ as a control system. (e) Three main energetic contributions and the total wetting energy of vesicle for constant bending rigidity of $\kappa = 12.6\ k_BT$ with varying line tension (closed squares). The black open circles corresponds to the data from DPD simulations with lateral box size of $L_{||} = 125\ d$ and $L_{||} = 120\ d$.

(II) Line tension with linear dependence on the interfacial tension: Then, we studied vesicle where the bending rigidity is constant $\kappa = 12.6\ k_BT$ and the line

tension is linearly dependent to interfacial tension $\bar{\Sigma}_{\alpha\beta} = -3.21\bar{\lambda}_{\alpha\beta\gamma} - 6.63$ as found for $f_{AH} = 25\ k_BT$, see chapter three for more details on the linear extrapolation of the results of DPD simulations. For these parameters, we find two distinct regimes of contact area, where the non-axisymmetric solutions exist, dark gray in Figure 4.2e. An intermediate regime exists, where only axisymmetric solutions are available, marked as the white region in Figure 4.2e. This observation is consistence with the results of DPD simulations, where the elongated contact line is only observed for large contact area $A^* > 0.9$, the open circles in Figure 4.2e. The blue region corresponds to the non-axisymmetric contact line observed for DPD simulations.

4.3.3 Effect of spontaneous curvature.

Nanodroplets of biomolecular condensates can induce spontaneous curvature because they can create an asymmetric aqueous environment in the $\alpha\gamma$ segment of the membrane. Albeit, the sign and magnitude of the induced spontaneous curvature by membrane-less organelles are unknown. A negative spontaneous curvature should facilitate engulfment of the nanodroplet, as it acts in the same direction as the capillary force. However, when the spontaneous curvature is positive, the system could gain bending energy by outward bulging of the $\alpha\gamma$ segment of the membrane, while the capillary force pushes the same segment inward. In both cases, negative line tension acts along the contact line to increase the length of the three-phase contact line. The competition between bending energy, interfacial energy as well as line energy determines whether an in-bud or out-bud morphology is favorable. Here we have studied two different cases with: i) varying interfacial tension and constant line tension $\lambda_{\alpha\beta\gamma} = -2\ pN$ and ii) varying line tension and constant interfacial tension $\Sigma_{\alpha\beta} = 55\ \mu N/m$. In both cases, the bending rigidity $\kappa = 50\ k_BT$, and the reduced volume of the vesicle $v = 0.75$ are kept unchanged.

The resulting morphologies are categorized into four different classes, based on the curvature of the $\alpha\gamma$ segment of the membrane and the symmetry of the three-phase contact line, as depicted in Figure 4.3a. Negative and positive curvature of $\alpha\gamma$ segment, determine two main classes of in-bud and out-bud morphologies, respectively. The symmetry of the contact line, then defines two sub-classes called symmetric (when the contact line is axisymmetric) and asymmetric (when the contact line is non-axisymmetric). For constant line tension, a large region of symmetric in-buds (dark blue) is found, see Figure 4.3b. In this region, the interfacial energy dominates over the line and bending energies. For large interfacial tension and moderate positive spontaneous curvature values, symmetric out-bud (green) is observed, which indicates that bending energy is dominated. However, for large positive spontaneous curvature values, the morphology transforms to asymmetric out-bud (yellow). This shows the dominant contribution of the line energy in the asymmetric out-bud region (yellow). Overall the same behavior

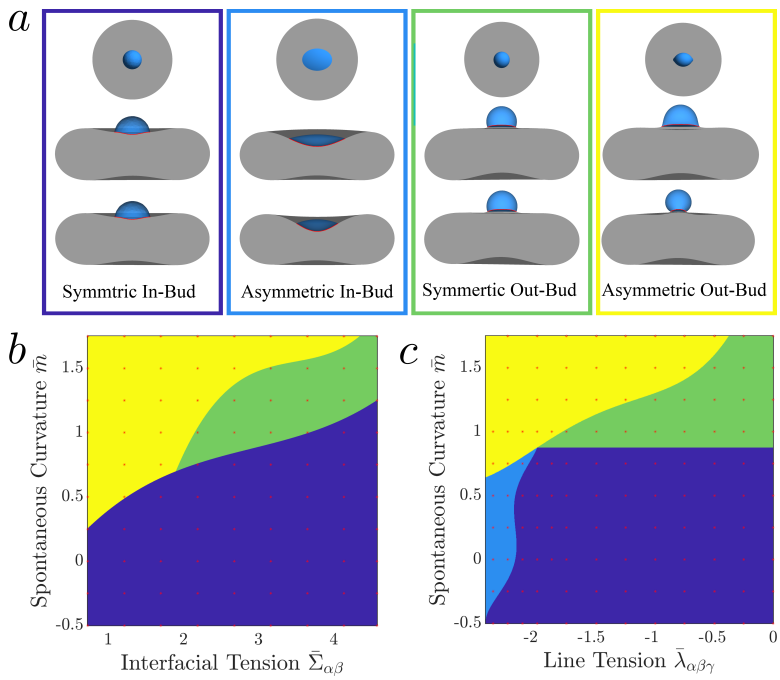

Figure 4.3. The nanodroplet-vesicle shape morphologies and morphology diagrams in the presence of spontaneous curvature. Here, morphology refers to the curvature of $\alpha\gamma$ segment and the symmetry of the three-phase contact line. (a) The shapes illustrate the four distinct morphologies: symmetric in-buds (first panel) and asymmetric in-buds (second panel) where the $\alpha\gamma$ segment bulges toward the interior γ phase, or symmetric out-buds (third panel) and asymmetric out-buds (fourth panel) where the $\alpha\gamma$ segment bulges toward the exterior α phase. The morphology diagrams of different parameter combinations are shown in (b) for a constant line tension of $\lambda_{\alpha\beta\gamma} = -2\ pN$ and (c) for constant interfacial tension of $\Sigma_{\alpha\beta} = 55\ \mu N/m$, for vesicles interacting with nanodroplets. The color definitions are the same as in Figure 4.1 and correspond to the morphologies in the box of the same color in (a). All calculations are done for constant bending rigidity $\kappa = 50\ k_BT$ and vesicle reduced volume $v = 0.75$. The scanned data points are shown by red stars. Boundaries between morphologies are estimated from these points using polynomials of order 3 to 5.

is found for the constant interfacial tension, as shown in Figure 4.3c. For negative line tensions with rather a large magnitude, asymmetric in-buds (light blue) observed, Figure 4.3c, which suggests that the line energy contribution is dominant. Note that the asymmetric in-buds are found for $\lambda_{\alpha\beta\gamma} < -2\ pN$, as used to generate Figure 4.3c. A regime of asymmetric in-buds may well appear in a similar morphology diagram at lower line tensions.

4.3.4 Symmetry hyper-surface for vanishing spontaneous curvature.

As elaborated in the previous sections, three main energetic contributions determine whether the contact line is axisymmetric or non-axisymmetric. Thus the boundary between symmetric and asymmetric solutions can be determined by a surface in three-dimensional parameter space, namely line tension, interfacial tension, and bending rigidity. We aim to construct such a dividing surface by exploring the boundary between symmetric and asymmetric contact line geometries, similar to the examples shown in Figure 4.3b,c, but for vanishing spontaneous curvature. We first keep the bending rigidity constant and scan isoline curves where line tension and interfacial tension determine the symmetry.

All results are shown in cyan data points in Figure 4.4a. These data points are in the boundary of symmetric and asymmetric solutions. The data points with zero line tension on the right-hand side of the y-axis, are the minimum interfacial tension allowed by thermally excited capillary waves. All data points appear in the low tension regime, highlighted by blue color in Figure 4.4a. The extrapolation of DPD results from high tension regime (red color in Figure 4.4a) predicts the existence of such a region in low tension regime.

Similar isoline for constant line tensions is obtained in the two-dimensional parameter space of interfacial tension and bending rigidity, as shown in Figure 4.4b. The geometry of the contact line is axisymmetric above iso-lines and non-axisymmetric below the iso-lines. By combining data in Figure 4.4a and b, in three dimensional parameter space the symmetry hyper-surface is constructed. Here, we use a two-variable polynomial of third-degree to fit the discrete data points, as shown by red stars in Figure 4.4c, to a surface by:

$$\bar{\Sigma}^{fit}_{\alpha\beta}(\bar{\lambda}_{\alpha\beta\gamma},\kappa) = \bar{\lambda}^{i}_{\alpha\beta\gamma} P_{ij} \kappa^{j} = \begin{pmatrix} \bar{\lambda}^{0}_{\alpha\beta\gamma} & \bar{\lambda}^{1}_{\alpha\beta\gamma} & \bar{\lambda}^{2}_{\alpha\beta\gamma} & \bar{\lambda}^{3}_{\alpha\beta\gamma} \end{pmatrix} \begin{pmatrix} P_{00} & P_{01} & P_{02} & P_{03} \\ P_{10} & P_{11} & P_{12} & P_{13} \\ P_{20} & P_{21} & P_{22} & P_{23} \\ P_{30} & P_{31} & P_{32} & P_{33} \end{pmatrix} \begin{pmatrix} \kappa^{0} \\ \kappa^{1} \\ \kappa^{2} \\ \kappa^{3} \end{pmatrix} \tag{4.3}$$

where the fit parameters read:

$$P_{ij} = \begin{pmatrix} 3.438 & -0.09775 & 0.0007452 & 2.615e-06 \\ 0.5401 & -0.01833 & 0.0002434 & 0 \\ -0.2254 & 0.00774 & 0 & 0 \\ -0.08202 & 0 & 0 & 0 \end{pmatrix} \tag{4.4}$$

$\bar{\Sigma}^{fit}_{\alpha\beta}(\bar{\lambda}_{\alpha\beta\gamma},\kappa)$ is called symmetry hyper-surface and is shown in Figure 4.4c. This symmetry hyper-surface has a simple interpretation: as long as we are above the surface in parameter space, the geometry of the contact line should remain axisymmetric, but in the parameter space below the surface, the symmetry of the contact line should transform to non-axisymmetric geometries. All calculations are done for constant reduced volume $v = 0.75$.

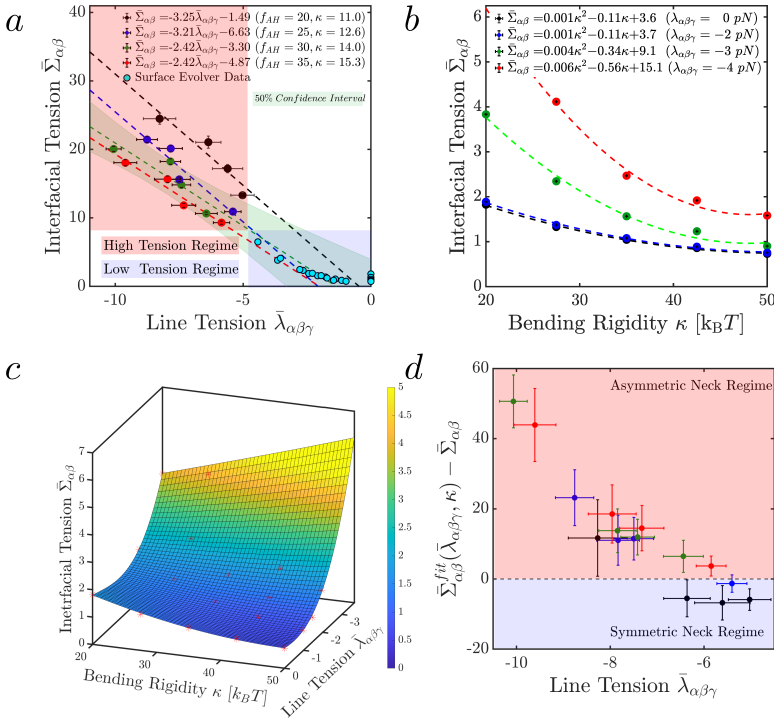

Figure 4.4. (a) The linear extrapolation of DPD simulations results to the low tensions regime. Each line corresponds to different DPD force parameters which leads to slightly different bending rigidities, $\kappa = 11\ k_BT$ (black line), $\kappa = 12.6\ k_BT$ (blue line), $\kappa = 14\ k_BT$ (green line) and $\kappa = 15.3\ k_BT$ (red line). The red and blue regions highlit the high tension and low tension regimes, respectively. The green region shows the 50% confidence limit of the linear fit for the green data points. The cyan data points in low tension regime show the boundary between axisymmetric and non-axisymmetric solutions in energy minimization for a range of bending rigidities κ =20, 30, 40 and 50 k_BT. (b) The symmetry isolines for constant line tensions. The solution of nanodroplet-vesicle shapes are axisymmetric above the isolines and non-axisymmetric below the isolines. (c) Symmetry hyper-surface. Red stars show the scanned data points. These are the same as the cyan data points in panel (a) and all data points in panel (b). The surface is a polynomial (degree of three with two variables) fit $\bar{\Sigma}^{fit}_{\alpha\beta}(\bar{\lambda}_{\alpha\beta\gamma},\kappa)$ over the red data points. The color of the surface is the reduced interfacial tension $\bar{\Sigma}_{\alpha\beta}$. The solution of nanodroplet-vesicle shapes are axisymmetric above the surface and non-axisymmetric below the surface. (d) The unitless tension difference obtained from symmetry hyper-surface $\bar{\Sigma}^{fit}_{\alpha\beta}(\bar{\lambda}_{\alpha\beta\gamma},\kappa)$ and from the stress profile $\bar{\Sigma}_{\alpha\beta}$ in DPD simulations. The colors of data points are the same as in panel (a) and Figure 3.10b of chapter three. The red and blue regions, illustrate the asymmetric and symmetric regimes of the three-phase contact line, respectively.

As a consistency check, we test the predictability of the surface for outcomes of DPD simulations, see chapter three. If $\bar{\Sigma}^{fit}_{\alpha\beta}(\bar{\lambda}_{\alpha\beta\gamma},\kappa) - \bar{\Sigma}^{DPD}_{\alpha\beta} > 0$ then the DPD system

is located below the symmetry surface and the contact line is non-axisymmetric, and vice-versa. The results for a wide range of DPD parameters are shown in Figure 4.4d. As expected, for the majority of data points, the contact line geometry is predicted to be non-axisymmetric. However, for a few data points, an axisymmetric contact line is predicted. We performed further DPD simulations for these data points to investigate the symmetry of the contact line. The results shows that the symmetry hyper-surface perform very well in prediction of contact line symmetry breaking.

5 Assembly and Polymorphism of Nanovesicles

5.1 Introduction

Biomembranes are based on fluid bilayers of lipid molecules. The lipids are assembled into two leaflets, with the polar head groups of the lipids pointing towards the surrounding aqueous solutions and the hydrocarbon chains forming the hydrophobic core of the bilayer. The fluidity allows these membranes to respond to changes in their aqueous environment by fast remodelling of both their molecular composition and their shape. To avoid a hydrophobic edge, a single bilayer, which has a thickness of about 4 nm, closes up into a unilamellar vesicle, thereby separating an interior aqueous compartment from the exterior bulk solution. The size of these vesicles varies over a wide range, from a few tens of nanometers to hundreds of micrometers. This size range applies both to synthetic lipid vesicles prepared from a small number of lipid components and to cellular vesicles that involve a complex assortment of lipids and membrane proteins.

For lipid vesicles, a variety of methods has been developed by which one can prepare nanovesicles with diameters within the range of 50 to 300 nm. These methods include extrusion of lipid dispersions through filters with a certain pore size [128, 129] and, more recently, microfluidic mixing [130]. In vivo, even smaller nanovesicles are frequently observed such as synaptic vesicles with a diameter that varies between 20 and 50 nm nm [131, 132] as well as exosomes, which represent small extracellular vesicles with a diameter between 25 and 100 nm [133, 134, 135]. In recent years, exosomes and somewhat larger extracellular vesicles have been intensely studied as possible biomarkers for diseases and as targeted drug delivery systems [136, 137, 138, 139].

The shapes of nanovesicles with a diameter below a few hundred nanometers, corresponding to the resolution limit of conventional optical microscopy, can be studied by variants of electron microscopy (EM) such as negative staining EM and cryo-EM [140]. Using such imaging methods, one often observes spherical nanovesicles but a variety of nonspherical shapes has also been reported [141, 142, 143, 144, 145]. All EM methods are, however, restricted to a single snapshot of each nanovesicle and cannot monitor the time-dependent behavior of individual vesicles.

In contrast, computer simulations with molecular resolution can reveal the nanoscale dynamics of lipids and bilayer membranes as has been demonstrated, e.g., for the self-

assembly of lipid bilayers in aqueous solution [23, 146] or for the closure of bilayer patches into nanovesicles [147]. In this chapter, we show that such simulations can also be used to monitor the shape transformations of individual nanovesicles, using the following simulation protocol. We first assembled spherical vesicles by placing $N_{\rm il}$ and $N_{\rm ol}$ lipid molecules onto two spherical shells, thereby constructing inner and outer leaflets, respectively. The assembled vesicles enclosed a certain number $N_{\rm W}^{\rm isp}$ of water beads which defined the initial vesicle volume. For a given volume, we studied spherical vesicles which contained the same total number of lipids, $N_{\rm lip}$, but slightly different lipid numbers $N_{\rm ol}$ and $N_{\rm il} = N_{\rm lip} - N_{\rm ol}$ within the inner and outer bilayer leaflets. Four such vesicles are displayed in the leftmost column of Figure 5.1a - d, corresponding to volume parameter $v = 1$.

When we reduced the volume of the spherical vesicles, thereby mimicking the experimental procedure of osmotic deflation, the vesicles underwent very different shape transformations as shown in Figure 5.1a - d. In fact, redistributing only 2% of the lipids between the two leaflets of the spherical vesicle led to a very different sequence of vesicle shapes. In this way, we directly demonstrate that molecular simulations provide a powerful method to explore the polymorphism of nanovesicles in a systematic manner by adjusting only three control parameters: the vesicle volume, the total number $N_{\rm lip}$ of lipids assembled in the bilayer as well as the lipid number $N_{\rm ol}$ or $N_{\rm il} = N_{\rm lip} - N_{\rm ol}$ within one of the two leaflets. This simulation method also enables us to monitor the time-dependent behavior of individual vesicles. Therefore, our simulations provide unprecedented insights into the shape transformations of nanovesicles, which have not been accessible, so far, to experimental studies.

The vesicle volume and the lipid numbers represent *global* control parameters that can be directly adjusted in the simulations but do not reveal the physical mechanisms and driving forces that lead to the different shape transformations. These mechanisms and forces can be understood in terms of *local* quantities, as provided by the mechanical tensions within the two leaflets and the associated dilations of the molecular areas per lipid. In order to measure these leaflet tensions and area dilations, it is necessary to determine, for a given vesicle volume and total lipid number $N_{\rm lip}$, the unique lipid number $N_{\rm ol}^*$ for which both leaflet tensions vanish simultaneously within the spherical bilayer.

The shapes and shape transformations obtained here by molecular simulations of nanovesicles are qualitatively similar to those seen by optical microscopy of giant vesicles, which have a typical size of tens of μm and are, thus, three orders of magnitude larger than the nanovesicles in Figure 5.1. Our understanding of giant vesicle behavior is based on the theoretical framework of curvature elasticity [148, 25, 27, 149]. Within this framework, one key parameter that determines the vesicle shape is the local spontaneous curvature. As shown at the end of this chapter, the latter curvature can be related to the first moment of the spherically symmetric stress profile across the

molecular bilayers.

Current chapter is organized as follows. We first describe the morphological responses of spherical nanovesicles to volume reduction and define the three parameters that determine the initial assembly of the spherical vesicle. We then compute the lipid areas in the two leaflets which are typically different, with the outer leaflet being more densely packed than the inner leaflet. Subsequently, we consider the stretching and compression of the bilayer leaflets and compute the individual leaflet tensions. We show that rather small changes in the vesicle volume reduce the overall bilayer tension by two orders of magnitude, thereby producing tensionless bilayers. These tensionless bilayers are characterized by nonzero leaflet tensions that change under the redistribution of the lipids between the two leaflets. We then identify the unique lipid distribution for which both leaflets of the vesicle membrane experience the same leaflet tension. When we reduce the volume of this vesicle, we obtain tensionless leaflets which define our unique reference state. At the end, we summarize our results and provide a short outlook on possible extensions and related systems to be addressed in future studies.

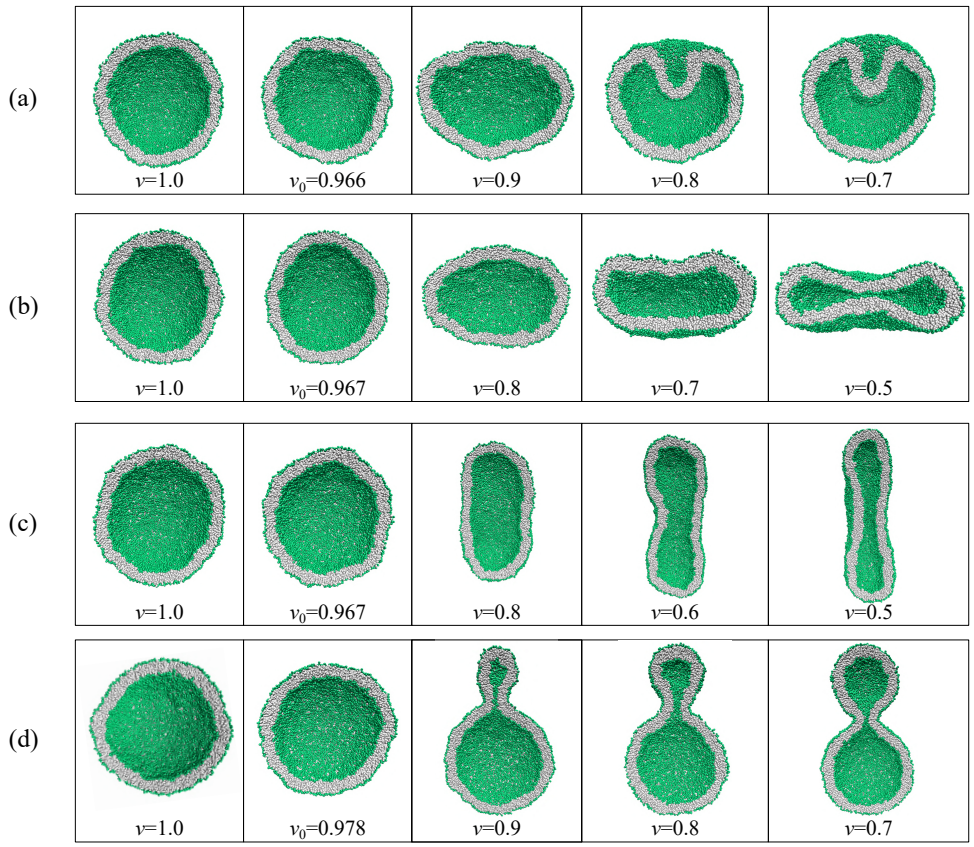

Figure 5.1. Distinct shape transformations of spherical nanovesciles in response to volume reduction: Each panel a - d displays a series of shapes that an individual vesicle attains when we decrease its volume as measured by the volume parameter v, see Eq. 5.2. In all four cases, we started from a spherical vesicle (leftmost snapshot, $v = 1$) that enclosed the same volume of water. In addition, the lipid bilayer of these vesicles contained the same total lipid number $N_{\mathrm{lip}} = 10\,100$. However, the spherical vesicles differed slightly in the lipid numbers N_{ol} and $N_{\mathrm{il}} = N_{\mathrm{lip}} - N_{\mathrm{ol}}$, within their inner and outer leaflets. We first reduced the vesicle volume by a few percent to $v = v_0 < 1$ to decrease the bilayer tension by two orders of magnitude and to obtain a spherical vesicle with a tensionless bilayer. A further reduction of volume then led to (a) a stomatocyte for $N_{\mathrm{ol}} = 5700$; (b) a discocyte for $N_{\mathrm{ol}} = 5900$; (c) a tube-like prolate for $N_{\mathrm{ol}} = 6100$; as well as (d) a dumbbell with a closed membrane neck for $N_{\mathrm{ol}} = 6300$. Thus, redistributing only 200 lipids, i.e., less than 2% of the total lipid number N_{lip}, from the inner to the outer leaflets leads to qualitatively different shape transformations. As shown below, this polymorphism can be understood in terms of different mechanical tensions within the inner and outer leaflets of the spherical vesicles. The simulations to generate this figure is done by Rikhia Ghosh.

5.2 Methods

5.2.1 Dissipative particle dynamics

We used dissipative particle dynamics (DPD) which is a coarse-grained molecular dynamics simulation technique, well suited to study nanoscale processes related to bilayer membranes. Our system is built up from three types of beads that represent small molecular groups corresponding to water (W) beads, lipid chain (C) beads, and lipid head (H) beads. The lipid molecules have a head group consisting of three H beads and two hydrocarbon chains, each of which consists of six C beads [14, 19]. The numerical values of the force parameters f_{ij} are displayed in Table 5.1. The technical details about the DPD simulations can be found in chapter two.

Table 5.1. Set of force parameters f_{ij} in units of $k_{\mathrm{B}}T/d$. The bead indices i and j can be H, C, or W. H denotes the lipid head beads, C the lipid chain beads and W the water beads.

f_{ij}	H	C	W
H	30	50	30
C	50	10	75
W	30	75	25

All DPD simulations were performed in the NVT ensemble. The bulk water density was chosen to have the standard DPD value $\rho_{\mathrm{W}} = 3/d^3$ to reproduce the compressibility of bulk water at room temperature $T = 298$ K. The nanovesicles were studied in a cubic simulation box with volume $(80\,d)^3$ and periodic boundary conditions. The initial spherical nanovesicles were assembled on two nested spherical shells with diameter $45\,d$ and $50\,d$, using the packmol software package [150]. We placed N_{il} and N_{ol} lipids within the inner and outer shell and varied these lipid numbers in such a way that the total number $N = N_{\mathrm{il}} + N_{\mathrm{ol}}$ was kept constant, see Figure 5.1. For the initial spherical nanovesicles, the interior and exterior aqueous compartment contained 90 400 and 1 350 000 water beads, respectively. For each vesicle volume, the simulation run time was at least 50 microseconds.

5.2.2 Curvature elastic membrane model

We used the energy minimization scheme introduced in chapter two to investigate the polymorphism of nanovesicles predicted by the curvature-elastic membrane model. The elastic membrane surface is modeled using a triangulated mesh. The deformation energy is calculated using the Helfrich Hamiltonian, the total energy, E, of the vesicle

reads:

$$E = \int dA[2\kappa(M-m)^2] + \Sigma A_{ves} - PV_{ves} \tag{5.1}$$

Elastic properties of the membrane characterize the elastic energy of membrane via bending rigidity κ, the spontaneous curvature m and the local mean curvature of membrane M. The last two terms in Eq. 5.1, employ two different Lagrange multipliers, namely, Σ and P, to keep the vesicle's area A_{ves} and volume V_{ves} constant. However, the last two terms do not contribute to the total energy of the system. To reduce the computational cost, we used four-fold rotationally symmetric vesicle shapes and calculate the membrane bending energies for several reduced volumes and spontaneous curvatures. We assume that spontaneous curvature is constant and independent of deflation state of the vesicle.

5.3 Results and Discussion

5.3.1 Initial assembly of spherical vesicles.

We consider closed nanovesicles formed by lipid bilayers in water and study their behavior by Dissipative Particle Dynamics. We use a coarse-grained model for the lipid and water molecules [14, 19], which are built up from beads with diameter $d \simeq 0.8\,\mathrm{nm}$. We first assembled spherical vesicles by placing lipid molecules onto two spherical shells corresponding to the two leaflets of the bilayer membranes. The size of these vesicles was primarily determined by the vesicle volume, *i.e.,* by the number of water beads enclosed by the inner leaflet of the membrane. This number was chosen in such a way that the head group layers of the inner and outer leaflets had a diameter of about $45\,d$ and $50\,d$, respectively. For a given volume, we placed N_{il} and N_{ol} lipids onto the inner and outer leaflets, respectively, and considered different vesicles with the same total lipid number $N_{\mathrm{lip}} = N_{\mathrm{il}} + N_{\mathrm{ol}}$. Thus, for given volume and constant total lipid number, we are left with a single assembly parameter, which we took to be the lipid number N_{ol} in the outer leaflet. The spherical vesicles assembled in this manner were found to be stable for the range of N_{ol}-values shown in Figure 5.1.

5.3.2 Vesicle volume and volume parameter.

Experimentally, the volume of a vesicle can be changed by osmotic deflation and inflation. In the simulations, we varied the vesicle volume by changing the number N_{W} of water beads enclosed by the inner leaflet of the vesicle membrane. This number determines the volume *via* $V \equiv N_{\mathrm{W}}\, d^3/3$ where the factor $1/3$ reflects the bulk water density $\rho_{\mathrm{W}} = 3/d^3$. To monitor the volume changes, we used the volume parameter v defined by

$$v \equiv \frac{N_{\mathrm{W}}}{N_{\mathrm{W}}^{\mathrm{isp}}} \tag{5.2}$$

where $N_{\mathrm{W}}^{\mathrm{isp}}$ is the number of water beads enclosed by the initial spherical vesicle. Thus, the initial vesicle is characterized by $v = 1$ and any volume reduction with $N_{\mathrm{W}} < N_{\mathrm{W}}^{\mathrm{isp}}$ leads to $v < 1$. Monitoring volume changes via the parameter v is rather convenient here because we can directly change the number N_{W} of water beads within the vesicle and thus compute the value of v without the necessity to determine any membrane surface, see Figure 5.1.

5.3.3 Diverse morphological responses to volume changes.

As we reduce the vesicle volume of a spherical nanovesicle, the vesicle can undergo a surprising variety of morphological transformations. In Figure 5.1, we display the morphological responses of four spherical vesicles that have the same volume, corresponding

to $N_{\mathrm{W}}^{\mathrm{isp}} = 90\,400$ water beads, and are bounded by bilayer membranes that contain the same overall number of lipids as given by $N_{\mathrm{lip}} = 10\,100$. However, the two leaflets of the bilayers contain somewhat different lipid numbers, N_{ol} and N_{il}, within their outer and inner leaflets.

The diverse responses of the spherical nanovesicles in Figure 5.1 can be understood by examining how the different lipid numbers N_{il} and N_{ol} change the areas per lipid in the two leaflets of the bilayers. Indeed, when we place, for fixed vesicle volume, somewhat different numbers of lipids on the inner and outer leaflets of the spherical bilayers, we obtain different molecular areas, a_{il} and a_{ol}, for the lipids in the two bilayer leaflets.

5.3.4 Lipid areas in the two leaflets.

To determine the two lipid areas a_{il} and a_{ol} in a quantitative manner, we introduce spherical coordinates with the radial coordinate r and place the center of each spherical vesicle at $r = 0$. Because of the spherical symmetry, all density profiles depend only on this radial coordinate. We then define the midsurface of each spherical nanovesicle via the corresponding density profile $\rho_{\mathrm{C}}(r)$ of the chain (C) beads that form the hydrophobic core of the vesicle membranes. As shown in Figure 5.2a, this density profile exhibits a pronounced maximum at $r = R_{\mathrm{C}} = 22\,d$ by which we define the radius R_{mid} of the bilayer's midsurface, as in previous studies [14, 19] of planar bilayers. In contrast to the neutral surface of a bilayer [151, 152], the midsurface considered here is not defined in terms of elastic deformations or stresses but represents the molecular interface between the two bilayer leaflets. Furthermore, as shown further below and summarized in Table 5.2, three alternative, physically meaningful definitions of this midsurface lead to essentially the same numerical value for the midsurface radius R_{mid}. In addition to the density profiles ρ_{C}, we consider the density profiles $\rho_{\mathrm{H}}(r)$ of the head (H) beads, see Figure 5.2b, which exhibit two peaks at $r = R_{\mathrm{iH}}$ for the inner head group layer and at $r = R_{\mathrm{oH}}$ for the outer one. The midsurface of the inner leaflet is then defined by $R_{\mathrm{il}} \equiv \frac{1}{2}(R_{\mathrm{iH}} + R_{\mathrm{C}})$ and the midsurface of the outer leaflet by $R_{\mathrm{ol}} \equiv \frac{1}{2}(R_{\mathrm{C}} + R_{\mathrm{oH}})$. Finally, the lipid areas in the inner and outer leaflets are obtained by dividing the areas of the leaflets' midsurfaces by the corresponding lipid numbers, *i.e.,* by

$$a_{\mathrm{il}} = \frac{4\pi R_{\mathrm{il}}^2}{N_{\mathrm{il}}} \quad \text{and} \quad a_{\mathrm{ol}} = \frac{4\pi R_{\mathrm{ol}}^2}{N_{\mathrm{ol}}}\,. \tag{5.3}$$

The numerical values of these lipid areas as obtained for the four spherical vesicles with $v = 1$ in Figure 5.1 are given in Table 5.3. In all cases, the lipid area a_{il} within the inner leaflet is larger than the lipid area a_{ol} within the outer leaflet which implies that the outer leaflets are more densely packed.

Table 5.2. Midsurface radius $R_{\mathrm{mid}} = R_{\mathrm{C}}$, R_{H}, and R_{COM} as obtained from CHAIN, HEAD, and COM for the five spherical vesicles in Figures 5.1 and 5.4a with $v = v_0$ and tensionless bilayers.

Figure	5.1a	5.1b	5.1c	5.1d	5.4a
R_{C} [d]	22.1	22.1	22.0	22.0	22.1
R_{H} [d]	22.1	21.9	21.9	21.7	21.9
R_{COM} [d]	22.3	22.3	22.3	22.4	22.3

5.3.5 Stretching and compression of the bilayer leaflets.

Intuitively, we expect that the inner and the outer leaflet of the vesicle membrane have an optimal area per lipid, a_{il}^0 and a_{ol}^0, corresponding to their natural packing densities and their elastically relaxed states. Let us assume, for a moment, that we knew these optimal lipid areas. If we now stretched the outer leaflet of the spherical bilayer, we would increase the lipid area to $a_{\mathrm{ol}} > a_{\mathrm{ol}}^0$. On the other hand, if we compressed the outer leaflet, we would reduce this lipid area to $a_{\mathrm{ol}} < a_{\mathrm{ol}}^0$. The same behavior applies to the inner leaflet of the spherical bilayer: $a_{\mathrm{il}} < a_{\mathrm{il}}^0$ corresponds to compression and $a_{\mathrm{il}} > a_{\mathrm{il}}^0$ corresponds to stretching of the inner leaflet.

To determine the optimal lipid areas a_{il}^0 and a_{ol}^0, we need to know the mechanical tensions, Σ_{il} and Σ_{ol}, that act within the inner and outer leaflets. These leaflet tensions were computed as follows. Because of the spherical symmetry, the local stress or pressure tensor has the general form [22]

$$\mathbf{P} = P_{\mathrm{N}}(r)\,\mathbf{e_r} \otimes \mathbf{e_r} + P_{\mathrm{T}}(r)\,[\mathbf{e}_\theta \otimes \mathbf{e}_\theta + \mathbf{e}_\phi \otimes \mathbf{e}_\phi] \tag{5.4}$$

with the normal component $P_{\mathrm{N}}(r)$ and the tangential component $P_{\mathrm{T}}(r)$ where $\mathbf{e_r}$, $\mathbf{e}_\theta$, and $\mathbf{e}_\phi$ are orthogonal unit vectors and the symbol $\otimes$ represents the dyadic product. The numerical values of $P_{\mathrm{N}}(r)$ and $P_{\mathrm{T}}(r)$ as well as the stress profile $s(r) \equiv P_{\mathrm{N}}(r) - P_{\mathrm{T}}(r)$ were calculated as described previously [153]. As shown in Figure 5.2c, the stress profiles $s(r)$ change strongly as we reshuffle lipids from one leaflet to the other, thereby changing the lipid numbers N_{ol} and $N_{\mathrm{il}} = N_{\mathrm{lip}} - N_{\mathrm{ol}}$. The bilayer tension Σ was obtained by

$$\Sigma = \int_0^\infty \mathrm{d}r\ [P_{\mathrm{N}}(r) - P_{\mathrm{T}}(r)] = \int_0^\infty \mathrm{d}r\, s(r)\,, \tag{5.5}$$

in close analogy to the interfacial tension [22] of a spherical liquid droplet, and the leaflet tensions Σ_{il} and Σ_{ol} by

$$\Sigma_{\mathrm{il}} = \int_0^{R_{\mathrm{C}}} \mathrm{d}r\, s(r) \quad \text{and} \quad \Sigma_{\mathrm{ol}} = \int_{R_{\mathrm{C}}}^\infty \mathrm{d}r\, s(r)\,. \tag{5.6}$$

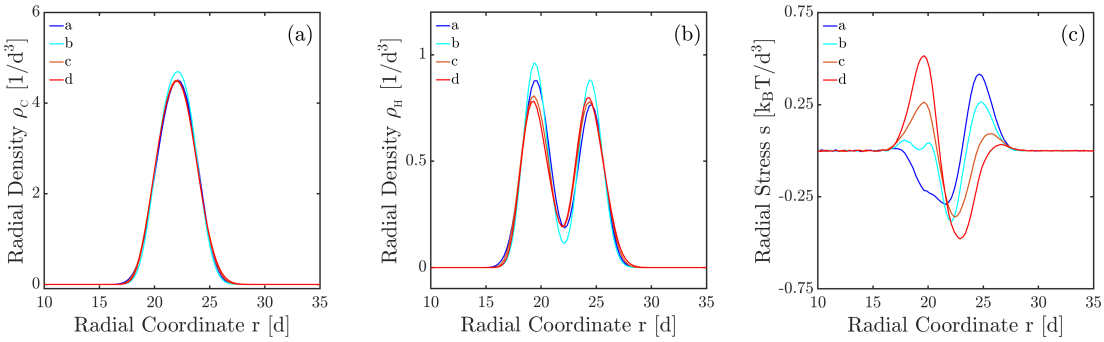

Figure 5.2. Density and stress profiles as functions of the radial coordinate r for four spherical vesicles with tensionless bilayers corresponding to $v = v_0 < 1$ in Figure 5.1: (a) Density profiles $\rho_C(r)$ of the chain (C) beads forming the hydrophobic core of the bilayers. These profiles exhibit a pronounced maximum that is located at the radial coordinate $r = 22\,d$ and is used to define the midsurface of the bilayers; (b) Density profiles $\rho_H(r)$ of the head (H) beads that form the two head group layers of the bilayers. These density profiles have two peaks which we take to define the locations of the head group layers; and (c) Stress profiles $s(r)$ with maxima and minima corresponding to stretched and compressed leaflets, respectively.

In this way, we obtained the numerical values of the bilayer tension $\Sigma = \Sigma_{il} + \Sigma_{ol}$ and the leaflet tensions for the four spherical vesicles in Figure 5.1, as given in Table 5.3 for $v = 1$.

5.3.6 Leaflet tensions of spherical bilayers.

The first column in Table 5.3 corresponds to the spherical vesicle displayed in Figure 5.1a with $N_{il} = 4400$, $N_{ol} = 5700$, and $N_W^{isp} = 90\,400$. In this case, the tension Σ_{ol} of the outer leaflet is positive whereas the tension Σ_{il} of the inner leaflet is negative. Thus, the outer leaflet is stretched whereas the inner leaflet is compressed. Furthermore, the overall bilayer tension Σ is quite substantial with a value of about $0.34\,k_BT/d^2$. The first column of Table 5.4 provides the tension values obtained after a slight reduction of the vesicle volume from $N_W^{isp} = 90\,400$ to $N_W = 87\,350$ water beads. For the latter volume, the slightly deflated vesicle attained a state for which the overall bilayer tension Σ was reduced by two orders of magnitude, from $\Sigma \simeq 0.34\,k_BT/d^2$ to $\Sigma = 0.05\,k_BT/d^2$, corresponding to a tensionless bilayer. However, the two leaflet tensions $\Sigma_{il} \simeq -0.82$ and $\Sigma_{ol} \simeq 0.87$ were still comparable with the leaflet tensions of the initial vesicle that enclosed $N_W^{isp} = 90\,400$ water beads, corresponding to an inner leaflet that is compressed and an outer leaflet that is stretched. Therefore, when we further reduce the volume of the vesicle, the inner leaflet would like to expand whereas the outer leaflet would like to shrink, thereby reducing the area difference $\Delta A = A_{ol} - A_{il}$ between the outer and the inner leaflet. As a consequence, the spherical vesicle in

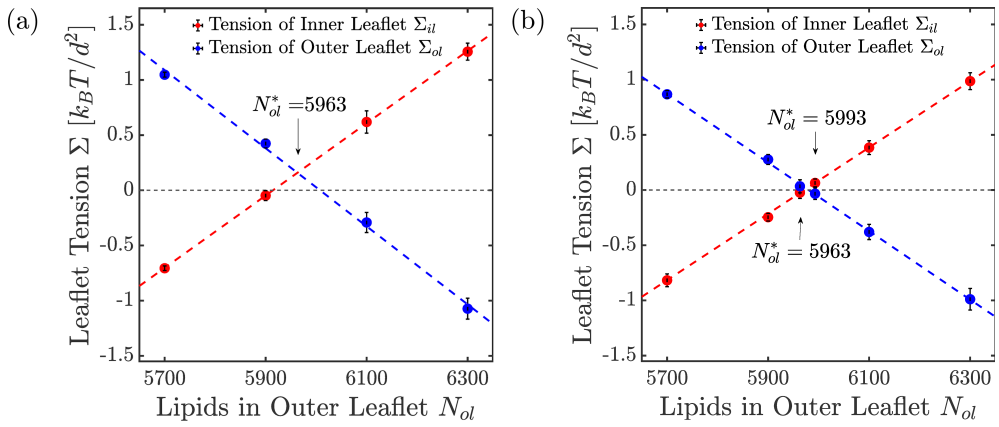

Figure 5.3. (a) Leaflet tensions $\Sigma_{\rm il}$ (red) and $\Sigma_{\rm ol}$ (blue) as functions of the lipid number $N_{\rm ol}$ in the outer leaflet for the four spherical vesicles displayed in the 1st column of Figure 5.1 with fixed total number $N = N_{\rm il} + N_{\rm ol} = 10\,100$ and volume parameter $v = 1$. The tension $\Sigma_{\rm il}$ in the inner leaflet increases whereas the tension $\Sigma_{\rm ol}$ in the outer leaflet decreases with increasing $N_{\rm ol}$. Furthermore, both sets of data are well fitted by straight lines which cross at $N^*_{\rm ol} = 5963$, corresponding to equal leaflet tensions $\Sigma_{\rm il} = \Sigma_{\rm ol} \simeq 0.16\,k_{\rm B}T/d^2$. The numerical parameter values are also given in Table 5.3. (b) Leaflet tensions $\Sigma_{\rm il}$ (red) and $\Sigma_{\rm ol}$ (blue) as functions of the lipid number $N_{\rm ol}$ in the outer leaflet for the four spherical vesicles displayed in the 2nd column of Figure 5.1, corresponding to $v = v_0 < 1$ and tensionless bilayers. The numerical parameter values are also given in Table 5.4. Both sets of data are well fitted by straight lines which cross at $N^*_{\rm ol} = 5993$ corresponding to tensionless leaflets.

Figure 5.1a is transformed into a stomatocyte which has a smaller area difference ΔA than the spherical vesicle.

Inspection of Table 5.3 shows that analogous results are obtained for the other three spherical vesicles with $v = 1$ in Figure 5.1b-d. For the spherical vesicle in Figure 5.1b, the tension $\Sigma_{\rm il}$ of the inner leaflet is again negative whereas the tension $\Sigma_{\rm ol}$ is again positive but these tensions are reduced compared to the spherical vesicle in Figure 5.1a. Thus, the inner leaflet is again compressed while the outer leaflet is again stretched. In contrast, for the spherical vesicles in Figure 5.1c and d, the inner leaflet tension $\Sigma_{\rm il}$ is positive while the outer leaflet tension $\Sigma_{\rm ol}$ is negative. Therefore, the inner leaflets are stretched and would like to shrink whereas the outer leaflets are compressed and would like to expand, thereby increasing the area difference ΔA. As a consequence, the spherical vesicles in Figure 5.1c and 5.1d transform into prolates and dumbbells, which have larger ΔA-values than the spherical vesicles.

To facilitate the comparison between the different spherical vesicles in Figure 5.1a-d, we always started from an initial volume with $N_{\rm W}^{\rm isp} = 90\,400$ water beads. In all four cases, we had to reduce the initial spherical nanovesicles with $v = 1$ by a few

Table 5.3. Parameter values for six spherical vesicles with $v = 1$ and $N_{\rm W} = 90\,400$, corresponding to the four panels in Figures 5.1, Figure 5.4a and the spherical vesicle with $N^*_{\rm ol} = 5993$ determined in Figure 5.3b. All vesicle membranes contain the same total number of lipids, $N_{\rm lip} = N_{\rm il} + N_{\rm ol} = 10\,100$. The midsurface radius $R_{\rm mid} = R_{\rm C}$ of the bilayer was defined by the peak in the chain bead density $\rho_{\rm C}(r)$, see Figure 5.2a, corresponding to CHAIN. The midsurface radii $R_{\rm il}$ and $R_{\rm ol}$ of the inner and outer leaflets were taken to be $R_{\rm il} = \frac{1}{2}(R_{\rm iH} + R_{\rm C})$ and $R_{\rm ol} = \frac{1}{2}(R_{\rm C} + R_{\rm oH})$ where $R_{\rm iH}$ and $R_{\rm oH}$ denote the location of the inner and outer peak of the head group density $\rho_{\rm H}(r)$, see Figure 5.2b

	Figure 5.1a	Figure 5.1b	Figure 5.1c	Figure 5.1d	Figure 5.4a	Figure 5.3b	units
$N_{\rm il}$	4400	4200	4000	3800	4137	4107	
$N_{\rm ol}$	5700	5900	6100	6300	$N^*_{\rm ol} = 5963$	$N^*_{\rm ol} = 5993$	
$N_{\rm W}$	90400	90400	90400	90400	90400	90400	
v	1	1	1	1	1	1	
Σ	0.341±0.02	0.376±0.02	0.328±0.02	0.184±0.03	0.366±0.02	0.36±0.02	$k_{\rm B}T/d^2$
$R_{\rm C}$	22.375±0.00	22.358±0.06	22.283±0.12	22.133±0.05	22.35±0.08	22.342±0.09	d
$\Sigma_{\rm il}$	-0.706±0.02	-0.048±0.04	0.619±0.10	1.256±0.08	0.157±0.07	0.259±0.07	$k_{\rm B}T/d^2$
$\Sigma_{\rm ol}$	1.047±0.02	0.424±0.04	-0.292±0.09	-1.073±0.09	0.209±0.06	0.101±0.07	$k_{\rm B}T/d^2$
$R_{\rm il}$	21.05±0.06	21.013±0.04	20.963±0.07	20.863±0.08	21.004±0.04	21.004±0.04	d
$R_{\rm ol}$	23.521±0.05	23.508±0.03	23.454±0.06	23.363±0.08	23.496±0.05	23.483±0.04	d
$a_{\rm il}$	1.266±0.01	1.321±0.01	1.381±0.01	1.439±0.01	1.34 ±0.01	1.35 ±0.01	d^2
$a_{\rm ol}$	1.22±0.01	1.177±0.00	1.133±0.01	1.089±0.01	1.163±0.01	1.156±0.00	d^2
$\mathcal{T}$	11.407±0.44	9.482±0.47	5.704±0.51	-0.21± 0.6	8.39±0.43	7.874±0.42	$k_{\rm B}T/d$
m	-0.331±0.01	-0.262±0.02	-0.14±0.02	0.052±0.02	-0.227±0.01	-0.213±0.01	$1/d$

percent to $v = v_0 < 1$, see second column of Figure 5.1 and Table 5.4 in order to reach a tensionless bilayer, corresponding to $\Sigma = \Sigma_{\rm il} + \Sigma_{\rm ol} \simeq 0$. The slightly deflated vesicles with $v = v_0 < 1$ and $\Sigma \simeq 0$ are still spherical and their snapshots cannot be distinguished from those for $v = 1$, see Figure 5.1.

5.3.7 Reference state with tensionless leaflets.

The four vesicles with $v = 1$ in Figure 5.1 were obtained by assembling different lipid numbers $N_{\rm il}$ and $N_{\rm ol}$ in the two leaflets, keeping the total lipid number $N = N_{\rm il} + N_{\rm ol}$ fixed. We can then reduce the number of parameters and focus on a single lipid number, say $N_{\rm ol}$. In Figure 5.3, we display the two leaflets tensions $\Sigma_{\rm il}$ and $\Sigma_{\rm ol}$ as functions of the lipid number $N_{\rm ol}$. The two sets of data points in this figure are well fitted by two straight lines that cross each other for $N_{\rm ol} = N^*_{\rm ol} = 5963$. At this crossing point, the two leaflet tensions are equal to $\Sigma_{\rm il} = \Sigma_{\rm ol} \simeq 0.16\, k_{\rm B}T/d^2$.

We then studied a spherical vesicle with $N_{\rm ol} = N^*_{\rm ol}$ and $N_{\rm il} = N^*_{\rm il} = N_{\rm lip} - N^*_{\rm ol}$, see Figure 5.4a, that encloses the same number of beads, $N^{\rm isp}_{\rm W} = 90\,400$, as the four spherical vesicles in Figure 5.1. As a result, we obtained the leaflet tensions $\Sigma_{\rm il} =$

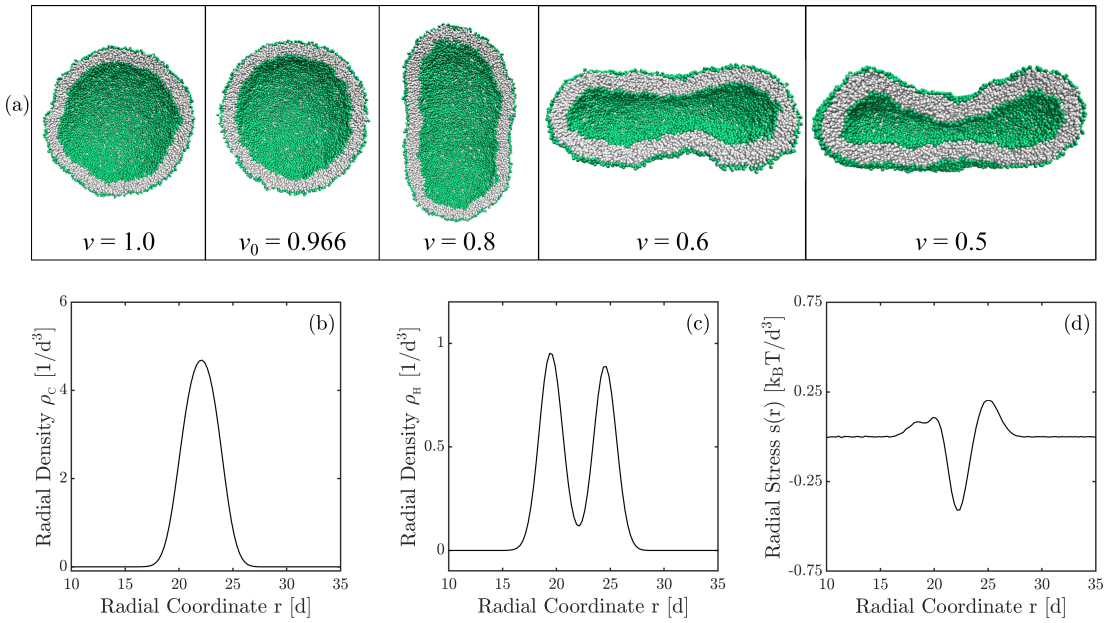

Figure 5.4. (a) Morphological transformations of the spherical nanovesicle with $N_{\mathrm{il}} = 4137$ and $N_{\mathrm{ol}} = 5963$ lipids in the inner and outer leaflet, enclosing $N_{\mathrm{W}}^{\mathrm{isp}} = 90\,400$ water beads. A slight deflation of this vesicle to $N_{\mathrm{W}} = 87\,360$ water beads and $v = v_0 = 0.966$ leads to the reference state with tensionless leaflets. As we continue to reduce the vesicle volume, the vesicle attains a prolate shape for $v = 0.8$ and $v = 0.7$, an oblate or discocyte shape for $v = 0.6$, and a stomatocyte shape for $v = 0.5$. (b-d) Density and stress profiles of the reference state with tensionless leaflets as functions of the radial coordinate r: (b) Density profile $\rho_{\mathrm{C}}(r)$ of the C beads; (c) Density profile $\rho_{\mathrm{H}}(r)$ of the H beads; and (d) Stress profile $s(r)$ across the bilayer membrane. Integrating this stress profile over the two leaflets as in Eq. 5.6, we obtain leaflet tensions Σ_{il} and Σ_{ol} close to zero (Table 5.4). The simulations to generate panel (a) of this figure is done by Rikhia Ghosh.

$0.157 \pm 0.07\, k_{\mathrm{B}}T/d^2$ and $\Sigma_{\mathrm{ol}} = 0.209 \pm 0.06$, in good agreement with the tension values $\Sigma_{\mathrm{il}} = \Sigma_{\mathrm{ol}} \simeq 0.16\, k_{\mathrm{B}}T/d^2$ as derived from the graphical interpolation in Figure 5.3. When we slightly deflated this vesicle and reduced its volume to $N_{\mathrm{W}} = 87\,360$, we obtained a spherical vesicle for which both leaflet tensions $\Sigma_{\mathrm{ol}} \simeq 0$ and $\Sigma_{\mathrm{il}} \simeq 0$, i.e., for which each leaflet tension vanished individually, see Table 5.4. Essentially the same reference state can be obtained by the following alternative procedure. We start from the same set of spherical vesicles as before (first column of Figure 5.1 and Table 5.3) but then deflate each vesicle to $v = v_0 < 1$ in order to obtain tensionless bilayers with $\Sigma = \Sigma_{\mathrm{il}} + \Sigma_{\mathrm{ol}} \simeq 0$ (second column of Figure 5.1 and Table 5.4). The corresponding leaflet tensions are plotted in Figure 5.3b as a function of N_{ol}. Graphical extrapolation of these data then leads to the outer lipid number $N_{\mathrm{ol}}^{*} = 5993$ for the reference state

Table 5.4. Parameter values for six spherical vesicles with $v = v_0 < 1$ and tensionless bilayers, corresponding to the four panels in Figure 5.1, Figure 5.4a, and the spherical vesicle with $N_{\mathrm{ol}}^* = 5993$ determined in Figure 5.3b. The radii of the different midsurfaces are defined in the same way as in Table 5.3.

	Figure 5.1a	Figure 5.1b	Figure 5.1c	Figure 5.1d	Figure 5.4a	Figure 5.3b	units
N_{il}	4400	4200	4000	3800	4137	4107	
N_{ol}	5700	5900	6100	6300	$N_{\mathrm{ol}}^* = 5963$	$N_{\mathrm{ol}}^* = 5993$	
N_{W}	87350	87420	87400	88400	87360	87400	
v_0	0.966	0.967	0.967	0.978	0.966	0.967	
Σ	0.05±0.04	0.03±0.03	0.005±0.04	-0.003±0.05	0.01±0.03	0.031±0.04	$k_{\mathrm{B}}T/d^2$
R_{C}	22.1±0.08	22.125±0.00	22.017±0.13	22.042±0.12	22.117±0.05	22.083±0.09	d
Σ_{il}	-0.818±0.06	-0.246±0.03	0.384±0.06	0.986±0.08	-0.024±0.05	0.064±0.04	$k_{\mathrm{B}}T/d^2$
Σ_{ol}	0.867±0.03	0.277±0.05	-0.38±0.07	-0.989±0.10	0.034±0.06	-0.033±0.05	$k_{\mathrm{B}}T/d^2$
R_{il}	20.808±0.14	20.771±0.11	20.688±0.15	20.638±0.15	20.792±0.10	20.733±0.13	d
R_{ol}	23.342±0.16	23.288±0.12	23.2±0.15	23.142±0.16	23.3±0.08	23.246±0.14	d
a_{il}	1.237±0.02	1.291±0.01	1.345±0.02	1.409±0.02	1.313±0.01	1.315±0.02	d^2
a_{ol}	1.201±0.02	1.155±0.01	1.109±0.01	1.068±0.01	1.144±0.01	1.133±0.01	d^2
$\mathcal{T}$	5.17±0.87	2.039±0.74	-1.352±0.82	-4.391±1.05	0.641±0.77	0.701±0.93	$k_{\mathrm{B}}T/d$
m	-0.117±0.03	-0.02±0.02	0.089±0.03	0.186±0.03	0.025±0.02	0.023±0.03	$1/d$

with tensionless leaflets. In this way, we obtain two slightly different estimates as given by $N_{\mathrm{ol}}^* = 5963$ (Figure 5.3a) and $N_{\mathrm{ol}}^* = 5993$ (Figure 5.3b), respectively. The small difference between these two values implies a high numerical accuracy of about 0.5 %.

The reference state with tensionless leaflets has the reduced volume $v = v_0 = 0.966$ as well as the lipid areas, $a_{\mathrm{ol}}^0 = 1.139\, d^2$ and $a_{\mathrm{il}}^0 = 1.318\, d^2$, corresponding to optimal packing densities within the outer and inner leaflets of the bilayer membrane. As shown in Figure 5.4a, a further reduction of the volume leads to prolates and discocytes.

For planar membranes, the reference state is provided by a symmetric and tensionless bilayer. In this case, both leaflets contain the same number of lipids, $N_{\mathrm{ol}} = N_{\mathrm{il}}$, have the same area per lipid, $a_{\mathrm{ol}} = a_{\mathrm{il}}$, and have the same leaflet tension, $\Sigma_{\mathrm{ol}} = \Sigma_{\mathrm{il}}$. Furthermore, if the bilayer is tensionless with $\Sigma_{\mathrm{il}} + \Sigma_{\mathrm{ol}} = 0$, it directly follows that both leaflet tensions vanish and $\Sigma = \Sigma_{\mathrm{il}} = \Sigma_{\mathrm{ol}} = 0$ [14]. In contrast, for the spherical nanovesicles considered here, the reference state with tensionless leaflets $\Sigma_{\mathrm{il}} = \Sigma_{\mathrm{ol}} = 0$ is characterized by $N_{\mathrm{il}} < N_{\mathrm{ol}}$ and $a_{il}^0 > a_{ol}^0$, see Table 5.4.

5.3.8 Area compressibility moduli of two leaflets.

The deviations of the lipid areas from their optimal values for the reference state are related to the leaflet tensions $\Sigma_{\rm il}$ and $\Sigma_{\rm ol}$ according to

$$\Sigma_{\rm il} \approx K_{\rm il}\Delta_{\rm il} \quad \text{with} \quad \Delta_{\rm il} \equiv \frac{a_{\rm il} - a_{\rm il}^0}{a_{\rm il}^0} \tag{5.7}$$

and

$$\Sigma_{\rm ol} \approx K_{\rm ol}\Delta_{\rm ol} \quad \text{with} \quad \Delta_{\rm ol} \equiv \frac{a_{\rm ol} - a_{\rm ol}^0}{a_{\rm ol}^0} \tag{5.8}$$

for small area dilations $\Delta_{\rm il}$ and $\Delta_{\rm ol}$ where $K_{\rm il}$ and $K_{\rm ol}$ represent the area compressibility moduli of the two leaflets. The corresponding data for leaflet tensions and dimensionless area dilations $\Delta_{\rm il}$ and $\Delta_{\rm ol}$ are plotted in Figure 5.5a for the five vesicle membranes wich bilayer tension $\Sigma = \Sigma_{\rm ol} + \Sigma_{\rm il} \simeq 0$, see also Table 5.4. Inspection of this figure shows that these data are well fitted, for the whole range of Δ-values studied here, by straight lines with the area compressibility moduli $K_{\rm il} = 13.9\, k_{\rm B}T/d^2$ and $K_{\rm ol} = 15.9\, k_{\rm B}T/d^2$. Therefore, the inner leaflet is found to be more compressible and softer than the outer leaflet. This result is consistent with the lipid areas $a_{\rm il}^0 = 1.31\, d^2$ and $a_{\rm ol}^0 = 1.14\, d^2$ for the two tensionless leaflets (Table 5.4). Indeed, the more loosely packed inner leaflet is expected to be softer than the more densely packed outer leaflets.

5.3.9 Alternative definitions of the bilayer's midsurface.

The numerical results described so far were obtained by locating the bilayer's midsurface at the peak position $r = R_{\rm C}$ of the C bead density $\rho_{\rm C}(r)$, see Figure 5.2a, and to define the midsurface radius via $R_{\rm mid} \equiv R_{\rm C}$, a definition that we now denote as CHAIN. We also explored two alternative, physically meaningful definitions of the midsurface radius. One alternative definition, HEAD, was based on the two peaks of the density profile $\rho_{\rm H}(r)$ for the head group layers, see Figure 5.2b, and on the corresponding radii $r = R_{\rm iH}$ and $r = R_{\rm oH}$. The midsurface radius was then defined by $R_{\rm mid} = R_{\rm H} \equiv \frac{1}{2}(R_{\rm iH} + R_{\rm oH})$. A second alternative definition, COM, used the center-of-mass radius $R_{\rm COM}$ of the combined density profile $\rho_{\rm C}(r) + \rho_{\rm H}(r)$ and defined the midsurface radius by $R_{\rm mid} \equiv R_{\rm COM}$.

Using these three definitions of the midsurface radius, we obtained the numerical values in Table 5.5 for the five spherical vesicles in Figures 5.1 and 5.4 with $v = v_0$, corresponding to tensionless bilayers. Inspection of this table shows that, for each vesicle, the three values $R_{\rm C}$, $R_{\rm H}$, and $R_{\rm COM}$ obtained for the midsurface radius $R_{\rm mid}$ were rather close and differed by at most 3%. Likewise, using COM, we also find different area compressibilities $K_{\rm il}$ and $K_{\rm ol}$ for the inner and outer leaflets, see Figure 5.5b, in agreement with the CHAIN results shown in Figure 5.5a.

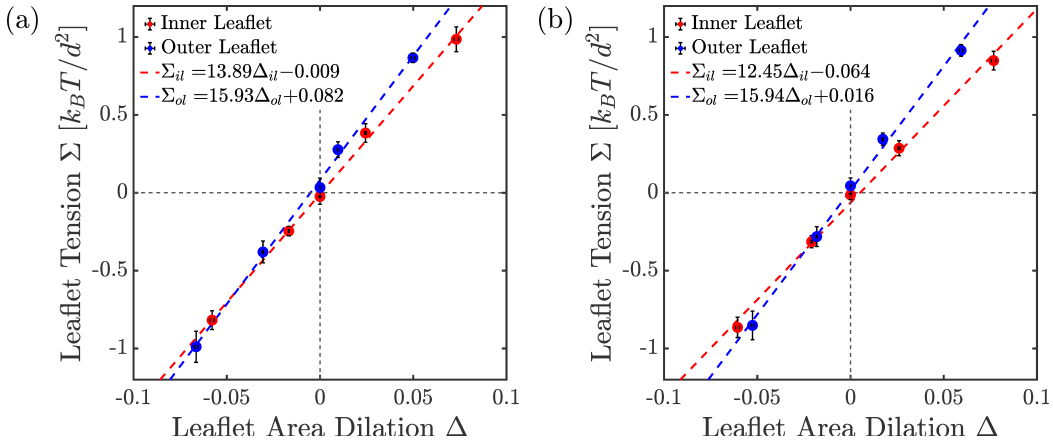

Figure 5.5. (a) Leaflet tension $\Sigma_{\rm il}$ (red) and $\Sigma_{\rm ol}$ (blue) as a function of the dimensionless area dilations $\Delta_{\rm il}$ and $\Delta_{\rm ol}$, defined in Eqs. 5.7 and 5.8. The straight lines represent least squares fits which determine the area compressibility modulus $K_{\rm il} = 13.89\,k_{\rm B}T/d^2$ and $K_{\rm ol} = 15.93\,k_{\rm B}T/d^2$ for the inner and outer leaflet, respectively. These results were obtained using the CHAIN definition for the bilayer's midsurface, see Table 5.4, and (b) using the midsurface radius $R_{\rm mid} = R_{\rm COM}$ corresponding to COM, see Table 5.6. The straight lines represent least squares fits which determine the area compressibility moduli $K_{\rm il} = 12.45\,k_{\rm B}T/d^2$ and $K_{\rm ol} = 15.94\,k_{\rm B}T/d^2$ for the inner and outer leaflets, respectively. Thus, the inner leaflet is more compressible and softer than the outer leaflet.

5.3.10 Torques generated by spherical membranes

To obtain an explicit expression for the local spontaneous curvature of the spherical vesicles considered here, we consider the first moment, $\mathcal{T}$, of the spherically symmetric stress profile $s(r)$ as given by

$$\mathcal{T} \equiv \int_0^\infty {\rm d}r\, s(r)\, r = \int_{-R_{\rm mid}}^\infty {\rm d}y\, s(R_{\rm mid}+y)\, y + \Sigma R_{\rm mid} \tag{5.9}$$

where the second equality follows from a change of variable from r to $y \equiv r - R_{\rm mid}$ with the radius $R_{\rm mid}$ of the bilayer's midsurface and the bilayer tension $\Sigma = \int {\rm d}r s(r)$. For a tensionless bilayer with $\Sigma = 0$, the last term in Eq 5.9 vanishes and we are left with

$$\mathcal{T} = \int_{-R_{\rm mid}}^\infty {\rm d}y\, \hat{s}(y)\, y \quad \text{with} \quad \hat{s}(y) \equiv s(R_{\rm mid}+y) \tag{5.10}$$

which we interpret as the microscopic torque per unit length with respect to $y = 0$. In the limit of large vesicles and, thus, large $R_{\rm mid}$, the integral in Eq. 5.10 becomes

Table 5.5. Parameter values for six spherical vesicles with $v = 1$ and $N_{\mathrm{W}} = 90\,400$, corresponding to the four panels in Figure 5.1, Figure 5.4a, and the spherical vesicle with $N_{\mathrm{ol}}^{*} = 5993$ determined in Figure 5.3b. The midsurface radius $R_{\mathrm{mid}} = R_{\mathrm{COM}}$ of the bilayer was defined by its center-of-mass, corresponding to COM. The midsurface radii R_{il} and R_{ol} of the inner and outer leaflets were taken to be $R_{\mathrm{il}} = \frac{1}{2}(R_{\mathrm{iH}} + R_{\mathrm{COM}})$ and $R_{\mathrm{ol}} = \frac{1}{2}(R_{\mathrm{COM}} + R_{\mathrm{oH}})$ where R_{iH} and R_{oH} denote the location of the inner and outer peak of the head group density $\rho_{\mathrm{H}}(r)$, see Figure 5.2b.

	Figure 5.1a	Figure 5.1b	Figure 5.1c	Figure 5.1d	Figure 5.4a	Figure 5.3b	units
N_{il}	4400	4200	4000	3800	4137	4107	
N_{ol}	5700	5900	6100	6300	$N_{\mathrm{ol}}^{*} = 5963$	$N_{\mathrm{ol}}^{*} = 5993$	
N_{W}	90400	90400	90400	90400	90400	90400	
v	1	1	1	1	1	1	
Σ	0.341±0.02	0.376±0.02	0.328±0.02	0.184±0.03	0.366±0.02	0.36±0.02	$k_{\mathrm{B}}T/d^2$
R_{COM}	22.446±0.00	22.447±0.01	22.445±0.01	22.461±0.01	22.448±0.01	22.449±0.01	d
Σ_{il}	-0.745±0.02	-0.1±0.03	0.507±0.03	1.04±0.04	0.097±0.03	0.189±0.02	$k_{\mathrm{B}}T/d^2$
Σ_{ol}	1.086±0.02	0.476±0.02	-0.179±0.02	-0.856±0.05	0.269±0.02	0.171±0.02	$k_{\mathrm{B}}T/d^2$
R_{il}	21.086±0.06	21.057±0.05	21.043±0.04	21.027±0.08	21.053±0.05	21.058±0.05	d
R_{ol}	23.557±0.05	23.553±0.04	23.535±0.03	23.527±0.08	23.545±0.05	23.537±0.03	d
a_{il}	1.27±0.01	1.327±0.01	1.391±0.01	1.462±0.01	1.346±0.01	1.357±0.01	d^2
a_{ol}	1.223±0.01	1.182±0.00	1.141±0.00	1.104±0.01	1.168±0.01	1.162±0.00	d^2
$\mathcal{T}$	11.407±0.44	9.482±0.47	5.704±0.51	-0.21±0.60	8.39±0.43	7.874±0.42	$k_{\mathrm{B}}T/d$
m	-0.35±0.02	-0.277±0.02	-0.15±0.02	0.052±0.02	-0.241±0.01	-0.226±0.01	$1/d$

Table 5.6. Parameter values for six spherical vesicles with $v = v_0 < 1$ and tensionless bilayers, corresponding to the four panels in Figure 5.1, Figure 5.4a, and the spherical vesicle with $N_{\mathrm{ol}}^{*} = 5993$ determined in Figure 5.3b. The radii of the different midsurfaces are defined in the same way as in Table 5.5.

	Figure 5.1a	Figure 5.1b	Figure 5.1c	Figure 5.1d	Figure 5.4a	Figure 5.3b	units
N_{il}	4400	4200	4000	3800	4137	4107	
N_{ol}	5700	5900	6100	6300	5963	5993	
N_{W}	87350	87420	87400	88400	87360	87400	
v_0	0.966	0.967	0.967	0.978	0.966	0.967	
Σ	0.05±0.04	0.03±0.03	0.005±0.04	-0.003±0.05	0.01±0.03	0.031±0.04	$k_{\mathrm{B}}T/d^2$
R_{COM}	22.315±0.02	22.308±0.01	22.325±0.01	22.387±0.02	22.306±0.01	22.314±0.02	d
Σ_{il}	-0.865±0.06	-0.314±0.04	0.286±0.05	0.849±0.06	-0.099±0.05	-0.013±0.03	$k_{\mathrm{B}}T/d^2$
Σ_{ol}	0.914±0.04	0.344±0.04	-0.282±0.06	-0.851±0.09	0.11±0.04	0.045±0.05	$k_{\mathrm{B}}T/d^2$
R_{il}	20.916±0.12	20.863±0.11	20.842±0.14	20.81±0.12	20.886±0.11	20.849±0.12	d
R_{ol}	23.449±0.14	23.379±0.12	23.354±0.14	23.314±0.13	23.395±0.09	23.361±0.12	d
a_{il}	1.249±0.01	1.302±0.01	1.365±0.02	1.432±0.02	1.325±0.01	1.33±0.02	d^2
a_{ol}	1.212±0.01	1.164±0.01	1.124±0.01	1.084±0.01	1.153±0.01	1.144±0.01	d^2
$\mathcal{T}$	5.17±0.87	2.039±0.74	-1.352±0.82	-4.391±1.05	0.641±0.77	0.701±0.93	$k_{\mathrm{B}}T/d$
m	-0.125±0.03	-0.023±0.02	0.09±0.03	0.193±0.04	0.023±0.03	0.021±0.03	$1/d$

asymptotically equal to the first moment of the stress profile for planar and tensionless bilayers. [14, 20]

In Figure 5.6a, we display the numerical values of $\mathcal{T}$ for the four spherical vesicles in

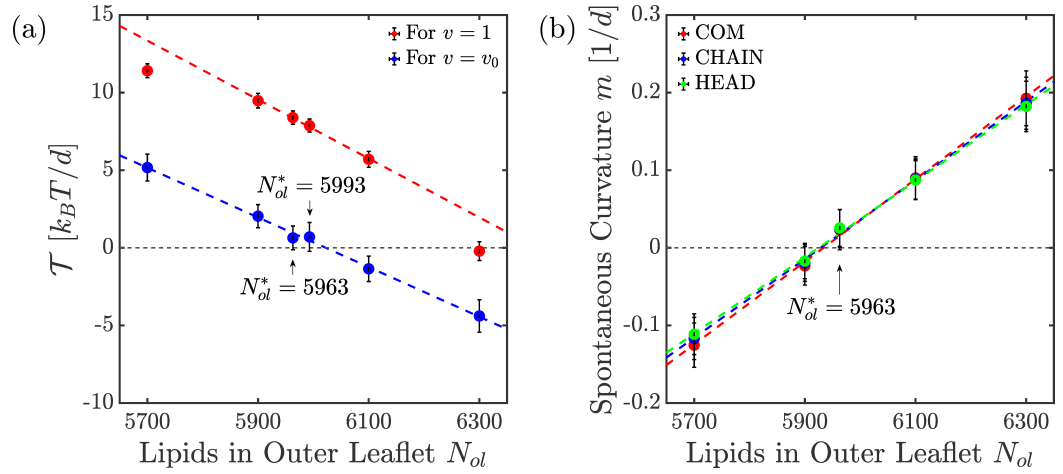

Figure 5.6. (a) First moment of stress profile, $\mathcal{T}$, as a function of the outer lipid number N_{ol} for the four spherical vesicles in Figure 5.1 and for the two spherical vesicles with $N^*_{\mathrm{ol}} = 5963$ and $N^*_{\mathrm{ol}} = 5993$ as determined in Figure 5.3. Two sets of data are displayed for each vesicle, corresponding to $v = 1$ and $N_{\mathrm{W}} = 90\,400$ (red) as well as to $v = v_0 < 1$ and $\Sigma \simeq 0$ (blue), see Tables 5.3 and 5.4. Note that the value of $\mathcal{T}$ does not depend on the definition of the bilayer's midsurface. (b) Local spontaneous curvature m versus lipid number N_{ol} in the outer leaflet, as obtained from Eq. 5.12 for bending rigidity $\kappa = 15\,k_{\mathrm{B}}T$ and three alternative definitions (CHAIN, HEAD, and COM) of the midsurface radius R_{mid}.

Figure 1 both for $v = 1$ and for $v = v_0$. Because the stress profiles $s(r)$ are limited to the vicinity of the bilayer, the r-integration in Eq. 5.9 was performed over the spherical shell defined by $r_{\mathrm{min}} = 12.125\,d < r < r_{\mathrm{max}} = 35.125\,d$.

On the other hand, for a lipid bilayer with bending rigidity κ and (local) spontaneous curvature m, a spherical membrane segment with radius R_{mid} generates the nanoscopic torque per unit length as given by [154, 155]

$$\mathcal{T}_{\mathrm{nan}} = 2\kappa(M_{\mathrm{mid}} - m) \quad \text{with } M_{\mathrm{mid}} \equiv 1/R_{\mathrm{mid}}. \tag{5.11}$$

When we identify the microscopic torque as given by Eq. 5.10 with the nanoscopic torque in Eq. 5.11 [154, 155], we obtain the relationship for spherical vesicles

$$2\kappa \left(\frac{1}{R_{\mathrm{mid}}} - m \right) = \int_0^\infty \mathrm{d}r\, s(r)\, r \tag{5.12}$$

between the bending rigidity κ, the midsurface radius R_{mid} of the spherical vesicle, the spontaneous curvature m, and the first moment of the stress profile $s(r)$.

5.3.11 Local and nonlocal spontaneous curvature

The shapes and shape transformations of nanovesicles as observed in our molecular simulations, see Figure 5.1, are qualitatively similar to those obtained from curvature models [148, 25, 27, 149]. In these models, the vesicle membranes are viewed as smooth surfaces and their behavior is described in terms of a few fluid-elastic parameters such as the bending rigidity κ and the local spontaneous curvature m. In fact, as far as vesicle shapes are concerned, the most important fluid-elastic parameter is the spontaneous curvature. For planar bilayers, this curvature can be computed by identifying the microscopic torque across the molecular bilayer with the nanoscopic torque as obtained from curvature elasticity [14, 20]. The extensions of the latter approach to spherical vesicles, using the corresponding nanoscopic torques [154, 155], leads to the Eq. 5.12 which provides the systematic way of calculating the spontaneous curvature.

The magnitude of the bending rigidity κ can be obtained from the area compressibility modulus K_A of the bilayer using the relationship $\kappa = K_A \ell_{\rm me}^2/48$ which provides the same κ-value as the computationally more expensive fluctuation analysis [13, 19]. For the vesicle membranes in Figure 5.1, the area compressibility $K_A = K_{\rm il} + K_{\rm ol} \simeq 30\, k_{\rm B}T$ and the membrane thickness $\ell_{\rm me} \simeq 5\ d$ which leads to $\kappa \simeq 15\, k_{\rm B}T$. Using this κ-value in Eq. 5.12, together with the $R_{\rm mid}$-values in Table 5.5 and the numerical values for the first moment $\mathcal{T}$ of the stress profile in Figure 5.6a and Table 5.4, we obtain the values of the local spontaneous curvature m as shown in Figure 5.6b. Inspection of this figure reveals that m increases linearly with the lipid number $N_{\rm ol}$ in the outer leaflet and that all three definitions, CHAIN, HEAD, and COM, of the midsurface radius $R_{\rm mid}$ lead to very similar values for the spontaneous curvature m, in accordance with the $R_{\rm mid}$-values in Table 5.5.

In the absence of flip-flops between the two leaflets, the theory of curvature elasticity predicts another nonlocal contribution to the spontaneous curvature [156, 149] arising from area-difference-elasticity [25, 27], which depends on the difference $\Delta A = A_{\rm ol} - A_{\rm il}$ between the outer leaflet area $A_{\rm ol}$ and the inner leaflet area $A_{\rm il}$. This nonlocal contribution to the spontaneous curvature is proportional to the deviation of ΔA from its reference value ΔA_0 for tensionless leaflets. However, the four spherical vesicles in Figure 5.1, corresponding to $v = v_0$ and tensionless bilayers, have practically the same midsurface radius $R_{\rm mid}$, see Table 5.5, and thus the same area difference as the relaxed vesicle in Figure 5.4a with $v = v_0$. Therefore, for these vesicle shapes, the nonlocal contribution to the spontaneous curvature is very small and can be ignored. On the other hand, once the nanovesicles have attained strongly nonspherical shapes, area-difference-elasticity should make a significant contribution, which is, however, difficult to determine quantitatively because it is shape-dependent and involves another elastic modulus.

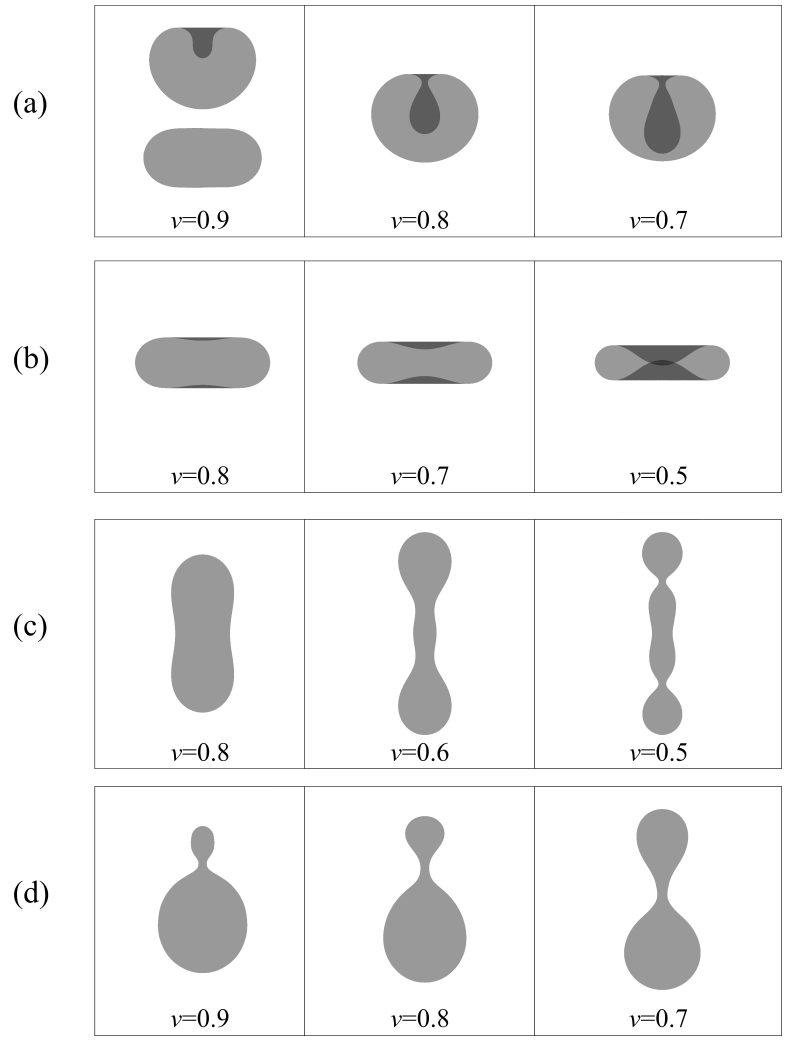

Figure 5.7. Shape transformations of the spherical vesicle in response to deflation. Each row has different spontaneous curvature, see Table 5.4 The first, second, and third panels in the figure correspond directly to the third, fourth, and fifth panels of Figure 5.1

5.3.12 Polymorphism of vesicle shapes from continuum model

The spontaneous curvature and the reduced volume are used as control parameters for energy minimization of vesicles. As a result of energy minimization, we found a set of similar morphologies as that of Figure 5.1 . The deflation trajectories as for morphologies of vesicles are shown in Figure 5.7 for different values of spontaneous curvature and deflation states. The first, second, and third panels of Figure 5.7 have one-to-one cor-

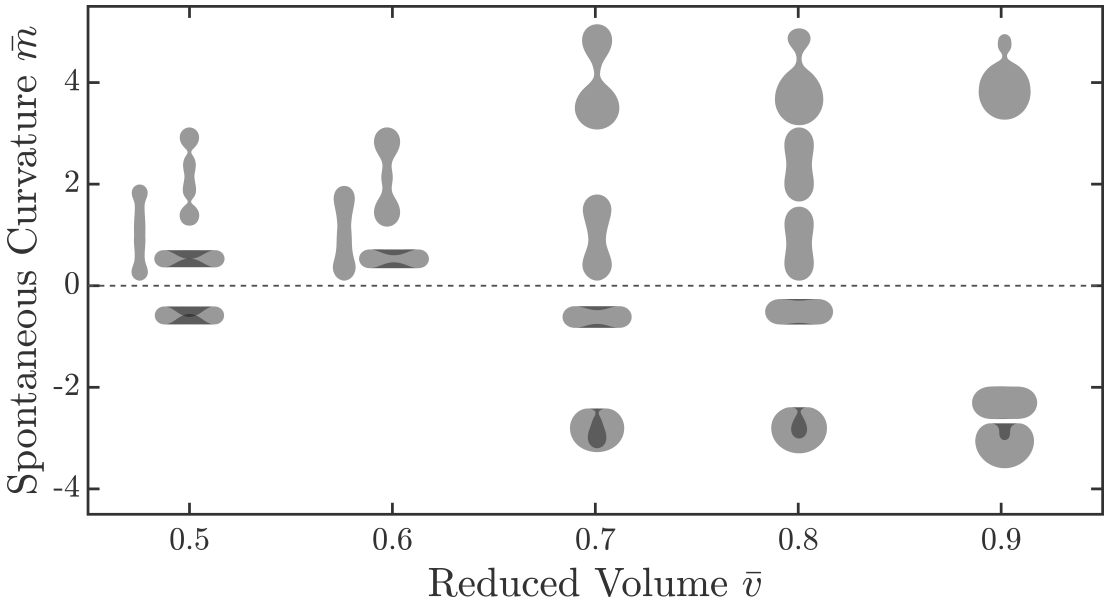

Figure 5.8. Vesicle Morphology diagram in the space of reduced spontaneous curvature $\bar{m}$ and vesicle reduced volume v. Vesicle shapes are obtained from energy minimization of triangulated membrane surface.

respondence with the third, fourth, and fifth panels of Figure 5.1. Unlike for the DPD simulations, energy minimization sometimes leads to two different co-existing solutions. For example, in a reduced volume of $v = 0.9$ in Figure 5.1a, both stomatocytes and prolate are existing solutions, where stomatocytes have lower energy. This qualitative similarity confirms our protocol for calculation of spontaneous curvature.

Figure 5.8, shows all shapes obtained from energy minimization in the space of spontaneous curvature and reduced volume. This sparse morphology diagram is in agreement with the outcomes of previous studies using variational calculus [7]. For a better description of the small vesicles, the effect of area difference elasticity, as an extra energetic contribution, should be taken into account. In addition, it is possible that the local spontaneous curvature can be coupled to deflated state. However, such coupling effects are not taken into account here. Further investigation is required to study the latter effect via analysis of three-dimensional stress profile.

6 Conclusions and Future Perspectives

6.1 Conclusions

In chapter three, we have shown that the line tension in DPD simulations of a nanodroplet adhering to a bilayer membrane is negative for a wide range of parameters. As the mechanical membrane tension is reduced, the negative line tension leads to a morphological transition from axisymmetric to non-axisymmetric membrane-droplet morphologies (Figure 3.3). The latter type of morphology persists until the nanodroplet is completely engulfed by the membrane and the membrane neck attains an elongated, tight-lipped shape, as displayed in Figures 3.3d and 3.13 for symmetric and asymmetric bilayers, respectively. The formation of such a membrane neck provides an example for a liquid nanostructure that undergoes a morphological transition with a spontaneously broken symmetry. We also argued that this unusual neck shape is likely to impedes pinocytosis and fluid-phase endocytosis of nanodroplets. Examples are provided by oil-in-water nanoemulsions [106, 107] as well as aqueous two-phase systems sufficiently far from the critical demixing point [78], which are both characterized by interfacial tensions $\Sigma_{\alpha\beta}$ of the order of 1 mN/m, in the same range as investigated here (Figure 3.10b). When such oil-in-water or water-in-water droplets interact with GUVs, they may be completely engulfed by the vesicle membrane but the resulting membrane neck will be stabilized against scission by its tight-lipped shape. When these droplets interact with cells, on the other hand, the cellular uptake often involves membrane-bound proteins such as clathrin or caveolae. Indeed, both clathrin-dependent [85, 83, 87] and caveolae-dependent [83] pathways have been discussed for pinocytosis and cellular uptake of nanoemulsion droplets.

In chapter four, we studied the interaction of nanodroplets with vesicles in the context of membrane-wetting theory. The studied nanodroplets have very low interfacial tensions comparable to biomolecular condensates of the order of μN/m. A new regime of broken symmetry is identified to appear at low contact area, where the droplet takes the form of two connected elliptical caps, Figure 4.2. Symmetry breaking in the high contact area regime is also observed, consistent with the DPD simulation results in chapter three. We showed that the adhesion of nanodroplets can transform the morphology of vesicles by wetting the membrane as a response to capillary forces, see Figure 4.1. We found that all three material parameters, including interfacial tension, bending rigidity and line tension, affect the shape transformation of vesicles. In addition, we found a

prominent effect of the spontaneous curvature on the membrane-droplet morphology, capable of changing of the membrane curvature in the segment which is in contact with nanodroplet, see Figure 4.3. For low positive spontaneous curvature, an in-bud morphology is observed, similar as for vanishing and negative spontaneous curvature. However, for higher positive spontaneous curvature, an out-bud morphology is predicted. The symmetry of the contact line is found to be broken for a broad range of parameters, also for the out-bud morphology. We introduce a contact line symmetry hyper-surface which separates the symmetric and asymmetric contact line geometries, in three-dimensional material parameter space obtained for zero spontaneous curvature, see Figure 4.4c.

In chapter five, we showed that spherical nanovesicles can transform into a multitude of nonspherical shapes- prolates, oblates, discocytes, stomatocytes, and dumbbells - as illustrated in Figure 5.1 and 5.4. This polymorphism has been obtained in DPD simulations by reducing the volume of an initially spherical vesicle for fixed total number of lipids and for a fixed distribution of the lipid molecules between the two leaflets. Alternatively, we may also consider a fixed volume and shuffle some lipids from the inner to the outer leaflet. Experimentally, the latter morphological pathway could be induced by adding lipid or surfactant molecules to the exterior solution which then insert into the outer membrane leaflet and increases its area. The different shapes displayed in Figure 5.1 and 5.4 arise from small variations of the number of lipid molecules in the two bilayer leaflets. The resulting shape transformations can be understood in terms of the individual leaflet tensions $\Sigma_{\rm il}$ and $\Sigma_{\rm ol}$, which act to stretch or compress these leaflets when we allow the vesicles to attain nonspherical shapes by reducing their volume. We also identified, for a given vesicle volume and total lipid number $N_{\rm lip} = N_{\rm il} + N_{\rm ol}$, the reference state of the spherical vesicle for which both leaflets are tensionless with $\Sigma_{\rm il} = \Sigma_{\rm ol} = 0$ (Figures 5.3 and 5.4). Even for vanishing leaflet tensions, the two leaflets had different areas per lipid, $a_{\rm il}^0 = 1.3\, d^2$ and $a_{\rm il}^0 = 1.1\, d^2$ (Table 5.4), corresponding to a more loosely packed inner leaflet and a more densely packed outer leaflet. To characterize the stress asymmetry of the spherical bilayer, we extended previous results on planar bilayers to obtain a simple relation between the radius of the midsurface, the (local) spontaneous curvature, and the first moment of the spherically symmetric stress profile (Eq. 5.12). The spontaneous curvature obtained from this expression, was found to increase linearly with the number of lipids in the outer leaflet as shown in Figure 5.6b. Finally, we also argued that the nonlocal contribution to the spontaneous curvature arising from area-difference-elasticity can be ignored for spherical bilayers.

6.2 Future Perspectives

One interesting question that requires further study is how protein-dependent pathways of pinocytosis are affected by a negative line tension of the nanodroplet. If the negative

line tension leads to a tight-lipped membrane neck as observed here in the absence of proteins, scission and cellular uptake of the completely engulfed droplet will be strongly suppressed. On the other hand, it is also conceivable that the protein coat can control the engulfment process in such a way that the closed neck becomes circular even for a negative line tension. Another open issue is the sign of the line tension for ultralow interfacial tensions $\Sigma_{\alpha\beta} \simeq 1\,\mu$N as found for aqueous two-phase systems close to their critical demixing point [78] as well as for biomolecular condensates [79, 157]. Linear extrapolation of our simulation data predicts a negative line tension for the whole physically meaningful range $\Sigma_{\alpha\beta} > 0$ (Figure 3.10b) but we cannot exclude the possibility that the line tension becomes positive for sufficiently small values of $\Sigma_{\alpha\beta}$. For rigid nanoparticles, clathrin-dependent endocytosis and cellular uptake depends nonmonotonically on the particle size, with an optimal diameter of about 50 nm [158]. This size dependence can be understood in terms of the spontaneous curvature $m_{\rm pro}$ generated by the protein coat which implies a preferred radius of $1/|m_{\rm pro}| \simeq 40\,$nm for the clathrin-encaged endocytic vesicle [159]. Because of this preferred size of the endocytic vesicle, the uptake of nanodroplets should also be characterized by a nonmonotonic dependence on the droplet size. The latter prediction is accessible to experimental studies in close analogy to those performed in Ref. 158.

The measurement of the line tension with available experimental methods is still very challenging. But, an observation of contact-line symmetry seems to be feasible using super-resolution microscopy at the nanometre scale, similar to the observation of endocytosis by proteins condensates [64]. Such observations, combined with the extrapolation of simulation results, suggests a possibility to estimate a range for the physically meaningful line tension values for vanishing spontaneous curvature.

In chapter three and four of the thesis, we studied nanodroplets with a constant, time-independent volume, but, based on our simulation results, we can also draw important conclusions for the closely related time-dependent processes corresponding to surface nucleation and growth of nanodroplets at membranes. A single droplet that has been nucleated at a membrane will initially attain a partially engulfed morphology as in Figures 3.2 or 4.1a and will keep this morphology during its diffusion-limited growth provided the membrane tension is sufficiently large. For small membrane tension, on the other hand, we will observe a competition between the engulfment and the growth of the droplet. If the growth is slow, the droplet can only grow up to a certain size before it is completely engulfed by the membrane. This competition becomes particularly interesting if we consider multi-site nucleation of several droplets because the tensions of the membrane segments along the contact line of one droplet will now depend on the engulfment states of all droplets. Thus, the first few droplets that are nucleated at a membrane may become completely engulfed but the nucleation of additional droplets will effectively increase the membrane tension which tends to open the closed membrane necks up again and to allow the droplets to continue their growth.

We are currently extending our computational approach to address these nucleation and growth phenomena in a systematic manner as will be described in a subsequent studies.

In chapter five, we focussed on nanovesicles with a single lipid component and studied several distributions of lipid numbers N_{il} and N_{ol} within the two leaflets, keeping the total number $N = N_{\mathrm{il}} + N_{\mathrm{ol}}$ fixed (Figures 5.1 and 5.4, Table 5.3-5.6). As a consequence, we explored a certain range of leaflet tensions Σ_{il} and Σ_{ol} as depicted in Figures 5.3 and 5.5. For this tension range, the lipids did not undergo flip-flops between the two leaflets over the time scales of our simulations, which were of the order of 50 μs. However, such lipid flip-flops are expected to occur if the lipid numbers N_{il} and N_{ol} become sufficiently different and the resulting leaflet tensions sufficiently large. An interesting objective for future studies regarding the outcomes of chapter five is to determine the corresponding threshold values for the leaflet tensions. A related problem is the relaxation of multi-component bilayers that contain (at least) one lipid component such as cholesterol that undergoes frequent flip-flops even for relatively small leaflet tensions. For planar bilayers, it has been recently shown that these flip-flops lead to bilayers with tensionless leaflets [20].

One type of cellular nanovesicle that has attracted a lot of recent interest is provided by exosomes, small extracellular vesicles, which are increasingly investigated as biomarkers for diseases and as targeted drug delivery systems [136, 137, 138, 139]. Exosomes are produced within late endosomes or multivesicular bodies by inward budding of the endosomal membrane and are released to the extracellular environment after fusion of the multivesicular bodies with the plasma membrane [134, 135]. These nanovesicles have a specific lipid composition enriched in cholesterol [160, 161] and can attain a variety of different morphologies [162, 137], including long tube-like shapes. Such shapes could be formed at various stages of the exosomes' biogenesis: already in the multivesicular bodies or during exocytosis or after release into the extracellular medium. One possibility is that these different environments impose different osmotic conditions on the vesicles. If these changing conditions lead to strong osmotic deflation of the exosomes, their morphology can be transformed from spheres to long tube-like prolates as in Figure 5.1c. Alternatively, the shape of extracellular vesicles could be molded by the activity of flippases which are present in their membranes [163, 164] and translocate lipids from one leaflet to the other.

7 Appendix 1

7.1 The Interpretation of Lagrange Multiplier Tensions

In this appendix, we show that Lagrange multipliers are essentially the membrane segments mechanical tensions. We take a two-step minimization approach as proposed in Ref. [21], but it is generalized to the case of the membrane with two-segments.

7.1.1 Incompressible membrane

The shape free energy of incompressible membrane exposed to three distinct aqueous phases (see Figure 3.2 and 3.5) can be written in the form of:

$$\mathcal{E}^{inc}_{mem}\{\mathcal{S}\} = \sum_{i=\alpha,\beta}\left[\mathcal{E}^{i\gamma}_{be}\{\mathcal{S}\}+(P_\gamma-P_i)\mathcal{V}_i\{\mathcal{S}\} +\Sigma_{i\gamma}\mathcal{A}_{i\gamma}\{\mathcal{S}\}\right]+\Sigma_{\alpha\beta}\mathcal{A}_{\alpha\beta}\{\mathcal{S}\}+\lambda_{\alpha\beta\gamma}\mathcal{L}_{\alpha\beta\gamma}\{\mathcal{S}\} \tag{7.1}$$

here the superscript *inc* denotes that membrane is incompressible and the curly brackets refer to being a functional of membrane shape $\mathcal{S}$. This shape energy can be written as an energy function of explicit control parameters:

$$\begin{aligned} E^{inc}_{mem}(\Delta P_{\alpha\gamma}, \Delta P_{\beta\gamma}, \Sigma_{\alpha\gamma}, \Sigma_{\beta\gamma}) = \sum_{i=\alpha,\beta}\left[E^{i\gamma}_{be}(V_i, A_{i\gamma}) + (P_\gamma - P_i)V_i + \Sigma_{i\gamma}A_{i\gamma}\right] \\ + \Sigma_{\alpha\beta}A_{\alpha\beta} + \lambda_{\alpha\beta\gamma}L_{\alpha\beta\gamma} \end{aligned} \tag{7.2}$$

The membrane bending energy can be expressed as a function of area of membrane segment and droplet volume using Legendre transformation of membrane energy and can be expressed in two forms for the $\alpha\gamma$ and $\beta\gamma$ segments of the membrane:

$$\begin{aligned} E^{\alpha\gamma}_{be}(V_\alpha, A_{\alpha\gamma}) =& E^{inc}_{mem} - E^{\beta\gamma}_{be}(V_\beta, A_{\beta\gamma}) - \sum_{i=\alpha,\beta}\left[(P_\gamma - P_i)V_i + \Sigma_{i\gamma}A_{i\gamma}\right] - \Sigma_{\alpha\beta}A_{\alpha\beta} \\ & - \lambda_{\alpha\beta\gamma}L_{\alpha\beta\gamma} = \mathcal{E}^{\alpha\gamma}_{be}\{\mathcal{S}^{eq}\} \end{aligned} \tag{7.3}$$

and:

$$E_{be}^{\beta\gamma}(V_\beta, A_{\beta\gamma}) = E_{mem}^{inc} - E_{be}^{\alpha\gamma}(V_\alpha, A_{\alpha\gamma}) - \sum_{i=\alpha,\beta}\left[(P_\gamma - P_i)V_i + \Sigma_{i\gamma}A_{i\gamma}\right] - \Sigma_{\alpha\beta}A_{\alpha\beta} - \lambda_{\alpha\beta\gamma}L_{\alpha\beta\gamma} = \mathcal{E}_{be}^{\beta\gamma}\{\mathcal{S}^{eq}\} \tag{7.4}$$

the two Lagrange multipliers $\Sigma_{\alpha\gamma}$ and $\Sigma_{\beta\gamma}$, which are introduced to assure the constant area implies that:

$$\Sigma_{\alpha\gamma} = -\left(\frac{dE_{be}^{\alpha\gamma}(V_\alpha, A_{\alpha\gamma})}{dA_{\alpha\gamma}}\right)_{(V_\alpha, V_\beta, A_{\beta\gamma}, A_{\alpha\beta}, L_{\alpha\beta\gamma})} \tag{7.5}$$

$$\Sigma_{\beta\gamma} = -\left(\frac{dE_{be}^{\beta\gamma}(V_\beta, A_{\beta\gamma})}{dA_{\beta\gamma}}\right)_{(V_\alpha, V_\beta, A_{\alpha\gamma}, A_{\alpha\beta}, L_{\alpha\beta\gamma})} \tag{7.6}$$

7.1.2 Compressible membrane

Now we include compressibility of the membrane by including the stretching energy and allowing the membrane segment's areas to change without any constrains. The shape functional of the compressible membrane can be written as:

$$\mathcal{E}_{mem}^{com}\{\mathcal{S}\} = \sum_{i=\alpha,\beta}\left[\mathcal{E}_{be}^{i\gamma}\{\mathcal{S}\} + \mathcal{E}_{str}^{i\gamma}\{\mathcal{S}\} + (P_\gamma - P_i)\mathcal{V}_i\{\mathcal{S}\}\right] + \Sigma_{\alpha\beta}\mathcal{A}_{\alpha\beta}\{\mathcal{S}\} + \lambda_{\alpha\beta\gamma}\mathcal{L}_{\alpha\beta\gamma}\{\mathcal{S}\} \tag{7.7}$$

now we can take two step minimization procedure as Ref. [21]. First we minimize the shape functional in the presence of Lagrange multipliers which we obtain by the same equation as Eqs. 7.3 and 7.4, *i.e.,* by setting $E_{be}^{\alpha\gamma}(V_\alpha, A_{\alpha\gamma}) = \mathcal{E}_{be}^{\alpha\gamma}\{\mathcal{S}^{eq}\}$ and $E_{be}^{\beta\gamma}(V_\beta, A_{\beta\gamma}) = \mathcal{E}_{be}^{\beta\gamma}\{\mathcal{S}^{eq}\}$; where the $\mathcal{S}^{eq}$ denotes to the membrane equilibrium shape. In the second step, the elastic energy should be minimized for both membrane segments. The total elastic energy functional reads:

$$\sum_{i=\alpha,\beta}\left[\mathcal{E}_{el}^{i\gamma}\{\mathcal{S}^{eq}\}\right] = \sum_{i=\alpha,\beta}\left[\mathcal{E}_{be}^{i\gamma}\{\mathcal{S}^{eq}\} + \mathcal{E}_{str}^{i\gamma}\{\mathcal{S}^{eq}\}\right] \tag{7.8}$$

and since the stretching energy is an explicit function of the segment areas, thus one can minimize the equilibrium elastic energy function instead of the equilibrium energy shape functional. The total elastic energy function reads:

$$\begin{aligned}\sum_{i=\alpha,\beta}\Big[E_{el}^{i\gamma}(V_i, A_{\alpha\gamma})\Big] &= \sum_{i=\alpha,\beta}\Big[E_{be}^{i\gamma}(V_i, A_{i\gamma}) + E_{str}^{i\gamma}(A_{i\gamma})\Big] \\ &= \sum_{i=\alpha,\beta}\Big[E_{be}^{i\gamma}(V_i, A_{i\gamma}) + \frac{1}{2}K_{i\gamma}\frac{(A_{i\gamma} - A_{i\gamma}^{opt})^2}{A_{i\gamma}^{opt}}\Big]\end{aligned} \tag{7.9}$$

In equilibrium, the change of total elastic energy with respect to the change in membrane segment area reads:

$$\Big(\frac{dE_{el}^{\alpha\gamma}(V_\alpha, A_{\alpha\gamma})}{dA_{\alpha\gamma}}\Big)_{(V_\alpha, V_\beta)} = 0 \tag{7.10}$$

$$\Big(\frac{dE_{el}^{\beta\gamma}(V_\beta, A_{\beta\gamma})}{dA_{\beta\gamma}}\Big)_{(V_\alpha, V_\beta)} = 0 \tag{7.11}$$

which determines the two equilibrium areas $A_{\alpha\gamma} = A_{\alpha\gamma}^{eq}$ and $A_{\beta\gamma} = A_{\beta\gamma}^{eq}$ and the equilibrium condition leads to:

$$K_{\alpha\gamma}\frac{(A_{\alpha\gamma}^{eq} - A_{\alpha\gamma}^{opt})}{A_{\alpha\gamma}^{opt}} = -\Big(\frac{dE_{be}^{\alpha\gamma}(V_\alpha, A_{\alpha\gamma}^{eq})}{dA_{\alpha\gamma}^{eq}}\Big)_{(V_\alpha, V_\beta, A_{\beta\gamma}, A_{\alpha\beta}, L_{\alpha\beta\gamma})} \tag{7.12}$$

$$K_{\beta\gamma}\frac{(A_{\beta\gamma}^{eq} - A_{\beta\gamma}^{opt})}{A_{\beta\gamma}^{opt}} = -\Big(\frac{dE_{be}^{\beta\gamma}(V_\beta, A_{\beta\gamma}^{eq})}{dA_{\beta\gamma}^{eq}}\Big)_{(V_\alpha, V_\beta, A_{\alpha\gamma}, A_{\alpha\beta}, L_{\alpha\beta\gamma})} \tag{7.13}$$

the left hand sides of the Eq. 7.12 and Eq. 7.13 are membrane segments mechanical tensions by definition, where the right hand sides are Lagrange multiplier tension as derived in Eq. 7.5 and Eq. 7.6. This leads us to the conclusion that Lagrange multiplier tensions are equal to mechanical tensions $\Sigma_{\alpha\gamma} = \Sigma_{\alpha\gamma}^{mec}$ and $\Sigma_{\beta\gamma} = \Sigma_{\beta\gamma}^{mec}$, in equilibrium.

8 Appendix 2

8.1 Force Balance of Droplets at Membranes

8.1.1 Parametrization of an axisymmetric shape

In this appendix, we provide the detailed derivation of the force balance at the contact line between two aqueous phases enclosed inside vesicles and the membrane (see Figure 8.1 and Eq. 3.9) for vanishing spontaneous curvature [33]. The force balance has an identical form for a single droplet adhering to a membrane [29], as shown in Figures 3.2 and 3.5.

The free energy of two aqueous phases enclosed inside the vesicle, as shown in Fig-

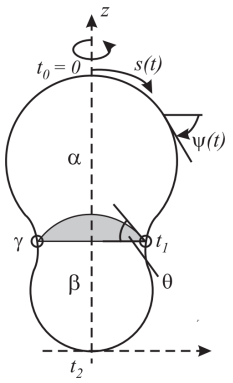

Figure 8.1. Cross section through an axisymmetric shape of a vesicle containing one α and one β droplet, with the axis of rotational symmetry aligned with the z-axis and the distance from this axis r. The arc length denoted by s, and the local tilt angle of the tangent by ψ . All of these variables depend on the contour parameter t with $t_0 = 0 \leq t \leq t_2$. The contact line is located at $t = t_1$. The gray area corresponds to the spherical cap with volume ΔV_β and tangent angle θ. The figure is adopted from Ref. 33.

ure 8.1, reads:

$$E = \sum_{i=\alpha,\beta} \left[\int dA_{i\gamma}[2\kappa_{i\gamma}(M-m_{i\gamma})^2+\kappa_{G,i\gamma}G]+(P_\gamma-P_i)V_i+\Sigma_{i\gamma}A_{i\gamma} \right] +\Sigma_{\alpha\beta}A_{\alpha\beta}+\lambda_{\alpha\beta\gamma}L_{\alpha\beta\gamma} \tag{8.1}$$

where M is the mean curvature of the vesicle which tries to adapt itself to the spontaneous curvatures $m_{\alpha\gamma}$ and $m_{\beta\gamma}$ of the two membrane segments. The bending rigidities and the Gaussian curvature moduli are denoted by $\kappa_{i\gamma}$ and $\kappa_{G,i\gamma}$ for the two membrane segments, respectively. The Lagrange multipliers $\Sigma_{i\gamma}$ and $(P_\gamma - P_i)$ are set to ensure that the area of the membrane segments and the droplet volumes are constant. We assume the identical bending rigidities and the Gaussian curvature moduli $\kappa_{\alpha\gamma} = \kappa_{\beta\gamma} = \kappa$ and $\kappa_{G,\alpha\gamma} = \kappa_{G,\beta\gamma}$ for both membrane segments, as well as vanishing spontaneous curvature $m_{i\gamma} = 0$, with $i = \alpha$ and β. Now we parametrize the energy of the membrane in axially symmetric geometry in cylindrical coordinates $(z(t), r(t))$ based on three parameters: distance from symmetry axis $r(t)$, local tilt angle $\psi(t)$ and the arc length $s(t)$, where t is the general contour parameter.

The volume contribution terms can be re-written as:

$$\sum_{i=\alpha,\beta}(P_\gamma - P_i)V_i = \sum_{i=\alpha,\beta}(P_\gamma - P_i)\int_i dt\pi s' r^2 sin\psi + (P_\alpha - P_\beta)\Delta V_\beta \tag{8.2}$$

now the second terms in the right-hand side of the Eq. 8.2 together with the interfacial energy in Eq. 8.1 can be parametrized by considering the area and the volume of the spherical cap and the Young-Laplace equation:

$$(P_\alpha - P_\beta)\Delta V_\beta + \Sigma_{\alpha\beta}A_{\alpha\beta} = \frac{-2\Sigma_{\alpha\beta}}{R}\Delta V_\beta + \Sigma_{\alpha\beta}A_{\alpha\beta} \tag{8.3}$$

where R is curvature radius of spherical cap. The spherical cap area and volume can be calculated as:

$$A_{\alpha\beta} = \int_0^\theta 2\pi R sin\omega R d\omega = 2\pi R^2(-cos\omega)\Big|_0^\theta = 2\pi R^2(1 - cos\theta) \tag{8.4}$$

and

$$\Delta V_\beta = \int_0^\theta \pi R^2 sin^2\omega R sin\omega d\omega = -\frac{1}{3}\pi R^3(3cos\omega - cos^3\omega)\Big|_0^\theta = \frac{1}{3}\pi R^3(2 - 3cos\theta + cos^3\theta) \tag{8.5}$$

substituting Eq. 8.4 and Eq. 8.5 into Eq. 8.3 leads to:

$$(P_\alpha - P_\beta)\Delta V_\beta + \Sigma_{\alpha\beta}A_{\alpha\beta} = \frac{2\pi}{3}(1 - cos^3\theta)\Sigma_{\alpha\beta}R^2 \tag{8.6}$$

$r_1 = Rsin\theta$ is the contact line radius. One can write:

$$cos^3\theta = \left[cos^2\theta\right]^{3/2} = \left[1 - sin^2\theta\right]^{3/2} = \left[1 - \left(\frac{r_1}{R}\right)^2\right]^{3/2} \tag{8.7}$$

Thus the right hand-side of Eq. 8.6 together with Eq. 8.7 can be written as:

$$\frac{2\pi}{3}(1 - cos^3\theta)\Sigma_{\alpha\beta}R^2 = \frac{2\pi}{3}\Sigma_{\alpha\beta}R^2\left[1 - \left[1 - \left(\frac{r_1}{R}\right)^2\right]^{3/2}\right] \tag{8.8}$$

Two local principal curvatures are $C_1 = \psi'/s'$ and $C_2 = sin\psi/r$ and $dA = 2\pi r ds(t) = 2\pi r s' dt$, where the prime indicates the derivative with respect to contour parameter t. The parametrized vesicle-droplet energy functional then has the form:

$$\frac{E}{2\pi} = \sum_{i=\alpha,\beta}\int dt\mathcal{L}_i + \lambda_{\alpha\beta\gamma}r + \frac{1}{3}\Sigma_{\alpha\beta}R^2\left[1 - \left[1 - \left(\frac{r_1}{R}\right)^2\right]^{3/2}\right] \tag{8.9}$$

with the Lagrange Functions:

$$\mathcal{L}_i = \frac{\kappa_i}{2}rs'\left(\frac{\psi'}{s'} + \frac{sin\psi}{r}\right)^2 + \Sigma_{i\gamma}rs' + \frac{1}{2}(P_\gamma - P_i)r^2 s' sin\psi + \Upsilon(r' - s'cos\psi) \tag{8.10}$$

here Υ is a Lagrange multiplier which is used to ensure the geometrical relation $r' = s'\cos\psi$.

8.1.2 First Variation

The first order variation of the energy functional Eq. 8.9 reads:

$$\begin{aligned}\frac{\delta E}{2\pi} = &\sum_{i=\alpha,\beta}\int_{t_1,i}^{t_2,i} dt\left\{\left[\frac{\partial\mathcal{L}_i}{\partial\psi_i} - \frac{d}{dt}\frac{\partial\mathcal{L}_i}{\partial\psi_i'}\right]\delta\psi + \left[\frac{\partial\mathcal{L}_i}{\partial r_i} - \frac{d}{dt}\frac{\partial\mathcal{L}_i}{\partial r_i'}\right]\delta r - \frac{d}{dt}\frac{\partial\mathcal{L}_i}{\partial s_i'}\delta s + \frac{\partial\mathcal{L}_i}{\partial\Upsilon}\delta\Upsilon\right\} \\ &+ \sum_{i=\alpha,\beta}\left\{\frac{\partial\mathcal{L}_i}{\partial\psi_i'}\delta\psi\Big|_{t_1,i}^{t_2,i} + \frac{\partial\mathcal{L}_i}{\partial r_i'}\delta r\Big|_{t_1,i}^{t_2,i} + \frac{\partial\mathcal{L}_i}{\partial s_i'}\delta s\Big|_{t_1,i}^{t_2,i}\right\} + \lambda_{\alpha\beta\gamma}\delta r + \Sigma_{\alpha\beta}r_1 cos\theta\delta r\end{aligned} \tag{8.11}$$

where the last term on the right-hand side of Eq. 8.11 is the first variation of Eq. 8.8 which reads:

$$\begin{aligned}\left\{\frac{2\pi}{3}\Sigma_{\alpha\beta}R^2\left[1-\left[1-\left(\frac{r_1}{R}\right)^2\right]^{3/2}\right]\right\}\delta r &= \frac{2\pi}{3}\Sigma_{\alpha\beta}R^2\left[-\frac{3}{2}\left[1-\left(\frac{r_1}{R}\right)^2\right]^{1/2}\times\left(-\frac{2}{R^2}r_1\right)\right]\\ &= 2\pi\Sigma_{\alpha\beta}\left[\left[1-\left(\frac{r_1}{R}\right)^2\right]^{1/2}r_1\right]\\ &= 2\pi\Sigma_{\alpha\beta}\left[\left[1-sin^2\theta\right]^{1/2}r_1\right]\\ &= 2\pi\Sigma_{\alpha\beta}\left[\left[cos^2\theta\right]^{1/2}r_1\right]\\ &= 2\pi\Sigma_{\alpha\beta}r_1 cos\theta\end{aligned} \tag{8.12}$$

8.1.3 Shape Equations

At equilibrium $\delta E = 0$, thus all terms in the first variation Eq. 8.11 should vanish. The bulk terms vanish when the Euler-Lagrange equation satisfies the conditions:

$$\begin{aligned}\left[\frac{\partial\mathcal{L}_i}{\partial\psi_i}-\frac{d}{dt}\frac{\partial\mathcal{L}_i}{\partial\psi_i'}\right]\delta\psi &= 0\\ \left[\frac{\partial\mathcal{L}_i}{\partial r_i}-\frac{d}{dt}\frac{\partial\mathcal{L}_i}{\partial r_i'}\right]\delta r &= 0\\ \left[-\frac{d}{dt}\frac{\partial\mathcal{L}_i}{\partial s_i'}\right]\delta s &= 0\\ \left[\frac{\partial\mathcal{L}_i}{\partial\Upsilon}\right]\delta\Upsilon &= 0\end{aligned} \tag{8.13}$$

which leads to the shape equations:

$$\begin{aligned}
\ddot{\psi} &= \frac{cos\psi sin\psi}{r^2} - \frac{\dot{\psi}}{r}cos\psi + \frac{(P_\gamma - P_i)}{2\kappa_i}rcos\psi + \frac{\Upsilon}{\kappa_i r}sin\psi \\
\dot{\Upsilon} &= \frac{k_i}{2}\dot{\psi}^2 - \frac{k_i sin^2\psi}{2r^2} + \Sigma_{i\gamma} + (P_\gamma - P_\alpha)rsin\psi \\
\dot{r} &= cos\psi
\end{aligned} \tag{8.14}$$

here the overdots denote to the derivative with respect to the arc length s, which is obtained by reparametrization of the shape using the s.

8.1.4 Boundary Conditions

By considering the fixed tilt angle of the membrane at the symmetry axis, one gets $\delta\psi(t_0) = \delta\psi(t_2) = 0$ and by coupling of the shape of two segments at contact line one obtains $\delta\psi(t_1 - \epsilon) = \delta\psi(t_1 + \epsilon) = \delta\psi(t_1)$. The stationarity of E with respect to the variation of $\delta\psi \neq 0$ leads to:

$$\begin{gathered}
\frac{\partial\mathcal{L}_\alpha}{\partial\psi'}\delta\psi\Big|_{t_0}^{t_1-\epsilon} + \frac{\partial\mathcal{L}_\beta}{\partial\psi'}\delta\psi\Big|_{t_1+\epsilon}^{t_2} = 0 \\
\left(\frac{\partial\mathcal{L}_\alpha}{\partial\psi'}\Big|_{t_1-\epsilon} - \frac{\partial\mathcal{L}_\beta}{\partial\psi'}\Big|_{t_1+\epsilon}\right)\delta\psi(t_1) = 0 \\
\frac{\partial\mathcal{L}_\alpha}{\partial\psi'}\Big|_{t_1-\epsilon} = \frac{\partial\mathcal{L}_\beta}{\partial\psi'}\Big|_{t_1+\epsilon}
\end{gathered} \tag{8.15}$$

using the Lagrange function Eq. 8.10 one obtains:

$$\frac{\partial\mathcal{L}(t)_i}{\partial\psi'} = \kappa_i r(t)\left(\frac{\psi'(t)_i}{s'(t)} + \frac{sin\psi(t)}{r(t)}\right) \tag{8.16}$$

and assuming the same curvature-elastic properties in both membrane segments (*i.e.* $\kappa_\alpha = \kappa_\beta$ and $m_{\alpha\gamma} = m_{\beta\gamma} = 0$) one obtains the first boundary condition at $s(t_1) = s_1$:

$$\dot{\psi}(s_1)_\alpha = \dot{\psi}(s_1)_\beta \tag{8.17}$$

where the overdot denotes the derivation with respect to the arc length s. This boundary condition represents the torque balance at the contact line

By considering the fixed radius of the membrane at the symmetry axis one gets $\delta r(t_0) = \delta r(t_2) = 0$ and by coupling of the shape of two segments at contact line one obtains $\delta r(t_1 - \epsilon) = \delta r(t_1 + \epsilon) = \delta r(t_1)$. The stationarity of E with respect to variation of $\delta r \neq 0$ leads to:

$$\begin{gathered}\frac{\partial \mathcal{L}_\alpha}{\partial r'}\delta r\Big|_{t_0}^{t_1-\epsilon} + \frac{\partial \mathcal{L}_\beta}{\partial r'}\delta r\Big|_{t_1+\epsilon}^{t_2} + \lambda_{\alpha\beta\gamma}\delta r + \Sigma_{\alpha\beta} r cos\theta \delta r = 0 \\ \left(\frac{\partial \mathcal{L}_\alpha}{\partial r'}\Big|_{t_1-\epsilon} - \frac{\partial \mathcal{L}_\beta}{\partial r'}\Big|_{t_1+\epsilon} + \lambda_{\alpha\beta\gamma} + \Sigma_{\alpha\beta} cos\theta r\right)\delta r(t_1) = 0\end{gathered} \tag{8.18}$$

using the Lagrange function Eq. 8.10 one obtains $\dfrac{\partial \mathcal{L}_i(t)}{\partial r'}\delta r = \Upsilon(t)$, and thus the second boundary condition reads:

$$\Upsilon(t_1 + \epsilon) - \Upsilon(t_1 - \epsilon) = \lambda_{\alpha\beta\gamma} + \Sigma_{\alpha\beta} cos\theta r(t_1) \tag{8.19}$$

which can be reparametrize with respect to the arc length s as:

$$\Upsilon(s_1 + \epsilon) - \Upsilon(s_1 - \epsilon) = \lambda_{\alpha\beta\gamma} + \Sigma_{\alpha\beta} cos\theta R(s_1) \tag{8.20}$$

By considering the fixed arc length of the membrane at the symmetry axis, one obtains $\delta s(t_0) = \delta s(t_2) = 0$ and by coupling of the shape of two segments at contact line one obtains $\delta s(t_1 - \epsilon) = \delta s(t_1 + \epsilon) = \delta s(t_1)$. The stationarity of E with respect to variation of $\delta s \neq 0$ leads to:

$$\begin{gathered}\frac{\partial \mathcal{L}_\alpha}{\partial s'}\delta s\Big|_{t_0}^{t_1-\epsilon} + \frac{\partial \mathcal{L}_\beta}{\partial s'}\delta s\Big|_{t_1+\epsilon}^{t_2} = 0 \\ \left(\frac{\partial \mathcal{L}_\alpha}{\partial s'}\Big|_{t_1-\epsilon} - \frac{\partial \mathcal{L}_\beta}{\partial s'}\Big|_{t_1+\epsilon}\right)\delta s(t_1) = 0 \\ \frac{\partial \mathcal{L}_\alpha}{\partial s'}\Big|_{t_1-\epsilon} = \frac{\partial \mathcal{L}_\beta}{\partial s'}\Big|_{t_1+\epsilon}\end{gathered} \tag{8.21}$$

using the Lagrange function Eq. 8.10 one obtains:

$$\frac{\partial \mathcal{L}_i(t)}{\partial s'(t)} = \frac{\kappa^i r(t)}{2}\left[-\Big(\frac{\psi'(t)}{s'(t)}\Big)^2+\Big(\frac{sin\psi(t)}{r(t)}\Big)^2\right]+\Sigma_{i\gamma}r(t)+\frac{P_\gamma - P_i}{2}r^2(t)sin\psi(t)-\Upsilon(t)cos\psi(t) \tag{8.22}$$

then Eq. 8.21 can be rewritten as:

$$\begin{aligned}
&\frac{\kappa_\alpha r(t_1)}{2}\left[-\Big(\frac{\psi'(t_1-\epsilon)}{s'(t_1-\epsilon)}\Big)^2+\Big(\frac{sin\psi(t_1)}{r(t_1)}\Big)^2\right]\\
&+\Sigma_{\alpha\gamma}r(t_1)+\frac{P_\gamma - P_\alpha}{2}r^2(t_1)sin\psi(t_1)-\Upsilon(t_1-\epsilon)cos\psi(t_1)=\\
&\frac{\kappa_\beta r(t_1)}{2}\left[-\Big(\frac{\psi'(t_1+\epsilon)}{s'(t_1+\epsilon)}\Big)^2+\Big(\frac{sin\psi(t_1)}{r(t_1)}\Big)^2\right]\\
&+\Sigma_{\beta\gamma}r(t_1)+\frac{P_\gamma - P_\beta}{2}r^2(t_1)sin\psi(t_1)-\Upsilon(t_1+\epsilon)cos\psi(t_1)
\end{aligned} \tag{8.23}$$

assuming the continuity of $r(s)$ and $\psi(s)$ along the contact line as well as the same curvature-elastic properties in the two membrane segments (*i.e.* $\kappa_\alpha = \kappa_\beta$ and $m_{\alpha\gamma} = m_{\beta\gamma} = 0$) together with the first boundary condition Eq. 8.17, we derive:

$$\begin{aligned}
\Sigma_{\beta\gamma}r(t_1)-\Sigma_{\alpha\gamma}r(t_1) &= cos\psi(t_1)\Big(\Upsilon(t_1+\epsilon)-\Upsilon(t_1-\epsilon)\Big)+\frac{P_\beta - P_\alpha}{2}r^2(t_1)sin\psi(t_1)\\
\Sigma_{\beta\gamma}r(t_1)-\Sigma_{\alpha\gamma}r(t_1) &= cos\psi(t_1)\Big(\Upsilon(t_1+\epsilon)-\Upsilon(t_1-\epsilon)\Big)+\Sigma_{\alpha\beta}r(t_1)sin\theta sin\psi(t_1)\\
\Sigma_{\beta\gamma}-\Sigma_{\alpha\gamma} &= \frac{cos\psi(t_1)}{r(t_1)}\Big(\Upsilon(t_1+\epsilon)-\Upsilon(t_1-\epsilon)\Big)+\Sigma_{\alpha\beta}sin\theta sin\psi(t_1)
\end{aligned} \tag{8.24}$$

where the Young-Laplace equation is used $P_\beta - P_\alpha = (2\Sigma_{\alpha\beta}sin\theta)/r$. Reparametrization of Eq. 8.24 with respect to the arc length s leads to:

$$\Sigma_{\beta\gamma}-\Sigma_{\alpha\gamma} = \frac{cos\psi(s_1)}{r(s_1)}\Big(\Upsilon(s_1+\epsilon)-\Upsilon(s_1-\epsilon)\Big)+\Sigma_{\alpha\beta}sin\theta sin\psi(s_1) \tag{8.25}$$

The first shape equation Eq. 8.14 together with the assumption of the continuity of

$r(s)$ and $\psi(s)$ along the contact line gives:

$$\begin{aligned}
\ddot{\psi}_\beta - \ddot{\psi}_\alpha &= \frac{sin\psi(s_1)}{\kappa r(s_1)}(\Upsilon(s_1+\epsilon) - \Upsilon(s_1-\epsilon) - \frac{(P_\gamma - P_\alpha)}{2\kappa} r(s_1) cos\psi(s1) \\
&\quad + \frac{(P_\gamma - P_\beta)}{2\kappa} r(s_1) cos\psi(s_1) \\
\ddot{\psi}_\beta - \ddot{\psi}_\alpha &= \frac{sin\psi(s_1)}{\kappa r(s_1)}(\Upsilon(s_1+\epsilon) - \Upsilon(s_1-\epsilon)) - \frac{(P_\beta - P_\alpha)}{2\kappa} r(s_1) cos\psi(s_1) \\
\ddot{\psi}_\beta - \ddot{\psi}_\alpha &= \frac{sin\psi(s_1)}{\kappa r(s_1)}(\Upsilon(s_1+\epsilon) - \Upsilon(s_1-\epsilon)) - \frac{\Sigma_{\alpha\beta}}{\kappa} sin\theta cos\psi(s_1)
\end{aligned} \tag{8.26}$$

By substituting the second boundary condition Eq. 8.20 into Eq. 8.25 we obtain:

$$\begin{aligned}
\Sigma_{\beta\gamma} - \Sigma_{\alpha\gamma} &= \frac{cos\psi(s_1)}{r(s_1)}\Big(\lambda_{\alpha\beta\gamma} + \Sigma_{\alpha\beta} cos\theta r(s_1)\Big) + \Sigma_{\alpha\beta} sin\theta sin\psi(s_1) \\
\Sigma_{\beta\gamma} - \Sigma_{\alpha\gamma} &= cos\psi(s_1)\frac{\lambda_{\alpha\beta\gamma}}{r(s_1)} + \Big(cos\theta cos\psi(s_1) + sin\theta sin\psi(s_1)\Big)\Sigma_{\alpha\beta}
\end{aligned} \tag{8.27}$$

Similarly, by substituting the second boundary condition Eq. 8.20 into Eq. 8.26 we obtain:

$$\begin{aligned}
\ddot{\psi}_\beta - \ddot{\psi}_\alpha &= \frac{sin\psi(s_1)}{\kappa r(s_1)}\Big(\lambda_{\alpha\beta\gamma} + \Sigma_{\alpha\beta} cos\theta r(s_1)\Big) - \frac{\Sigma_{\alpha\beta}}{\kappa} sin\theta cos\psi(s_1) \\
\ddot{\psi}_\beta - \ddot{\psi}_\alpha &= \frac{sin\psi(s_1)}{\kappa r(s_1)}\lambda_{\alpha\beta\gamma} + \Big(cos\theta sin\psi(s_1) - sin\theta cos\psi(s_1)\Big)\frac{\Sigma_{\alpha\beta}}{\kappa}
\end{aligned} \tag{8.28}$$

By knowing the geometrical relations of $\theta^*_\alpha = \psi(s_1) - \theta$ one can write:

$$cos(\theta^*_\alpha) = sin\psi(s_1) sin\theta + cos\psi(s_1) cos\theta \tag{8.29}$$

$$sin(\theta^*_\alpha) = sin\psi(s_1) cos\theta - cos\psi(s_1) sin\theta \tag{8.30}$$

where θ^*_α is called intrinsic contact angle. Thus the second equations in Eqs. 8.27 and 8.28 can be written in alternative form of:

$$\Sigma_{\beta\gamma} - \Sigma_{\alpha\gamma} = \Sigma_{\alpha\beta} cos\theta^*_\alpha + \frac{\lambda_{\alpha\beta\gamma}}{R_{co}} cos\psi_{co} \tag{8.31}$$

$$\ddot{\psi}_\beta - \ddot{\psi}_\alpha = \frac{\Sigma_{\alpha\beta}}{\kappa} sin\theta^*_\alpha + \frac{\lambda_{\alpha\beta\gamma}}{\kappa R_{co}} sin\psi_{co} \tag{8.32}$$

where $R_{co} = R(s_1)$ is the contact line radius and $\psi_{co} = \psi(s_1)$ in the angle between the vesicle contour and the projected contact line. The boundary conditions Eqs. 8.31 and 8.32 describe the tangential and perpendicular force balance, respectively, along the contact line of smoothly curved membrane.

9 Appendix 3

9.1 Calculation of the Bending Energy of Membranes from MD Trajectories

Calculation of bending energy from particle-based molecular dynamics simulations (MD) based on the curvature-elastic model, requires the construction of a bilayer surface. This can for example be based on the position of head-group beads. A practical way is to construct a triangulated mesh from the bead coordinates and find the mean-curvature and area for each vertex on the mesh. Then using the Helfrich bending energy one can calculate the bending energy. To do this, the bending rigidity of the membrane still needs to be estimated separately using the area compressibility modulus or the membrane fluctuation spectrum. Because of the thermal fluctuations in MD simulations, such triangulations lead to a very rough surface with extremely high bending energy, because of numerous kinks on the mesh which are formed during triangulation. To reduce such roughness, we use the mean face normal filter for smoothing the triangular mesh. Such a smoothing procedure can either be applied iteratively for a finite number of steps or terminated after an energy criterion is met, *e.g.,* the bending energy change corresponding to one iteration falls below the energy threshold.
The continuum model predicts zero bending energy for the flat membrane and $8\pi\kappa$ for a spherical vesicle, respectively, for vanishing spontaneous curvature. Here we test our protocol to calculate the bending energy for control systems of the flat membrane and a vesicle with vanishing spontaneous curvature. The calculated numerical bending energy from the proposed protocol is in good agreement with the theoretical predictions. Finally, we have applied the method to calculate system of non-trivial geometry of the membrane bud with an elongated neck as shown in chapter three. The present method can also be applied to calculate the energy arising from the area difference of the bilayer leaflets as well as the stretching energy.

Theory

Helfrich bending energy. The energy of an elastic membrane can be described using Helfrich bending energy by:

$$E_b = 2\kappa \int (M - m)^2 dA \tag{9.1}$$

where κ is bending energy, m is spontaneous curvature, M is the mean curvature, and dA is the area element of the elastic surface. Helfrich energy describes the bending energy of a continuum thin surface. However, lipid bilayers are discrete surfaces because of molecular excluded volume. In addition, due to thermal fluctuations, the atoms which belong to lipid hydrophilic head group, can be considered as the cloud of points. It is the same for the model of membrane in particle-based simulations. Even though constructing such a continuum surface from the cloud of points is challenging, yet, one can build a discrete surface using a triangulated mesh from the coordinates of lipid head beads. Then, a plausible alternative of continuum bending energy is the discrete counterpart of the Helfrich energy functional:

$$E_b = 2\kappa \sum_v (M_v - m_v)^2 A_v \tag{9.2}$$

where the summation is over all vertices and subscript v denotes the vertex. Here A_v is an effective vertex area. Since each facet has three vertices, the associated area of each vertex is $A_v = A_{nf}/3$ where A_{nf} is the total area of the neighboring facets of vertex v. As a consistency check, if we calculate the the total membrane area A using summation over the facet areas A_f, the outcome is identical to the sum over the effective vertex area $A = \sum_f A_f = \sum_v A_v$.

Stretching energy. When the area of the membrane A deviates from the optimal packing area A_0, then membrane experiences a mechanical tension in the form of stretching or compression. This would lead to another source of energy termed by stretching energy:

$$E_{st} = (1/2)K_A \frac{(A - A_0)^2}{A_0} \tag{9.3}$$

where K_A is the area compressibility modulus. The stretching energy contributions can be calculated from the area of membrane midsurface using the simple expression:

$$A = \sum_f A_f = \sum_v A_v \tag{9.4}$$

where membrane area A can be estimated both from the sum of facet area A_f or sum of the effective area of vertex A_v. Area compressibility modulus still has to be determined separately via tension change as a function of area dilation $\Sigma_{mech} = K_A(A - A_0)/A_0$ or from bending rigidity by $\kappa = K_A \ell_{me}^2/48$.

Area difference elasticity. The area difference between leaflets can introduce an extra energy contribution to the total energy of the system. This energy contribution is

expressed in the area difference elasticity model:

$$E_{ADE} = \frac{\kappa_\Delta \pi}{2A\ell_{me}^2}(\Delta A - \Delta A_0)^2 \tag{9.5}$$

where κ_d is the non-local bending rigidity, ℓ_{me} is the membrane thickness, A is the total area of the membrane and ΔA_0 is the optimal area difference of the two leaflets in vanishing tension and ΔA is the area difference of two leaflets under tension. The latter energy contributions can be calculated from the area of membrane leaflets using the simple expression:

$$\Delta A = \sum_{f \in f_{out}} A_f - \sum_{f \in f_{in}} A_f \tag{9.6}$$

here f_{out} and f_{in}, are the facets in outer and inner leaflet, respectively.

9.1.1 Numerical algorithm

In MD simulations, due to thermal fluctuations, lipid head beads can delocalize along the membrane normal and form a layer with finite thickness. Thus, immediate construction of triangulated surfaces from MD trajectories results in a very rough surface full of sharp kinks with very high bending energy output. Such artificial high-energy can be resolved if we systematically smooth the surface. Here we tackle this issue using an easy-to-use protocol. First, we introduce the method for finding the midsurface. Second, we explain the triangulation procedure and the parameters that can affect the quality of the mesh. And finally, we elaborate on the calculation of mean curvature and smoothing algorithm.

Construction of the bilayer midsurface and leaflet surface. For a flat lipid bilayer it is rather easy to find the midsurface by averaging the height function. Even for vesicles with spherical geometry, it is possible to find the midsurface using the Cartesian coordinate transformation into the spherical coordinate system. However, for highly deformed bilayer with non-trivial shape, none of those methods can be applied to calculate the midsurface. Here we use a relatively easy and fast algorithm to find the midsurface using the nearest neighbor scheme. We first construct a list of the nearest neighbors from the other leaflet for each lipid head beads in each leaflet. Then we find the arithmetic average of the Cartesian coordinates of these neighbors which should lie in the midsurface. On the other hand, construction of the leaflet surface is relatively easy. To construct the leaflet surface, one can take the head bead coordinates separately in each leaflets of the bilayer and find the alpha shape of two leaflet surfaces. Caution should be applied when choosing the number of neighbors used for averaging.

The number of neighbor beads depends on the density of lipids, and it should be tuned for different models. For instance, the choice of 10-20 nearest neighbors seems reasonable for dissipative particle dynamic (DPD) models used in this thesis.

Triangulation of the membrane surface. Delaunay triangulation is a conventional way of surface reconstruction from the cloud of points. Employing this method, along with criteria for finding alpha shapes (*i.e.*, class of piecewise linear curves related to the shape of cloud of points), leads to a very powerful tool in surface reconstruction. There is a shrinkage factor s associated with all triangulation algorithms which affects the alpha-shape. The choice of a small shrinkage factor leads to formation of holes in the triangulated surface while a large shrinkage factor results in an unintended connection between adjacent parts of the deformed membrane in one leaflet. A reasonable choice of shrinkage factor would be $s = 3$ for DPD models. This factor should be tuned for other models.

Calculation of the mean curvature. Mean curvature is the average of the principal curvatures $M = (C_1 + C_2)/2$. In the discrete form of the surface, M can be calculated by different numerical schemes. Here, we calculate the mean curvature M_v of a vertex in three consecutive steps:

1. Mesh is rotated to be described in the XY plane, where the normal vector of the vertex lines up in [-1 0 0] direction.

2. A least-squares quadratic patch $f(x, y) = ax^2 + by^2 + cxy + dx + ey + g$ is used to fit the local neighborhood of each vertex

3. The vertex mean curvature (M_v) is calculated from the eigenvectors and eigenvalues of the Hessian matrix. In summary, Hessian of the function $f(x, y)$ reads

$$H(f) = \begin{bmatrix} f_{xx} & f_{xy} \\ f_{yx} & f_{yy} \end{bmatrix} = \begin{bmatrix} 2a & c \\ c & 2b \end{bmatrix} \tag{9.7}$$

where the matrix is symmetric $f_{xy} = f_{yx}$. In order to find the eigenvalues of the Hessian $|H(f) - CI| = 0$ we need to find the roots of following quadratic equation $C^2 - (f_{xx} + f_{yy})C + (f_{xx}f_{yy} - f_{xy}^2) = 0$, where the two roots are the principal curvatures:

$$C_1 \ \& \ C_2 = \frac{1}{2}\left(f_{xx} + f_{yy} \pm \sqrt{(f_{xx} - f_{yy})^2 + 4f_{xy}^2}\right) \tag{9.8}$$

for the function $f(x, y)$ the mean curvature will boil down into a simple expression: $M = \frac{1}{2}(C_1 + C_2) = a + b$.

The algorithm has been introduced by Dirk-Jan Kroon [101]. The second and third neighbor list of each vertex can be used for fitting. Using the third neighbor of vertices for fitting makes the curvature of the surface smoother but less local.

Smoothing of the triangulated mesh using mean face normal filter. Among the methods used for triangulated mesh denoising, the mean face normal filter [102] is one of the most robust algorithms which exclude drawbacks such as oversmoothing [165]. In summary, the mean face normal filter works based on averaging of the facet normals in three consecutive steps:

1. For each facet on the mesh compute the facet normal $\mathbf{n}$(f) and calculate the area weighted average:
$$\mathbf{m}_w(f) = \frac{1}{\sum A_n} \sum_{nf} A_{nf} \mathbf{n}(f) \tag{9.9}$$
where nf refers to all the neighboring facets with a common vertex or edge with facet f.

2. Normalize the average normal:
$\mathbf{m}_w(f) \leftarrow \frac{\mathbf{m}_w(f)}{||\mathbf{m}_w(f)||}$

3. For each vertex of the facet f update the vertex position $\mathbf{X(v)}$:
$$\mathbf{X}_{new}(v) \leftarrow \mathbf{X}_{old}(v) + \frac{1}{\sum A(f)} \sum A(f)\mathbf{P}(f) \tag{9.10}$$
where vector $\mathbf{P} = [\overrightarrow{XC}.\mathbf{m}_w(f)]\mathbf{m}_w(f)$ is the projection of $\overrightarrow{XC}$ onto the direction of the $\mathbf{m}_w(f)$ and C is the centroid of the facet. The summation is taken for all neighboring facets of vertex v.

Applying these three steps iteratively leads to a smooth triangulated surface without sharp kinks. Normally 10-30 iterations seem to be enough for convergence [102] of most of the noisy meshes, see Figures 9.1, 9.2 and 9.3. In the case of lipid membranes, one can use a bending energy criterion for smoothing. For instance, one can calculate the bending energy of the surface after each step of smoothing. Then, if the energy difference of two consecutive steps $|\Delta E_b|$ falls below a specified energy tolerance E_T we can stop the smoothing procedure ($|\Delta E_b| < E_T$), Fig.9.4. The choice of a very low energy tolerance leads to very slow convergence and oversmoothing of the mesh.

Such oversmoothing leads to two different unintended outcomes, i) vanishing the small undulation on the membrane and/or ii) removing the large deformations of highly curved segments of the membrane.

Numerical algorithm in summary. Our protocol for calculation of the bending energy follows six main steps:

1. Construction of membrane surface from head groups coordinates, separately for inner and outer leaflets or for membrane midsurface.
2. Triangulation of each surface based on the Delaunay scheme combined with alpha-shape criteria.
3. Calculation of the vertex mean curvature M_v and the effective vertex area A_v.
4. Calculation of the bending energy based on the discrete expression of Helfrich energy Eq. 9.2.
5. Smoothing the triangulated mesh using the mean face normal filter [102].
6. Repeating steps 3 to 5 until reaching to the specified number of smoothing steps, or once bending energy change is below specified threshold $|\Delta E_b| < E_T$.

9.1.2 Control systems:

To test the proposed algorithm, we first need to calibrate the protocol for systems of flat membrane patches and the spherical vesicles. A flat membrane and a spherical vesicle are a good choice since we know the theoretical estimate for their bending energies as discussed earlier.

The flat membrane has zero curvature. Thus the bending energy is zero for vanishing spontaneous curvature in minimum energy state. However, The calculated energy should be slightly higher than the theoretical estimate because of the undulations caused by thermal fluctuations in MD simulations, see Figure 9.1.

A spherical vesicle has a constant mean curvature $M = 1/R$ and a constant area $A = 4\pi R^2$. Thus for vanishing spontaneous curvature, the bending energy reads $E_b = 2\kappa_A(1/R^2)4\pi R^2 = 8\pi\kappa$. If the algorithm reproduces a numerical outcome close to the theoretical estimate, it can be considered a reliable method and can be applied to geometries with more complex shapes.

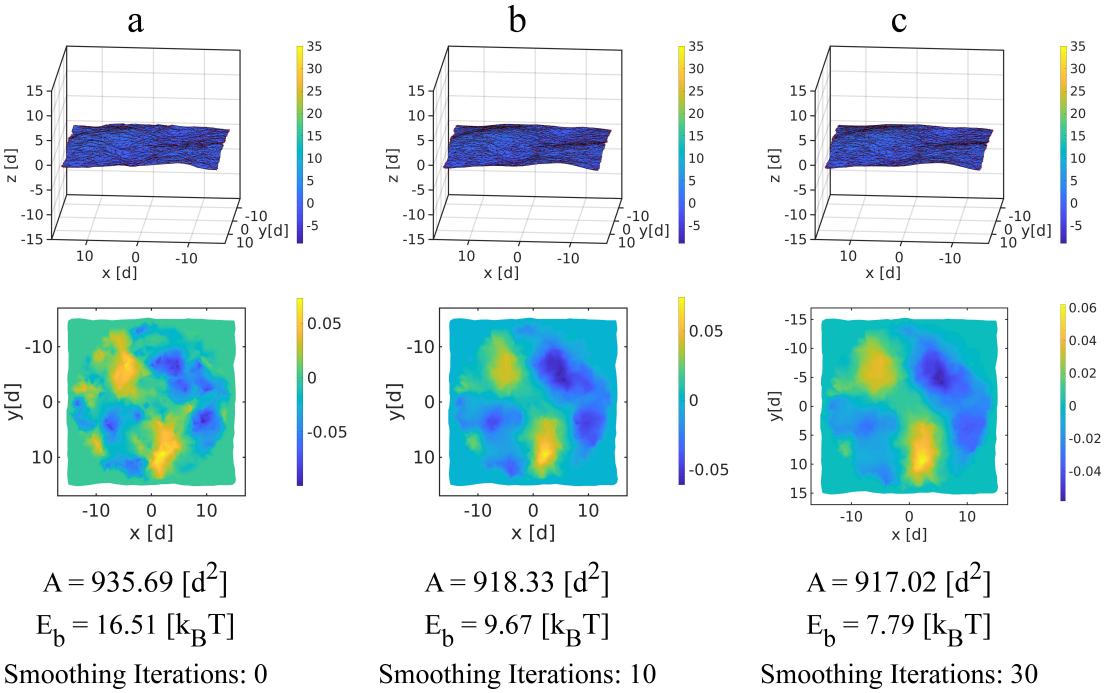

Figure 9.1. Triangulated mesh and calculated mean curvature for the midsurface of a flat membrane from DPD simulations. The panel in the top row shows the side view of the triangulated mesh, and the bottom row shows the top view of the calculated mean curvature. The column (a-c) show the effect of smoothing iteration on the quality of the mesh and the total area and the bending energy.

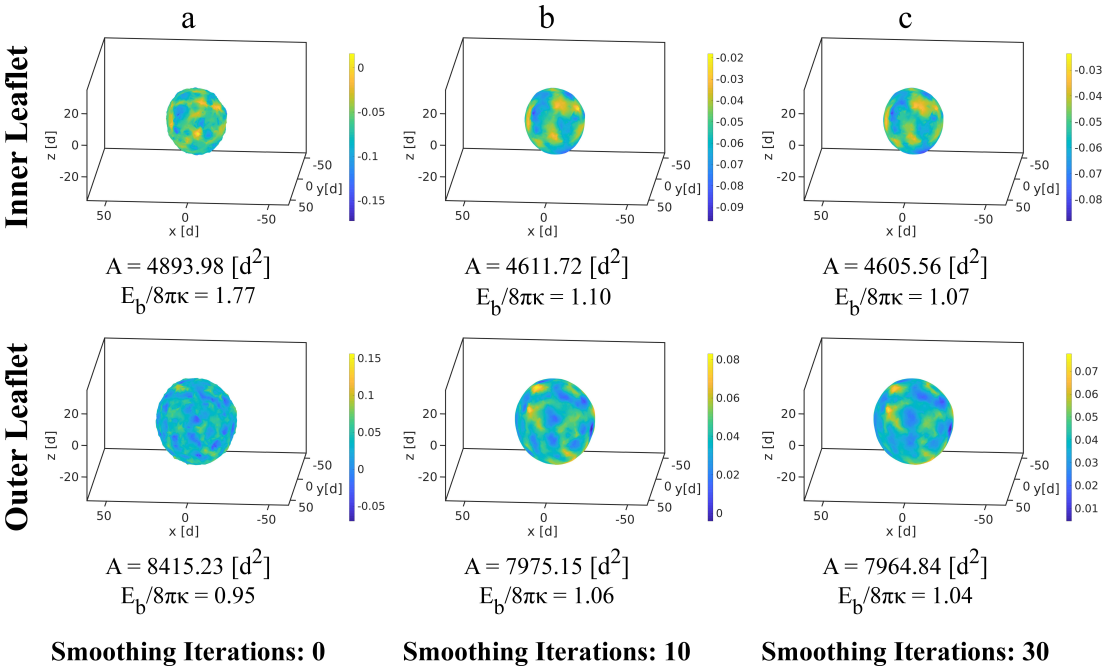

Figure 9.2. Calculated mean curvature for the inner leaflet and outer leaflet of a vesicle from DPD simulations. The panel in the top row shows the side view of the calculated mean curvature for the inner leaflet and the panel in the bottom row shows the same calculations for the outer leaflet. The columns (a-c) show the effect of smoothing iteration on the quality of the mesh and the total area and the bending energy.

In addition, we studied the effect of the smoothing iterations on the calculated total area and energy for both membrane leaflets, see Figure 9.3. The result suggests that 30 steps of smoothing seem reasonable, as the area and energy converge to the expected values.

Finally, we have applied the method to calculate bending energy and the area of non-trivial geometry of the membrane bud with an elongated neck, as shown in Figure 9.4. The effect of smoothing algorithms on the calculated bending energy is also investigated. We find that face normal smoothing performs better compared to Laplacian smoothing, see Figure 9.4. Face normal smoothing can remove the kinks in the initial triangulated mesh but do not affect the large undulations and the general geometry. However, the Laplacian smoothing, remove the kinks and change the geometry of the membrane in highly curved segments, compare the neck region in Figure 9.4a-d.

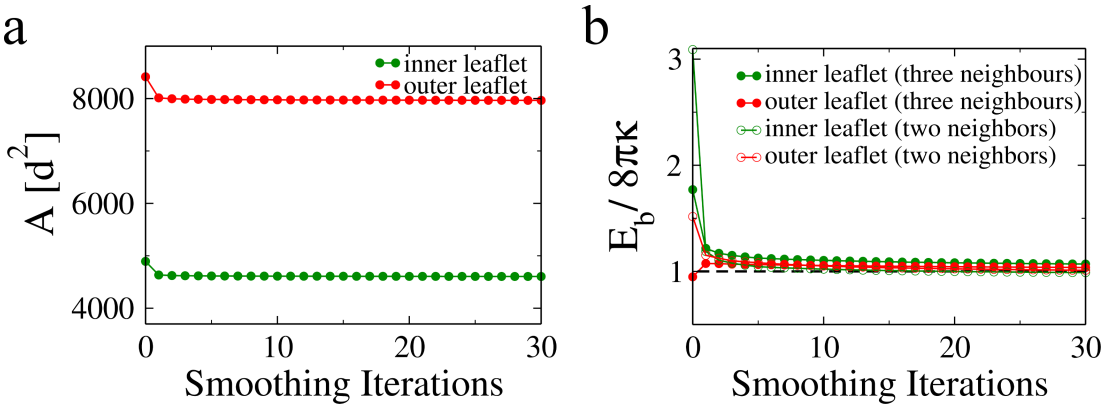

Figure 9.3. a) The effect of smoothing iteration on the calculated total area for both membrane leaflets of spherical vesicle, and b) The effect of smoothing iteration and the second and third neighbor vertices, adapted for fitting in mean curvature calculation, on the calculated bending energy for both vesicle leaflets.

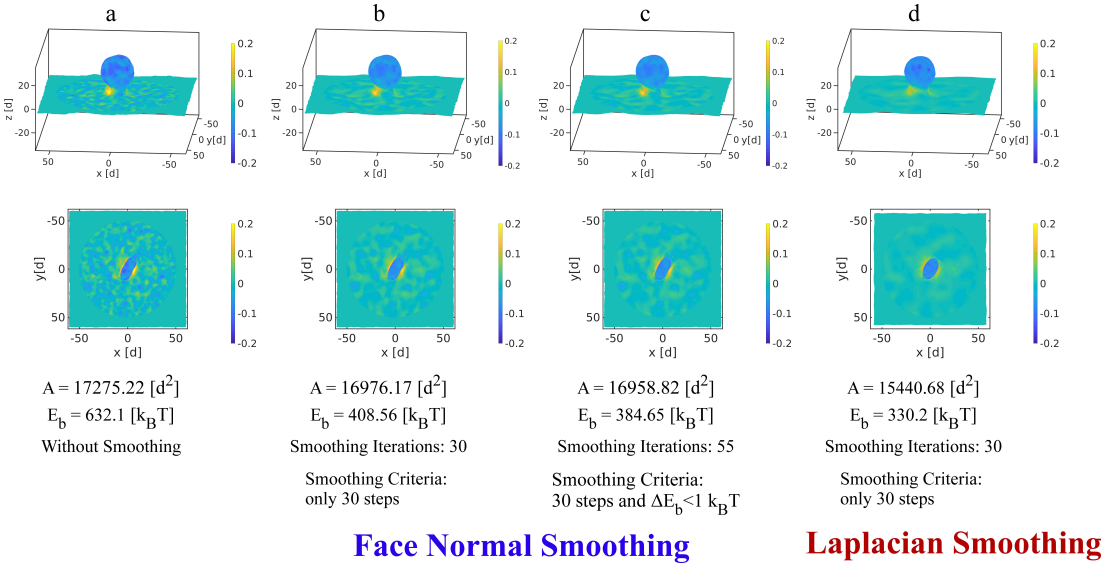

Figure 9.4. The effect of smoothing criteria on the calculated bending energy. a) Initial mesh without smoothing. b) Only 30 steps of face normal smoothing are used. c) The smoothing is initiated with 30 steps of face normal smoothing, and then the energy criteria are used to perform extra face normal smoothing steps. If the energy difference of two consecutive steps is $\Delta E < 1\ k_BT$ then smoothing stops automatically. Here we need 25 more steps to reach bending energy difference below energy tolerance of $1\ k_BT$. d) Only 30 steps of Laplacian smoothing are used. The large deformations do not get affected by face normal smoothing, but Laplacian smoothing has a long-range smoothing effect, compare the neck geometry in panels a-d.

10 List of Symbols and Abbreviations

C_1	First principal curvatures.
C_2	Second principal curvatures.
M	Mean curvature.
K	Gaussian curvature.
κ	Bending rigidity.
κ_G	Gaussian curvature modulus.
κ_Δ	Non-local bending rigidity.
m	Spontaneous curvature.
$\bar{m}$	Reduced spontaneous curvature.
m_{nlo}	Non-local spontaneous curvature.
m_{eff}	Effective spontaneous curvature.
$S(q)$	Undulation spectrum.
K_A	Area compressibility modulus.
ℓ_{me}	Bilayer thickness.
P_N	Normal component of pressure tensor.
P_T	Tangential component of pressure tensor.
ΔA_0	Optimal area difference between leaflets.
I_M	Integrated mean curvature.
ρ_{ext}	Density of osmotically active molecules in the bulk solution.
$s(z)$	Stress profile in Cartesian coordinates.
$s(z, r)$	Stress profile in cylindrical coordinates.

$s(r)$	Stress profile in spherical coordinates.
σ_{pr}	Protrusion tension.
σ	Spontaneous tension
$\hat{\Sigma}$	Total membrane tension.
Σ_{mec}	Mechanical tension.
Σ	Lagrange multiplier conjugated to vesicle area.
ΔP	Lagrange multiplier conjugated to vesicle volume.
$\mathcal{T}_{nan}$	Nanoscopic torque density.
$\mathcal{T}_{mic}$	Microscopic torque density.
$\mathrm{E_{be}}$	Bending energy of a membrane.
$\mathrm{E_{st}}$	Stretching energy of a membrane.
$\mathrm{E_{ADE}}$	Non-local area difference elasticity energy of a membrane.
$\mathrm{E_{vol}}$	Volume energy of vesicle.
$\mathrm{E_{tot}}$	Total energy of a membrane.
$\mathrm{E_W}$	Total energy of wetted state.
$\mathrm{E_{NW}}$	Total energy of non-wetted state.
$\Delta \mathrm{E}$	Wetting energy.
θ_α	Apparent contact angle of the α phase with the membrane.
θ_β	Apparent contact angle of the β phase with the membrane.
θ_γ	Apparent contact angle of the γ phase with the membrane.
θ^*_α	Intrinsic contact angle of the α phase with the membrane.
θ^*_β	Intrinsic contact angle of the β phase with the membrane.
$M_{\alpha\gamma}$	Curvature of the spherical cap in $\alpha\gamma$ segment of the membrane.
$M_{\beta\gamma}$	Curvature of the spherical cap in $\beta\gamma$ segment of the membrane.
$m_{\alpha\gamma}$	Spontaneous curvature of $\alpha\gamma$ segment of the membrane.

$m_{\beta\gamma}$	Spontaneous curvature of $\beta\gamma$ segment of the membrane.
$\Sigma_{\alpha\gamma}$	Mechanical segment tension of $\alpha\gamma$ segment of the membrane.
$\Sigma_{\beta\gamma}$	Mechanical segment tension of $\beta\gamma$ segment of the membrane.
$W_{\alpha\gamma}$	Adhesive strength of $\alpha\gamma$ segment of the membrane.
$W_{\beta\gamma}$	Adhesive strength of $\beta\gamma$ segment of the membrane.
$\Sigma_{\alpha\beta}$	Interfacial tension of $\alpha\beta$ interface.
$\bar{\Sigma}_{\alpha\beta}$	Reduced interfacial tension of $\alpha\beta$ interface.
$\bar{\Sigma}_{\alpha\beta}^{DPD}$	Reduced interfacial tension obtained from DPD simulation.
$\Delta_{\Sigma,co}$	Curvature dependent contribution to the force balance.
$\lambda_{\alpha\beta\gamma}$	Three-phase contact line $\alpha\beta\gamma$ tension.
$\bar{\lambda}_{\alpha\beta\gamma}$	Reduced line tension.
λ_{eff}	Effective line tension.
$L_{\alpha\beta\gamma}$	Length of three-phase contact line.
$A_{\alpha\beta}$	Area of $\alpha\beta$ interface.
$A_{\alpha\gamma}$	Area of $\alpha\gamma$ membrane segment.
$A_{\beta\gamma}$	Area of $\beta\gamma$ membrane segment.
V_{α}	Nanodroplet volume.
$s(t)$	Arc length as a function of general contour parameter t.
$\psi(t)$	Tilt angle as a function of general contour parameter t.
$r(t)$	Symmetry axis as a function of general contour parameter t.
ψ_{co}	Tilt angle at the contact line.
R_{co}	Radius of the contact line.
∇_{LB}	Laplace-Beltrami operator.
Ω	Grand canonical free energy .
$\Omega^{\alpha\beta}$	Surface excess of $\alpha\beta$ interface to the grand canonical free energy.

$\Omega^{\alpha\gamma}$	Surface excess of $\alpha\gamma$ interface to the grand canonical free energy.
$\Omega^{\beta\gamma}$	Surface excess of $\beta\gamma$ interface to the grand canonical free energy.
$\Omega^{\alpha\beta\gamma}$	Linear excess to the grand canonical free energy.
θ	Droplet contact angle on a solid surface.
θ_Y	Macroscopic Young's contact angle.
ξ	Line tension length.
ξ_S	Spreading pressure line tension.
S	Spreading coefficient.
l_{cap}^{-1}	Capillary length.
f_{ij}	DPD force parameter between bead types i and j.
F_{ij}^{C}	DPD conservative force between bead types i and j.
F_{ij}^{D}	DPD dissipative force between bead types i and j.
F_{ij}^{R}	DPD random force between bead types i and j.
γ_{ij}^{R}	Friction coefficient.
ζ_{ij}	Gaussian white noise.
k_b	Spring constant.
k_ϕ	Bending constant.
r_{ij}^{eq}	Equilibrium separation of adjacent beads of type i and j.
θ_{ijk}^{eq}	Equilibrium angle of three consecutive beads of type i, j and k.
M_v	Mean curvature of vertex v.
A_v	The area of adjacent facets of vertex v.
$L_{\|\|}$	Lateral simulation box size parallel to the bilayer plane.
$A_{\|\|}$	Base area of the cuboid simulation box.
Δ_{aff}	Affinity contrasts.
$\rho(r, z)$	Density profile in cylindrical coordinate.

$\rho(r)$	Density profile in spherical coordinates.
$a_{l,\beta\gamma}$	Area per lipid in $\beta\gamma$ segment of the membrane.
$a_{l,\alpha\gamma}$	Area per lipid in $\alpha\gamma$ segment of the membrane.
I_s	Index of sphericity.
r_c	Lennard-Jones potential cut-off.
τ	Basic time scale of DPD.
k_B	Boltzmann Constant
T	Temperature
A_{ves}	Area of vesicle.
V_{ves}	Volume of vesicle.
R_{ves}	Vesicle characteristic length scale.
v	Reduced volume of vesicle.
$\bar{\Sigma}^{fit}_{\alpha\beta}$	Symmetry hyper-surface.
A^*	Fraction of contact area of the droplet.
N_{il}	Number of lipids in the inner leaflet of the vesicle.
N_{ol}	Number of lipids in the outer leaflet of the vesicle.
N_{lip}	Total number of lipids in the the vesicle.
N^*_{il}	Unique number of lipids in the inner leaflet for which both leaflet tensions vanish.
N^*_{ol}	Unique number of lipids in the outer leaflet for which both leaflet tensions vanish.
N^{isp}_W	Number of water beads enclosed by the initial spherical vesicle.
N_W	Number of water beads enclosed by vesicle.
$\rho_C(r)$	Density profile of the chain beads.
$\rho_H(r)$	Density profile of the head beads.

R_{mid}	Radius of the bilayer's midsurface
R_{il}	Midsurface of the inner leaflet.
R_{ol}	Midsurface of the outer leaflet.
a_{il}	Lipid area in the inner leaflet.
a_{ol}	Lipid area in the outer leaflet.
Σ_{il}	Mechanical tension of the inner leaflet.
Σ_{ol}	Mechanical tension of the outer leaflet.
Δ_{il}	Area dilation of the inner leaflet.
Δ_{ol}	Area dilation of the outer leaflet.
Σ_{il}	Mechanical tension of the inner leaflet.
Σ_{ol}	Mechanical tension of the outer leaflet.
K_{il}	Area compressibility modulus of the inner leaflet.
K_{ol}	Area compressibility modulus of the outer leaflet.
GUV	Giant unilamellar vesicles.
LUV	Large unilamellar vesicles.
SUV	Small unilamellar vesicles.
DPD	Dissipative particle dynamics.
MD	Molecular dynamics.
PEG	Poly(ethylene glycol).
CW	Complete wetting.
PW	Partial wetting.
AA	All-atoms.
CG	Coarse-grained.
FDT	Fluctuation-dissipation theorem.
AFM	Atomic force microscopy.

IDRs	Intrinsically disordered regions in proteins.
ODE	Ordinary differential equation.
PDE	Partial differential equations.
EM	Electron microscopy
NVT	Canonical ensemble.
NPT	Isothermal-isobaric ensemble.
COM	Center of mass.
PBC	Periodic boundary conditions.
LJ	Lennard-Jones potential.

Bibliography

[1] Takeshi Harayama and Howard Riezman. Understanding the diversity of membrane lipid composition. *Nature reviews Molecular cell biology*, 19(5):281, 2018.

[2] Patricia Bassereau, Rui Jin, Tobias Baumgart, Markus Deserno, Rumiana Dimova, Vadim A Frolov, Pavel V Bashkirov, Helmut Grubmüller, Reinhard Jahn, H Jelger Risselada, et al. The 2018 biomembrane curvature and remodeling roadmap. *Journal of physics D: Applied physics*, 51(34):343001, 2018.

[3] Tripta Bhatia, Jaime Agudo-Canalejo, Rumiana Dimova, and Reinhard Lipowsky. Membrane nanotubes increase the robustness of giant vesicles. *Acs Nano*, 12(5):4478–4485, 2018.

[4] Erdinc Sezgin, Ilya Levental, Satyajit Mayor, and Christian Eggeling. The mystery of membrane organization: composition, regulation and roles of lipid rafts. *Nature reviews Molecular cell biology*, 18(6):361, 2017.

[5] Reinhard Lipowsky. Understanding membranes and vesicles: A personal recollection of the last two decades. In *Physics of Biological Membranes*, pages 3–44. Springer, 2018.

[6] Petra Schwille, Joachim Spatz, Katharina Landfester, Eberhard Bodenschatz, Stephan Herminghaus, Victor Sourjik, Tobias J Erb, Philippe Bastiaens, Reinhard Lipowsky, Anthony Hyman, et al. Maxsynbio: avenues towards creating cells from the bottom up. *Angewandte Chemie International Edition*, 57(41):13382–13392, 2018.

[7] Udo Seifert, Karin Berndl, and Reinhard Lipowsky. Shape transformations of vesicles: Phase diagram for spontaneous-curvature and bilayer-coupling models. *Physical Review A*, 44(2):1182, 1991.

[8] U Seifert and R Lipowsky. Morphology of vesicles. *Handbook of biological physics*, 1:403–464, 1995.

[9] Manfredo P Do Carmo. *Differential Geometry of Curves and Surfaces: Revised and Updated Second Edition*. Courier Dover Publications, 2016.

[10] Joshua Zimmerberg and Michael M Kozlov. How proteins produce cellular membrane curvature. *Nature reviews Molecular cell biology*, 7(1):9, 2006.

[11] Wolfgang Helfrich. Elastic properties of lipid bilayers: theory and possible experiments. *Zeitschrift für Naturforschung C*, 28(11-12):693–703, 1973.

[12] Rumiana Dimova. Recent developments in the field of bending rigidity measurements on membranes. *Advances in colloid and interface science*, 208:225–234, 2014.

[13] R. Goetz, G. Gompper, and R. Lipowsky. Mobilitiy and Elasticity of Self-Assembled Membranes. *Phys. Rev. Lett.*, 82:221–224, 1999.

[14] Bartosz Różycki and Reinhard Lipowsky. Spontaneous curvature of bilayer membranes from molecular simulations: Asymmetric lipid densities and asymmetric adsorption. *J. Chem. Phys.*, 142(5):02B601_1, 2015.

[15] Mingyang Hu, John J Briguglio, and Markus Deserno. Determining the gaussian curvature modulus of lipid membranes in simulations. *Biophysical journal*, 102(6):1403–1410, 2012.

[16] Reinhard Lipowsky. Spontaneous tubulation of membranes and vesicles reveals membrane tension generated by spontaneous curvature. *Faraday discussions*, 161:305–331, 2013.

[17] Raktim Dasgupta, Markus S Miettinen, Nico Fricke, Reinhard Lipowsky, and Rumiana Dimova. The glycolipid gm1 reshapes asymmetric biomembranes and giant vesicles by curvature generation. *Proceedings of the National Academy of Sciences*, 115(22):5756–5761, 2018.

[18] Marzieh Karimi, Jan Steinkühler, Debjit Roy, Raktim Dasgupta, Reinhard Lipowsky, and Rumiana Dimova. Asymmetric ionic conditions generate large membrane curvatures. *Nano letters*, 18(12):7816–7821, 2018.

[19] A. Sreekumari and R. Lipowsky. Lipids with Bulky Head Groups Generate Large Membrane Curvatures by Small Compositional Asymmetries. *J. Chem. Phys.*, 149:084901, 2018.

[20] Markus Sakari Miettinen and Reinhard Lipowsky. Bilayer membranes with frequent flip-flops have tensionless leaflets. *Nano letters*, 2019.

[21] Reinhard Lipowsky. Coupling of bending and stretching deformations in vesicle membranes. *Advances in colloid and interface science*, 208:14–24, 2014.

[22] J.S. Rowlinson and B. Widom. *Molecular Theory of Capillarity*. Clarendon Press, Oxford, 1989.

[23] R. Goetz and R. Lipowsky. Computer Simulations of Bilayer Membranes: Self-Assembly and Interfacial Tension. *J. Chem. Phys.*, 108:7397–7409, 1998.

[24] Juan M Vanegas, Alejandro Torres-Sánchez, and Marino Arroyo. Importance of force decomposition for local stress calculations in biomembrane molecular simulations. *Journal of chemical theory and computation*, 10(2):691–702, 2014.

[25] Ling Miao, Udo Seifert, Michael Wortis, and Hans-Günther Döbereiner. Budding transitions of fluid-bilayer vesicles: the effect of area-difference elasticity. *Physical Review E*, 49(6):5389, 1994.

[26] Vasil N Georgiev, Andrea Grafmüller, David Bléger, Stefan Hecht, Sonja Kunstmann, Stefanie Barbirz, Reinhard Lipowsky, and Rumiana Dimova. Area increase and budding in giant vesicles triggered by light: behind the scene. *Advanced Science*, 5(8):1800432, 2018.

[27] Udo Seifert. Configurations of fluid membranes and vesicles. *Advances in physics*, 46(1):13–137, 1997.

[28] Ou-Yang Zhong-Can and Wolfgang Helfrich. Instability and deformation of a spherical vesicle by pressure. *Physical review letters*, 59(21):2486, 1987.

[29] Halim Kusumaatmaja and Reinhard Lipowsky. Droplet-induced budding transitions of membranes. *Soft Matter*, 7(15):6914–6919, 2011.

[30] Frank Jülicher and Reinhard Lipowsky. Domain-induced budding of vesicles. *Physical review letters*, 70(19):2964, 1993.

[31] Frank Jülicher and Reinhard Lipowsky. Shape transformations of vesicles with intramembrane domains. *Physical Review E*, 53(3):2670, 1996.

[32] Jaime Agudo-Canalejo and Reinhard Lipowsky. Critical particle sizes for the engulfment of nanoparticles by membranes and vesicles with bilayer asymmetry. *ACS nano*, 9(4):3704–3720, 2015.

[33] Halim Kusumaatmaja, Yanhong Li, Rumiana Dimova, and Reinhard Lipowsky. Intrinsic contact angle of aqueous phases at membranes and vesicles. *Phys. Rev. Lett.*, 103(23):238103, 2009.

[34] Weria Pezeshkian, Melanie König, Siewert Jan Marrink, et al. A multi-scale approach to membrane remodeling processes. *Frontiers in molecular biosciences*, 6:59, 2019.

[35] Amir Houshang Bahrami, Reinhard Lipowsky, and Thomas R Weikl. Tubulation and aggregation of spherical nanoparticles adsorbed on vesicles. *Physical review letters*, 109(18):188102, 2012.

[36] Erwin Gutlederer, Thomas Gruhn, and Reinhard Lipowsky. Polymorphism of vesicles with multi-domain patterns. *Soft Matter*, 5(17):3303–3311, 2009.

[37] Jinglei Hu, Thomas Weikl, and Reinhard Lipowsky. Vesicles with multiple membrane domains. *Soft Matter*, 7(13):6092–6102, 2011.

[38] Francesco Bonazzi and Thomas R Weikl. Membrane morphologies induced by arc-shaped scaffolds are determined by arc angle and coverage. *Biophysical journal*, 116(7):1239–1247, 2019.

[39] Daan Frenkel and Berend Smit. *Understanding molecular simulation: from algorithms to applications*, volume 1. Elsevier, 2001.

[40] Julian C Shillcock and Reinhard Lipowsky. The computational route from bilayer membranes to vesicle fusion. *Journal of Physics: Condensed Matter*, 18(28):S1191, 2006.

[41] Yonggang Liu, Jaime Agudo-Canalejo, Andrea Grafmüller, Rumiana Dimova, and Reinhard Lipowsky. Patterns of flexible nanotubes formed by liquid-ordered and liquid-disordered membranes. *ACS Nano*, 10(1):463–474, 2015.

[42] Simón Poblete, Matej Praprotnik, Kurt Kremer, and Luigi Delle Site. Coupling different levels of resolution in molecular simulations. *The Journal of chemical physics*, 132(11):114101, 2010.

[43] PJ Hoogerbrugge and JMVA Koelman. Simulating microscopic hydrodynamic phenomena with dissipative particle dynamics. *EPL (Europhysics Letters)*, 19(3):155, 1992.

[44] Pep Espanol and Patrick Warren. Statistical mechanics of dissipative particle dynamics. *EPL (Europhysics Letters)*, 30(4):191, 1995.

[45] Robert D Groot and Patrick B Warren. Dissipative particle dynamics: Bridging the gap between atomistic and mesoscopic simulation. *J. Chem. Phys.*, 107(11):4423–4435, 1997.

[46] Yanhong Li, Reinhard Lipowsky, and Rumiana Dimova. Transition from complete to partial wetting within membrane compartments. *Journal of the American Chemical Society*, 130(37):12252–12253, 2008.

[47] R. Lipowsky. Response of Membranes and Vesicles to Capillary Forces Arising from Aqueous Two-Phase Systems and Water-in-Water Emulsions. *J. Phys. Chem. B*, 122:3572–3586, 2018.

[48] J Willard Gibbs. The collected works of j. willard gibbs. Technical report, Yale Univ. Press„ 1948.

[49] Makoto Kunieda. Molecular dynamics study of oil-water interfacial equilibrium in petroleum engineering. 2012.

[50] Mingzhe Shao, Jianjun Wang, and Xin Zhou. Anisotropy of local stress tensor leads to line tension. *Sci. Rep.*, 5, 2015.

[51] L. Guzzardi, R. Rosso, and E. G. Virga. Residual stability of sessile droplets with negative line tension. *Phys. Rev. E*, 73:021602, 2006.

[52] Bruce M Law, Sean P McBride, Jiang Yong Wang, Haeng Sub Wi, Govind Paneru, Santigo Betelu, Baku Ushijima, Youichi Takata, Bret Flanders, Fernando Bresme, et al. Line tension and its influence on droplets and particles at surfaces. *Progress in surface science*, 92(1):1–39, 2017.

[53] *The Scientific Papers of J. Willard Gibbs*, volume I. Longman, Green, and Co., 1906.

[54] B. M. Law, S. P. McBride, J. Y. Wang, H. S. Wie, G. Paneru, S. Betelu, B. Ushijima, Y. Takata, B. Flanders, F. Bresme, H. Matsubara, T. Takiue, and M. Aratono. Line Tension and Its Influence on Droplets and Particles at Surfaces. *Progr. Surf. Sci.*, 92:1–39, 2017.

[55] JO Indekeu. Line tension near the wetting transition: results from an interface displacement model. *Physica A: Statistical Mechanics and its Applications*, 183(4):439–461, 1992.

[56] Richard C Tolman. The effect of droplet size on surface tension. *The journal of chemical physics*, 17(3):333–337, 1949.

[57] JY Wang, S Betelu, and BM Law. Line tension effects near first-order wetting transitions. *Phys. Rev. Lett.*, 83(18):3677, 1999.

[58] John K Berg, Constans M Weber, and Hans Riegler. Impact of negative line tension on the shape of nanometer-size sessile droplets. *Physical review letters*, 105(7):076103, 2010.

[59] Joost H Weijs, Antonin Marchand, Bruno Andreotti, Detlef Lohse, and Jacco H Snoeijer. Origin of line tension for a lennard-jones nanodroplet. *Phys. Fluids*, 23(2):022001, 2011.

[60] Jun Zhang, Pengfei Wang, Matthew K Borg, Jason M Reese, and Dongsheng Wen. A critical assessment of the line tension determined by the modified young's equation. *Physics of Fluids*, 30(8):082003, 2018.

[61] Binyu Zhao, Shuang Luo, Elmar Bonaccurso, Günter K Auernhammer, Xu Deng, Zhigang Li, and Longquan Chen. Resolving the apparent line tension of sessile droplets and understanding its sign change at a critical wetting angle. *Physical review letters*, 123(9):094501, 2019.

[62] Yongdae Shin and Clifford P Brangwynne. Liquid phase condensation in cell physiology and disease. *Science*, 357(6357):eaaf4382, 2017.

[63] Simon Alberti, Amy Gladfelter, and Tanja Mittag. Considerations and challenges in studying liquid-liquid phase separation and biomolecular condensates. *Cell*, 176(3):419–434, 2019.

[64] Louis-Philippe Bergeron-Sandoval, Hossein Khadivi Heris, Adam G Hendricks, Allen J Ehrlicher, Paul Francois, Rohit V Pappu, and Stephen W Michnick. Endocytosis caused by liquid-liquid phase separation of proteins. *bioRxiv*, page 145664, 2017.

[65] J. C. Shillcock and R. Lipowsky. Equilibrium Structure and Lateral Stress Distribution of Amphiphilic Bilayers from Dissipative Particle Dynamics Simulations. *J. Chem. Phys.*, 117:5048–5061, 2002.

[66] Andrea Grafmüller, Julian Shillcock, and Reinhard Lipowsky. The Fusion of Membranes and Vesicles: Pathway and Energy Barriers from Dissipative Particle Dynamics. *Biophys. J.*, 96(7):2658–2675, 2009.

[67] Kurt A Smith, David Jasnow, and Anna C Balazs. Designing synthetic vesicles that engulf nanoscopic particles. *J. Chem. Phys.*, 127(8):08B612, 2007.

[68] Tongtao Yue and Xianren Zhang. Cooperative effect in receptor-mediated endocytosis of multiple nanoparticles. *ACS Nano*, 6(4):3196–3205, 2012.

[69] Jian Mao, Pengyu Chen, Junshi Liang, Ruohai Guo, and Li-Tang Yan. Receptor-Mediated Endocytosis of Two-Dimensional Nanomaterials Undergoes Flat Vesiculation and Occurs by Revolution and Self-Rotation. *ACS Nano*, 10:1493–1502, 2016.

[70] Pengyu Chen, Zihan Huang, Junshi Liang, Tianqi Cui, Xinghua Zhang, Bing Miao, and Li-Tang Yan. Diffusion and directionality of charged nanoparticles on lipid bilayer membrane. *ACS Nano*, 10(12):11541–11547, 2016.

[71] Zhiqiang Shen, Huilin Ye, Martin Kröger, and Ying Li. Aggregation of polyethylene glycol polymers suppresses receptor-mediated endocytosis of pegylated liposomes. *Nanoscale*, 10(9):4545–4560, 2018.

[72] Steve Plimpton. Fast parallel algorithms for short-range molecular dynamics. *J. Comput. Phys.*, 117(1):1–19, 1995.

[73] Kenneth A Brakke. The surface evolver. *Experimental mathematics*, 1(2):141–165, 1992.

[74] P. A. Albertsson. *Partition of Cell Particles and Macromolecules: Separation and Purification of Biomolecules, Cell Organelles Membranes, and Cells in Aqueous Polymer Two-Phase Systems and Their Use in Biochemical Analysis and Biotechnology.* Wiley, 3 edition, 1986.

[75] J. Esquena. Water-in-Water (W/W) emulsions. *Curr. Opin. Colloid Interface Sci.*, 25:109–119, 2016.

[76] R. R. G. Soares, A. M. Azevedo, J. M. Van Alstine, and M. R Aires-Barros. Partitioning in Aqueous Two-Phase Systems: Analysis of Strengths, Weaknesses, Opportunities and Threats. *Biotechnol. J.*, 10:1158–1169, 2015.

[77] A. L. Grilo, M. R. Aires-Barros, and A. M. Azevedo. Partitioning in Aqueous Two-Phase Systems: Fundamentals, Applications and Trends. *Sep. Purif. Rev.*, 45:68–80, 2016.

[78] Yonggang Liu, R. Lipowsky, and R. Dimova. Concentration dependence of the interfacial tension for aqueous two-phase polymer solutions of dextran and polyethylene glycol. *Langmuir*, 28:3831–3839, 2012.

[79] C. P. Brangwynne, C. R. Eckmann, D. S. Courson, A. Rybarska, C. Hoege, J. Gharakhani, F. Jülicher, and A. A. Hyman. Germline P Granules Are Liquid Droplets That Localize by Controlled Dissolution/Condensation. *Science*, 324:1729 – 1732, 2009.

[80] S. F. Banani, H. O. Lee, A. A. Hyman, and M. K. Rosen. Biomolecular Condensates: Organizers of Cellular Biochemistry. *Nature Rev.: Mol. Cell Biol.*, 18:285–298, 2017.

[81] Yanhong Li, Reinhard Lipowsky, and Rumiana Dimova. Transition from complete to partial wetting within membrane compartments. *J. Am. Chem. Soc.*, 130(37):12252–12253, 2008.

[82] M. S. Long, A. S. Cans, and C. D. Keating. Budding and Asymmetric Protein Microcompartmentation in Giant Vesicles Containing Two Aqueous Phases. *JACS*, 130:756–762, 2008.

[83] S. Hak, E. Helgesen, H. H. Hektoen, E. M. Huuse, P. A. Jarzyna, W. J. M. Mulder, O. Haraldseth, and C. de Lange Davies. The Effect of Nanoparticle Polyethylene Glycol Surface Density on Ligand-Directed Tumor Targeting Studied in Vivo by Dual Modality Imaging. *ACS Nano*, 6(6):5648 – 5658, 2012.

[84] W. Jiang, Q. Li, L. Xiao, J. Dou, Y. Liu, W. Yu, Y. Ma, X. Li, Y.-Z. You, Z. Tong, H. Liu, H. Liang, L. Lu, X. Xu, Y. Yao, G. Zhang, Y. Wang, and J. Wang. Hierarchical Multiplexing Nanodroplets for Imaging-guided Cancer Radiotherapy via DNA Damage Enhancement and Concomitant DNA Repair Prevention. *ACS Nano*, 12:5684 – 5698, 2018.

[85] F. Gao, Z. Zhang, H. Bu, Y. Huang, Z. Gao, J. Shen, C. Zhao, and Y. Li. Nanoemulsion Improves the Oral Absorption of Candesartan Cilexetil in Rats: Performance and Mechanism. *J. Control. Release*, 149:168 – 174, 2011.

[86] J. Ye, Y. Liu, X. Xia, L. Meng, W. Dong, R. Wang, Z. Fu, H. Liu, and R. Han. Improved Safety and Efficacy of a Lipid Emulsion Loaded with a Paclitaxel-Cholesterol Complex for the Treatment of Breast Tumors. *Oncol. Rep.*, 36:399 – 409, 2016.

[87] Y. Singh, J. Gopal Meher, K. Raval, F. A. Khan, M. Chaurasia, N. K. Jain, and M. K. Chourasia. Nanoemulsion: Concepts, Development and Applications in Drug Delivery. *J. Control. Release*, 252:28 – 49, 2017.

[88] S. Singh Cameotra and P. Singh. Synthesis of Rhamnolipid Biosurfactant and Mode of Hexadecane Uptake by Pseudomonas Species. *Microb. Cell Fact.*, 8:16, 2009.

[89] P. Chandran and N. Das. Role of Sophorolipid Biosurfactant in Degradation of Diesel Oil by Candida Tropicalis. *Bioremediat. J.*, 16(1):19 – 30, 2012.

[90] John K Berg, Constans M Weber, and Hans Riegler. Impact of negative line tension on the shape of nanometer-size sessile droplets. *Phys. Rev. Lett.*, 105(7):076103, 2010.

[91] H. Matsubara, B. Ushijima, B. M. Law, T. Takiue, and M. Aratono. Line Tension of Alkane Lenses on Aqueous Surfactant Solutions at Phase Transitions of Coexisting Interfaces. *Adv. Colloid Interfac.*, 206:186 – 194, 2014.

[92] J.-C. Geminard, A. Zywocinski, F. Caillier, and P. Oswald. Observation of Negative Line Tensions from Plateau Border Regions in Dry Foam Films. *Phil. Mag. Let.*, 84(3):199 – 204, 2004.

[93] B. Antonny, C. Burd, P. de Camilli, E. Chen, O. Daumke, K. Faelber, M. Ford, V. A. Frolov, A. Frost, J. E. Hinshaw, T. Kirchhausen, M. M. Kozlov, M. Lenz, H. H. Low, H. McMahon, C. Merrifield, T. D. Pollard, P. J. Robinson, A. Roux, and S. Schmid. Membrane Fission by Dynamin: What We Know and What We Need to Know. *Embo J.*, 35:2270 – 2284, 2016.

[94] J. Schöneberg, I.-H. Lee, J. H. Iwasa, and J. H. Hurley. Reverse-topology membrane scission by the escrt proteins. *Nature Rev.: Mol. Cell Biol.*, 18:5–17, 2017.

[95] J. Agudo-Canalejo and R. Lipowsky. Domes and Cones: Adhesion-Induced Fission of Membranes by ESCRT Proteins. *PLoS Comp. Biol.*, 14:e1006422, 2018.

[96] The Mathworks, Inc., Natick, Massachusetts. *MATLAB Version 8.5.0.197613 (R2015a)*, 2015.

[97] William Humphrey, Andrew Dalke, and Klaus Schulten. VMD – Visual Molecular Dynamics. *J. Mol. Graph. Model.*, 14:33–38, 1996.

[98] Herman JC Berendsen, JPM van Postma, Wilfred F van Gunsteren, ARHJ DiNola, and JR Haak. Molecular dynamics with coupling to an external bath. *J. Chem. Phys.*, 81(8):3684–3690, 1984.

[99] Takenobu Nakamura, Wataru Shinoda, and Tamio Ikeshoji. Novel numerical method for calculating the pressure tensor in spherical coordinates for molecular systems. *J. Chem. Phys.*, 135(9):094106, 2011.

[100] Takenobu Nakamura, Shuhei Kawamoto, and Wataru Shinoda. Precise calculation of the local pressure tensor in cartesian and spherical coordinates in lammps. *Comput. Phys. Commun.*, 190:120–128, 2015.

[101] Dirk Jan Kroon. Patch curvature. *http://uk.mathworks.com/matlabcentral/fileexchange/32573-patch-curvature.*, 2014.

[102] Hirokazu Yagou, Yutaka Ohtake, and Alexander Belyaev. Mesh smoothing via mean and median filtering applied to face normals. In *null*, page 124. IEEE, 2002.

[103] H. Kusumaatmaja, Yanhong Li, R. Dimova, and R. Lipowsky. Intrinsic contact angle of aqueous phases at membranes and vesicles. *Phys. Rev. Lett.*, 103:238103, 2009.

[104] R. Lipowsky, P. Lenz, and P. Swain. Wetting and Dewetting of Structured or Imprinted Surfaces. *Colloid. Surface. A*, 161:3–22, 2000.

[105] R. Dimova. Recent Developments in the Field of Bending Rigidity Measurements on Membranes. *Adv. Colloid Interface Sci.*, 208:225–234, 2014.

[106] P. Posocco, A. Perazzo, V. Preziosi, E. Laurini, S. Pricl, and S. Guido. Interfacial Tension of Oil/Water Emulsions with Mixed Non-Ionic Surfactants: Comparison Between Experiments and Molecular Simulations. *RSC Adv.*, 6:4723 – 4729, 2016.

[107] N. Kumar and A. Mandal. Surfactant Stabilized Oil-in-Water Nanoemulsion: Stability, Interfacial Tension, and Rheology Study for Enhanced Oil Recovery Application. *Energy Fuels*, 32:6452 – 6466, 2018.

[108] B. Widom. Surface Tension and Molecular Correlations Near the Critical Point. *J. Chem. Phys.*, 43:3892–3897, 1965.

[109] Constantin Ionescu-Tirgoviste, Paul A Gagniuc, Elvira Gubceac, Liliana Mardare, Irinel Popescu, Simona Dima, and Manuella Militaru. A 3d map of the islet routes throughout the healthy human pancreas. *Scientific reports*, 5:14634, 2015.

[110] Y. Avalos-Padilla, R. L. Knorr, R. Javier-Reyna, G. García-Rivera, R. Lipowsky, R. Dimova, and E. Orozco. The Conserved ESCRT-III Machinery Participates in the Phagocytosis of Entamoeba Histolytica. *Front. Cell. Infect. Microbiol.*, 8, DOI: 10.3389/fcimb.2018.00053, 2018.

[111] Yanhong Li, H. Kusumaatmaja, R. Lipowsky, and R. Dimova. Wetting-induced budding of vesicles in contact with several aqueous phases. *J. Phys. Chem. B*, 116:1819–1823, 2012.

[112] Pierre-Gilles De Gennes, Françoise Brochard-Wyart, and David Quéré. *Capillarity and Wetting Phenomena: Drops, Bubbles, Pearls, Waves*. Springer Science & Business Media, 2013.

[113] Rumiana Dimova and Reinhard Lipowsky. Giant vesicles exposed to aqueous two-phase systems: Membrane wetting, budding processes, and spontaneous tubulation. *Advanced Materials Interfaces*, 4(1):1600451, 2017.

[114] Reinhard Lipowsky. Response of membranes and vesicles to capillary forces arising from aqueous two-phase systems and water-in-water droplets. *The Journal of Physical Chemistry B*, 122(13):3572–3586, 2018.

[115] Clifford P Brangwynne, Christian R Eckmann, David S Courson, Agata Rybarska, Carsten Hoege, Jöbin Gharakhani, Frank Jülicher, and Anthony A Hyman. Germline p granules are liquid droplets that localize by controlled dissolution/condensation. *Science*, 324(5935):1729–1732, 2009.

[116] Shana Elbaum-Garfinkle, Younghoon Kim, Krzysztof Szczepaniak, Carlos Chih-Hsiung Chen, Christian R Eckmann, Sua Myong, and Clifford P Brangwynne. The disordered p granule protein laf-1 drives phase separation into droplets with tunable viscosity and dynamics. *Proceedings of the National Academy of Sciences*, 112(23):7189–7194, 2015.

[117] Louise M Jawerth, Mahdiye Ijavi, Martine Ruer, Shambaditya Saha, Marcus Jahnel, Anthony A Hyman, Frank Jülicher, and Elisabeth Fischer-Friedrich. Salt-dependent rheology and surface tension of protein condensates using optical traps. *Physical review letters*, 121(25):258101, 2018.

[118] Yonggang Liu, Reinhard Lipowsky, and Rumiana Dimova. Concentration dependence of the interfacial tension for aqueous two-phase polymer solutions of dextran and polyethylene glycol. *Langmuir*, 28(8):3831–3839, 2012.

[119] Yongdae Shin, Yi-Che Chang, Daniel SW Lee, Joel Berry, David W Sanders, Pierre Ronceray, Ned S Wingreen, Mikko Haataja, and Clifford P Brangwynne. Liquid nuclear condensates mechanically sense and restructure the genome. *Cell*, 175(6):1481–1491, 2018.

[120] Roland L. Knorr, Franzmann Titus, Feeney Mistianne, Frigerio Lorenzo, Hyman. Anthony A., Rumiana Dimova, and Reinhard Lipowsky. Wetting and molding of membranes by biomolecular condensates. *Under Revsion*, 2019.

[121] Oliver Beutel, Riccardo Maraspini, Karina Pombo-Garcia, Cecilie Martin-Lemaitre, and Alf Honigmann. Phase separation of zonula occludens proteins drives formation of tight junctions. *Available at SSRN 3362257*, 2019.

[122] Dragomir Milovanovic, Yumei Wu, Xin Bian, and Pietro De Camilli. A liquid phase of synapsin and lipid vesicles. *Science*, 361(6402):604–607, 2018.

[123] Vahid Satarifard, Andrea Grafmüller, and Reinhard Lipowsky. Nanodroplets at membranes create tight-lipped membrane necks via negative line tension. *ACS nano*, 12(12):12424–12435, 2018.

[124] Sabyasachi Dasgupta, Thorsten Auth, and Gerhard Gompper. Shape and orientation matter for the cellular uptake of nonspherical particles. *Nano letters*, 14(2):687–693, 2014.

[125] Qingfen Yu, Sameh Othman, Sabyasachi Dasgupta, Thorsten Auth, and Gerhard Gompper. Nanoparticle wrapping at small non-spherical vesicles: curvatures at play. *Nanoscale*, 10(14):6445–6458, 2018.

[126] Dirk GAL Aarts, Matthias Schmidt, and Henk NW Lekkerkerker. Direct visual observation of thermal capillary waves. *Science*, 304(5672):847–850, 2004.

[127] JO Indekeu. Line tension at wetting. *Int. J. Mod. Phys. B*, 8(03):309–345, 1994.

[128] MJ Hope, MB Bally, G Webb, and PR Cullis. Production of large unilamellar vesicles by a rapid extrusion procedure. characterization of size distribution, trapped volume and ability to maintain a membrane potential. *Biochimica et Biophysica Acta (BBA)-Biomembranes*, 812(1):55–65, 1985.

[129] Robert C MacDonald, Ruby I MacDonald, Bert Ph M Menco, Keizo Takeshita, Nanda K Subbarao, and Lan-rong Hu. Small-volume extrusion apparatus for preparation of large, unilamellar vesicles. *Biochimica et Biophysica Acta (BBA)-Biomembranes*, 1061(2):297–303, 1991.

[130] Andreas Jahn, Samuel M Stavis, Jennifer S Hong, Wyatt N Vreeland, Don L DeVoe, and Michael Gaitan. Microfluidic mixing and the formation of nanoscale lipid vesicles. *ACS nano*, 4(4):2077–2087, 2010.

[131] Lei Qu, Yulia Akbergenova, Yunming Hu, and Thomas Schikorski. Synapse-to-synapse variation in mean synaptic vesicle size and its relationship with synaptic morphology and function. *Journal of Comparative Neurology*, 514(4):343–352, 2009.

[132] Blake R Hopiavuori, Lea D Bennett, Richard S Brush, Matthew J Van Hook, Wallace B Thoreson, and Robert E Anderson. Very long-chain fatty acids support synaptic structure and function in the mammalian retina. *OCL*, 23(1):D113, 2016.

[133] Rose M Johnstone, Mohammed Adam, JR Hammond, L Orr, and Claire Turbide. Vesicle formation during reticulocyte maturation. association of plasma membrane activities with released vesicles (exosomes). *Journal of Biological Chemistry*, 262(19):9412–9420, 1987.

[134] Mikael Simons and Graça Raposo. Exosomes–vesicular carriers for intercellular communication. *Current opinion in cell biology*, 21(4):575–581, 2009.

[135] Phyllis I Hanson and Anil Cashikar. Multivesicular body morphogenesis. *Annual review of cell and developmental biology*, 28:337–362, 2012.

[136] Lucio Barile and Giuseppe Vassalli. Exosomes: Therapy delivery tools and biomarkers of diseases. *Pharmacology & therapeutics*, 174:63–78, 2017.

[137] Cecilia Lässer, Su Chul Jang, and Jan Lötvall. Subpopulations of extracellular vesicles and their therapeutic potential. *Molecular aspects of medicine*, 60:1–14, 2018.

[138] Sophia G Antimisiaris, Spyridon Mourtas, and Antonia Marazioti. Exosomes and exosome-inspired vesicles for targeted drug delivery. *Pharmaceutics*, 10(4):218, 2018.

[139] Liu Han, Eric W-F Lam, and Yu Sun. Extracellular vesicles in the tumor microenvironment: old stories, but new tales. *Molecular cancer*, 18(1):59, 2019.

[140] Ulrich Baxa. Imaging of liposomes by transmission electron microscopy. In *Characterization of Nanoparticles Intended for Drug Delivery*, pages 73–88. Springer, 2018.

[141] BL Mui, PR Cullis, EA Evans, and TD Madden. Osmotic properties of large unilamellar vesicles prepared by extrusion. *Biophysical journal*, 64(2):443–453, 1993.

[142] BL Mui, HG Döbereiner, TD Madden, and PR Cullis. Influence of transbilayer area asymmetry on the morphology of large unilamellar vesicles. *Biophysical journal*, 69(3):930–941, 1995.

[143] Peter M Frederik and DHW Hubert. Cryoelectron microscopy of liposomes. In *Methods in enzymology*, volume 391, pages 431–448. Elsevier, 2005.

[144] Nina Dragicevic-Curic, Dietrich Scheglmann, Volker Albrecht, and Alfred Fahr. Temoporfin-loaded invasomes: development, characterization and in vitro skin penetration studies. *Journal of Controlled Release*, 127(1):59–69, 2008.

[145] Dganit Danino. Cryo-tem of soft molecular assemblies. *Current opinion in colloid & interface science*, 17(6):316–329, 2012.

[146] Satoru Yamamoto, Yutaka Maruyama, and Shi-aki Hyodo. Dissipative particle dynamics study of spontaneous vesicle formation of amphiphilic molecules. *The Journal of chemical physics*, 116(13):5842–5849, 2002.

[147] Siewert J Marrink and Alan E Mark. Molecular dynamics simulation of the formation, structure, and dynamics of small phospholipid vesicles. *Journal of the American Chemical Society*, 125(49):15233–15242, 2003.

[148] Udo Seifert, Karin Berndl, and Reinhard Lipowsky. Shape transformations of vesicles: Phase diagram for spontaneous-curvature and bilayer-coupling models. *Physical Review A*, 44(2):1182, 1991.

[149] Reinhard Lipowsky. Understanding giant vesicles–a theoretical perspective. In *The Giant Vesicle Book*. CRC Press, 2019.

[150] Leandro Martínez, Ricardo Andrade, Ernesto G Birgin, and José Mario Martínez. Packmol: a package for building initial configurations for molecular dynamics simulations. *Journal of computational chemistry*, 30(13):2157–2164, 2009.

[151] Mathias Winterhalter and Wolfgang Helfrich. Bending elasticity of electrically charged bilayers: coupled monolayers, neutral surfaces, and balancing stresses. *The Journal of Physical Chemistry*, 96(1):327–330, 1992.

[152] RH Templer. On the area neutral surface of inverse bicontinuous cubic phases of lyotropic liquid crystals. *Langmuir*, 11(1):334–340, 1995.

[153] Takenobu Nakamura, Shuhei Kawamoto, and Wataru Shinoda. Precise calculation of the local pressure tensor in cartesian and spherical coordinates in lammps. *Computer Physics Communications*, 190:120–128, 2015.

[154] Jean-Baptiste Fournier. On the stress and torque tensors in fluid membranes. *Soft Matter*, 3(7):883–888, 2007.

[155] Markus Deserno. Fluid lipid membranes: From differential geometry to curvature stresses. *Chemistry and physics of lipids*, 185:11–45, 2015.

[156] H-G Döbereiner, Evan Evans, Martin Kraus, Udo Seifert, and Michael Wortis. Mapping vesicle shapes into the phase diagram: A comparison of experiment and theory. *Physical Review E*, 55(4):4458, 1997.

[157] M. Feric, N. Vaidya, T. S. Harmon, R. W. Kriwacki, R. V. Pappu, and C. P. Brangwynne. Coexisting Liquid Phases Underlie Nucleolar Subcompartments. *Cell*, 165:1686 – 1697, 2016.

[158] B. D. Chithrani and W. C. W. Chan. Elucidating the Mechanism of Cellular Uptake and Removal of Protein-Coated Gold Nanoparticles of Different Sizes and Shapes. *Nano Lett.*, 7(6):1542 – 1550, 2007.

[159] J. Agudo-Canalejo and R. Lipowsky. Critical Particle Sizes for the Engulfment of Nanoparticles by Membranes and Vesicles with Bilayer Asymmetry. *ACS Nano*, 9:3704–3720, 2015.

[160] W Möbius, E Van Donselaar, Y Ohno-Iwashita, Y Shimada, HFG Heijnen, JW Slot, and HJ Geuze. Recycling compartments and the internal vesicles of multivesicular bodies harbor most of the cholesterol found in the endocytic pathway. *Traffic*, 4(4):222–231, 2003.

[161] Tore Skotland, Nina P Hessvik, Kirsten Sandvig, and Alicia Llorente. Exosomal lipid composition and the role of ether lipids and phosphoinositides in exosome biology. *Journal of lipid research*, 60(1):9–18, 2019.

[162] Davide Zabeo, Aleksander Cvjetkovic, Cecilia Lässer, Martin Schorb, Jan Lötvall, and Johanna L Höög. Exosomes purified from a single cell type have diverse morphology. *Journal of extracellular vesicles*, 6(1):1329476, 2017.

[163] Débora L Oliveira, Juliana Rizzo, Luna S Joffe, Rodrigo Godinho, and Marcio L Rodrigues. Where do they come from and where do they go: candidates for regulating extracellular vesicle formation in fungi. *International journal of molecular sciences*, 14(5):9581–9603, 2013.

[164] Katharina B Beer, Jennifer Rivas-Castillo, Kenneth Kuhn, Gholamreza Fazeli, Birgit Karmann, Jeremy F Nance, Christian Stigloher, and Ann M Wehman. Extracellular vesicle budding is inhibited by redundant regulators of tat-5 flippase localization and phospholipid asymmetry. *Proceedings of the National Academy of Sciences*, 115(6):E1127–E1136, 2018.

[165] Ying Zhang and A Ben Hamza. Vertex-based anisotropic smoothing of 3d mesh data. In *2006 Canadian Conference on Electrical and Computer Engineering*, pages 202–205. IEEE, 2006.

Declaration:

I declare that I have completed the thesis independently using only the aids and tools specified. I have not applied for a doctor's degree in the doctoral subject elsewhere and do not hold a corresponding doctor's degree. I have taken due note of the Faculty of Mathematics and Natural Sciences PhD Regulations, published in the Official Gazette of Humboldt-Universität zu Berlin no. 42/2018 on 11/07/2018.

Berlin, 22. Dezember 2020 Vahid Satarifard

Acknowledgement

First of all, I would like to express my sincere gratitude to my supervisor Prof. Reinhard Lipowsky for his guidance and endless support during the past years. I have learned and enjoyed a lot from all discussions we had throughout my Ph.D.

This study was supported by the International Max Planck Research School (IMPRS) on Multiscale Bio-Systems. I would like to thank the IMPRS committee for providing me with this scholarship and especially Angelo Valleriani for his clear instructions in different stages of the program.

I thank Andrea Grafmüller for her willingness to share her scientific knowledge and for always being available for open discussions. I am thankful for the time she spared for the careful reading of my thesis. Additionally, I would like to thank Rikhia and Aparna for their friendship, collaborations, and cautious reading of my thesis, I have learned a lot from them.

I would like to thank all colleagues and collaborators at the department of Theory and Bio-Systems in the Max Planck Institute of Colloids and interfaces, where this thesis has been developed; in particular, Ana Vila Verde, Markus Miettinen, Roland Knorr and Joao Robalo for so many stimulating discussions and helping me to develop new ideas. I am also grateful to Susann Weber and René Genz for being so helpful, they made my life a hundred times easier at MPI.

I thank all of my wonderful friends for always being there for me, in particular Yahya and Sadra, for their sincere friendship. A very special thanks to my parents and my siblings for their unwavering support and love. This thesis is dedicated to my beloved family and to the memory of Mojtaba Mardi, who left fingerprints of grace on our lives. You shan't be forgotten.

List of publications

Publications related to the thesis (*Equal Contribution):

- **Vahid Satarifard**, Andrea Grafmüller and Reinhard Lipowsky
  Nanodroplets at Membranes Create Tight-Lipped Membrane Necks via Negative Line Tension. ACS Nano, 12 (12), 12424-12435 (2018).

- **Vahid Satarifard**, and Reinhard Lipowsky
  Wetting of Vesicles by Nanodroplets. In preparation (2020).

- Rikhia Ghosh*, **Vahid Satarifard***, Andrea Grafmüller and Reinhard Lipowsky
  Spherical Nanovesicles Transform into a Multitude of Nonspherical Shapes. Nano Letter, 19 (11), 7703-7711 (2019).

In addition, during the work for this thesis I also contributed to the following research:

- **Vahid Satarifard**, Sadra Kashefolgheta, Ana Vila Verde and Andrea Grafmüller
  Is the Solution Activity Derivative Sufficient to Parametrize Ion-Ion Interactions? Ions for TIP5P Water. J. Chem. Theory Comput, 13 (5), 2112-2122 (2017).

- Rikhia Ghosh, **Vahid Satarifard**, Andrea Grafmüller and Reinhard Lipowsky
  Multiresponsive Behavior of Nanovesicles to Adsorption of Small Solutes: Budding, Bistable Necks, and Neck Fission. In preparation (2020).